PARTICLE-SCALE NUMERICAL SIMULATION OF THE THERMAL BEHAVIOUR OF GRANULAR MATERIALS

A thesis submitted in fulfillment of the requirements for the degree of Doctor of Philosophy of Imperial College London and the Diploma of Imperial College London by

TOKIO MORIMOTO



IMPERIAL COLLEGE LONDON

DEPARTMENT OF CIVIL AND ENVIRONMENTAL ENGINEERING

OCTOBER 2022

– DECLARATION OF ORIGINALITY –

The work presented in this thesis was carried out in the Geotechnical section of the Department of Civil and Environmental Engineering at Imperial College London.

This thesis is the result of my own work and any quotation from, or description of the work of others is acknowledged herein by reference to the sources, whether published or unpublished. This thesis is not the same as any that I have submitted for any degree, diploma or other qualification at any other university. No part of this thesis has been or is being concurrently submitted for any such degree, diploma or other qualification.

Tokio Morimoto
London, October 2022

– COPYRIGHT STATEMENT –

The copyright of this thesis rests with the author. Unless otherwise indicated, its contents are licensed under a Creative Commons Attribution-Non Commercial 4.0 International Licence (CC BY-NC).

Under this licence, you may copy and redistribute the material in any medium or format. You may also create and distribute modified versions of the work. This is on the condition that: you credit the author and do not use it, or any derivative works, for a commercial purpose.

When reusing or sharing this work, ensure you make the licence terms clear to others by naming the licence and linking to the licence text. Where a work has been adapted, you should indicate that the work has been changed and describe those changes.

Please seek permission from the copyright holder for uses of this work that are not included in this licence or permitted under UK Copyright Law.

– ABSTRACT –

Granular materials experience temperature changes in a variety of engineering applications and industrial processes including energy geostructures and packed-bed energy storage. Characterising heat transfer and the thermal expansion properties of granular materials is crucial for ensuring efficient and safe operation of many facilities and processes. As a consequence of their multi-phase nature, granular materials exhibit complex heat transfer and thermal expansion behaviours, which impose technical challenges when modelling such materials. This study conducts particle-scale numerical analyses to contribute towards a better understanding and ability to model the complex thermal behaviour of granular materials.

In this study, the Discrete Element Method (DEM) is employed to consider the movement of particles and force transmission between particles. The project included development of an existing DEM software to simulate the thermal behaviour of granular materials by considering heat transfer through particles and their thermal expansion. Heat transfer between particles is modelled using a heat pipe network model, which idealizes the system as a network of pipes to simulate heat transfer from each particle to its neighbouring particles. The effect of the fluid between the particles on the effective thermal conductance of the heat pipe is considered and validated by solving the heat equation using the Finite Element Method. Thermal expansion of particles is considered by modifying the particle radius based on the coefficient of thermal expansion and temperature of the particles. The developed thermal DEM is employed to link contact-scale properties of granular materials to sample-scale thermal properties of granular materials.

This study considers fluid flow through granular materials using a Pore Network Model (PNM), which considers a fluid pipe connecting adjacent pores. PNMs are known to be a fast method to simulate fluid flow through granular materials; however, hitherto the accuracy of PNMs has been limited due to difficulties in modelling the hydraulic conductance of fluid pipes. This study proposes a novel conductance model based on an analytical study which is validated using Computational Fluid Dynamics (CFD) simulations and which is measurably more accurate than previously proposed models.

Building upon the new por-scale fluid flow model, a pore-scale particle-fluid conduction model, which works in a thermal PNM framework, is developed based on previous studies investigating wall-fluid conduction in fluid flow through pipes. CFD simulations for regular and random packings are conducted considering the energy transport equation to validate the proposed particle-fluid conduction model.

The developed models will enable accurate and efficient particle-scale numerical simulations of the thermal behaviour of granular materials, which are useful for both industry and research in a variety of fields. Throughout this thesis the developed models are applied to advance understanding of heat transfer and thermal expansion phenomena in granular materials.

– ACKNOWLEDGEMENTS –

First of all, I am profoundly grateful to my supervisor, Prof. Catherine O'Sullivan, who has provided me with continuous support and inspirational discussions. She has also helped me stay healthy both physically and mentally, not just for my research. I also would like to thank my co-supervisor, Dr. David M. G. Taborda for his support and discussions on mathematics, physics, and finite element methods. My whole PhD study became more rigorous thanks to him. My examiners, Dr. Henry Burridge in Fluid Section at Imperial College London and Prof. Stefano Utili in Newcastle University, helped me to organise the structure of my thesis in a more effective way. I really appreciate their enthusiasm.

My special thanks to Prof. Charley Wu in University of Surrey, who has coordinated the MATHEGRAM project. He has been always proactive to maximise my experience through the project.

My gratitude is expressed to colleagues in Geotechnics Section at Imperial College - Marina Schnaider Bortolotto, who has been funded by the same research program, for discussions on thermal behaviour of sands (and also on paper work for the project), colleagues in Micromechanics Group, Tara Sassel, Dr. Peter Adesina, Dr. Deyun Liu, Dr. Sara Bandera, Dr. Budi Zhao, Dr. Hanqiao Che, Dr. Fernando Patino Ramirez, Jose Salomon, and Yohei Nakamichi for conducting inspirational collaboration studies with me and their friendship beyond research, and Dr. Kika Moeller and Dr. Camelia Dominguez Quintans for being supportive flatmates during the difficult COVID period.

Most of my numerical studies were conducted using Imperial College London Research Computing Service (RCS) facilities (DOI: 10.14469/hpc/2232), which enabled extensive parametric studies and thought experiments.

This PhD project was funded by the European Union's Horizon 2020 research and innovation programme under the Marie Sklodowska-Curie Grant agreement MATHEGRAM No 813202. This project would not have been possible without their financial support. In addition, they provided opportunities for collaborations with other researchers in different fields, which certainly broadened my horizons. I really appreciate the programme.

– CONTENTS –

List of Figures **17**

List of Tables **25**

List of Acronyms **27**

List of Symbols **29**

1 Introduction **39**

1.1 Background 39
1.2 Scope of research 40
1.3 Research objectives 41
1.4 Outline of thesis 43

Part I: Analyses of system responses with stagnant pore fluids **45**

2 Literature review **47**

2.1 Introduction 47
2.2 Heat transfer within granular materials with stagnant pore fluids 47
2.2.1 Mechanisms of heat transfer within granular materials with stagnant pore fluid 47
2.2.2 Fully-resolved numerical simulation of heat transfer within granular materials with stagnant pore fluids 52
2.2.3 Heat pipe network model 53
2.3 Effects of temperature change on granular materials 60
2.3.1 Thermal expansion of materials 60
2.3.2 Key observations on the effects of temperature change on granular materials 61
2.4 Discrete Element Method to study the response of granular materials to changes in temperature 62
2.4.1 Mechanical part 62

2.4.2 Thermal behaviour of particles 65
2.5 Summary 65

3 Development and validation of thermal DEM **69**
3.1 Introduction 69
3.2 Development of thermal DEM 70
3.3 Validation and verification of thermal DEM 70
3.3.1 Validation of the implemented modified BOB model 70
3.3.2 Validation of the implemented heat pipe network model with the modified BOB model 71
3.3.3 Verification of transient heat transfer simulations using the implemented heat pipe network model 74
3.4 Summary 75

4 Linking elastic stiffness and thermal conduction of granular materials **79**
4.1 Background 79
4.2 Analytical modelling 80
4.2.1 Use of Effective Medium Theory (EMT) to Determine Elastic Moduli 80
4.2.2 Relationship between the ETC and Packing Characteristics and Elastic Moduli 83
4.3 Numerical Modelling Using DEM 85
4.3.1 Sample Generation Using the Discrete Element Method (DEM) 86
4.3.2 Small Deformation Probes to Determine Elastic Moduli 93
4.3.3 Heat Transfer Simulations 98
4.4 Exploring the link between the ETC and Packing Characterisitcs, Elastic Moduli and Stress Level 100
4.4.1 Young's Modulus and ETC 100
4.4.2 Effective Thermal Conductivity 100
4.4.3 Proposed Expression Relating the ETC to Young's Modulus and Void Ratio 104
4.5 Summary 105

5 Thermal stress in granular materials **109**
5.1 Background 109
5.2 Analytical model 110
5.2.1 Analytical estimate of stress 110
5.2.2 Increment in contact force 111
5.2.3 Analtyical estimation of stress increase 111
5.3 DEM simulation approach 113

5.3.1 Sample generation . . . 113
5.3.2 Isotropic compression . . . 113
5.3.3 Radius expansion . . . 116
5.4 Comparison of analytical model and DEM results . . . 116
5.4.1 Regular packings . . . 117
5.4.2 Random packings . . . 117
5.5 Improving the analytical model using DEM results . . . 120
5.6 Summary . . . 124

6 Effect of cyclic temperature variations on granular materials 129
6.1 Background . . . 129
6.2 Methodology . . . 130
6.2.1 Model parameters . . . 130
6.2.2 Simulation procedure . . . 132
6.3 Sample homogeneity . . . 134
6.4 Evolution of mechanical strain . . . 136
6.4.1 Concept of mechanical strain . . . 136
6.4.2 Effect of initial void ratio and anisotropic degree on mechanical strain evolution . . . 141
6.4.3 Effect of magnitude of isotropic stress . . . 144
6.5 Evolution of packing characteristics due to thermal cycles . . . 146
6.6 Summary . . . 146

Part II: Analyses of system responses with pore fluids flowing 149

7 Literature review 151
7.1 Introduction . . . 151
7.2 Governing equations of incompressible viscous fluid flow . . . 151
7.3 Analysis of fluid flow behaviour using dimensionless numbers . . . 152
7.3.1 Reynolds number . . . 152
7.3.2 Peclet number . . . 153
7.3.3 Prandtl number . . . 154
7.3.4 Characteristic length . . . 154
7.4 Numerical simulations of fluid flow through granular materials . . . 155
7.4.1 Fully-resolved CFD . . . 155
7.4.2 Coarse-grid CFD . . . 156
7.4.3 Pore Network Model . . . 156
7.4.4 Coupling DEM with CFD . . . 157
7.5 Summary . . . 157

8 Modelling fluid flow through granular materials using PNM and FVM 161
8.1 Introduction . . . 161
8.2 Pore Network Models (PNMs) . . . 162
8.2.1 Domain discretisation and local flow calculation in Pore Network Model (PNM) . . . 162
8.2.2 Local intrinsic conductance model in PNM . . . 164
8.2.3 Calculation of fluid-particle interaction force in a PNM . . . 167
8.3 Analytical study to estimate the Γ and α values of throats in regular packing of uniform spheres . . . 169
8.3.1 Global permeability of regular packing . . . 169
8.3.2 Back-calculation of Γ . . . 171
8.3.3 Variation in shape factor α with packing density for lattice packings 174
8.4 PNM and Computational Fluid Dynamics (CFD) models to assess applicability of new conductance expressions to randomly packed assemblies of spheres . . . 177
8.4.1 PNM Implementation . . . 177
8.4.2 PNM simulations . . . 178
8.4.3 OpenFOAM (OF) simulation using random packings and post-processing . . . 181
8.4.4 Empirical calculation of fluid-particle interaction force . . . 185
8.5 Analysis of PNM performance for randomly packed spheres . . . 187
8.5.1 Analysis of local flow direction . . . 187
8.5.2 α values in monodisperse packing . . . 191
8.5.3 α values in linearly graded packing . . . 193
8.5.4 α values in bimodal packing . . . 200
8.5.5 Global permeability prediction using developed models . . . 202
8.6 Fluid-particle interaction force vector from OF, a PNM and an empirical method . . . 209
8.6.1 Fluid-particle interaction force magnitude from OF and a PNM with three types of local conductance models . . . 209
8.6.2 Comparison with an empirical method . . . 215
8.7 Summary . . . 220

9 Pore-scale modelling of heat transport due to advection and conduction 227
9.1 Introduction . . . 227
9.2 Characterising particle-fluid conduction using the Nusselt number . . . 228
9.2.1 Energy transport equation and the role of the Nusselt number in a CFD-Discrete Element Method (DEM) framework . . . 228
9.2.2 Another perspective: Nusselt number of fluid flow in a pipe . . . 231

9.3 Development and validation of model predicting Nu of fluid flow in a throat in PNM based on fully-resolved CFD simulations 243
9.3.1 Overview of fully-resolved CFD simulations 244
9.3.2 Validation of fully-resolved CFD simulations 244
9.3.3 Fluid flow through regular packings 249
9.3.4 Fluid flow through random packings 252
9.4 Results 253
9.4.1 Regular packings 253
9.4.2 Random packings 259
9.5 Summary 263

10 Conclusions **265**
10.1 Summary 265
10.2 Key findings 268
10.3 Recommendations for future work 270
10.3.1 Additional research into the effective thermal conductivity of granular materials 271
10.3.2 Future study on stress induced by temperature change 272
10.3.3 Future study on volume change behaviour when thermal cycles are applied 272
10.3.4 Hydro-mechanical behaviour of granular materials 273
10.3.5 Heat transfer mechanisms in granular materials with fluid flow . 274
10.3.6 Thermo-hydro-mechanical coupled simulations 275

References **277**

Appendices **291**
A Copyright permissions 291
B Repeatability of effective thermal conductivity of DEM samples 293
C Verification of analytically determined Γ value 297
D Consideration of periodic boundaries in a pore network model 299
E Relationship between fRe and shape factor for a hydrodynamically fully-developed flow in a pipe 303

– LIST OF FIGURES –

2.1 Schematic illustration of heat transfer mechanisms in granular materials with stagnant pore fluids. 49
2.2 Schematic illustration of the conductive heat transfer through a volume element. 51
2.3 An example of mesh discretising the solid phase and fluid phase in a granular medium. Elements are coloured based on their temperature values. Reproduced from Birkholz, Gan and Kamlah (2019) with permission obtained from Elsevier. 54
2.4 Schematic illustration of definition of thermal conductance and effective thermal conductance. 55
2.5 Schematic illustration of one element within a heat pipe network model after Morimoto, O'Sullivan and Taborda (2022) (permission obtained from American Society of Civil Engineers). 56
2.6 Schematic illustration of r_{c} and h after Morimoto, O'Sullivan and Taborda (2022) (permission obtained from American Society of Civil Engineers). . . 57
2.7 Schematic illustration of the modified BOB model by Dai, Hanaor and Gan (2019) 59
2.8 Volume change of glass beads experiencing thermal cycles after Chen et al. (2006) 61
2.9 Schematic illustration of the stick (no-slip) and slip regions and the normal and shear stress distribution at the contact between two spheres. Reproduced from Otsubo (2016) under the terms of the CC BY-NC-ND 4.0 license. (a) Normal pressure distribution. (b) Shear stress distributionn with no-slip. (c) Shear stress distribution with partial slip. (d) Shear stress distribution with full slip. 66

3.1 FEM model of two particles and pore fluid after Morimoto, O'Sullivan and Taborda (2022) (permission obtained from American Society of Civil Engineers). 71

3.2 Comparison of FEM and DEM simulation results. Reproduced from Morimoto, O'Sullivan and Taborda (2022) (permission obtained from American Society of Civil Engineers). 72
3.3 Samples considered for the validation of the implemented heat pipe network model and BOB model. 73
3.4 FEM and DEM samples used for the validation of the implemented heat pipe network model. 76
3.5 Comparison of FEM (solid line) and DEM (dashed line with markers) simulation results. 77

4.1 Typical sample after Morimoto, O'Sullivan and Taborda (2022) (permission obtained from American Society of Civil Engineers) 88
4.2 Packing characteristics of the samples after Morimoto, O'Sullivan and Taborda (2022) (permission obtained from American Society of Civil Engineers). For IC and K0 samples, there are 5 samples for each stress level (5 different e values). For TCUL and TEUL samples, there are 15 samples for each stress level (5 different e values and 3 different a values). 91
4.3 Stress-strain relationships during probes after Morimoto, O'Sullivan and Taborda (2022) (permission obtained from American Society of Civil Engineers). 96
4.4 E_z and E_x values of the samples after Morimoto, O'Sullivan and Taborda (2022) (permission obtained from American Society of Civil Engineers). . . 97
4.5 Relationship between k^*_{zz}/k_{f} and e after Morimoto, O'Sullivan and Taborda (2022) (permission obtained from American Society of Civil Engineers). . . 99
4.6 Relationship between k^*_{ii}/k_{f} and E_i after Morimoto, O'Sullivan and Taborda (2022) (permission obtained from American Society of Civil Engineers). Grayscale gives the values of e so that a darker color indicates a denser. The symbol shape indicates the sample type. 101
4.7 E_{DEM} and E_{EMT} after Morimoto, O'Sullivan and Taborda (2022) (permission obtained from American Society of Civil Engineers) 102
4.8 Plots regarding $k^{\beta*}_{ij}$ and k^{h*}_{ij} ($\kappa = 500$) after Morimoto, O'Sullivan and Taborda (2022) (permission obtained from American Society of Civil Engineers). The symbol shape indicates the stress level. The symbol color indicates the sample type. 103
4.9 Actual and predicted $k^*_{ii}/k_{\mathrm{ref}}$ values after Morimoto, O'Sullivan and Taborda (2022) (permission obtained from American Society of Civil Engineers). The symbol shape indicates the stress level. The symbol color indicates the sample type. 106

5.1 Schematic illustrations of a change in (a) the contact overlap δ and (b) the contact force F after a temperature change from T to $T + \Delta T$. 112

5.2 Typical samples 115

5.3 Comparison between Analytical and DEM $\sigma_{\text{iso},T+\Delta T}$ values ($\sigma_{\text{iso},T}$ = 100 kPa). Reproduced from Morimoto, O'Sullivan and Taborda (2021), under the terms of the CC BY 4.0 license. 121

5.4 Error in $\Delta\sigma_{\text{iso},\Delta T}$ versus normalised mean particle displacement. (a) normalised by particle radius R_T. (b) normalised by $R_T\alpha_{\text{L}}\Delta T$. 122

5.5 Normalised mean particle displacement versus the packing variable $\mathcal{P}$. (a) normalised by particle radius R_T. (b) normalised by $R_T\alpha_{\text{L}}\Delta T$. 125

5.6 Comparison between corrected analytical and DEM $\sigma_{\text{iso},T+\Delta T}$ values ($\sigma_{\text{iso},T}$ = 100 kPa). 126

6.1 Particle size distribution (PSD). 131

6.2 Temperature distribution in a sample during a transient heat transfer simulation. 135

6.3 Sample homogeneity analysis of ISO-100-L. 137

6.4 Sample homogeneity analysis of ISO-100-D. 138

6.5 Sample homogeneity analysis of ANI3%-100-L. 139

6.6 Sample homogeneity analysis of ANI3%-100-D. 140

6.7 Volume change behaviour of ISO-100-L due to thermal cycles. 141

6.8 Evolution of $\varepsilon_{\text{mech}}$ of a sample with $\sigma_{\text{iso}} = 100$ kPa during temperature cycles. 142

6.9 Volume change behaviour of Toyoura sand with a variety of void ratios due to thermal cycles after Ng, Wang and Zhou (2016). 144

6.10 Evolution of the $\varepsilon_{\text{mech}}$ values in samples with numbeer of temperature cycles. 145

6.11 Volume change behaviour of loose Toyoura sand specimens with different σ_{iso} values due to thermal cycles after Ng, Wang and Zhou (2016). 145

6.12 Volume change behaviour of loose DEM samples with different σ_{iso} values due to thermal cycles. 146

6.13 Evolution of the $\overline{Z}$ values in sampleswith number of temperature cycles. . . 147

6.14 Evolution of the a values in samples with number of temperature cycles. . . 148

7.1 Schematic illustration of the three types of CFD methods to simulate fluid flow through particles 158

8.1 Schematic illustration of the PNM framework. (a) three-dimensional (3D) schematic illustrations of fluid domain discretization using the weighted Delaunay triangulation (b) two-dimensional (2D) schematic illustration of definition of pores, throats, pore centres and two adjacent pores. The yellow spheres mark the location of the nodes, the turquoise blue lines are the edges of the network, i.e. the pore connections. p_a and p_b are the pressures at pore a and b, respectively, Q_{ab} is the volume flow rate from pore a to pore b and L_{ab} is the length of throat ab. Reproduced from Morimoto et al. (2022), under the terms of the CC BY 4.0 license. 163

8.2 Schematic illustration of throat face geometries with a definition of an inscribed circle. (a) Closed throat face. (b) Throat face with a large open edge. Reproduced from Morimoto et al. (2022), under the terms of the CC BY 4.0 license. 165

8.3 Schematic illustration of the total volume of throat ab (V_{ab}), the volume of the fluid in throat ab (Θ_{ab}) and the surface area ($\gamma_{m,ab}$) and the volume ($V_{m,ab}$) of sphere segment m. Reproduced from Morimoto et al. (2022), under the terms of the CC BY 4.0 license. 167

8.4 Schematic illustration of $A_{m,ab}$ and A_{f}. 168

8.5 Schematic illustration of connected pores, unit throats, and unit throat faces in Simple Cubic (SC), Body Centred Cubic (BCC), Face Centred Cubic (FCC) packings. Reproduced from Morimoto et al. (2022), under the terms of the CC BY 4.0 license. 170

8.6 Schematic illustration of connected pores, unit throats, and unit throat faces in SC, BCC, FCC packings. Reproduced from Morimoto et al. (2022), under the terms of the CC BY 4.0 license. 175

8.7 Back-calculated α values for a variety of packings and void ratios. (a) α vs e^*. (b) α vs ξ. Reproduced from Morimoto et al. (2022), under the terms of the CC BY 4.0 license. 176

8.8 Particle Size Distribution (PSD) considered in this study for OF simulations using random packings. 179

8.9 Schematic illustration of OF simulations using FCC packings for validation. (a) The geometry of an FCC model and the pressure distribution (b) Mesh seeds on a sphere surface ($D_{\mathrm{min}}/30$) and the definition of ds_c. Reproduced from Morimoto et al. (2022), under the terms of the CC BY 4.0 license. . . 183

8.10 Validation of OF study results in terms of c_{d} versus e using FCC packings. Reproduced from Morimoto et al. (2022), under the terms of the CC BY 4.0 license. 183

8.11 Geometry of a random packing OF model with a flow velocity field ($Cu = 1.01$, $e = 1.525$). Reproduced from Morimoto et al. (2022), under the terms of the CC BY 4.0 license. 184
8.12 Schematic illustration on the definition of θ^{q}. Reproduced from Morimoto et al. (2022), under the terms of the CC BY 4.0 license. 188
8.13 Distribution of θ^{q}. Reproduced from Morimoto et al. (2022), under the terms of the CC BY 4.0 license. 188
8.14 An example of faces whose flow direction a PNM failed to capture. Face geometry was transformed based on the OF flow vector, which shows that the flow is not normal to the throat face. Reproduced from Morimoto et al. (2022), under the terms of the CC BY 4.0 license. 189
8.15 Comparison of normalized local volume flow rate (in $[m^3 s^{-1}]$) between OF and PNM (*HR* model with $\alpha_{\mathrm{HR}} = 1/8$) for a packing with $Cu = 1.01$ and $e = 0.536$. (a) Coloured by θ^{q} values. (b) Markers with $0 < \theta^{\mathrm{q}} < \pi/4$ are highlighted. Reproduced from Morimoto et al. (2022), under the terms of the CC BY 4.0 license. 191
8.16 Variation in α with e^*: comparison of an OF simulation and analytical models for $Cu = 1.01$ and $e = 0.764$. Marker colour gives the maximum angle of the throat face ($\theta^{\mathrm{tri}}_{\mathrm{max}}$). Reproduced from Morimoto et al. (2022), under the terms of the CC BY 4.0 license. 194
8.17 Variation in $\alpha_{\text{ER-HR}}$ with ξ: comparison of an OF simulation and analytical models for $Cu = 1.01$ and $e = 0.764$. Marker colour gives the maximum angle of the throat face ($\theta^{\mathrm{tri}}_{\mathrm{max}}$). 194
8.18 Variation in α with e^*: comparison of an OF simulation and analytical models for $Cu = 1.01$ and $e = 0.536$. Marker colour gives the maximum angle of the throat face ($\theta^{\mathrm{tri}}_{\mathrm{max}}$). Reproduced from Morimoto et al. (2022), under the terms of the CC BY 4.0 license. 195
8.19 Variation in $\alpha_{\text{ER-HR}}$ with ξ: comparison of an OF simulation and analytical models for $Cu = 1.01$ and $e = 0.536$. Marker colour gives the maximum angle of the throat face ($\theta^{\mathrm{tri}}_{\mathrm{max}}$). 195
8.20 Variation in α_{ER} with e^*: comparison of an OF simulation and analytical models for $Cu = 1.01$ and $e = 0.764$. Marker colour gives the normalised throat length (L_{ab}/r_{eff}). Reproduced from Morimoto et al. (2022), under the terms of the CC BY 4.0 license. 196
8.21 Variation in α with e^*: comparison of an OF simulation and analytical models for $Cu = 2.00$ and $e = 0.751$. Marker colour gives the maximum angle of the throat face ($\theta^{\mathrm{tri}}_{\mathrm{max}}$). Reproduced from Morimoto et al. (2022), under the terms of the CC BY 4.0 license. 197

8.22 Variation of $\alpha_{\text{ER-HR}}$ with ξ: comparison of an OF simulation and analytical models for $Cu = 2.00$ and $e = 0.751$. Marker colour gives the maximum angle of the throat face ($\theta^{\text{tri}}_{\text{max}}$). 197
8.23 Variation in α with e^*: comparison of an OF simulation and analytical models for $Cu = 2.00$ and $e = 0.468$. Marker colour gives the maximum angle of the throat face ($\theta^{\text{tri}}_{\text{max}}$). Reproduced from Morimoto et al. (2022), under the terms of the CC BY 4.0 license. 198
8.24 Variation in $\alpha_{\text{ER-HR}}$ with ξ: comparison of an OF simulation and analytical models for $Cu = 2.00$ and $e = 0.468$. Marker colour gives the maximum angle of the throat face ($\theta^{\text{tri}}_{\text{max}}$). 198
8.25 Variation in α_{ER} with e^*: comparison of an OF simulation and analytical models for $Cu = 2.00$ and $e = 0.468$. Marker colour gives the normalised throat length (L_{ab}/r_{eff}). Reproduced from Morimoto et al. (2022), under the terms of the CC BY 4.0 license. 199
8.26 Four types of throat faces in a gap graded sphere packing with $SR = 4.0$. . 202
8.27 Variation in α with e^*: comparison of an OF simulation and analytical models for $SR = 4.00$, $FC = 0.35$ and $e = 0.351$. Marker colour gives the types of the throat face. 203
8.28 Variation in α with ξ: comparison of an OF simulation and analytical models for $SR = 4.00$, $FC = 0.35$ and $e = 0.351$. Marker colour gives the types of the throat face. 203
8.29 Variation in α with e^*: comparison of an OF simulation and analytical models for $SR = 4.00$, $FC = 0.11$ and $e = 0.550$. Marker colour gives the types of the throat face. 204
8.30 Variation in α with ξ: comparison of an OF simulation and analytical models for $SR = 4.00$, $FC = 0.11$ and $e = 0.550$. Marker colour gives the types of the throat face. 204
8.31 Two throat topologies which have a similar $\alpha_{\text{ER-HR}}$ value but a different e^* value. (a) one of F-F-C faces in the packing with $SR = 4.0$ ($\alpha_{\text{ER-HR}} = 0.133$, $e^* = 0.307$, $\xi = 0.612$). (b) a throat face of the densest SC packing ($\alpha_{\text{ER-HR}} = 0.114$, $e^* = 0.910$, $\xi = 0.594$). 205
8.32 Variation in global permeabilities with e: comparison of an OF simulation and analytical models based on e^* for random dense linearly graded packings. Reproduced from Morimoto et al. (2022), under the terms of the CC BY 4.0 license. 206
8.33 Varaition in global permeabilities with e: comparison of an OF simulation and a PNM with the $\alpha_{\text{ER-HR}}(e^*)$ and $\alpha_{\text{ER-HR}}(\xi)$ for random dense linearly graded packings. 207

8.34 Comparison of global permeabilities between an OF simulation and a PNM with the *HR*, $\alpha_{\text{ER-HR}}(e^*)$, and $\alpha_{\text{ER-HR}}(\xi)$ models for random dense bimodal packings for $SR = 2$. 210
8.35 Comparison of global permeabilities between an OF simulation and a PNM with the *HR*, $\alpha_{\text{ER-HR}}(e^*)$, and $\alpha_{\text{ER-HR}}(\xi)$ models for random dense bimodal packings for $SR = 4$. 211
8.36 Comparison of the normalised drag force obtained from the OF and PNM simulations for linearly graded PSD with $Cu = 1.01$, $e = 0.610$. 212
8.37 Comparison of the normalised drag force obtained from the OF and PNM simulations for linearly graded PSD with $Cu = 2.00$, $e = 0.603$. 212
8.38 Comparison of the normalised drag force obtained from the OF and PNM simulations for bimodal PSD with $SR = 2$, $FC = 0.10$, $e = 0.610$. 213
8.39 Comparison of the normalised drag force obtained from the OF and PNM simulations for bimodal PSD with $SR = 2$, $FC = 0.35$, $e = 0.608$. 215
8.40 Comparison of the normalised drag force obtained from the OF and PNM simulations for bimodal PSD with $SR = 4$, $FC = 0.11$, $e = 0.460$. 215
8.41 Comparison of the normalised drag force on fine particles obtained from the OF and PNM simulations for bimodal PSD with $SR = 4$, $FC = 0.11$, $e = 0.460$. 216
8.42 Comparison of the normalised drag force obtained from the OF and PNM simulations for bimodal PSD with $SR = 4$, $FC = 0.35$, $e = 0.536$. 216
8.43 Comparison of the normalised drag force on fine particles obtained from the OF and PNM simulations for bimodal PSD with $SR = 4$, $FC = 0.35$, $e = 0.536$. 216
8.44 Relative error in normalised fluid-particle interaction force versus particle diameter normalised by D_{min} for the linearly graded random dense packing with $Cu = 1.01$, $e = 0.610$. 218
8.45 Relative error in normalised fluid-particle interaction force versus particle diameter normalised by D_{min} for the linearly graded random dense packing with $Cu = 2.00$, $e = 0.603$. 219
8.46 Probability density function of relative error in $\overline{F^{f\to p}}$ for the bimodal random dense packing with $SR = 2$, $FC = 0.10$ and $e = 0.610$. 221
8.47 Probability density function of relative error in $\overline{F^{f\to p}}$ for the bimodal random dense packing with $SR = 4$, $FC = 0.11$ and $e = 0.460$. 222
8.48 Schematic illustration on the definition of $\theta^{\mathbf{F}}{}_{\text{PNM}}$ and $\theta^{\mathbf{F}}{}_{\text{global}}$. 223
8.49 The probability distribution of $\cos\theta^{\mathbf{F}}$. For PNM, $\alpha_{\text{ER-HR}}(\xi)$ model was used. (a) Linearly graded PSD with $Cu = 2.00$ and $e = 0.603$ (b) Gap graded PSD with $SR = 4.0$, $FC = 0.11$, and $e = 0.11$. 224

9.1 Schematic illustration of the thermal PNM proposed by Caulk et al. (2020) (in 2D for simplicity). 229
9.2 Schematic illustration of velocity profile of laminar fluid flow in a pipe. . . 235
9.3 Schematic illustration of temperature profile of laminar fluid flow in a pipe. 235
9.4 Schematic illustration on the calculation of an analytically-derived temperature driving force 237
9.5 Comparison of the Mean Temperature Difference (MTD) and the Logarithmic Mean Temperature Difference (LMTD) 240
9.6 The geometry of the validation case. 245
9.7 Comparison results at $D/ds_c = 50$ against previous CFD studies (Romkes et al., 2003; Calis et al., 2001). 248
9.8 Geometry of regular packings. (a) SC (b) SC throat (c) BCC (d) BCC throat (e) FCC (f) FCC throat. (a), (c), and (e) are coloured based on the velocity and (b), (d), and (f) are coloured based on the heat flux. 251
9.9 2D Schematic illustration of the definition of inlet and outlet velocities ($\mathbf{u}_{\text{in}}$ and $\mathbf{u}_{\text{out}}$), inlet and outlet face normal ($\mathbf{u}_{\text{in}}$ and $\mathbf{u}_{\text{out}}$) and particle surface heat flux q_{h} for analysis of a whole throat. 252
9.10 Variation of $\overline{Nu}_{d_{\text{h}}}$ with L^*: comparison between two definitions of ϑ (LMTD and MTD). 254
9.11 Variation of $\overline{Nu}_{d_{\text{h}}}$ with L^*: comparison between the densest SC, BCC, FCC packings, and a circular pipe. 256
9.12 Variation of $\overline{Nu}_{d_{\text{h}}}$ with L^*: comparison between SC, BCC and FCC packings with a similar density. 257
9.13 $\alpha_{\text{HR}}\overline{Nu}_{d_{\text{h}}}$ versus L^* for the BCC packings with different void ratios. 258
9.14 $\alpha_{\text{HR}}^{1/3}\overline{Nu}_{d_{\text{h}}}$ versus L^* for the BCC packings with different void ratios. 259
9.15 Nu of throats in three types of regular packings with various void ratios and Nu predicted by Eq. (9.54). 260
9.16 Actual Nu and predicted Nu for $Pc = 150$. 261
9.17 Actual Nu and predicted Nu for $Pc = 15$. 262

– LIST OF TABLES –

2.1 Thermal conductivity of a variety of materials. 50

3.1 Comparison of simulation conditions and results between Yun and Evans (2010) and this study 74

4.1 Simulation parameters 87
4.2 Sample size effect after Morimoto, O'Sullivan and Taborda (2022) (permission obtained from American Society of Civil Engineers) 90
4.3 ω_{E}, ω_{e} and R^2 after Morimoto, O'Sullivan and Taborda (2022) (permission obtained from American Society of Civil Engineers). 105

5.1 DEM simulation parameters. Reproduced from Morimoto, O'Sullivan and Taborda (2021), under the terms of the CC BY 4.0 license. 114
5.2 Validity of assumptions 117
5.3 Analytical $\sigma_{\mathrm{iso},T+\Delta T}$ values for the regular packings. Reproduced from Morimoto, O'Sullivan and Taborda (2021), under the terms of the CC BY 4.0 license. 118
5.4 DEM $\sigma_{\mathrm{iso},T+\Delta T}$ values for the regular packings. Reproduced from Morimoto, O'Sullivan and Taborda (2021), under the terms of the CC BY 4.0 license. . 118
5.5 e_T and $\overline{Z}_T$ values of the random packings. Reproduced from Morimoto, O'Sullivan and Taborda (2021), under the terms of the CC BY 4.0 license. . 118
5.6 Differences in $\Delta\sigma_{\mathrm{iso},\Delta T}$ values between the analytical model and the DEM result (*Fix* case). Reproduced from Morimoto, O'Sullivan and Taborda (2021), under the terms of the CC BY 4.0 license. 119
5.7 $\overline{Z}_{T+\Delta T}$ from the DEM result (*Fix* case). 120
5.8 Differences in $\Delta\sigma_{\mathrm{iso},\Delta T}$ values between the analytical model and the DEM result (*Release case*). Reproduced from Morimoto, O'Sullivan and Taborda (2021), under the terms of the CC BY 4.0 license. 121
5.9 $\overline{Z}_{T+\Delta T}$ from the DEM result (*Release* case). 123
5.10 Differences in $\Delta\sigma_{\mathrm{iso},\Delta T}$ values between the corrected analytical model and the DEM result (*Release* case). 126

6.1 Particle size distribution (PSD). 130
6.2 Samples and simulation parameters. 134

7.1 Typical values for Prandtl numbers (Coulson et al., 1999) 154

8.1 Linear graded samples used in OF and PNM simulations 180
8.2 Bimodal samples used in OF and PNM simulations 180
8.3 Tabular summary of distributions of $\theta^{\mathbf{q}}$ values for various packings. 190
8.4 Tabular summary of X_1, X_2 and X_3 values in Eq. (8.60) for a variety of packings. 193
8.5 Tabular summary of PCC and R^2 values of analytical and the least squares (LSQ) best-fit to the OF data for various models. 201
8.6 The permeability values (in $[m^2]$) of a variety of linearly graded packings obtained from the OF and PNM simulations. The values in brackets are relative errors from the value obtained from the OF simulations. 208
8.7 The permeability values (in $[m^2]$) of a variety of bimodal packings obtained from the OF and PNM simulations. The values in brackets are relative errors from the value obtained from the OF simulations. 209
8.8 Relative error analysis in the $\overline{F^{f\to p}}$ values between OF, PNMs, and empirical method for linearly graded samples. 214
8.9 Relative error analysis in the $\overline{F^{f\to p}}$ values between OF, PNMs, and empirical method for bimodal samples. 217

9.1 Tabular summary of models predicting the Nusselt number 232
9.2 Effect of inlet and outlet region lengths on Nu 247
9.3 Effect of inlet and outlet region lengths on f 247
9.4 Effect of mesh size on Nu ($Pr = 2.28$) 248
9.5 Effect of mesh size on f 248
9.6 Effect of mesh size on Nu ($Pr = 7000$) 249
9.7 Regular packings considered in this chapter 249

– List of Acronyms –

2D	Two-dimensional
3D	Three-dimensional
BCC	Body Centred Cubic
BOB	Batchelor And O'Brien (1977)
CFD	Computational Fluid Dynamics
DEM	Discrete Element Method
EMT	Effective Medium Theory
ER model	Effective Radius Model
ETC	Effective Thermal Conductivity
FA model	Fluid Area Model
FCC	Face Centred Cubic
FD	Fully-Developed
FEM	Finite Element Method
FVM	Finite Volume Method
GZ	Graetz
HR model	Hydraulic Radius Model
LBM	Lattice Boltzmann Method
LV	Leveque
LMTD	Logarithmic Mean Temperature Difference
LSQ	Least Squares
MSP	`MeshSpherePacking`

MTD	Mean Temperature Difference
OF	OpenFOAM
PNM	Pore Network Model
PSD	Particle Size Distribution
SC	Simple Cubic
SD	Simultaneously-Developing
TNM	Thermal Network Model

– LIST OF SYMBOLS –

Subscripts

$\bullet_a$	pore a
$\bullet_{ab}$	pores a and b
$\bullet_{\mathrm{c}}$	property at particle-particle contact
$\bullet_{\mathrm{diag}}$	diagonal component of a second order tensor
$\bullet_{\mathrm{f}}$	material property of fluid
$\bullet_{\mathrm{h}}$	horizontal
$\bullet_i$	vector notation
$\bullet_{ij}$	second order tensor notation
$\bullet_{\mathrm{iso}}$	isotropic
$\bullet_m$	particle m
$\bullet_{mn}$	particles m and n
$\bullet_{\mathrm{max}}$	maximum
$\bullet_{\mathrm{min}}$	minimum
$\bullet_{\mathrm{p}}$	material property of particle
$\bullet_{\mathrm{RP}}$	regular packing
$\bullet_{\mathrm{ref}}$	reference
$\bullet_{\mathrm{s}}$	material property of solid
$\bullet_{\mathrm{v}}$	vertical

Superscripts

$\bar{\bullet}$	mean quantity
$\bullet^*$	effective quantity
$\dot{\bullet}$	rate
$\hat{\bullet}$	normalised quantity

Greek symbols

α	shape factor of a pipe $[-]$
α_{dif}	thermal diffusivity [m^2/s]
α_{L}	linear thermal expansion coefficient [/K]
α_{V}	volumetric thermal expansion coefficient [/K]
β	normalised contact radius used in the BOB model $= \frac{\kappa r_{\text{c}}}{R_{ab}}$ $[-]$
Γ	conductance multiplied by the pipe length $= \mathcal{G}L$ [m^4]
Γ_{ab}^{fp}	Γ value of a fluid pipe connecting pore a to pore b [m^4]
Γ^{RP}	Γ value of a fluid pipe in a regular packing [m^4]
γ	surface area [m^2]
γ_{ab}	solid surface area of throat ab [m^2]
$\gamma_{m,ab}$	surface area of the part of particle m touching throat ab [m^2]
γ_{Ω}	spherical surface area of a sphere segment with a solid angle Ω [m^2]
Δ	distance [m]
$\overline{\Delta}$	the mean distance between the centres of contacting particles [m]
$\Delta\bullet$	increment $[-]$
δ	contact overlap or deformation [m]
δ_h	hydrodynamic boundary layer thickness [m]
δ_t	thermal boundary layer thickness [m]
δ_{ij}	Kronecker delta
ε	strain
ζ	partial slip
η	heat rate per volume [W]
Θ	fluid volume [m^3]
Θ_{ab}	fluid volume of throat ab [m^3]
ϑ	temperature driving force [K]
θ	angle [rad]
$\theta^{\mathbf{q}}$	angle between two flow vectors [rad]
$\theta^{\mathbf{F}}$	angle between two force vectors [rad]
$\theta_{\text{max}}^{\text{tri}}$	maximum angle of a triangle [rad]
κ	ratio of the thermal conductivity of the solid phase to that of the fluid phase in a granular material $= k_{\text{s}}/k_{\text{f}}$ $[-]$
λ	normalised gap distance used in the BOB model $[-]$
μ	Dynamic viscosity [Pa·s]

μ_{fric}	friction coefficient $[-]$
ν	Poisson's ratio $[-]$
ν_{p}	particle Poisson's ratio $[-]$
ν_{vis}	kinematic viscosity [m^2/s]
Ξ	emissivity $[-]$
ξ	non-dimensional fluid volume to solid surface ratio $[-]$
Π	probability $[-]$
ρ	density [kg/m^3]
Σ	radiation constant [W/m^{2}K^4]
σ	stress [Pa]
σ_{iso}	isotropic stress [Pa]
σ	stress tensor [Pa]
σ_{dev}	deviatoric stress tensor [Pa]
τ	shear stress [Pa]
χ	parameter used in the BOB model $[-]$
ϕ	solid fraction $[-]$
ψ	angle in spherical coordinates [rad]
Ω	solid angle [sr=steradian]
$\Omega_{m,ab}$	solid angle of the part of particle m touching throat ab [sr]
ω	material constant $[-]$

Latin symbols

A	area [m^2]
A_{f}	fluid face area of throat [m^2]
$A_{m,ab}$	area of the union of particle m and the face of throat ab [m^2]
AR	aspect ratio $[-]$
a	degree of anisotropy $[-]$
$\mathcal{C}$	elasticity stiffness [Pa]
C	thermal conductance [W/K]
C^*	effective thermal conductance [W/K]
C^{*hp}	effective thermal conductance of heat pipe hp [W/K]
$C^{*(c)}$	effective thermal conductance of heat pipe c between two contacting particles [W/K]

$C^{*hp,s}$	effective thermal conductance of heat pipe hp, s between two non-contacting (separated) particles [W/K]
C_{c}	thermal conductance of a contact [W/K]
C_a	thermal conductance of particle a [W/K]
C^*_{ab}	effective thermal conductance of a heat pipe connecting particle a to particle b [W/K]
Cu	Coefficient of uniformity $[-]$
CV	Coefficient of variation $[-]$
c	specific heat [J/K·kg]
c_{p}	specific heat of a particle [J/K·kg]
c_{f}	specific heat of a fluid [J/K·kg]
c_{d}	drag coefficient $[-]$
$\mathcal{D}$	mass diffusivity [m^2/s]
D	diameter [m]
D_{p}	particle diameter [m]
D_{50}	mass median diameter [m]
d	diameter of circle or cylinder [m]
d_{h}	hydraulic diameter [m]
ds_c	mesh length [m]
$\mathcal{E}$	relative error $[-]$
E	Young's modulus [Pa]
e	void ratio $[-]$
e^*	local void ratio $[-]$
F	force $[N]$
$\overline{F}$	mean contact normal force $[N]$
$\mathbf{F}$	force vector $[N]$
$F^{f\to p}$	fluid-particle interaction force [N]
$\mathbf{F}^{f\to p}$	fluid-particle interaction force vector $= \mathbf{F}^{\mathrm{p}} + \mathbf{F}^{\mathrm{d}}$ [N]
$\mathbf{F}^{f\to p}_m$	fluid-particle interaction force on particle m [N]
$\mathbf{F}^{f\to p,CG}_m$	fluid-particle interaction force on particle m in a coarse-grid CFD [N]
$\mathbf{F}^{f\to p}_{m,ab}$	fluid-particle interaction force on particle m at throat ab [N]
$\overline{F^{f\to p}}$	normalised fluid-particle interaction force $[-]$

$F_m^{f\to p,OF}$ fluid-particle interaction force on particle m obtained from an OF simulation [N]

$\overline{F_m^{f\to p,OF}}$ normalised fluid-particle interaction force on particle m obtained from an OF simulation $[-]$

$F_m^{f\to p,PNM}$ fluid-particle interaction force on particle m obtained from a PNM simulation [N]

$\overline{F_m^{f\to p,PNM}}$ normalised fluid-particle interaction force on particle m obtained from a PNM simulation $[-]$

F^{d} viscous drag force [N]

$\mathbf{F}^{\mathrm{d}}$ viscous drag force vector [N]

$\mathbf{F}_m^d$ viscous drag force on particle m [N]

$\mathbf{F}_m^{d,CG}$ viscous drag force on particle m in a coarse-grid CFD [N]

$\mathbf{F}_{m,ab}^{\mathrm{d}}$ viscous drag force on the part of particle m at throat ab [N]

F^{p} pressure gradient force [N]

$\mathbf{F}^{\mathrm{p}}$ pressure gradient force vector [N]

$\mathbf{F}_m^p$ pressure gradient force on particle m [N]

$\mathbf{F}_m^{p,CG}$ pressure gradient force on particle m in a coarse-grid CFD [N]

$\mathbf{F}^{\mathrm{p}}{}_{m,ab}$ pressure gradient force on the part of particle m at throat ab [N]

F^{Stokes} Stokes force [N]

F_m^{Stokes} Stokes force on particle m [N]

Fo Fourier number $[-]$

$\bar{F}$ force normalised by Stokes force

$\mathbf{F}$ fabric tensor (vector notation) $[-]$

F_{ij} fabric tensor (tensor notation) $[-]$

FC fraction of fine contents by mass $[-]$

f friction factor $[-]$

$\mathcal{G}$ intrinsic conductance of a pipe [m^3]

G shear modulus [Pa]

G_{p} particle shear modulus [Pa]

G_{ij} shear modulus corresponding to shearing within the ij plane [Pa]

g hydraulic conductance of a pipe [m^3/(Pa·s)]

$\mathbf{g}$ gravity acceleration vector [$\mathrm{m/s}^2$]

H heat rate [W]

H_{ab} heat that moves from particle a to particle b [W]

H_{norm}	normalised heat $[-]$
H^{steady}	steady state heat per second [W]
$\mathcal{H}_c$	term expressing an increase in a thermal conduction through a contact area $[-]$
$\mathcal{H}_f$	term expressing a decrease in a thermal conduction through gap fluid $[-]$
h	heat transport coefficient [W/(m^{2}K)]
h	gap distance [m]
h_{ab}	gap between particles a and b [m]
I	Moment of inertia [kg·m^2]
$\mathbf{I}$	second order unit tensor $[-]$
$\mathcal{K}$	bulk modulus [Pa]
K_{sec}	secant stiffness [N/m]
K_{tan}	tangent stiffness [N/m]
k	thermal conductivity [W/(m·K)]
k^*	effective thermal conductivity [W/(m·K)]
k_{ij}^*	effective thermal conductivity tensor [W/(m·K)]
k_{ij}^{c*}	effective thermal conductivity tensor only considering heat pipes between contacting particles [W/(m·K)]
k_{ij}^{s*}	effective thermal conductivity tensor only considering heat pipes between separated particles [W/(m·K)]
$k_{ij}^{\beta*}$	effective thermal conductivity tensor depending on β [W/(m·K)]
$k_{ij}^{(h=0)*}$	effective thermal conductivity tensor only considering heat pipes between touching particles [W/(m·K)]
k_{ij}^{h*}	effective thermal conductivity tensor depending on h [W/(m·K)]
k_{h}	permeability [m^2]
$k_{\text{h,RP}}$	permeability of a regular packing [m^2]
L	length [m]
L^+	non-dimensional hydrodynamic length $[-]$
L^*	non-dimensional thermal length $[-]$
$\mathcal{L}$	characteristic length [m]
L^{fp}	length of fluid pipe fp [m]
L^{hp}	length of heat pipe hp [m]
$L^{(c)}$	length of heat pipe c between contacting particles [m]
$L^{hp,s}$	length of heat pipe hp, s between separated particles [m]

L^{RP}	length of a fluid pipe in a regular packing [m]
l	length of the unit cell of a regular packing [m]
$\mathcal{M}$	material variable $= \frac{G_\mathrm{p}}{1-\nu_\mathrm{p}}$ [Pa]
M	Moment [N·m]
m	mass [kg]
m_v	contact density [m^{-3}]
$\mathcal{N}$	material constant
N_c	number of contacts $[-]$
N_c^{p1}	number of contacts particle $p1$ has $[-]$
N_hp	number of heat pipes $[-]$
$N_\mathrm{hp,s}$	number of heat pipes between separated particles $[-]$
N_p	number of particles in the system $[-]$
N_pore	number of pores in the system $[-]$
N_p^C	number of coarse particles in the system $[-]$
N_p^F	number of fine particles in the system $[-]$
Nu	Nusselt number $[-]$
N_a	number of neighbours that particle a has $[-]$
n	porosity $[-]$
$\mathbf{n}$	unit vector $[-]$
$\mathbf{n_{ab}}$	unit vector normal to the face of throat ab and pointing from pore node a to pore node b $[-]$
n^{fp}	normal unit vector expressing the direction of fluid pipe fp $[-]$
n^{hp}	normal unit vector expressing the direction of heat pipe hp $[-]$
$n^{(c)}$	normal unit vector expressing the direction of contact c between particles $[-]$
$n^{hp,s}$	normal unit vector expressing the direction of heat pipe hp, s between separated particles $[-]$
$\mathcal{P}$	packing variable $= \frac{\overline{Z}}{1+e}$ $[-]$
P	perimeter [m]
p	pressure [Pa]
Δp^{fp}	pressure drop through pipe fp [Pa]
PCC	Pearson's correlation coefficient $[-]$
Pc	Peclet number $[-]$

Pr	Prandtl number $[-]$
Q_{f}	fluid source and/or sink [S^{-1}]
Q	volumetric flow rate [$\mathrm{m}^3\mathrm{s}^{-1}$]
Q^*	local volumetric flow rate [$\mathrm{m}^3\mathrm{s}^{-1}$]
Q^{fp}	volumetric flow rate through pipe fp [$\mathrm{m}^3\mathrm{s}^{-1}$]
q_{h}	heat flux [$\mathrm{W/m}^2$]
$\mathbf{q}_{\mathrm{h}}$	heat flux vector [$\mathrm{W/m}^2$]
$\mathbf{q}$	mass flux vector [m/s]
R	radius of particle [m]
R_m	radius of particle m [m]
R^2	coefficient of determination $[-]$
R_{ab}	equivalent radius of particles a and b [m]
R_{FEM}	radius of a quadrant in a FEM simulation [m]
Ra	Rayleigh number $[-]$
Re	Reynolds number $[-]$
r	radius of circle or cylinder [m]
r_{c}	contact radius [m]
$\overline{r_{\mathrm{c}}}$	mean contact radius [m]
r_{eff}	effective radius [m]
r_{eq}	equivalent radius [m]
r_{ic}	radius of inscribed circle [m]
r_{h}	hydraulic radius [m]
Sc	Schmidt number $[-]$
SD	standard deviation
SR	size ratio $[-]$
STR	stress ratio $[-]$
$\mathbf{s}$	face area vector [m^2]
T	temperature [K]
T_{AVG}	average absolute temperature [K]
T^o	bulk temperature [K]
T_{lower}	temperature of the lower boundary [K]
T_{upper}	temperature of the upper boundary [K]
∇T	temperature gradient [K/m]

t	time [s]
u	flow velocity [m/s]
u_{inlet}	inlet flow velocity [m/s]
V	volume [m^3]
V_{ab}	volume of throat ab (solid and fluid phases) [m^3]
$V_{m,ab}$	volume of the part of particle m touching throat ab [m^3]
V_Ω	spherical volume of a sphere segment with a solid angle Ω [m^3]
v	velocity [m/s]
w	angular velocity [rad/s]
X	Constant for a LSQ fitting $[-]$
$\mathbf{x}$	coordinates [m]
x_m	normalised volume of particle m used in van der Hoef, Beetstra and Kuipers (2005) $[-]$
Y	Number generated by random number generator $[-]$
y_m	normalised diameter of particle m used in van der Hoef, Beetstra and Kuipers (2005) $[-]$
Z	coordination number $[-]$
$\overline{Z}$	mean coordination number $[-]$

CHAPTER 1

INTRODUCTION

1.1 Background

Granular materials, which consist of solid particles and fluid-filled pores, are widely encountered as forms of soil, chemical products, food grains, pharmaceutical tablets etc. In general, granular materials behave differently from both pure solids and fluids and their responses to mechanical and thermal loading is often complex. Examining these responses are of great importance for many engineering and industrial applications. In many situations and processes granular materials experience temperature changes, for example: sintering, fresh concrete, and stored food grains subject to seasonal temperature variations. In geotechnical engineering, understanding the effects of heating on soil is an emerging problem.

Energy geo-structures, which are a recently developed air conditioning method, are particularly useful in cold regions where a significant amount of energy is consumed in heating buildings. Energy geo-structures include different types of foundations that exchange heat between an upper structure and soil around the geo-structure while supporting the upper structure mechanically (Laloui & Di Donna, 2013). Air conditioning systems that exploit energy geo-structures are more efficient, and thus more environmentally friendly, than conventional air conditioners, which exchange heat with the open air. However, soils near energy geo-structures may experience heat cycles of approx. ± 40 °C (Bourne-Webb et al., 2009) due to alternating heat extraction and release by energy geo-structures. The consequences of the repeated heat cycles are not well understood.

Previous studies (Voight & Faust, 1982; Cecinato, Zervos & Veveakis, 2011; Alonso, Zervos & Pinyol, 2016) have pointed out that in landslides frictional heat may be generated in shear bands. The frictional heat may be sufficient to increase the temperature of the soil in and adjacent to the shear band to more than 100 °C in 10 seconds according to numerical

analyses by Cecinato, Zervos and Veveakis (2011). If such a rapid rise in temperature happens, the pore water pressure will increase due to the thermal expansion of the pore-water being larger than that of the soil skeleton. As a result, there may be a reduction in shear strength, contributing to the development of the instability. Characterisation of the permeability of the soil and heat transfer due to fluid movement in the soil is essential to assess the additional hazard posed by the response of soil to temperature changes during landslides.

Laboratory experiments have been the primary research tool to investigate the macroscopic or overall response of samples of granular material including soil to both mechanical and thermal loading. During thermal or mechanical loading, numerous particle-particle and particle-fluid interactions take place within the granular material. While these interactions determine the thermo-mechanical behaviour of the material, they cannot be easily measured or observed in laboratory experiments. Accurate numerical studies are essential to examine the fundamental mechanisms underlying the complex thermo-mechanical behaviour to complement these experimental studies.

The Discrete Element Method (DEM) originally proposed by Cundall and Strack (1979) is a powerful numerical tool to simulate granular particles; however, the orignial DEM only considers the mechanical behaivour of the particles; specifically contact between particles and movement of particles. Recently, a variety of numerical frameworks to simulate multi-physical behaviour of granular materials by coupling the DEM with other numerical methods have been proposed. However, these frameworks are either "fast but inaccurate" or "accurate but slow" due to challenges involved in modelling the microscopic (particle-scale) thermal behaviour of granular materials.

1.2 Scope of research

The overall aim of this study is to make a contribution towards the understanding of the fundamental mechanisms underlying the complex thermo-mechanical behaviour of granular materials that are either dry or fully saturated with a liquid. This study focuses on the DEM coupled with other numerical methods to consider heat transfer and liquid flow through granular materials in addition to the mechanical behaviour of particles. A heat pipe network model for heat transfer and a pore network model for fluid flow, which are accepted numerical frameworks, are employed to enable computationally efficient simulations. In a heat pipe network model, the granular system is idealised as a network of pipes to simulate heat transfer from each particle to its neighbouring particles. In a pore network model, the pore region of the granular system is descretised into pores and a fluid pipe is considered between adjacent pores. In a heat pipe network model, a model

predicting the thermal conductance of the system consisting of two particles and gap fluid is necessary, while in a pore network model, a model predicting the conductance of the fluid pipes is required. In addition, heat conduction between fluid and particles has been rarely modelled in previous pore-scale studies. This study focuses on tackling some of the shortcomings of existing models and proposes new, more accurate particle-scale heat transfer and fluid flow models. Analytical studies and numerical simulations (Finite Element Method and Finite Volume Method) are conducted to aid the development of the novel models. This study also examines upscaling from particle-scale properties to the macro-scopic thermal behaviour of granular materials.

1.3 Research objectives

This doctoral research has made three distinct contributions to advancing particle scale simulation of the thermal response of granular materials as follows:

1. Development of the DEM coupled with a heat pipe network model and application of the developed code.
2. Development of an accurate PNM to simulate fluid flow and particle-fluid interaction.
3. Development of a particle-fluid heat transfer model for a thermal PNM.

The specific research objectives that underpin the first contribution (i.e. development and application of the DEM coupled with a heath pipe network model) were:

- Development, implementation, and validation of the DEM coupled with a heat pipe network model.
- Development, implementation, and validation of a local thermal conductance model for heat pipe network models applicable to soils.
- Implementation and validation of a thermal expansion model for particles.
- Exploration of how the packing characteristics of a granular medium affect its thermal properties (effective thermal conductivity, thermal stress, and thermal volume change).
- Development of a model to predict thermal properties of a granular medium from particle-scale data.

The developed thermal DEM can complement experimental studies to investigate the thermal behaviour of granular materials in research and industry. Such experiments are challenging and require specially-designed apparatus and measurement tools. The details on the implementation provided here are of value to both research groups and

software companies who are working to develop DEM software for applications outside of geotechnical engineering. Consequently, this fundamental analysis of the coupling of a heat pipe model with DEM has potential applications beyond the examples given in Chapters 4 to 6 of this thesis.

The research objectives identified to deliver the second contribution (i.e. an accurate PNM) were:

- Development of an accurate local conductance model for a PNM to simulate fluid flow from one void to another.
- Development of a dataset on local flow field and fluid-particle interaction forces using Finite Volume Method (FVM) with a mesh that is sufficiently fine to resolve fluid flow around particles.
- Validation of a PNM that includes the novel conductance model using the dataset generated using FVM.

A PNM with the developed local conductance models can be used to investigate hydro-mechanical behaviour of granular materials as well as thermal behaviour of granular materials. There are many practical applications related to hydro-mechanical processes in granular materials e.g. liquefaction phenomenon of sand during seismic event and suffusion phenomenon i.e. migration of fine particles in gap graded granular soil. The development of a PNM that can simulate the fluid particle interaction forces with reasonable accuracy is essential to enable fundamental analysis of these phenomena; the more established coupling strategies for DEM that use a continuum based approach to model the fluid phase cannot simulate systems that are sufficiently large to be meaningful for engineering practice.

The specific research objectives required to deliver the third contribution (i.e. a particle-fluid heat transfer mode) were identified as

- Development of an accurate model to describe heat conduction between particles and fluid for implementation in a PNM to simulate heat transfer in granular materials with pore fluid flowing.
- Development of a dataset on heat fluxes between particles and fluid using FVM model with a fine mesh.
- Validation of a PNM with the novel conductance model between particles and fluid using the FVM dataset.

A thermal PNM with the developed particle-fluid heat transfer model is an accurate and fast option to simulate industrial and engineering processes which extract or store

heat in granular particles. Again the developments described in Chapter 9 are of benefit to researchers and software companies developing DEM software for a broad range of applications.

1.4 Outline of thesis

This thesis consists of ten chapters. Chapter 1 has introduced the subject, scope and objectives of the research. The main contents of the thesis, which is divided in two parts, are outlined in this section.

The first part focuses on specific cases where the fluid flow in a granular medium can be neglected when modelling the thermal response of granular materials. Chapter 2 outlines the key response characteristics of single-phase materials subjected to a temperature change, specifically heat transfer and thermal expansion. Chapter 2 then shows that the heat transfer and thermal expansion behaviours of granular materials, which are multi-phase materials, are much more complex than in the case of single-phase materials. In addition, numerical methods to simulate behaviour of granular materials subjected to a temperature change are reviewed in Chapter 2. This review of numerical modelling focuses on discrete element methods (DEMs) and heat pipe network models. A thermal DEM, in which heat transfer between particles and thermal expansion of particles can be simulated, is proposed in Chapter 3. A heat pipe network model is used to simulate the heat transfer through a granular medium. This heat-pipe thermal model is validated using both particle-scale and continuum-scale finite element analyses. After presenting the details of the proposed thermal DEM in Chapter 3, Chapters 4 to 6 introduce a variety of applications of the thermal DEM to link macroscopic thermal properties of granular materials Chapter 4 develops an analytical study to link the effective thermal conductivity to the elastic stiffness of granular materials using the heat pipe network model and the BOB model. Chapter 5 presents the analytical study predicting thermal-induced stress in granular media using the packing properties of the granular material and the material properties of the particles. Chapter 6 presents simulation results using the thermal DEM where cyclic temperature changes are applied under an isotropic stress condition.

The latter part of the thesis considers granular materials with pore fluid flowing. Chapter 7 summarises a literature review that considered how the hydrodynamic an thermal behaviour of the fluid can be expressed and simulated. Three types of Computational Fluid Dynamics (CFD) (fully-resolved CFD, coarse-grid CFD, and PNM) are introduced. Chapter 7 argues that while PNMs are an efficient method to simulate fluid flow through granular materials the accuracy of PNMs has been compromised due to over-simplifications in the model for local-scale fluid flow. Following the discussion in Chapter 7, Chapter 8

firstly proposes a novel local-scale fluid flow model which is derived from an analytical study using regular (lattice) packings. To validate the novel model, Chapter 8 develops a dataset for fluid flow through packings of randomly placed spheres using a Computational Fluid Dynamics (CFD) simulation with a mesh that is sufficiently fine so that fluid flow around particles can be characterised (fully-resolved CFD). Finally, comparisons between a PNM with the local-scale flow model developed in the thesis and simulations using the fully-resolved CFD approach are documented in terms of local-scale permeabilities, global-scale permeabilities, and fluid-particle interaction forces on particles. After successfully modelling the fluid flow using the PNM in Chapter 8, Chapter 9 proposes a novel fluid-particle heat transfer model which can be used in a thermal PNM. A brief summary of a thermal PNM and fluid-particle heat transfer models proposed in previous studies is presented in this Chapter. It is argued that previous fluid-particle heat transfer models are formulated using sample-scale flow properties and packing properties, so that these models cannot fully characterise local heterogeneity in granular materials. Chapter 9 includes a literature review that considers previous studies considering fluid flow through circular and non-circular pipes with a constant wall temperature. Based on a model developed for non-circular pipes, Chapter 9 proposes a new local-scale fluid-particle heat transfer model for granular materials. To validate the model, a dataset for fluid flow through regular and random packings is developed using the fully-resolved CFD in Chapter 9. The particle-fluid heat transfer model is compared with the developed dataset.

Finally, conclusions drawn from the research and recommendations for future work are summarised in Chapter 10.

– PART I –

ANALYSES OF SYSTEM RESPONSES WITH STAGNANT PORE FLUIDS

CHAPTER 2

LITERATURE REVIEW

2.1 Introduction

This chapter presents a review of the literature relevant to this study to provide readers with an overview of the relevant physics and numerical methods and to summarise the outcomes and shortcomings of prior studies. There are two key aspects to the thermal behaviours of materials, namely heat transfer and thermal expansion, thus, this chapter consists of two main sections. Section 2.2 reviews the heat transfer mechanisms within granular materials and summarises approaches that have been used to model heat transfer. Section 2.3 reviews complex thermo-mechanical behaviour arising from the thermal expansion of the granular particles. Section 2.4 considers methods to simulate the complex thermo-mechanical behaviour.

2.2 Heat transfer within granular materials with stagnant pore fluids

2.2.1 Mechanisms of heat transfer within granular materials with stagnant pore fluid

Granular materials consist of a solid particle phase and a pore fluid phase, therefore there are a number of mechanisms for heat transfer through granular materials. This study considers heat transfer through sand (particle diameter $(D) < 2$ mm) at a moderate temperature ($T < 500$ K). In this case, radiative heat transfer is negligible (Wakao & Kato, 1969; Johansen, 1977). In addition, the initial contributions in the study presented in this thesis consider the case where assumes that the pore fluid is stagnant; thus, advective heat transfer due to the fluid flow is neglected and the pore fluid can be treated as a static

continuum material existing between the solid particles. Consequently, only conductive heat transfer needs to be considered. Considering two particles with different temperatures in contact and stagnant pore fluid existing between them (Fig. 2.1(a)), conductive heat transfer takes place through the solid particles and the pore fluid as shown in Fig. 2.1(b).

Fourier's law states that the heat flux within a continuum is proportional to the negative sign of the temperature gradient within the continuum (Fourier, 1878). Fourier's law is expressed as

$$\mathbf{q}_{\mathrm{h}} = -k\nabla T \tag{2.1}$$

where $\mathbf{q}_{\mathrm{h}}$ is the heat flux in W/m^2, k is the thermal conductivity of the material in W/m · K, and ∇T is the gradient of the temperature in K/m. Fourier's law is an empirical relationship based on experimental observations (Fourier, 1878). Fourier's law can be applied within a solid particle using the thermal conductivity of the solid particle (k_{s}) as shown in Fig. 2.1(b). Fourier's law is also applicable within the pore fluid by using the thermal conductivity of the fluid (k_{f}) as shown in Fig. 2.1(b). The thermal conductivity values of common solids, fluids and soil minerals are summarised in Table 2.1. Although it is difficult to experimentally measure the thermal conductivity of a sand grain, it can be estimated from the mineral composition as in Lee et al. (2016). Referring to Table 2.1, in general, the thermal conductivity value increases in the order of a gas, a liquid, a nonmetal solid, and a metal solid.

Using Fourier's law (Eq. (2.1)), a general partial differential equation of the temperature (T) can be derived in terms of time (t) and the Cartesian coordinates (x, y, and z) as following (Fourier, 1878). Considering a volume element with lengths of dx, dy, and dz shown in Fig. 2.2, the heat flux through the face at $x = x + \mathrm{d}x$ ($q_{\mathrm{h},x}|_{x=x+\mathrm{d}x}$) is expressed using the heat flux through the face at $x = x$ ($q_{\mathrm{h},x}|_{x=x}$) as

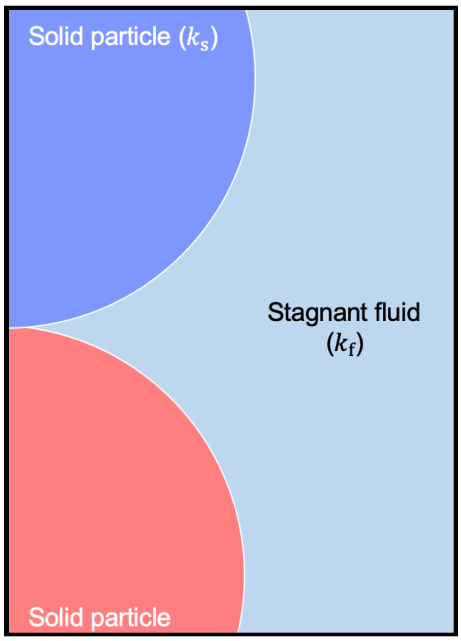
$$q_{\mathrm{h},x}|_{x=x+\mathrm{d}x} = q_{\mathrm{h},x}|_{x=x} + \frac{\partial q_{\mathrm{h},x}}{\partial x}\mathrm{d}x \tag{2.2}$$

The nex flux resulting from the conductive heat transfer through the two faces is

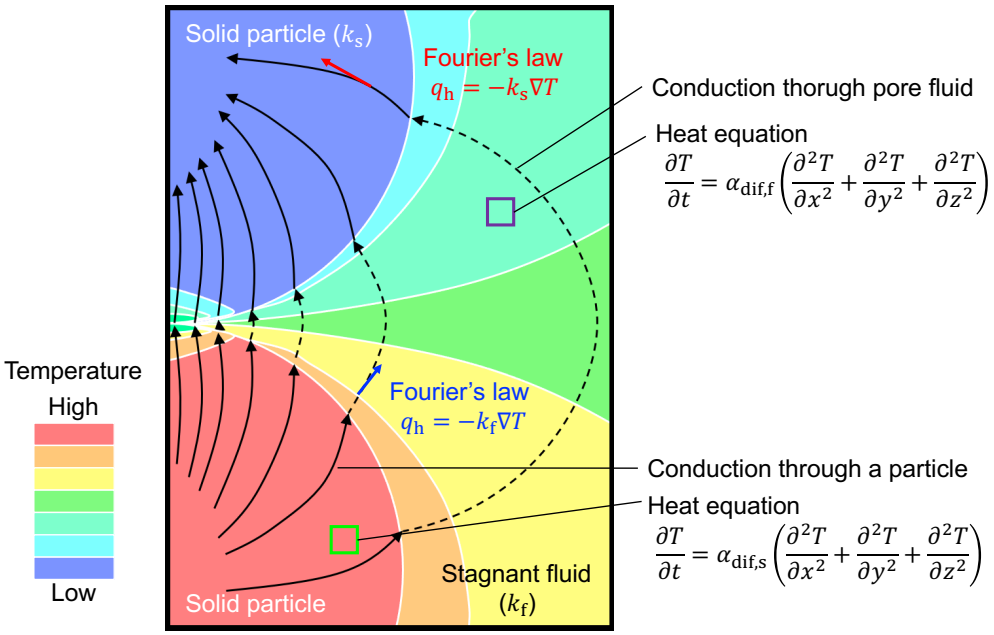
$$(q_{\mathrm{h},x}|_{x=x} - q_{\mathrm{h},x}|_{x=x+\mathrm{d}x})\mathrm{d}y\mathrm{d}z\mathrm{d}t = -\left(\frac{\partial q_{\mathrm{h},x}}{\partial x}\mathrm{d}x\right)\mathrm{d}y\mathrm{d}z\mathrm{d}t \tag{2.3}$$

Combining Eq. (2.1) and Eq. (2.3),

$$-\left(\frac{\partial q_{\mathrm{h},x}}{\partial x}\mathrm{d}x\right)\mathrm{d}y\mathrm{d}z\mathrm{d}t = -\left(\frac{\partial(-k\frac{\partial T}{\partial x})}{\partial x}\mathrm{d}x\right)\mathrm{d}y\mathrm{d}z\mathrm{d}t = k\frac{\partial^2 T}{\partial x^2}\mathrm{d}x\mathrm{d}y\mathrm{d}z\mathrm{d}t \tag{2.4}$$



(a) Schematic illustration of two particles in contact and stagnant pore fluids between the particles.



(b) Schematic illustration of the temperature distribution and heat flux within the system shown in (a). Black lines indicate the heat flux and white lines indicate the temperature contours.

Figure 2.1: Schematic illustration of heat transfer mechanisms in granular materials with stagnant pore fluids.

Table 2.1: Thermal conductivity of a variety of materials.

Classification	Material	Thermal conductivity	Temperature	Source
Gas	Air	0.0268	35 °C	Nozad, Carbonell and Whitaker (1985)
	Helium	0.1567	27 °C	Lide (2004)
Liquid	Glycerol	0.294	35 °C	Nozad, Carbonell and Whitaker (1985)
	Water	0.623	35 °C	Nozad, Carbonell and Whitaker (1985)
Nonmetals	Urea-formaldehyde	0.744	35 °C	Nozad, Carbonell and Whitaker (1985)
	Glass	1.09	35 °C	
	Quartz (parallel to c-axis)	12	0 °C	Lide (2004)
	Quartz (perpendicular to c-axis)	6.8	0 °C	Lide (2004)
Metals	Stainless steel (#302)	21.5	35 °C	Nozad, Carbonell and Whitaker (1985)
	Bronze (SAE 464)	117.1	35 °C	
	Aluminum	218.1	35 °C	
Geological materials (nonmetals)	Quartz	7.70±0.88	20 °C	Brigaud and Vasseur (1989)
	Calcite	3.26±0.23		
	Dolomite	5.33±0.26		
	Anhydrite	6.32±0.13		
	Smectite	1.88±0.15		
	Kaolonite	2.64±0.20		
	Chlorite	3.26±0.25		
	Illite	1.85±0.54		

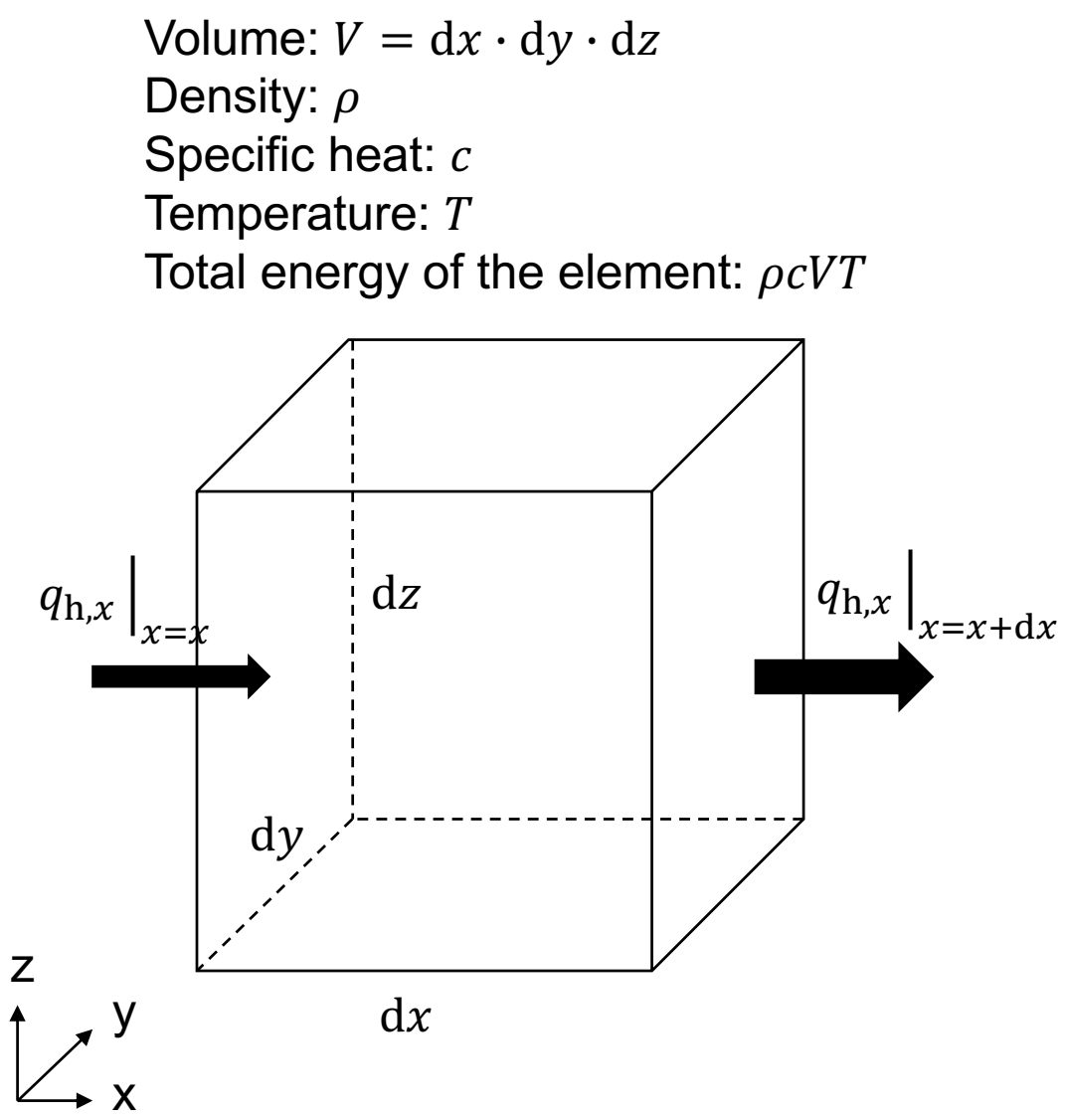


Figure 2.2: Schematic illustration of the conductive heat transfer through a volume element.

The calculation outlined in Eqs. (2.2) to (2.4) also can be carried out for y and z directions, and then the net flux from the conductive heat transfer through all the faces of the element is calculated as

$$k\left(\frac{\partial^2 T}{\partial x^2}+\frac{\partial^2 T}{\partial y^2}+\frac{\partial^2 T}{\partial z^2}\right)\mathrm{d}x\mathrm{d}y\mathrm{d}z\mathrm{d}t \tag{2.5}$$

The net flux in Eq. (2.5) results in a temperature change in the volume. Using the specific heat (c in J/K·kg) and the density (ρ in kg/m^3) of the volume, the total energy change in the volume is written in terms of the temperature change of the volume as:

$$\rho c\mathrm{d}x\mathrm{d}y\mathrm{d}z\left(\frac{\partial T}{\partial t}\mathrm{d}t\right) \tag{2.6}$$

Combining Eqs. (2.5) and (2.6),

$$\rho c\frac{\partial T}{\partial t}=k\left(\frac{\partial^2 T}{\partial x^2}+\frac{\partial^2 T}{\partial y^2}+\frac{\partial^2 T}{\partial z^2}\right) \tag{2.7}$$

Eq. (2.7) can be rewritten using the thermal diffusivity ($\alpha_{\text{dif}}=k/\rho c$ in m^2/s) as

$$\frac{\partial T}{\partial t}=\alpha_{\text{dif}}\left(\frac{\partial^2 T}{\partial x^2}+\frac{\partial^2 T}{\partial y^2}+\frac{\partial^2 T}{\partial z^2}\right) \tag{2.8}$$

Eq. (2.8) is called as heat equation. The heat equation can be applied within the solid particle using the thermal diffusivity of the solid particle ($\alpha_{\text{dif,s}}$). The heat equation also governs the temperature change and distribution of the stagnant pore fluid.

2.2.2 Fully-resolved numerical simulation of heat transfer within granular materials with stagnant pore fluids

Due to the complex geometry existing in granular materials and different material properties for the solid phase and the fluid phase, it is generally impossible to obtain the analytical solution (the time history and the distribution of the temperature) of Eq. (2.8) in granular materials with stagnant pore fluids. However, the numerical solution can be obtained by discretising the solid particles and pore fluid domains into small elements (such that shown in Fig. 2.3) and solving the heat equation for each element using a computer. There are several numerical methods to solve the heat equation e.g. traditional Finite Element Method (Fei & Narsilio, 2020), Fast Fourier Transformation (Calvet, Vanson & Masson, 2022) and the Lattice Boltzmann Method (Askari, Ikram & Hejazi, 2017). In this thesis, this type of numerical simulations, where the mesh is fine enough to represent the geometry of the

granular medium, is called as a "fully-resolved" numerical simulation. A fully-resolved numerical solution result depends on the resolution of the mesh so it is important to ensure that the mesh is fine enough by conducting preliminary studies varying the mesh size. The main disadvantage of this type of numerical simulations is the very significant computer resources required. Thus, it is impractical to simulate a representative element volume of granular materials using this type of method. It is also computationally too expensive to study cases where heat transfer takes place and particles thermally expanding at the same time.

2.2.3 Heat pipe network model

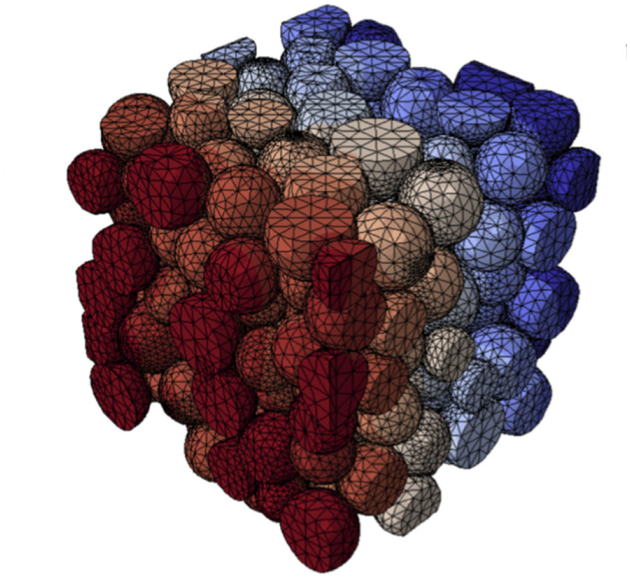
As discussed above, solving the heat equation numerically is computationally expensive, and thus some modellings are required to feasibly simulate heat transfer through granular materials. Heat pipe network models are efficient approaches to simulate heat transfer within a granular medium (Cheng, Yu & Zulli, 1999; Vargas & McCarthy, 2001; Siu & Lee, 2004; Yun & Evans, 2010). Before introducing the concept of a heat pipe network model, it is useful to define the thermal conductance of a medium. Adopting the one-dimensional form of Eq. (2.1), the heat conduction through an element of a continuum with a constant cross-sectional area A and a length L (Fig. 2.4(a)) can be described as:

$$H = q_{\mathrm{h}} A = -kA\frac{\Delta T}{L} = -C\Delta T \tag{2.9}$$

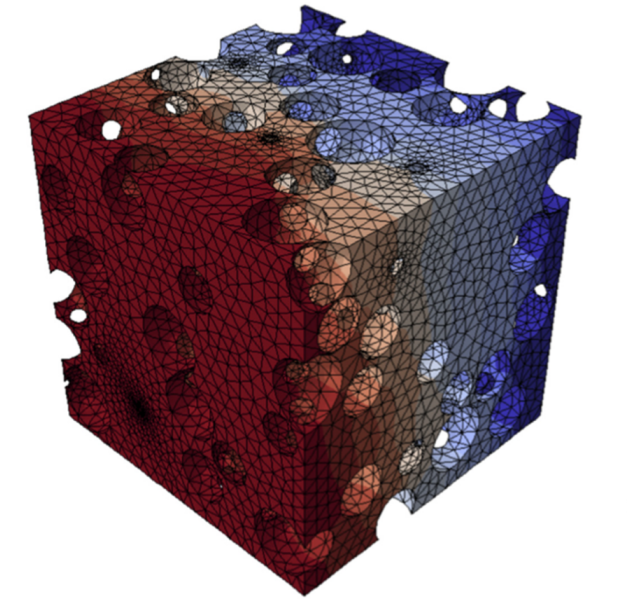
where H is the amount of heat transferred per unit time, C is the thermal conductance, and ΔT is the temperature difference across the element. For a continuum, the thermal conductance C is equivalent to kA/L. For a multi-phase system with an arbitrary shape such as the system consisting of two particles in contact and pore fluid between (Fig. 2.4(b)), the "effective" thermal conductance (C^*) is defined as

$$C^* = -\frac{H}{\Delta T} \tag{2.10}$$

In the heat pipe network model, each particle is assumed to be isothermal, with a heat core whose temperature represents the particle's temperature. If two particles, $p1$ and $p2$, are in contact or sufficiently close to each other, a heat pipe is created between these particles. Supposing that the effective thermal conductance of the system consisting of the two particles (in contact or separated) and the pore fluid (C^*_{p1p2}) is available, the amount of heat moving from particle $p1$ to particle $p2$ per unit time (H_{p1p2}) is calculated following Eq. (2.9):

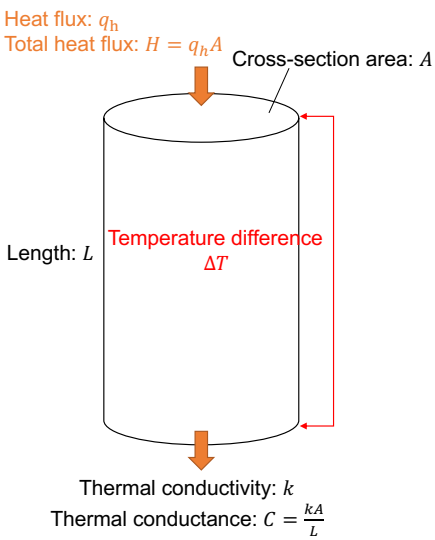


(a) Solid phase.

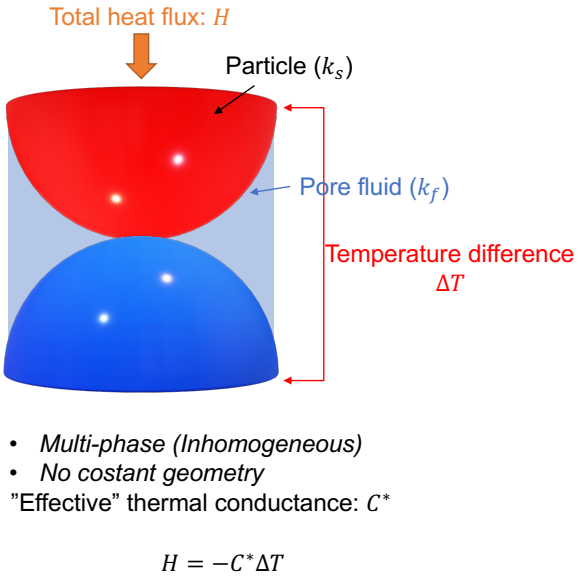


(b) Fluid phase.

Figure 2.3: An example of mesh discretising the solid phase and fluid phase in a granular medium. Elements are coloured based on their temperature values. Reproduced from Birkholz, Gan and Kamlah (2019) with permission obtained from Elsevier.



(a) Continuum.



(b) System consisting of two particles in contact and pore fluid between.

Figure 2.4: Schematic illustration of definition of thermal conductance and effective thermal conductance.

$$H_{p1p2} = -C^*_{p1p2}\left(T_{p1} - T_{p2}\right) \tag{2.11}$$

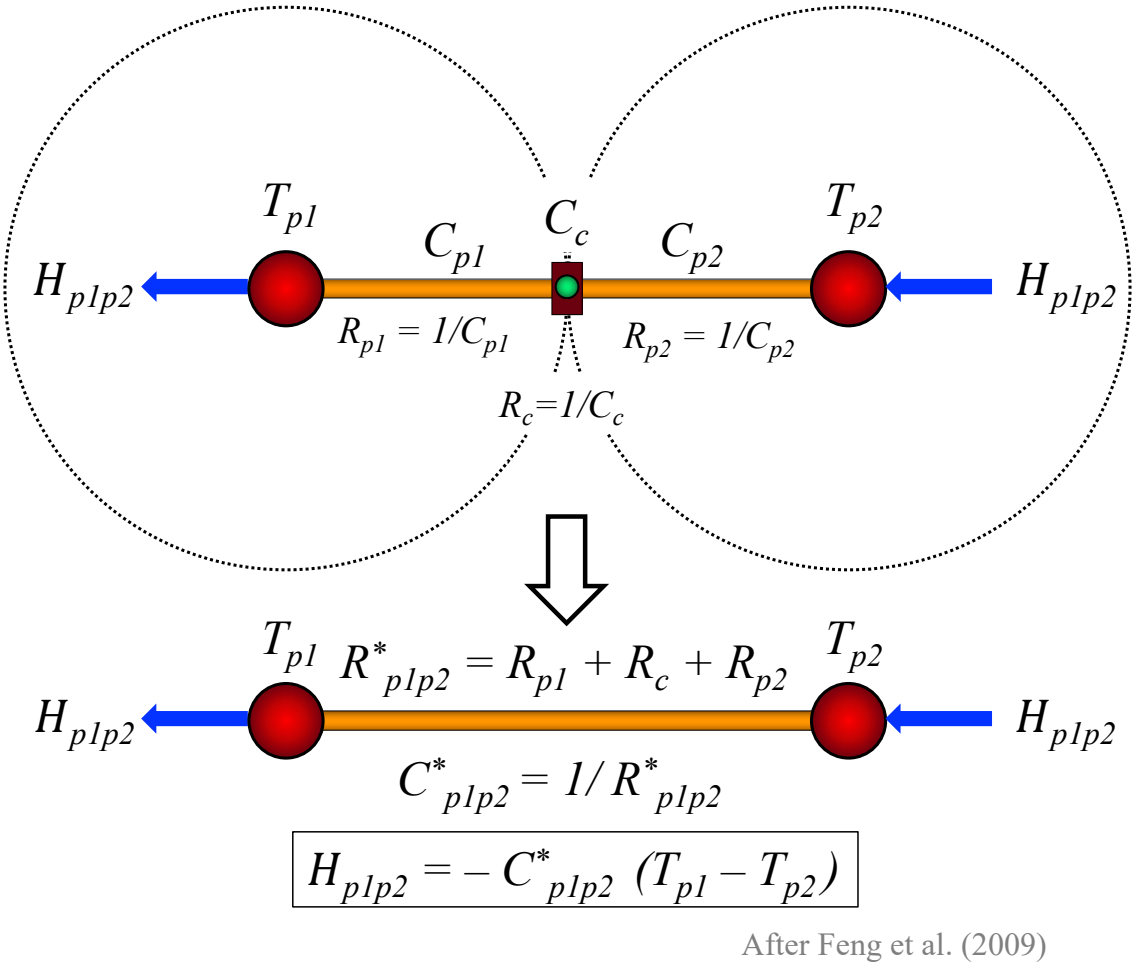
The increment in the temperature of particle $p1$ ($\Delta T_{p1}^{(\Delta t)}$) is then calculated as:

$$\Delta T_{p1}^{(\Delta t)} = \frac{\sum_{p2=1}^{N_c{}^{(p1)}} H_{p1p2}\Delta t}{c_{p1} m_{p1}} \tag{2.12}$$

where $N_c{}^{(p1)}$ is the number of the contacts involving particle $p1$, and c_{p1} and m_{p1} are the specific heat capacity and the mass of the particle $p1$, respectively. The temperature of particle $p1$ at timestep $t + \Delta t$ is calculated by:

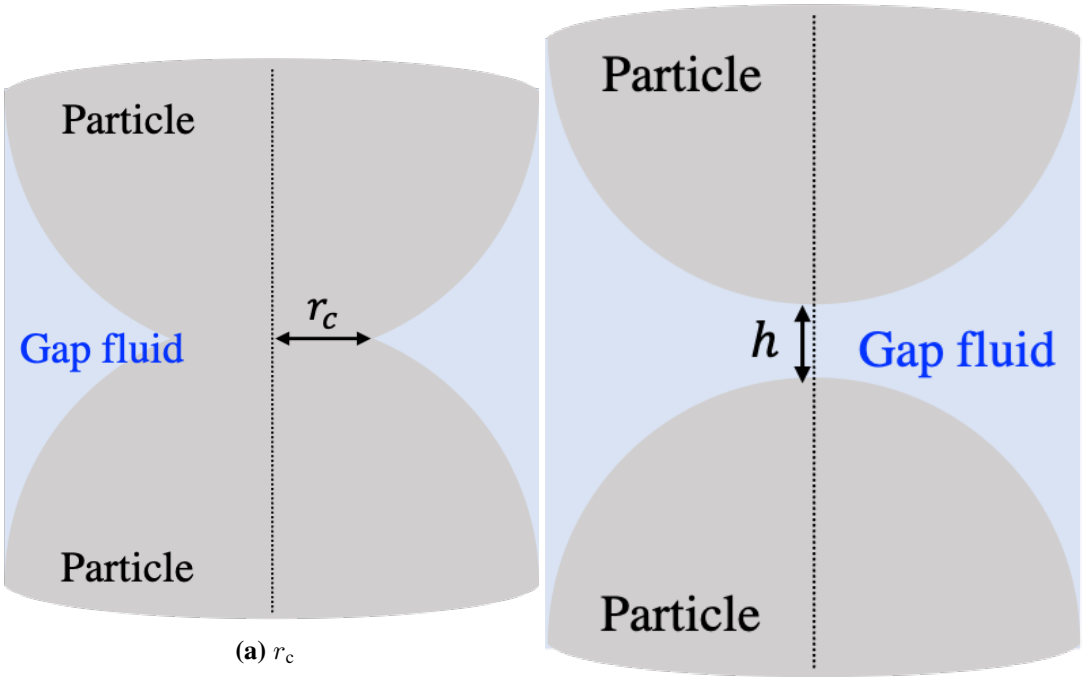
$$T^{(t+\Delta t)} = T^{(t)} + \Delta T_{p1}^{(\Delta t)} \tag{2.13}$$

Repeating Eqs. (2.11) to (2.13), the distribution and time history of a granular sample can be obtained. The main advantage of the heat pipe network model is that number of elements is much less than in the fully-resolved approach and thus the simulation is much faster. However, the accuracy of a heat pipe network model depends on the choice of the model predicting the effective thermal conductance.



After Feng et al. (2009)

Figure 2.5: Schematic illustration of one element within a heat pipe network model after Morimoto, O'Sullivan and Taborda (2022) (permission obtained from American Society of Civil Engineers).



(a) r_c **(b)** h

Figure 2.6: Schematic illustration of r_c and h after Morimoto, O'Sullivan and Taborda (2022) (permission obtained from American Society of Civil Engineers).

Batchelor and O'Brien (BOB) model

An appropriate model for the effective thermal conductance of heat pipes (Eq. (2.25)) needs to be selected to simulate heat transfer within a granular medium. Batchelor and O'Brien (1977) conducted an analytical study of heat conduction through two particles considering the fluid in the gap between the two particles just adjacent to the contact point (Fig. 2.6). Referring to Fig. 2.6, they modelled the thermal conductance of the contact and the gap fluid between two particles (C_c) as a function of the contact radius, r_c, if the two particles are contacting, and as a function of the gap distance, h, if the two particles are separated (Fig. 2.6). Kanuparthi et al. (2008) and Yun and Evans (2010) implemented this model in their heat pipe network models, and obtained good agreement with experimental results. Dai, Hanaor and Gan (2019) conducted particle-scale FEM analyses where they varied the thermal conductivity ratio, κ, and confirmed the excellent agreement between the FEM results and a modified version of the original Batchelor and O'Brien (BOB) model for a wide range of κ values (4 to 1000). In addition, Yun and Evans (2010) and Dai, Hanaor and Gan (2019) demonstrated that a pipe-network model employing the BOB model agrees very well with experimental data for various solid-fluid combinations under different stress levels (glass-air, glass-water, sand-air, sand-water, and steel-air).

A brief summary of the modified BOB model proposed in Dai, Hanaor and Gan (2019) as implemented for the current study is provided here. If two particles are separated, the

conductance ($C_c^{separated}$) through the pore fluid is based on a dimensionless number λ which depends on h:

$$\lambda = \kappa^2 \frac{h}{R_{p1p2}} \tag{2.14}$$

where R_{p1p2} is is the harmonic mean of the radii of particles $p1$ and $p2$ (R_{p1} and R_{p2}, respectively):

$$R_{p1p2} = \frac{2R_{p1}R_{p2}}{R_{p1} + R_{p2}} \tag{2.15}$$

Dai, Hanaor and Gan (2019) found that the following expressions for $C_c^{separated}$ agree well with their FEM simulation results where particles are not contacting:

$$C_c^{separated} = \begin{cases} \pi k_{\mathrm{f}} R_{p1p2} \ln\left(\kappa^2\right) & (\lambda < 0.01) \\ \pi k_{\mathrm{f}} R_{p1p2} \ln\left[1 + R_{p1p2}/h\right] & (\lambda > 100) \\ \text{Minimum value of the above two} & (\text{otherwise}) \end{cases} \tag{2.16}$$

Where there is contact between particles $p1$ and $p2$, the $C_c^{contact}$ proposed by Dai, Hanaor and Gan (2019) is given as:

$$C_c^{contact} = \pi k_{\mathrm{f}} R_{p1p2} \left(\mathcal{H}_c\left(\beta\right) + \mathcal{H}_f\left(\beta\right) + \ln\left(\kappa^2\right)\right) \tag{2.17}$$

where β is a dimensionless number defined by Batchelor and O'Brien (1977) as a function of r_{c}/R_{p1p2}:

$$\beta = \kappa \frac{r_{\mathrm{c}}}{R_{p1p2}} \tag{2.18}$$

and r_{c} is calculated based on Hertzian contact theory as:

$$r_{\mathrm{c}} = \sqrt{\frac{R_{p1p2}(R_{p1} + R_{p2} - \Delta)}{2}} \tag{2.19}$$

where Δ is the distance between the centroids of the two contacting particles. $\mathcal{H}_c\left(\beta\right)$ in Eq. (2.17) expresses an increase in the heat conduction through the contact due to an increase in the contact radius (r_{c}) (Batchelor & O'Brien, 1977). In turn, $\mathcal{H}_f\left(\beta\right)$ in Eq. (2.17) expresses a decrease in the heat conduction through the pore fluid due to an increase in the contact radius (r_{c}). When $\beta = 0$ i.e. when the contact radius, r_{c}, is zero, $\mathcal{H}_c\left(\beta\right) = \mathcal{H}_f\left(\beta\right) = 0$ and Eq. (2.17) is identical to Eq. (2.16) when the gap distance h is zero. Dai, Hanaor and Gan (2019) proposed the following expressions for $\mathcal{H}_c\left(\beta\right)$ and $\mathcal{H}_f\left(\beta\right)$:

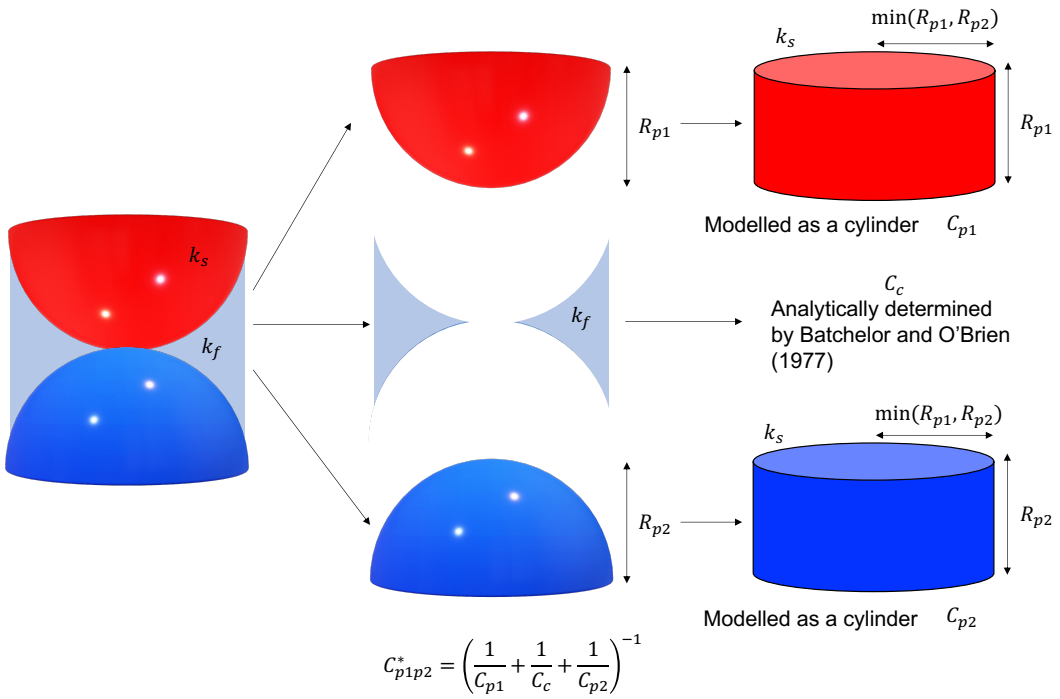


Figure 2.7: Schematic illustration of the modified BOB model by Dai, Hanaor and Gan (2019)

$$\mathcal{H}_c(\beta) = \begin{cases} 0.22\beta^2 & (\beta < 1) \\ 2\beta/\pi & (\beta > 100) \\ \text{Linear interpolation between the above two} & (\text{otherwise}) \end{cases} \tag{2.20}$$

$$\mathcal{H}_f(\beta) = \begin{cases} -0.05\beta^2 & (\beta < 1) \\ -\ln\beta^2 & (\beta > 100) \\ \text{Linear interpolation between the above two} & (\text{otherwise}) \end{cases} \tag{2.21}$$

Substituting Eq. (2.20) and Eq. (2.21) into Eq. (2.17), for a given contact, the combined thermal conductance through the contact area and the pore fluid is written as:

$$C_c^{contact} = \begin{cases} \pi k_f R_{p1p2}\left(0.17\beta^2 + \ln(\kappa^2)\right) & (\beta < 1) \\ \pi k_f R_{p1p2}\left(2\beta/\pi - \ln\beta^2 + \ln(\kappa^2)\right) & (\beta > 100) \\ \text{Linear interpolation between the above two} & (\text{otherwise}) \end{cases} \tag{2.22}$$

Dai, Hanaor and Gan (2019) modeled each particle as a cylinder to determine its thermal conductance (Fig. 2.7), with the conductance of each of the contacting particles $p1$ and $p2$ being given by:

$$C_{p1\,or\,p2} = \frac{\pi \left(\chi \min\left[R_{p1}, R_{p2}\right]\right)^2 k_{\mathrm{s}}}{R_{p1\,or\,p2}} \tag{2.23}$$

where the parameter χ is a function of κ (Dai, Hanaor & Gan, 2019):

$$\chi = 1.3121\kappa^{-0.19} \tag{2.24}$$

Alternatively, the parameter χ can be calibrated from laboratory experimental data as in Yun and Evans (2010).

Finally C^*_{p1p2}, the effective thermal conductance of the heat pipe established between particles $p1$ and $p2$ is calculated from C_{p1}, C_{p2} and C_{c} as:

$$C^*_{p1p2} = \left(\frac{1}{C_{p1}} + \frac{1}{C_{\mathrm{c}}} + \frac{1}{C_{p2}}\right)^{-1} \tag{2.25}$$

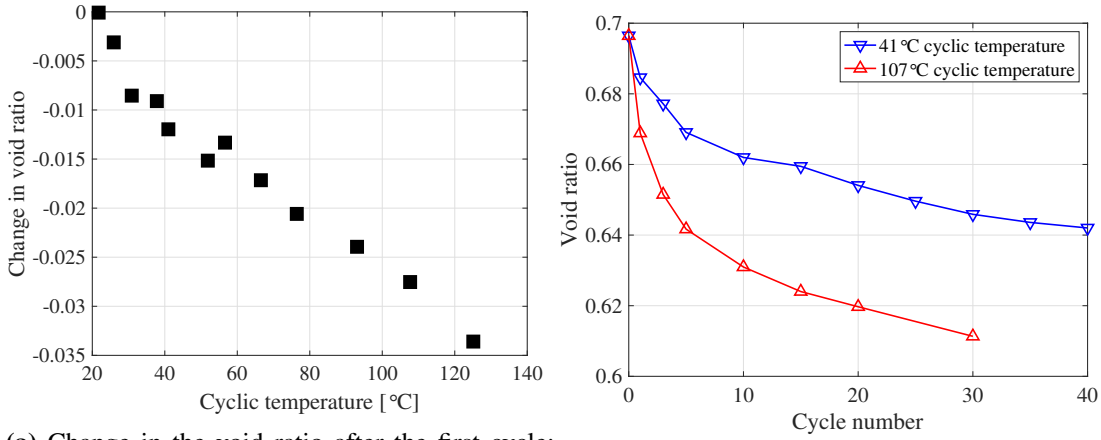
2.3 Effects of temperature change on granular materials

In this section, an overview of the relevant physics and model on the effects of temperature changes on granular materials. This study does not consider the phase change of the particles and the pore fluid e.g. the freezing and evaporation of the pore fluid and the sintering of the particles are not considered in this study.

2.3.1 Thermal expansion of materials

When a rise in the temperature of a single-phase material takes place, the vibration of atoms (or molecules) becomes more frequent, which results in a larger distance between atoms (or molecules). This phenomenon can be observed as a volume change of the material, which will be referred to as 'thermal expansion' of the material hereinafter. From the perspective of mass conservation, the thermal expansion is equivalent to a decrease in the density of the material. The thermal expansion of a material is characterised using linear or volumetric thermal expansion coefficient (α_{L} or α_{V}), which are defined as

$$\alpha_{\mathrm{L}} = \frac{1}{L}\frac{\mathrm{d}L}{\mathrm{d}T} \tag{2.26}$$



(a) Change in the void ratio after the first cycle: effect of the magnitude of the temperature

(b) Void ratio versus number of thermal cycles

Figure 2.8: Volume change of glass beads experiencing thermal cycles after Chen et al. (2006)

$$\alpha_{\mathrm{v}} = \frac{1}{V}\frac{\mathrm{d}V}{\mathrm{d}T} \tag{2.27}$$

under a constant stress condition.

If the strain of the material is fixed, there is an increase in the stress of the material (thermal stress). If a granular medium is subjected to a temperature change, such a thermal expansion/contraction of solid particles and pore fluid takes place, which leads to a complex mechanical behaviour of the medium.

2.3.2 Key observations on the effects of temperature change on granular materials

Chen et al. (2006) revealed that if heating-cooling cycles are applied to a granular material, a densification of the granular material happens due to the rearrangement of the solid particles. They placed glass beads in a cylinder with no vertical loading and applied heat cycles to the beads by putting the cylinder in a heater and then in a room with a constant temperature. Their results show that even one heat cycle induced a settlement (densification) of the beads (Fig. 2.8(a)) and additional settlement developed in each cycle. They applied a maximum of 40 heat cycles and the settlement continued to develop (Fig. 2.8(b)). It is noteworthy that measurable settlements occurred even with a moderate cyclic temperature amplitude of 40 °C. Their experiments indicate that the long-term use of energy geo-structures may lead to the settlement of upper structures.

A similar volume change behaviour was observed for sand under an oedometric condition (Nadimi & Fonseca, 2016; Pan, Coulibaly & Rotta Loria, 2022) and under a traixial condition (Ng, Wang & Zhou, 2016), which can be associated with the migration of some

particles due to the thermal expansion of individual particles. Therefore, the thermal expansion of granular materials is much more complex than a single phase material and to investigate such a complex behaviour, a sophisticated particle-scale numerical method is required.

2.4 Discrete Element Method to study the response of granular materials to changes in temperature

This section introduces the Discrete Element Method (DEM), which is a powerful numerical tool to simulate granular materials originally proposed by Cundall and Strack (1979). In the original DEM, only the mechanical behaviour of particles is considered; thus, simulating the thermal behaviour of particles requires modification of the algorithm. This section introduces the formulation of the mechanical part in the DEM then discusses how the thermal behaviour of particles can be additionally taken into account in the DEM.

2.4.1 Mechanical part

In the DEM, the mechanical behaviour of each particle is governed by Newton's second law:

$$m_{p1}\frac{\mathrm{d}\mathbf{v}_{p1}}{\mathrm{d}t} = m_{p1}\mathbf{g} + \sum_{p2=1}^{N_{\mathrm{c}}^{p1}}(F_{\mathrm{N},p1p2}\mathbf{n}_{p1p2} + F_{\mathrm{T},p1p2}\mathbf{t}_{p1p2}) \tag{2.28}$$

$$\mathbf{I}_{p1}\frac{\mathrm{d}\mathbf{w}_{p1}}{\mathrm{d}t} = \sum_{p2=1}^{N_{\mathrm{c}}^{p1}}(\mathbf{r}_{p1p2} \times (F_{\mathrm{T},p1p2}\mathbf{t}_{p1p2})) \tag{2.29}$$

where

- m_{p1} = mass of particle $p1$
- $\mathbf{v}_{p1}$ = velocity vector of particle $p1$
- $\mathbf{g}$ = gravity acceleration vector
- N_{c}^{p1} = number of contacts particle $p1$ has
- $p2$ = particle $p2$ in contact with particle $p1$
- $F_{\mathrm{N},p1p2}$ = the magnitude of the normal force acting between particles $p1$ and $p2$
- $\mathbf{n}_{p1p2}$ = the unit vector expressing the direction of normal force $F_{\mathrm{N},p1p2}$
- $F_{\mathrm{T},p1p2}$ = the magnitude of the tangential force acting between particles $p1$ and $p2$

- $\mathbf{t}_{p1p2}$ = the unit vector expressing the direction of tangential force $F_{\mathrm{T},p1p2}$
- $\mathbf{I}_{p1}$ = moment of inertia of particle $p1$
- $\mathbf{w}_{p1}$ = the angular velocity of particle $p1$
- $\mathbf{r}_{p1p2}$ = the distance vector from the torque axis to the center of mass for $F_{\mathrm{T},p1p2}$

There are several models to calculate the contact normal force between particles $p1$ and $p2$ ($F_{\mathrm{N},p1p2}$). The simplest model is the linear spring model, where the contact normal force is determined using the normal secant stiffness of the contact ($K_{\mathrm{secN}} = const.$) and the contact overlap between particles (δ) as

$$F_{\mathrm{N},p1p2} = K_{\mathrm{sec,N}}\delta \tag{2.30}$$

where δ is defined as

$$\delta = R_{p1} + R_{p2} - \Delta \tag{2.31}$$

where Δ is the distance between particles $p1$ and $p2$ and R_{p1} and R_{p2} are the radii of particles $p1$ and $p2$. However, the linear spring model cannot represent the evolution in the contact area, and hence the effective stiffness of the particle-particle contacts, with increasing stress. In the context of soil mechanics, the Hertzian contact model (Hertz, 1882), in which the normal spring stiffness increases under an increasing normal contact force, is often used. In the Hertzian contact model, the normal secant stiffness is modelled as

$$K_{\mathrm{sec,N}} = \frac{4}{3}E^*_{p1p2}R^{*0.5}_{p1p2}\delta^{0.5} \tag{2.32}$$

where E^*_{p1p2} is the equivalent Young's modulus of particles $p1$ and $p2$ and R^*_{p1p2} is the equivalent radius of particles $p1$ and $p2$. E^*_{p1p2} and R^*_{p1p2} are defined as

$$E^*_{p1p2} = \left(\frac{1-\nu^2_{p1}}{E_{p1}} + \frac{1-\nu^2_{p2}}{E_{p2}}\right)^{-1} \tag{2.33}$$

$$R^*_{p1p2} = \left(\frac{1}{R_{p1}} + \frac{1}{R_{p2}}\right)^{-1} \tag{2.34}$$

where E_{p1} and E_{p2} are the Young's modulus of particles $p1$ and $p2$ and ν_{p1} and ν_{p2} are the Poisson's ratio of particles $p1$ and $p2$.

There are also several models for calculating the tangential or shear force acting between particles $p1$ and $p2$ ($F_{\mathrm{T},p1p2}$). The simplest model is the linear tangential spring stiffness model, in which the tangential stiffness of the contact is assumed to be constant. However, this model has the same drawback as the linear normal spring stiffness model, where the variation in the contact area under an increasing the stress cannot be represented. Mindlin (1949) developed a model predicting tangential stiffness of the contact between two smooth elastic spheres based on Hertzian contact model (so-called Mindlin contact model). In the Mindlin contact model, $F_{\mathrm{T},p1p2}$ is incrementally calculated from the tangential incremental stiffness ($K_{\mathrm{tan,T}}$) and a tangential displacement (Δs) as

$$\Delta F_{\mathrm{T},p1p2} = K_{\mathrm{tan,T}} \Delta s \tag{2.35}$$

The tangential incremental stiffness $K_{\mathrm{tan,T}}$ is modelled as

$$K_{\mathrm{tan,T}} = 8 G^*_{p1p2} \zeta r_{\mathrm{c}} \tag{2.36}$$

where ζ is so-called degree of partial slip (will be explained later), G^*_{p1p2} is the equivalent shear modulus of particles $p1$ and $p2$ and r_{c} is the contact radius, which are calculated as

$$G^*_{p1p2} = \left(\frac{2 - \nu_{p1}}{G_{p1}} + \frac{2 - \nu_{p2}}{G_{p2}} \right)^{-1} \tag{2.37}$$

$$r_{\mathrm{c}} = \sqrt{R^*_{p1p2} \delta} \tag{2.38}$$

where G_{p1} and G_{p2} are the shear modulus of particles $p1$ and $p2$. When the tangential displacement between two elastic particles takes place, whole the contact area is not slipping (see Fig. 2.9(b)) and then the edge of the contact area starts to slip (Fig. 2.9(c)) as the tangential dispalcement increases. Eventually, whole the contact area slips as shown in Fig. 2.9(d) ("full slip" state). The degree of partial slip (ζ) expresses such a slip-stick behaviour at the contact. $\zeta = 1$ at the no-slip state, $\zeta = 0$ at the full slip state, and $0 < \zeta < 1$ at the partial slip state. Mindlin and Deresiewicz (1953) modeled ζ considering varying normal contact force and shear load reversal; however, consequently, the formulation of the Mindlin and Deresiewicz (1953) contact model is complex. Tsuji, Tanaka and Ishida (1992) considered a simplified version of the Mindlin and Deresiewicz (1953) contact model, where $\zeta = 1$ is used in Eq. (2.36) i.e.

$$K_{\mathrm{tan,T}} = 8 G^*_{p1p2} r_{\mathrm{c}} \tag{2.39}$$

If $F_{\mathrm{T},p1p2}$ exceeds the slip limit ($\mu_{\mathrm{fric}} F_{\mathrm{N},p1p2}$), $F_{\mathrm{T},p1p2}$ is fixed as

$$F_{\mathrm{T},p1p2} = \mu_{\mathrm{fric}} F_{\mathrm{N},p1p2} \tag{2.40}$$

As shown above, the simplified version of Mindlin and Deresiewicz (1953) by Tsuji, Tanaka and Ishida (1992)'s model does not consider the partial slip state (only no-slip and full slip states). This model is often called as simplified Hertz-Mindlin contact model or no-slip Hertz-Mindlin contact model. Many DEM studies have been conducted using the simplified Hertz-Mindlin contact model including the commercial DEM software PFC3D (Itasca, 2007); therefore, the simplified Hertz-Mindlin model is used in this thesis.

2.4.2 Thermal behaviour of particles

As discussed above, there are two key phenomenon related to the thermal behaviour of granular materials; heat transfer and thermal expansion. To consider heat transfer, many previous studies coupled the DEM with a heat pipe network model (Shimizu, 2006; Vargas & McCarthy, 2007; Kloss et al., 2012). A heat pipe network model uses similar information to calculate heat flow between particles e.g. the positions and the radii of the particles as the DEM does to calculate contact forces between particles; thus, an efficient coupling is possible.

Thermal expansion of particles can be considered by modifying the radius of a particle based on the temperature of the particle (Lu, Abdou & Ying, 2001; Vargas & McCarthy, 2007; Zhao et al., 2017; Iliev et al., 2019). With this model, the radius of particle $p1$ at time t is updated using the linear thermal expansion coefficient (α_{L}), the temperature at the time ($T^{(t)}$) and reference radius R_{ref} at reference temperature T_{ref}:

$$R^{(t)} = R_{\mathrm{ref}}(1 + \alpha_{\mathrm{L}}(T^{(t)} - T_{\mathrm{ref}})) \tag{2.41}$$

2.5 Summary

This chapter summarised the key observations and numerical models regarding thermo-mechanical behaviour of granular materials. It was shown that only the conductive heat transfer needs to be consiered when the pore fluid is stagnant and the temperature is moderate. It was clarified that the conductive heat transfer is governed by the heat equation; however, directly solving the heat equation in a granular medium at the particle scale is computationally expensive due the complex two-phase structure existing in the granular medium. The details of the heat pipe network model, which is computationally

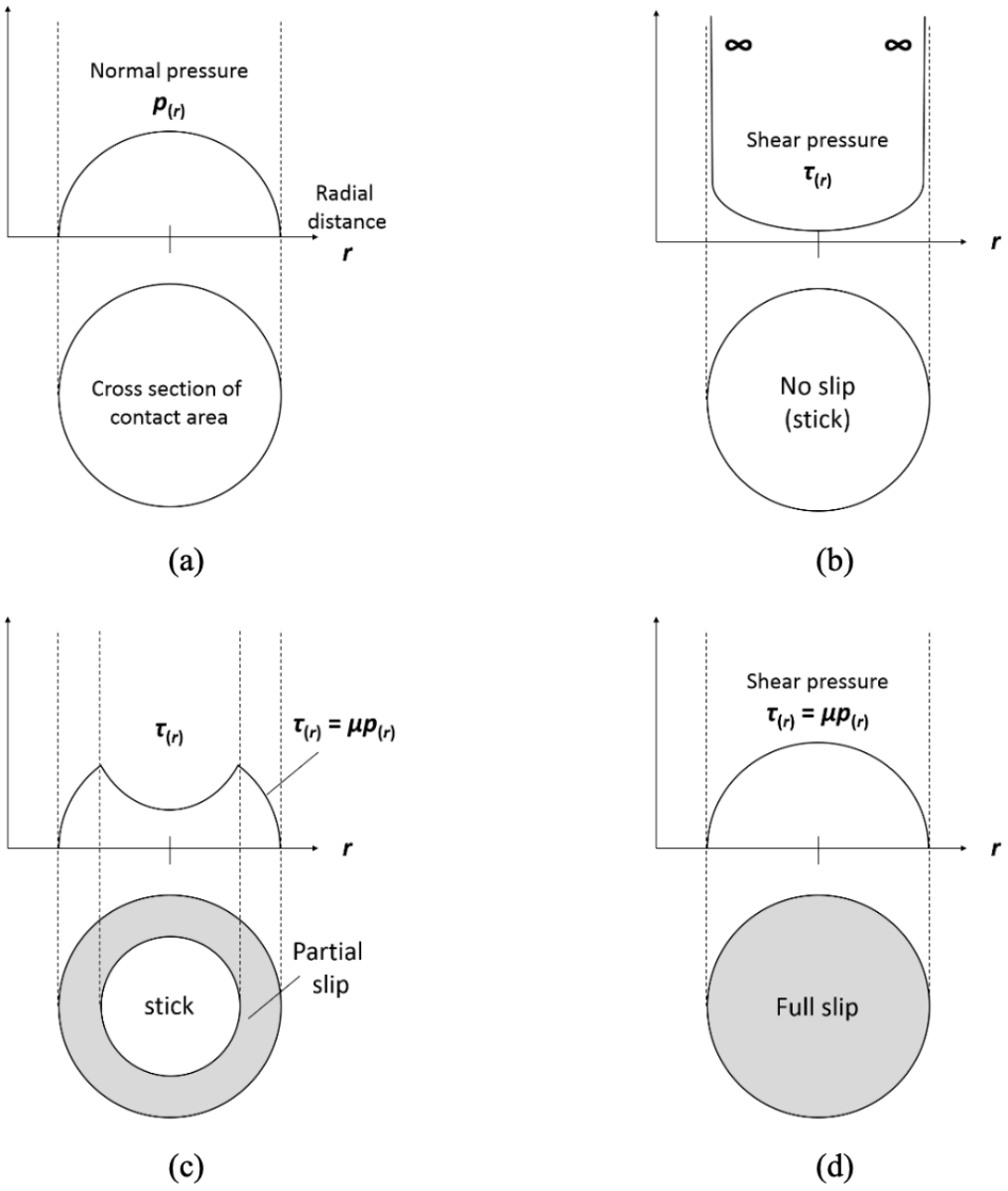


Figure 2.9: Schematic illustration of the stick (no-slip) and slip regions and the normal and shear stress distribution at the contact between two spheres. Reproduced from Otsubo (2016) under the terms of the CC BY-NC-ND 4.0 license. (a) Normal pressure distribution. (b) Shear stress distributionn with no-slip. (c) Shear stress distribution with partial slip. (d) Shear stress distribution with full slip.

much more efficient than directly solving the heat equation while also being capable of capturing complex geometry exising in a granular medium, was reviewed.

Experimental studies on the volume change of granular materials subjected to thermal cycles due to the thermal expansion of particles were reviewed. The DEM coupled with a heat pipe network model to simulate such a complex thermo-mechanical behaviour was reviewed.

The first part of this thesis focuses on the development of accurate heat pipe network model and their coupling with a DEM. The accuracy of a heat pipe network model is critically assessed using data obtained from numerical methods with finer meshes to solve the heat equation. Another aim is to enhance the understanding of the mechanisms underlying the complex thermo-mechanical behaviour of granular matereials using the developed thermal DEM.

CHAPTER 3

DEVELOPMENT AND VALIDATION OF THERMAL DEM

3.1 Introduction

The DEM originally proposed by Cundall and Strack (1979) has been a powerful tool to investigate fundamental mechanisms underlying the mechanical behaviour of granular materials; however, the thermal behaviour of particles, namely heat transfer and thermal expansion, was not considered in the original publication by Cundall and Strack (1979). As introduced in Section 2.4, there are previous studies coupling the heat pipe network model with the DEM. Vargas and McCarthy (2007) developed an in-house code to consider heat conduction and thermal expansion of particles while simulating the movement of solid particles and contact interacion between particles. The open-sourse DEM code `LIGGGHTS` (Kloss et al., 2012) includes a heat pipe network model and can consider the thermal expansion of the particles. Dai, Hanaor and Gan (2019) implemented a modified version of the BOB model (Batchelor & O'Brien, 1977) in `LIGGGHTS` so that they could consider various combinations of the solid particles and the pore fluid. These previous implementations did not allow for full control of the stress state during application of temperature changes; this capability is important to understand thermal-induced strains and fabric evolution.

The open-source DEM software `LAMMPS` was originally developed by Plimpton (1995) and then researchers in Imperial College London (Hanley, O'Sullivan & Huang, 2015; Huang et al., 2014a) implemented specific features to simulate soil particles including contact models introduced in Section 2.4 and the stress-control algorithm (servo-control algorithm). The modified version of `LAMMPS` is MPI parallelised, the source code is accessible and so the consideration of the thermal behaviour of particles in the modified

LAMMPS will offer a very useful option for research and industrial design regarding thermal effects on soils. This chapter reports the implementation of the heat pipe network model and the thermal expansion model to the modified LAMMPS and also the validation of the developed code.

3.2 Development of thermal DEM

This study made a further modification on LAMMPS to consider heat transfer and thermal expansion of particles. All code modifications were made by the programming language C++. To consider heat conduction through particles and pore fluid, the heat pipe network model introduced in Section 2.2.3 was implemented in the modified LAMMPS. The Batchelor and O'Brien (1977) model modified by Dai, Hanaor and Gan (2019) has been implemented to calculate the effective thermal conductance (C^*) of the heat pipe established between two particles. In addition, the thermal expansion of particles was considered, following the method described in Section 2.4.

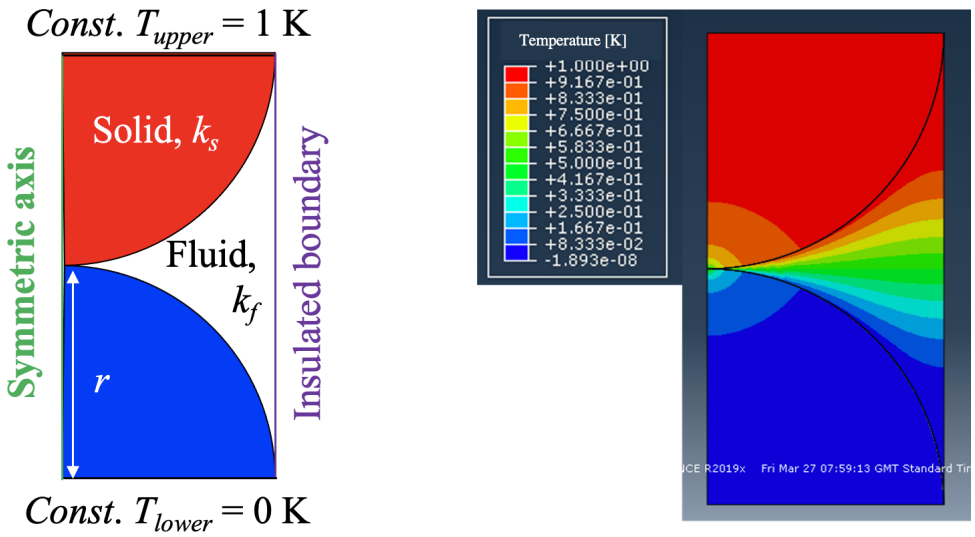
3.3 Validation and verification of thermal DEM

3.3.1 Validation of the implemented modified BOB model

The implementation of the modified BOB model was validated by a FEM model consisting of two hemispheres and the pore fluid using ABAQUS (Dassault Systèmes, 2019) following Dai, Hanaor and Gan (2019). A schematic illustration of the system considered in this validation is shown in Fig. 3.1(a). An axisymmetric system was employed to reduce thee computational time. Three h/R values of 0.002, 0.02, and 0.2 were considered for cases where two hemispheres are separated while two r_c/R values of 0.002 and 0.02 were considered for cases where two hemispheres are in contact. Three κ values of 50, 100, and 500 were considered. Steady state heat transfer simulations were conducted where the temperature difference between the upper and the lower boundaries (ΔT) was 1 K. Heat transferred through the upper or bottom boundaries (H_{FEM}) was measured within a time increment of Δt. The temperature distribution predicted by a representative FEM model is shown in Fig. 3.1(b).

The same system consisting of two spheres was created in the LAMMPS DEM code. The difference in the initial temperatures of the two particles (ΔT) was set to be 1 K. Heat transferred between the particles (H_{BOB}) was measured within a time increment of Δt.

Dai, Hanaor and Gan (2019) defined the normalised heat (denoted H_{norm} here) as H normalised by Δt, ΔT, R, and k_s so that:



(a) Schematic illustration

(b) Temperature distribution within a FEM model

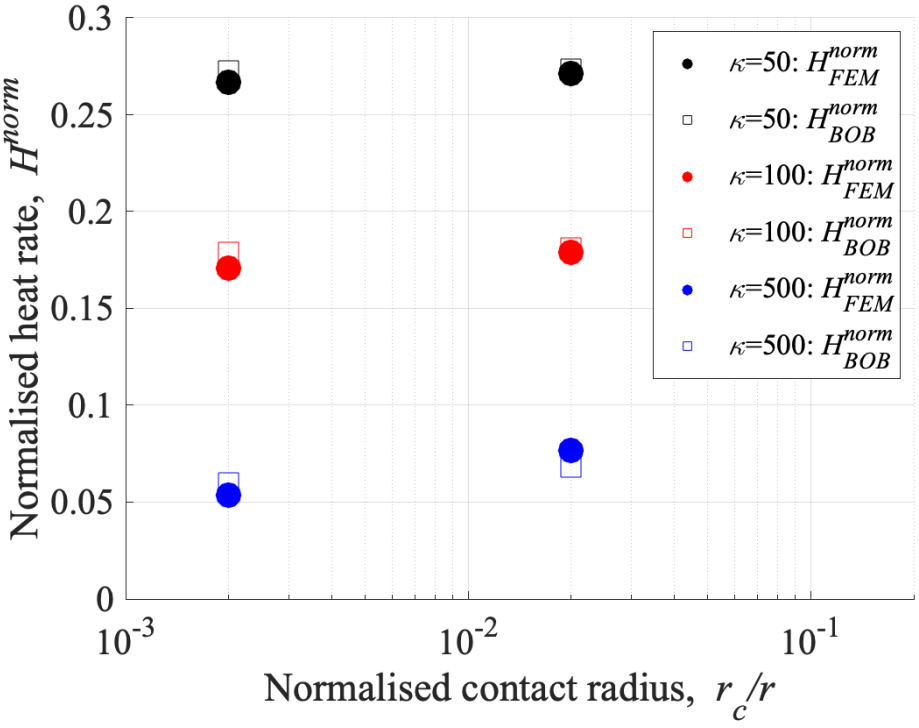
Figure 3.1: FEM model of two particles and pore fluid after Morimoto, O'Sullivan and Taborda (2022) (permission obtained from American Society of Civil Engineers).

$$H_{\text{norm}} = \frac{H}{\Delta t \Delta T r k_{\text{s}}} \tag{3.1}$$

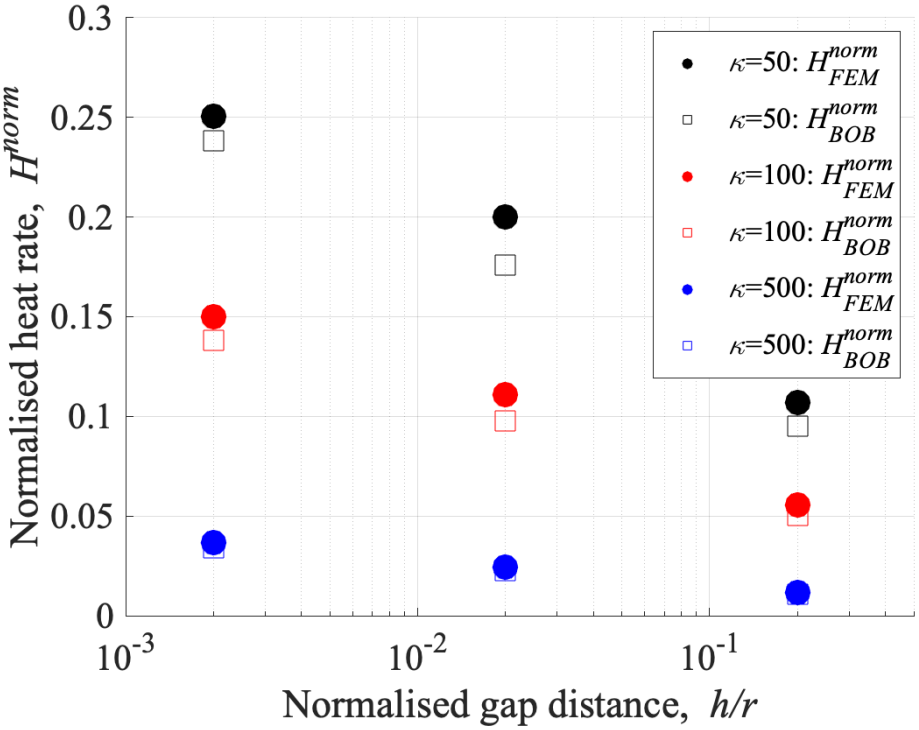
Fig. 3.2 compares H_{norm} values obtained in FEM and DEM simulations, demonstrating a good agreement.

3.3.2 Validation of the implemented heat pipe network model with the modified BOB model

The heat pipe network model implemented in this study was further verified using the heat pipe network simulation data by Yun and Evans (2010). Samples equivalent to those used by Yun and Evans (2010) were created and the effective thermal conductivity (ETC)s of the samples were measured using the modified BOB model. The sample considered in Yun and Evans (2010) is shown in Fig. 3.3(a) and the sample considered in this study is shown in Fig. 3.3(b). Instead of using Eq. (2.24) $\chi = 0.5$ was used following Yun and Evans (2010). The simulation parameters, sample properties, and the ETC values are presented in Table 3.1. The ETC values obtained from the implemented heat pipe network model agree well with those obtained by Yun and Evans (2010).

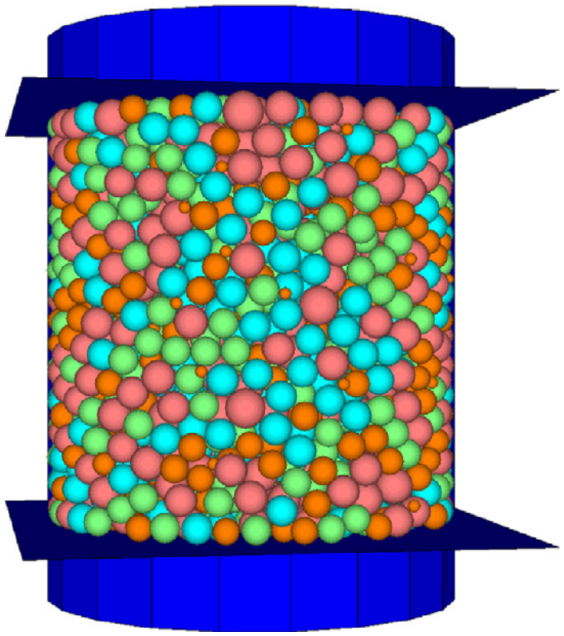


(a) Contacting cases

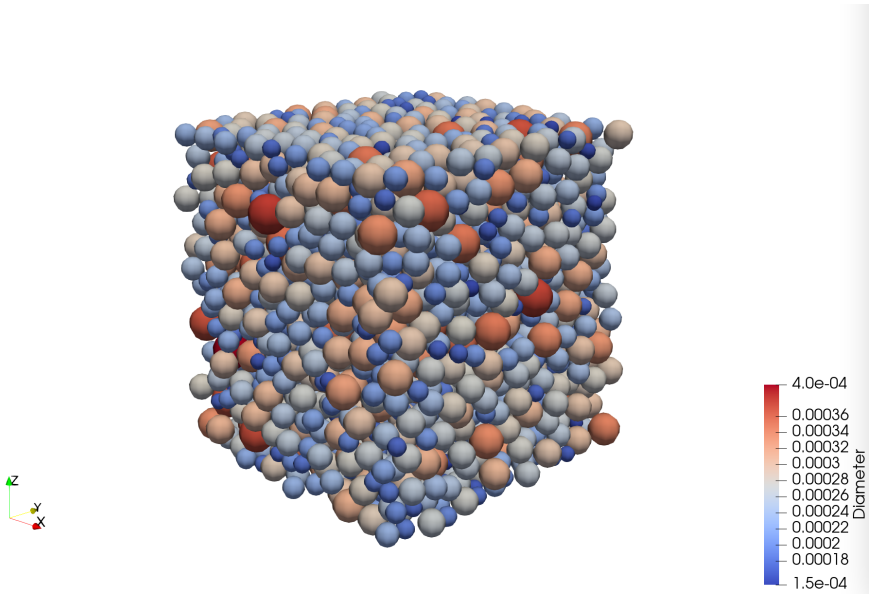


(b) Separated cases

Figure 3.2: Comparison of FEM and DEM simulation results. Reproduced from Morimoto, O'Sullivan and Taborda (2022) (permission obtained from American Society of Civil Engineers).



(a) Yun and Evans (2010)'s sample. Reproduced from Yun and Evans (2010) (Permission obtained from Elsevier).



(b) Sample used in this study.

Figure 3.3: Samples considered for the validation of the implemented heat pipe network model and BOB model.

Table 3.1: Comparison of simulation conditions and results between Yun and Evans (2010) and this study

	Comparison 1		Comparison 2	
	Yun and Evans (2010)	This study	Yun and Evans (2010)	This study
Sample shape	Cylinder	Cube	Cylinder	Cube
Contact model	Simplified Hertz-Mindlin contact model (See Section 2.4)			
G_{p} and G_{wall}	29 GPa			
ν_{p} and ν_{wall}	0.31			
σ_{iso}	10.7 kPa		1.1 kPa	
Porosity	0.414	0.413	0.374	0.376
N_{p}	2199	2290	2389	2341
k_{s}	3.0 W/m.K (Ottawa sand)		1.124 W/m.K (Glass beads)	
k_{f}	0.025 W/m.K (air)		0.025 W/m.K (air)	
k_{eff}	0.29 W/m.K	0.28928 W/m.K	0.21 W/m.K	0.22567 W/m.K
Relative error		0.24 %		7.46 %

3.3.3 Verification of transient heat transfer simulations using the implemented heat pipe network model

Transient heat transfer simulations were verified by considering the heat equation (Eq. (2.8)). A cubically-shaped homogeneous continuum enclosed by six rigid walls was considered for the comparison with the heat equation and a constant temperature boundary condition was applied at all the six walls. For both the FE model and the DEM model, the initial temperature of the sample was set to be 298 K and the temperatures of all the boundaries were set to be 358 K. The heat equation under the condition was solved using `ABAQUS` (Dassault Systèmes, 2019). For the thermal DEM, simple cubic packings enclosed by six rigid walls were considered for the verification. As the FEM sample is homogeneous continuum, it was more rational to use a regular packing rather than a disordered packing. Two sample sizes (7 particles in each direction (343 particles in total) and 19 particles in each direction (6859 particles in total)) were used. Similar to the FE model, a constant temperature boundary condition was applied at all the rigid wall boundaries. The thermal expansion was neglected in the FEM and DEM simulations. For the comparison, the Fourier number (a non-dimensional measure of time) was calculated for both the FE model and the DEM model:

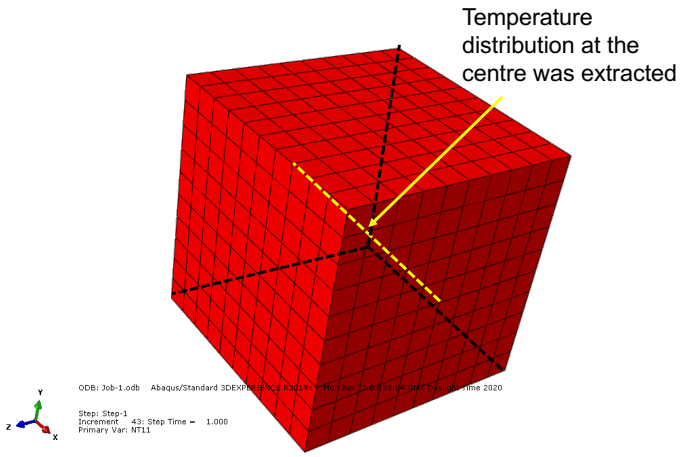
$$Fo = \frac{k}{c\rho\frac{L^2}{4}}t \tag{3.2}$$

Temperature distributions at the center of the samples at a similar Fourier number from the FE and DEM were plotted in Fig. 3.5. Regardless of the sample size, the transient heat transfer simulations using the developed thermal DEM agree with the heat equation solution.

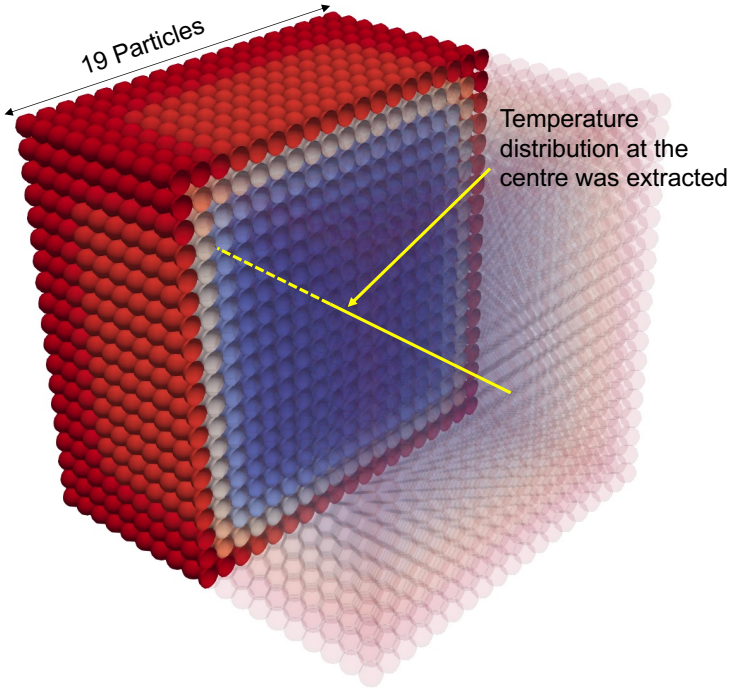
3.4 Summary

This Chapter has reported the development and validation of a thermal DEM. To simulate heat transfer through particles, a heat pipe network model introduced in Section 2.2.3 was considered. The thermal conductance model between two contacting or separated particles by Batchelor and O'Brien (1977), Yun and Evans (2010) and Dai, Hanaor and Gan (2019) was employed (Section 2.2.3). A simple thermal expansion model for particles (Section 2.4), adopted by Lu, Abdou and Ying (2001) and Vargas and McCarthy (2007), was implemented.

Section 3.3 summarised the validation and verification of the developed thermal DEM. The implemented BOB model predicting the thermal conductance of the two contacting or separated particles and the pore fluid was validated using equivalent FEM simulations. The implementation of the BOB model and the heat pipe network model was validated by reproducing the Results reported by Yun and Evans (2010) for a steady-state condition. It was also shown that the implemented heat pipe network model can accurately simulate transient heat transfer in a granular packing. The developed thermal DEM will be used in following chapters to study various thermal behaviours of granular materials.

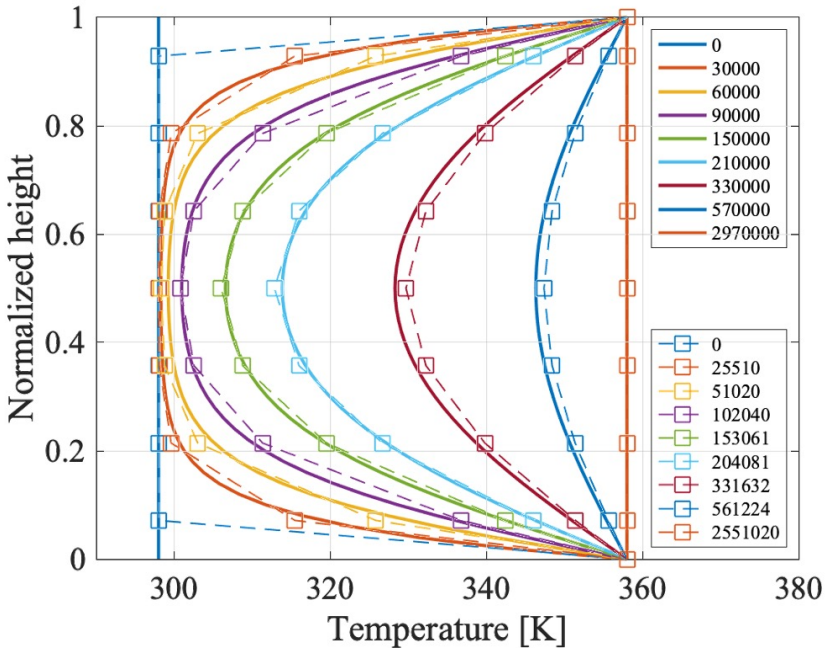


(a) FEM sample. The actual sample had $50 \times 50 \times 50$ elements.

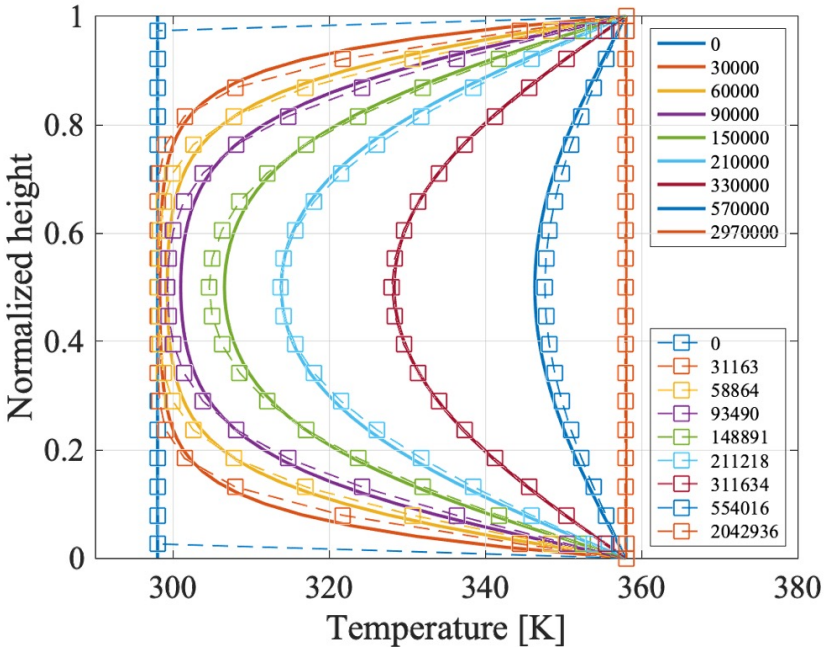


(b) DEM sample (19 particles in each direction).

Figure 3.4: FEM and DEM samples used for the validation of the implemented heat pipe network model.



(a) Sample with 7 particle in each direction



(b) Sample with 19 particles in each direction

Figure 3.5: Comparison of FEM (solid line) and DEM (dashed line with markers) simulation results.

CHAPTER 4

LINKING ELASTIC STIFFNESS AND THERMAL CONDUCTION OF GRANULAR MATERIALS

4.1 Background

Granular materials are encountered in a number of engineering fields and subjected to temperature changes in a variety of situations. Such temperature changes can be applied artificially, for example, to enhance chemical reactions of powders, process food grains, store thermal energy in packed beds, or exploit heat from soils for geothermal heat pumps. Chemical or nuclear reactions can lead to a change in the temperature of granular materials (e.g. hydration of cement). Climate-induced temperature changes include the seasonal temperature changes experienced by food grains in silos. In all cases, understanding the ETC of the granular materials considered is important to effectively run facilities and manage processes or to avoid significant failure of structures.

Both experimental and numerical studies have shown that the ETC of granular materials is affected by various factors. The experimental studies by Yun and Santamarina (2008) showed that the contact area and the particle stresses have a measurable effect on the ETC of granular materials. The ETC of a granular material is not always isotropic; for example, the experimental studies presented in Garrett and Ban (2011) demonstrated that the ETC can develop a significant directional dependency under anisotropic stress conditions. A numerical study by El Shamy, De Leon and Wells (2013) also suggested that the mean coordination number and the anisotropy of the contact normal orientations affect the ETC, however these parameters cannot easily be measured in experiments. Thus, in order to estimate the ETC of a granular material, all of these factors need to be

accounted for. However, none of the available theoretical models, which are summarised in van Antwerpen, Du Toit and Rousseau (2010), can effectively include the effects of all of these factors.

On the other hand, the direct measurement of the ETC of granular materials is technically challenging, as it requires specific and often expensive temperature controlled devices. In particular, experimental systems that can measure accurately the response to changes in temperature while allowing control of the packing and stress state of granular materials remain very rare. This is due to the difficulties associated with the concurrent application of thermal and mechanical loads and also to the detrimental effects of changes in temperature on the accuracy of the equipment required to measure the sample deformations.

Motivated by the observations presented above, this study explores the possibility of indirectly determining the ETC of granular materials by relating it to the small-strain elastic moduli of granular materials, which are also determined by the material packing characteristics and which can be more easily measured experimentally. This study employed both analytical and numerical models. In the analytical model Effective Medium Theory is used to express the elastic moduli of a granular material as a function of its basic packing characteristics (coordination number, contact radius, and void ratio). Then, a relationship between the ETC and the packing characteristics is formulated assuming a uniform temperature gradient within a granular medium. Comparing the expressions for the ETC and the Young's modulus of a granular medium, a relationship between these two properties is proposed. Complementary numerical analyses employed the Discrete Element Method (Cundall & Strack, 1979) to create samples with differing void ratios, coordination numbers and contact normal anisotropies. Small deformation probes were simulated to measure the elastic moduli and heat pipe network simulations were conducted. These data confirmed the viability of the relationship developed analytically. Using the analytical model and the DEM results, a simple method to estimate the ETC of granular samples using the Young's modulus and the void ratio of a granular material is proposed and its predictive potential is demonstrated using the DEM-generated data.

4.2 Analytical modelling

4.2.1 Use of Effective Medium Theory (EMT) to Determine Elastic Moduli

In soil mechanics, Hardin and Richart (1963) suggested that the Young's Modulus in a certain direction i (E_i) is proportional to a certain function of e ($f(e)$) and the ω_σ-th power of the normal stress in the same direction (σ_i):

$$E_i = Af(e)\sigma_i^{\omega_\sigma} \tag{4.1}$$

where A is a material constant. Although there are several definitions of $f(e)$, Hardin and Richart (1963) proposed:

$$f(e) = \frac{(B-e)^2}{1+e} \tag{4.2}$$

where B is a material constant, which can be related to the angularity of the particles. Hoque and Tatsuoka (1998)'s experimental results supported Hardin and Richart (1963)'s statement that E_i is independent of the normal stresses in the other directions.

In granular physics/granular mechanics, a number of attempts have been made to predict the elastic moduli of granular materials theoretically. Chang and Liao (1994) calculated the elastic moduli of a granular medium from the material properties of the particles, the packing characteristics, and the stresses, assuming that a uniform strain field applies in a granular medium when the granular medium deforms (*kinematic assumption*). The packing characteristics can be expressed in terms of the void ratio (e), i.e. the ratio of the volume of the voids (V_v) to the volume of the solids (V_s):

$$e = \frac{V_\mathrm{v}}{V_\mathrm{s}} \tag{4.3}$$

The mean coordination number ($\overline{Z}$) is a particle-scale measure to quantify the overall sample packing density, which is defined as

$$\overline{Z} = \frac{2N_\mathrm{c}}{N_\mathrm{p}} \tag{4.4}$$

Where N_c is the number of contacts and N_p is the number of particles. Considering the case of an isotropic granular medium subject to an isotropic stress condition and a simplified Hertz-Mindlin contact model and applying a no-slip condition, Otsubo (2016) adopted the kinematic assumption proposed by Chang and Liao (1994) and expressed the Young's modulus of a granular material as a function of e and $\overline{Z}$:

$$E = \frac{2\left(5-4\nu_\mathrm{p}\right)}{5-3\nu_\mathrm{p}}\left[\frac{\sqrt{3}}{\sqrt{2}\pi(1-\nu_\mathrm{p})}\right]^{2/3} G_\mathrm{p}^{2/3}\left[\frac{\overline{Z}}{1+e}\right]^{2/3}\sigma_\mathrm{iso}^{1/3} \equiv \mathcal{N}_E\left[\frac{\overline{Z}}{1+e}\right]^{2/3}\sigma_\mathrm{iso}^{1/3} \tag{4.5}$$

where the term $\mathcal{N}_{\mathrm{E}}$ depends upon the material properties of the particles:

$$\mathcal{N}_E \equiv \frac{2\left(5-4\nu_{\mathrm{p}}\right)}{5-3\nu_{\mathrm{p}}}\left[\frac{\sqrt{3}}{\sqrt{2}\pi(1-\nu_{\mathrm{p}})}\right]^{2/3} G_{\mathrm{p}}^{2/3} \tag{4.6}$$

EMT predicts that the parameter ω_σ should be $1/3$; however, experimental data have repeatedly shown that ω_σ is higher than $1/3$ (Hoque & Tatsuoka, 1998; Kuwano & Jardine, 2002). The higher value of ω_σ observed experimentally is attributed to the surface roughness and the shape of the particles (Goddard, 1990; Yimsiri & Soga, 2000; Otsubo & O'Sullivan, 2018). Some studies (Makse et al., 1999; La Ragione & Magnanimo, 2012; Khalili et al., 2017) showed that EMT over-predicts the moduli of granular media; however, La Ragione and Magnanimo (2012) showed that the EMT prediction of the ratio of a modulus to a reference modulus is reasonably accurate.

Here a new method is explored that can calculate key contact parameters, namely the mean contact radius and the mean coordination number, from E and σ_{iso} exploiting EMT. Following Chang, Sundaram and Misra (1989), an expression can be derived to relate an isotropic stress, σ_{iso}, to the ratio of the mean contact radius, $\overline{r_{\mathrm{c}}}$ (calculated from Eq. (2.19)), to the particle radius, R:

$$\sigma_{\mathrm{iso}} = \frac{2}{3\pi}\frac{G_{\mathrm{p}}}{1-\nu_{\mathrm{p}}}\frac{\overline{Z}}{1+e}\left(\frac{\overline{r_{\mathrm{c}}}}{R}\right)^3 \equiv \mathcal{N}_\sigma \frac{\overline{Z}}{1+e}\left(\frac{\overline{r_{\mathrm{c}}}}{R}\right)^3 \tag{4.7}$$

Using Eq. (4.7), Eq. (4.5) can be rewritten in terms of $\dfrac{\overline{r_{\mathrm{c}}}}{R}$ as:

$$E = \frac{2\left(5-4\nu_{\mathrm{p}}\right)}{5-3\nu_{\mathrm{p}}}\left[\frac{G_{\mathrm{p}}}{\pi\left(1-\nu_{\mathrm{p}}\right)}\right]\left[\frac{\overline{Z}}{1+e}\right]\left(\frac{\overline{r_{\mathrm{c}}}}{R}\right) \equiv \mathcal{N}'_E\left[\frac{\overline{Z}}{1+e}\right]\left(\frac{\overline{r_{\mathrm{c}}}}{R}\right) \tag{4.8}$$

where the term $\mathcal{N}'_E$ depends upon the material properties of particles:

$$\mathcal{N}'_E \equiv \frac{2\left(5-4\nu_{\mathrm{p}}\right)}{5-3\nu_{\mathrm{p}}}\left[\frac{G_{\mathrm{p}}}{\pi\left(1-\nu_{\mathrm{p}}\right)}\right] \tag{4.9}$$

From Eq. (4.7) and Eq. (4.8), $\dfrac{\overline{r_{\mathrm{c}}}}{R}$ and $\dfrac{\overline{Z}}{1+e}$ can be expressed in terms of σ_{iso} and E:

$$\frac{\overline{r_{\mathrm{c}}}}{R} = \left(\frac{\mathcal{N}'_E}{\mathcal{N}_\sigma}\right)^{0.5}\left(\frac{\sigma_{\mathrm{iso}}}{E}\right)^{0.5} \tag{4.10}$$

$$\frac{\overline{Z}}{1+e} = \frac{\mathcal{N}_\sigma^{0.5}}{\mathcal{N}'_E}\frac{E^{1.5}}{\sigma_{\mathrm{iso}}^{0.5}} \tag{4.11}$$

Eq. (4.10) and Eq. (4.11) thus give expressions for the mean contact radius and the packing density ($\overline{Z}$ and E) in terms of the elastic moduli and the current stress level.

4.2.2 Relationship between the ETC and Packing Characteristics and Elastic Moduli

Itasca (2007) and El Shamy, De Leon and Wells (2013) calculated the effective thermal conductivity tensor (k_{ij}^{*}) of a granular sample from the effective thermal conductance of heat pipes in the sample assuming that the temperature gradient within the granular sample is uniform as:

$$k_{ij}^{*} = \frac{1}{V}\sum_{hp=1}^{N_{\text{hp}}} C^{*hp}\left[L^{hp}\right]^{2} n^{hp}{}_{i} n^{hp}{}_{j} \tag{4.12}$$

where V is the sample volume, N_{hp} is the number of the heat pipes in the sample, and C^{*hp}, L^{hp}, and $\mathbf{n^{hp}}$ are the effective thermal conductance, the length, and the unit vector describing the orientation of heat pipe hp, respectively. This section presents novel analytical analyses relating the effective thermal conductivity of granular media to the elastic modulus and the void ratio of the media based on Eq. (4.12).

In a heat pipe network model that adopts the BOB model, there are two types of heat pipes: type 1 for contacting particles and type 2 for to separated particles, and so Eq. (4.12) can be rewritten as:

$$k_{ij}^{*} = \frac{1}{V}\sum_{c}^{N_{\text{c}}} C^{*(c)}\left[L^{(c)}\right]^{2} n^{(c)}{}_{i} n^{(c)}{}_{j} + \frac{1}{V}\sum_{hp,s=1}^{N_{\text{hp,s}}} C^{*hp,s}\left[L^{hp,s}\right]^{2} n^{hp,s}{}_{i} n^{hp,s}{}_{j} \equiv k_{ij}^{c*} + k_{ij}^{s*} \tag{4.13}$$

where hp, s is a heat pipe between two non-contacting (separated) particles, and the number of these heat pipes is $N_{\text{hp,s}}$. The unit vectors $\mathbf{n^{(c)}}$ and $\mathbf{n^{hp,s}}$ give the contact normal orientations and the orientation of the heat pipes between separated particles, respectively. As shown in Eq. (4.13), the number and the length of the heat pipes between the contacting particles are identical to the number of the contacts and the length of the branch vectors that join the centroids of contacting particles. Assuming that the sample consists of monodisperse spheres and is isotropic:

$$k_{ij}^{c*} \approx \frac{4R^{2}\overline{C^{*(c)}}}{V}\sum_{c}^{N_{\text{c}}} n^{(c)}{}_{i} n^{(c)}{}_{j} = \frac{4R^{2}\overline{C^{*(c)}}}{V}\frac{\overline{Z}N_{\text{p}}}{2}\frac{1}{3}\delta_{ij} \tag{4.14}$$

where δ_{ij} is the Kronecker delta. The sample volume V can be expressed in terms of the void ratio e:

$$V = \frac{4}{3}\pi R^3 N_{\mathrm{p}}(1+e) \tag{4.15}$$

Using the BOB model and substituting Eq. (2.17) and Eq. (2.23) into Eq. (2.25)

$$\overline{C^{*(c)}} \approx \frac{\pi k_{\mathrm{f}} R \chi^2 \kappa \left(\mathcal{H}_c\left(\overline{\beta}\right) + \mathcal{H}_f\left(\overline{\beta}\right) + \ln\left(\kappa^2\right)\right)}{2\left(\mathcal{H}_c\left(\overline{\beta}\right) + \mathcal{H}_f\left(\overline{\beta}\right) + \ln\left(\kappa^2\right) + \frac{1}{2}\chi^2\kappa\right)} \tag{4.16}$$

where $\overline{C^{*(c)}}$ is assumed to be the $C^{*(c)}$ value for the mean β $\left(= \kappa\dfrac{r_{\mathrm{c}}}{R}\right)$ value of all the contacts. Substituting Eq. (4.15) and Eq. (4.16) into Eq. (4.14),

$$k_{ij}^{c*} \approx \frac{1}{2}\frac{\overline{Z}}{1+e}\frac{k_{\mathrm{f}}\chi^2\kappa\left(\mathcal{H}_c\left(\overline{\beta}\right) + \mathcal{H}_f\left(\overline{\beta}\right) + \ln\left(\kappa^2\right)\right)}{2\left(\mathcal{H}_c\left(\overline{\beta}\right) + \mathcal{H}_f\left(\overline{\beta}\right) + \ln\left(\kappa^2\right) + \frac{1}{2}\chi^2\kappa\right)}\delta_{ij} \tag{4.17}$$

The magnitude of the combined term $\mathcal{H}_c\left(\overline{\beta}\right) + \mathcal{H}_f\left(\overline{\beta}\right)$ depends on κ and $\overline{r_{\mathrm{c}}}/R$. $\overline{r_{\mathrm{c}}}/R$ can be calculated from Eq. (4.7), provided that $\overline{Z}$, e and $\sigma_{\mathrm{iso}}/\omega_\sigma$ are known. According to Song, Wang and Makse (2008), $0.58 < e < 0.82$ and $4 < \overline{Z} < 6$ for monodisperse spheres. In the case of samples with $\kappa < 500$ and $\sigma_{\mathrm{iso}}/\omega_\sigma < 1.29 \times 10^{-4}$, the combined term $\mathcal{H}_c\left(\overline{\beta}\right) + \mathcal{H}_f\left(\overline{\beta}\right)$ is small compared to the term $\ln\left(\kappa^2\right) + \frac{1}{2}\chi^2\kappa$ (at most 20%); thus, the combined term $\mathcal{H}_c\left(\overline{\beta}\right) + \mathcal{H}_f\left(\overline{\beta}\right)$ in the denominator can be omitted from Eq. (4.17) to give:

$$\begin{aligned} k_{ij}^{c*} \approx \frac{1}{2}\frac{\overline{Z}}{1+e}\frac{k_{\mathrm{f}}\chi^2\kappa\left(\mathcal{H}_c\left(\overline{\beta}\right) + \mathcal{H}_f\left(\overline{\beta}\right)\right)}{2\left(\ln\left(\kappa^2\right) + \frac{1}{2}\chi^2\kappa\right)}\delta_{ij} + \frac{1}{2}\frac{\overline{Z}}{1+e}\frac{k_{\mathrm{f}}\chi^2\kappa\ln\left(\kappa^2\right)}{2\left(\ln\left(\kappa^2\right) + \frac{1}{2}\chi^2\kappa\right)}\delta_{ij} \\ \equiv k_{ij}^{\beta*} + k_{ij}^{(h=0)*} \end{aligned} \tag{4.18}$$

The first term is the contribution to k_{ij}^* that depends on β (defined in Eq. (2.18)) and the second term is denoted as $k_{ij}^{(h=0)*}$ because the term $\ln\left(\kappa^2\right)$ in the BOB model comes from the analytical result with a gap distance $h \to 0$.

When $\beta \ll 1$, the term $\mathcal{H}_c\left(\overline{\beta}\right) + \mathcal{H}_f\left(\overline{\beta}\right)$ is proportional to β^2, which indicates:

$$k_{ij}^{\beta*} \propto \frac{\overline{Z}}{1+e}\left(\frac{\overline{r_{\mathrm{c}}}}{R}\right)^2 \tag{4.19}$$

Referring to Eq. (4.10) and Eq. (4.11):

$$\frac{\overline{Z}}{1+e}\left(\frac{\overline{r_{\mathrm{c}}}}{R}\right)^2 = \frac{1}{\mathcal{N}'^{0.5}_{\mathrm{E}}\mathcal{N}^{0.5}_{\sigma}}E^{0.5}\sigma^{0.5}_{\mathrm{iso}} \tag{4.20}$$

and so we can state that

$$k^{\beta*}_{ij} \propto E^{0.5}\sigma^{0.5}_{\mathrm{iso}} \quad (\overline{\beta} \ll 1) \tag{4.21}$$

Using linear interpolation (see Eq. (2.20) and Eq. (2.21)) for $\overline{\beta} > 1$:

$$\mathcal{H}_c\left(\overline{\beta}\right) + \mathcal{H}_f\left(\overline{\beta}\right) = 0.549\overline{\beta} - 0.379 \tag{4.22}$$

When $0.549\overline{\beta}$ is sufficiently larger than 0.379, $k^{\beta*}_{ij}$ is proportional to $\overline{\beta}$; thus,

$$k^{\beta*}_{ij} \propto \frac{\overline{Z}}{1+e}\frac{\overline{r_{\mathrm{c}}}}{R} \propto E \quad (0.549\overline{\beta} \gg 0.379) \tag{4.23}$$

and so the dependency on σ_{iso} is removed.

When $\mathcal{H}_c\left(\overline{\beta}\right) + \mathcal{H}_f\left(\overline{\beta}\right) \ll \ln\left(\kappa^2\right) + \frac{1}{2}\chi^2\kappa$, the remaining terms k^{s*}_{ij} and $k^{(h=0)*}_{ij}$ are independent of the contact radius, and dependent on the distribution of h values for the sample. Thus, these components are denoted as:

$$k^{s*}_{ij} + k^{(h=0)*}_{ij} \equiv k^{h*}_{ij} \tag{4.24}$$

In denser systems, a larger number of small h values are expected. Thus, we predict that the term k^{h*}_{ij} has a correlation with e, which is explored using simulation results later.

To sum up with, the ETC of a granular medium (k^{*}_{ij}) can be divided in two components as

$$k^{*}_{ij} = k^{\beta*}_{ij} + k^{h*}_{ij} \tag{4.25}$$

and the EMT-based analysis presented here indicates that $k^{\beta*}_{ij}$ can be correlated with E and σ_{iso} and that k^{h*}_{ij} can be correlated with e.

There are a number of assumptions inherent to this proposition and so a numerical exploration of these correlations is needed to explore their applicability.

4.3 Numerical Modelling Using DEM

4.3.1 Sample Generation Using the Discrete Element Method (DEM)

Samples of spheres with various packing densities and confining stresses were created using the Discrete Element Method (DEM). A modified version of `LAMMPS` (Plimpton, 1995), an open-source DEM software, was used. A simplified Hertz-Mindlin contact model was employed (See Section 2.4). The particle size distribution was relatively uniform, having a coefficient of uniformity D_{60}/D_{10} of 1.1 (60% of particles by volume have a particle diameter less than D_{60} and 10% of particles by volume have a particle diameter smaller than D_{10}). In general, periodic boundaries are useful to reduce the boundary effects; however, in the simulations to measure effective thermal conductivity outlined below, different temperature values had to be assigned for the upper and lower x, y, or z boundaries, and thus periodic boundaries could not be used. Consequently, the samples were enclosed by three pairs of smooth rigid walls (instead of periodic boundaries); each pair of walls was orthogonal to on of the three Cartesian (x, y, z) axes. Detailed simulation parameters are presented in Table 4.1. In most cases the samples comprised 21,217 particles; a limited number of additional simulations were completed including 41,444 particles to confirm the results were independent of sample size.

Four sets of samples were produced as described below so that different levels of sample anisotropy could be considered. The anisotropy was quantified using the the second order fabric tensor (F_{ij}) based on the contact normal orientations, as follows:

$$F_{ij} = \frac{1}{N_\mathrm{c}} \sum_{c}^{N_\mathrm{c}} {n^{(c)}}_i {n^{(c)}}_j \tag{4.26}$$

where $\mathbf{n^{(c)}}$ is the unit vector of describing the contact normal orientation for contact c. The integral form of F_{ij} can be expressed using the distribution function of $\mathbf{n}$ ($E(\psi, \theta)$):

$$F_{ij} = \int_0^{2\pi} \int_0^{\pi} n_i n_j E(\psi, \theta) \sin\psi d\psi d\theta \tag{4.27}$$

For a cross-anisotropic case, Chang, Sundaram and Misra (1989) expressed $E(\psi, \theta)$ using Fourier series, taking advantage of symmetry about the z-axis:

$$E(\psi, \theta) = \frac{3(1 + a\cos 2\psi)}{4\pi(3 - a)} \tag{4.28}$$

where a expresses the degree of anisotropy which is normally $-1 < a < 1$, with $a = 0$ corresponding to a perfectly isotropic distribution of the contact normals. A positive a indicates the sample has more contacts in the z-direction, with the opposite being true for

Table 4.1: Simulation parameters

Parameters	Values
Number of particles	21,217, 41,444 (A complementary study)
D_{50}	1.0 mm
Cu	1.1
Contact model	Simplified Hertz-Mindlin model
G_p	29.2 GPa
ν_{p}	0.20
ρ_p	2600 kg/m^3
$\mu_{\mathrm{fric,p}}$ (During *IC* and K_0)	0.01, 0.05, 0.10, 0.20, 0.34
$\mu_{\mathrm{fric,p}}$ (During *TCUL* and TEUL)	0.35
$\mu_{\mathrm{fric,p}}$ (During small deformation probes)	0.40 - 0.45
$\mu_{\mathrm{fric,wall}}$	0.00
k_{s} and k_{wall}	1.0 W/m·K
$\kappa = k_{\mathrm{s}}/k_{\mathrm{f}}$	10, 30, 50, 100, 150, 300, 500
$*$ D_{50} ... the median particle diameter	
$*$ Cu ... the coefficient of uniformity	
$*$ G_p ... the shear moduli of the particles	
$*$ ν_{p} ... the Poisson's ratios of the particles	
$*$ ρ_p ... the density of the particles	
$*$ $\mu_{\mathrm{fric,p}}$ and $\mu_{\mathrm{fric,wall}}$ ... the friction coefficients of the particles and the walls, respectively	
$*$ k_{s} and k_{wall} ... the thermal conductivity of the particles and the walls, respectively	

negative a values. Based on Eq. (4.28), Yimsiri and Soga (2010) express the fabric tensor of a cross-anisotropic sample in terms of a only:

$$F_{ij} = \begin{bmatrix} \frac{3a-5}{5(a-3)} & 0 & 0 \\ 0 & \frac{3a-5}{5(a-3)} & 0 \\ 0 & 0 & \frac{-5-a}{5(a-3)} \end{bmatrix} = \frac{1}{3}\mathbf{I} + \begin{bmatrix} \frac{-4a}{15(3-a)} & 0 & 0 \\ 0 & \frac{-4a}{15(3-a)} & 0 \\ 0 & 0 & \frac{8a}{15(3-a)} \end{bmatrix} \tag{4.29}$$

where $\mathbf{I}$ is the second order identity tensor. In this study, the parameter a was used to quantify the anisotropy of the samples, which was determined by comparing the calculated contact normal based fabric tensor (Eq. (4.26)) with that expressed in Eq. (4.29).

Isotropic compression samples (IC)

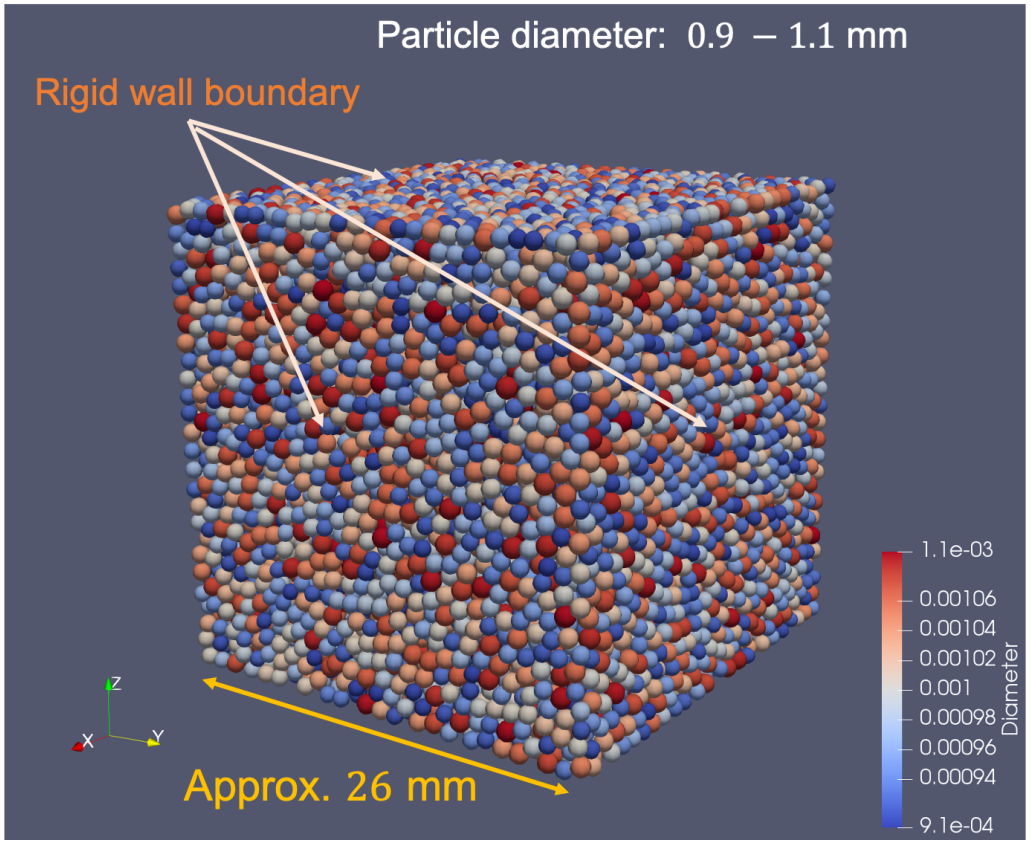


Figure 4.1: Typical sample after Morimoto, O'Sullivan and Taborda (2022) (permission obtained from American Society of Civil Engineers)

The particles were randomly generated within the rigid wall boundaries by the following procedure.

1. Set the initial void ratio ($e = 2.0$ in this study).
2. Calculate the initial sample size so that there were at least 20,000 particles.
3. Randomly generate the radius of each particle using the pseudo random number generator Mersenne twister (Matsumoto & Nishimura, 1998) available in `MATLAB` (MathWorks, 2020) according to the particle size distribution. In this study, the linear particle size distribution with a coefficient of uniformity (Cu) of 1.1 and the median particle diameter (D_{50}) was used. The minimum and maximum particle diameters (D_{min} and D_{max}) can be analytically determined. Denoting the output from the random number generator as $Y \in [0, 1)$, the generated particle radius can be expressed as $D = D_{\text{min}} + Y(D_{\text{max}} - D_{\text{min}})$.
4. Place the generated particles one by one by iterating following steps 5-7 until all the particles are placed.
5. Pick the largest particle among the particles which have not been placed in the domain yet.
6. Generate the coordinate of the picked particle using the random number generator. Generate three random numbers as $(Y_1, Y_2, Y_3) \in [0, 1)$, with which the coordinates of the particle can be expressed as $(x, y, z) = (Y_1 L_x, Y_2 L_y, Y_3 L_z)$, where L_i is the length of the domain in the i-th direction.
7. Check if there is any overlap between the generated particle and any of the previously generated particles. If there is any overlap, go back to step 6 to generate a new coordinate of the particle. If there is no overlap, go to step 5 to place another particle.

Even though the random number generator was used, step 7 may induce a certain bias in the distribution of the particles in the domain. Complementary study results which are using the same procedure with different initial seeds are presented in Appendix to show such a bias does not affect the thermal conductivity value. After the particles were generated, the six rigid walls were moved inward until an isotropic stress (σ_{iso}) of 1 kPa was achieved using a servo-control algorithm. The friction coefficient of the particles was varied ($\mu_{\text{fric}} = 0.01, 0.05, 0.10, 0.20, 0.34$) to produce samples with a range of packing densities. Viscous damping with a damping coefficient of 0.1 was applied to minimize the kinetic energy of the particles. During compression the positions of the 6 rigid walls were adjusted using a servo-controlled algorithm until the isotropic stress reached a target value with the viscous damping on. The target isotropic stresses were 10, 100, and 1000 kPa. After the target isotropic stress was achieved, a vertical body force was applied to simulate

Table 4.2: Sample size effect after Morimoto, O'Sullivan and Taborda (2022) (permission obtained from American Society of Civil Engineers)

Sample properties	$N_{\mathrm{p}} = 21,217$	$N_{\mathrm{p}} = 41,444$
σ_{iso} [kPa]	100	100
e	0.669	0.666
$\overline{Z}$	5.10	5.08
a	0.00	0.00
E_{zz} [MPa]	334	333
$k^*_{zz}/k_{\mathrm{f}}(\kappa = 100)$	12.0	12.0

gravity. Gravity was applied to avoid the presence of a large number of non-physical rattler particles that do not engage in any contacts, whose presence may affect the ETC of the sample because the BOB model includes heat conduction through separated particles. Gravity was introduced only after isotropic compression to achieve an ideal, isotropic packing. A typical sample after an isotropic compression is shown in Fig. 4.1. A total of 15 *IC* samples were considered.

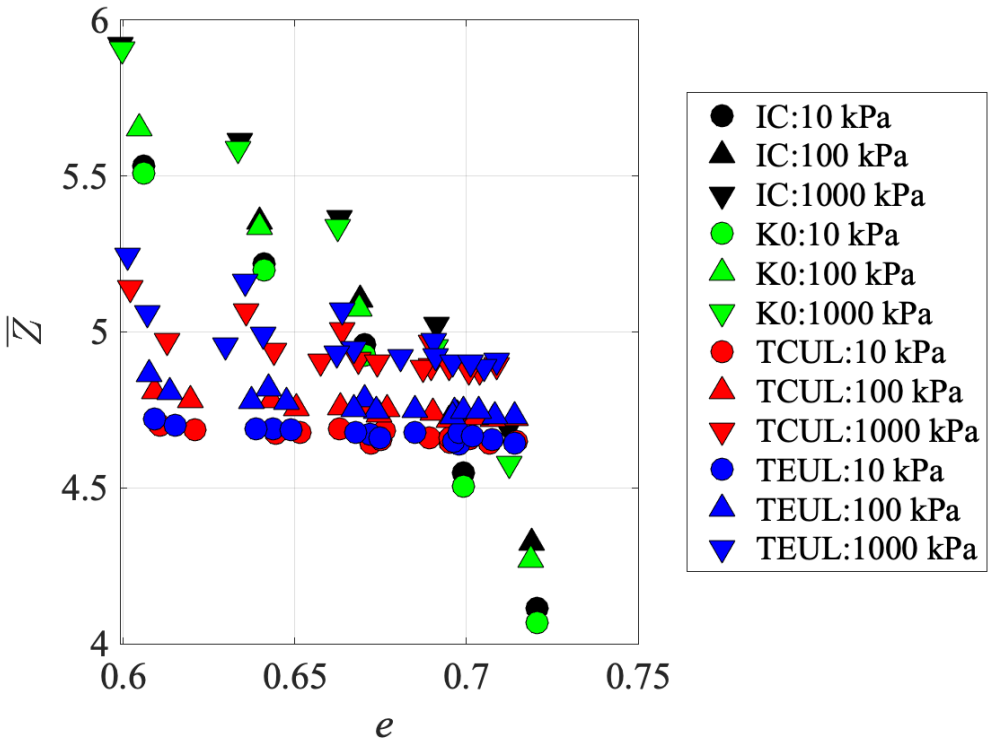
Summary data on the packing characteristics of the *IC* samples after application of gravity are provided on Fig. 4.2. Referring to Fig. 4.2 (a), the $\overline{Z}$ values ranged between 4.07 and 5.92, while the e values were between 0.600 and 0.721. The magnitude of the anisotropy, $|a|$, was < 0.01, confirming isotropic samples were indeed attained.

Samples formed by 1D compression (K_0)

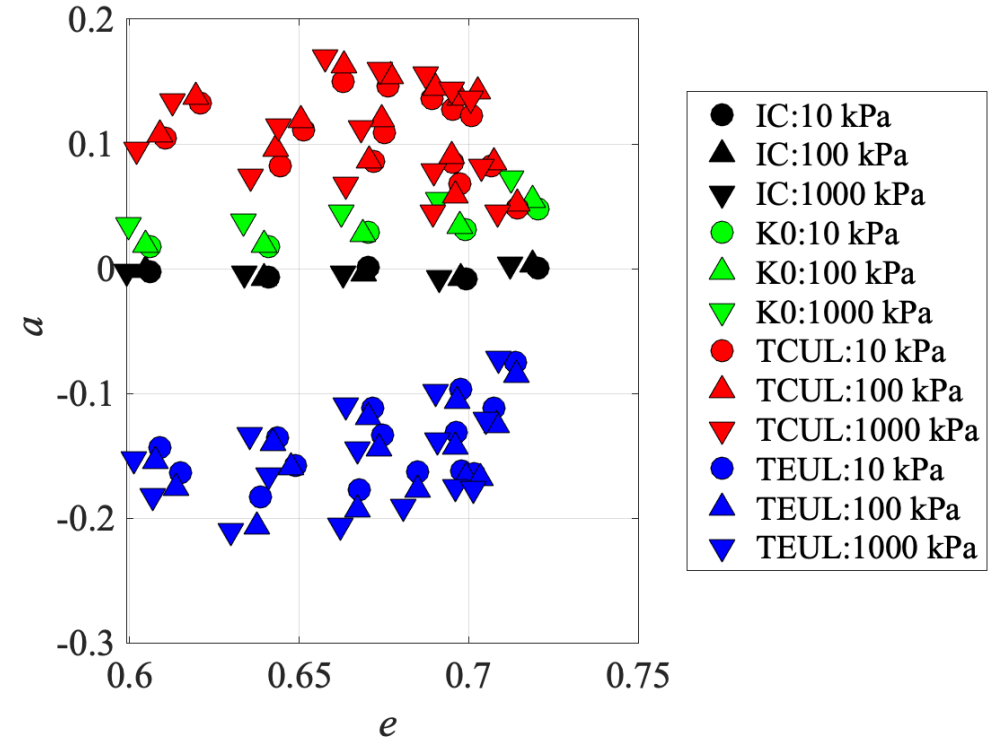
For the K_0 samples the generation procedure initially followed the process used for the *IC* samples, i.e. random generation of particles and isotropic compression to $\sigma_{\mathrm{iso}} = 1kPa$ while applying viscous damping. Once the assembly of particles was judged to be stable at $\sigma_{\mathrm{iso}} = 1kPa$, the positions of the walls normal to the horizontal direction (i.e. the walls normal to the x and y axes) were fixed and the walls normal to the vertical direction (walls normal to the z-axis) were moved until a target vertical stress (σ_{zz}) of 10, 100, or 1000 kPa was achieved. As for the IC samples, various friction coefficients ($\mu_{\mathrm{fric}} = 0.01, 0.05, 0.10, 0.20, 0.34$) were considered. Also as before, after the target vertical stress was achieved, a vertical body force was applied to simulate gravity. Typically in soil mechanics one dimensional compression is referred to as K_0 compression, hence these samples are denoted K_0. A total of 15 K_0 samples were created.

Note that σ_{xx} and σ_{yy} were not controlled during the 1D compression while σ_{zz} was controlled. The ratio of the horizontal stress to the vertical stress (STR) was calculated as:

$$STR = \frac{\sigma_h}{\sigma_v} \equiv \frac{\left(\sigma_{xx} + \sigma_{yy}\right)/2}{\sigma_{zz}} \tag{4.30}$$



(a) Mean coordination versus void ratio



(b) Anisotropy versus void ratio

Figure 4.2: Packing characteristics of the samples after Morimoto, O'Sullivan and Taborda (2022) (permission obtained from American Society of Civil Engineers). For IC and K0 samples, there are 5 samples for each stress level (5 different e values). For TCUL and TEUL samples, there are 15 samples for each stress level (5 different e values and 3 different a values).

In this study, the STR value varied from 0.654 to 0.946, and reduced with increasing μ_{fric} and increasing σ_{zz}. Note that a lower STR value indicates a more anisotropic stress state. The aspect ratio of the sample, AR, was defined as:

$$AR = \frac{L_h}{L_v} \equiv \frac{(L_x + L_y)/2}{L_z} \tag{4.31}$$

The minimum AR value of the K_0 samples was 0.997, which indicates the shapes of the K_0 samples were consistently nearly cubic.

Summary data on the packing characteristics of the K_0 samples following compression are provided on Fig. 4.2. Referring to Fig. 4.2 (a), the $\overline{Z}$ and e values were very similar to those obtained for the *IC* samples. For these cases a range of anisotropy values were attained so that $0.01 < a < 0.07$. In general a tended to increase with increasing μ_{fric} and increasing σ_{zz}, which is attributed to a higher difference between σ_v and σ_h.

Triaxial compression and unloading samples (TCUL)

In order to increase the level of fabric anisotropy of the samples, the "pre-shearing" approach described by Wei and Wang (2017) (a modification of the approach proposed by Yimsiri and Soga (2010)) was conducted. The *IC* samples were used to produce these samples. All of the *IC* samples were subjected to triaxial compression, where ε_{zz} was increased at a constant rate while σ_{xx} and σ_{yy} were maintained effectively constant using the servo-controlled algorithm, until a target vertical strain (ε_{zz}) was achieved. The target ε_{zz} values considered were 1%, 3%, and 10%. After reaching the target value, ε_{zz} was then decreased while σ_{xx} and σ_{yy} were again maintained approximately constant using the servo-control system, until σ_{zz} returned to the initial value. Throughout these procedures, the friction coefficient of the particles was set to be 0.35. The value of 0.35 was chosen referring to previous studies using interparticle friction apparatus. Cavarretta (2009) reported that the friction coefficient of dry smooth glass ballotini was between 0.084 and 0.351 and Senetakis, Coop and Todisco (2013) reported that the friction coefficient for contact between quartz sand particles was between 0.12 and 0.35. 45 *TCUL* (triaxial compression and unloading) samples were created.

As a result of the generation process, in the *TCUL* samples more contacts are orientated in the z-direction than in the x- and y-directions even though the stress state is isotropic. Referring to Fig. 4.2(a) the *TCUL* samples attained a similar range of void ratios when compared with the *IC* and K_0 samples, but the range of $\overline{Z}$ values was significantly smaller ($4.64 < \overline{Z} < 5.15$). This confirms that there is not a unique relationship between e and $\overline{Z}$. The range of anisotropies attained was higher than in the K_0 cases, with $0.04 < a < 0.17$ (Fig. 4.2(b)).

Triaxial extension and unloading samples (TEUL)

In this case the *IC* samples were also subjected to triaxial extension, where, in contrast to the *TCUL* samples, a negative vertical strain rate was applied to extend the sample. As a result, ε_{zz} decreased, becoming negative (note that the soil mechanics convention where compressive strains are positive is adopted), while the values of σ_{xx} and σ_{yy} were maintained constant. The triaxial extension was stopped when a target ε_{zz} value of -1%, -3%, or -10% was achieved. Then ε_{zz} was increased until σ_{zz} returned to its initial value. Throughout this deformation process σ_{xx} and σ_{yy} were maintained constant. 45 *TEUL* (triaxial extension and unloading) samples were created.

When compared with the *TCUL* samples, the *TEUL* samples have more contacts in the lateral (x and y) directions, explaining the negative a values observed in (Fig. 4.2(b)), however the magnitudes of the anisotropies were similar with $0.07 < |a| < 0.21$. A similar range of e and $\overline{Z}$ were obtained for the *TEUL* samples when compared with the *TCUL* samples (Fig. 4.2(b)), providing further evidence of the non-uniqueness of the e-$\overline{Z}$ relationship.

4.3.2 Small Deformation Probes to Determine Elastic Moduli

Overview of Elastic Moduli

Granular materials exhibit an elastic load-deformation response when subjected to deformations that result in small strains (Jardine, 1992). Here we followed the process used in experimental soil mechanics where small increments of strain (termed probes) are applied to a sample, in order to determine the elastic moduli.

The samples prepared in this study should have transverse isotropy (i.e. they should be cross-anisotropic) such that, referring to Eq. (4.26), $F_{xx} = F_{yy}$. This anisotropy in the fabric tensor should be reflected in the cross-anisotropy of the sample's elastic moduli. In engineering, the relationships between increments in the stress components and the resulting incremental strain components of a transversely isotropic elastic material can be written as:

$$\begin{bmatrix} \Delta\varepsilon_{xx} \\ \Delta\varepsilon_{yy} \\ \Delta\varepsilon_{zz} \\ \Delta\varepsilon_{yz} \\ \Delta\varepsilon_{zx} \\ \Delta\varepsilon_{xy} \end{bmatrix} = \begin{bmatrix} 1/E_x & -\nu_{yx}/E_x & -\nu_{zx}/E_z & 0 & 0 & 0 \\ -\nu_{xy}/E_x & 1/E_x & -\nu_{zx}/E_z & 0 & 0 & 0 \\ -\nu_{xz}/E_z & -\nu_{xz}/E_z & 1/E_z & 0 & 0 & 0 \\ 0 & 0 & 0 & 1/G_{xz} & 0 & 0 \\ 0 & 0 & 0 & 0 & 1/G_{xz} & 0 \\ 0 & 0 & 0 & 0 & 0 & 2(1+\nu_{xy})/E_x \end{bmatrix} \begin{bmatrix} \Delta\sigma_{xx} \\ \Delta\sigma_{yy} \\ \Delta\sigma_{zz} \\ \Delta\sigma_{yz} \\ \Delta\sigma_{zx} \\ \Delta\sigma_{xy} \end{bmatrix} . \tag{4.32}$$

where E_i is the Young's modulus in direction i, and G_{ij} and ν_{ij} are the shear modulus and the Poisson's ratio corresponding to shearing within the ij plane, respectively. In experimental studies in soil mechanics, some or all of these components are conventionally obtained as a result of triaxial tests in which stress or strain probes are applied or/and bender element tests (Hoque & Tatsuoka, 1998; Kuwano & Jardine, 2002). Only five of these constants should be independent.

In DEM simulations using a periodic cell, it is easier to maintain accurately $\Delta\varepsilon_{ij} = 0$ than to maintain $\Delta\sigma_{ij} = 0$. Therefore, it is more convenient to re-write the constitutive equations in Eq. (4.32) as:

$$\begin{bmatrix} \Delta\sigma_{xx} \\ \Delta\sigma_{yy} \\ \Delta\sigma_{zz} \\ \Delta\sigma_{yz} \\ \Delta\sigma_{zx} \\ \Delta\sigma_{xy} \end{bmatrix} = \begin{bmatrix} \mathcal{C}_{11} & \mathcal{C}_{12} & \mathcal{C}_{13} & 0 & 0 & 0 \\ \mathcal{C}_{12} & \mathcal{C}_{11} & \mathcal{C}_{23} & 0 & 0 & 0 \\ \mathcal{C}_{13} & \mathcal{C}_{23} & \mathcal{C}_{33} & 0 & 0 & 0 \\ 0 & 0 & 0 & \mathcal{C}_{44} & 0 & 0 \\ 0 & 0 & 0 & 0 & \mathcal{C}_{44} & 0 \\ 0 & 0 & 0 & 0 & 0 & \mathcal{C}_{66} \end{bmatrix} \begin{bmatrix} \Delta\varepsilon_{xx} \\ \Delta\varepsilon_{yy} \\ \Delta\varepsilon_{zz} \\ \Delta\varepsilon_{yz} \\ \Delta\varepsilon_{zx} \\ \Delta\varepsilon_{xy} \end{bmatrix} . \tag{4.33}$$

By comparing Eq. (4.33) and Eq. (4.32), the following relationships between the two sets of moduli can be obtained (Lubarda & Chen, 2008):

$$E_z = \mathcal{C}_{33} - \frac{2\mathcal{C}_{13}^2}{\mathcal{C}_{11} + \mathcal{C}_{12}} \tag{4.34}$$

$$E_x = E_y = \frac{(\mathcal{C}_{11} - \mathcal{C}_{12})(\mathcal{C}_{11}\mathcal{C}_{33} + \mathcal{C}_{12}\mathcal{C}_{33} - 2\mathcal{C}_{13}^2)}{\mathcal{C}_{11}\mathcal{C}_{33} - \mathcal{C}_{13}^2} \tag{4.35}$$

$\mathcal{C}_{11}$, $\mathcal{C}_{12}$, and $\mathcal{C}_{13}$ can be measured by a small deformation probe where a small increment in $\Delta\varepsilon_{xx}$ is applied while maintaining $\Delta\varepsilon_{yy} = \Delta\varepsilon_{zz} = 0$. $\mathcal{C}_{11}$, $\mathcal{C}_{12}$, and $\mathcal{C}_{13}$ can be calculated using the changes in the three orthogonal stresses ($\Delta\sigma_{xx}$, $\Delta\sigma_{yy}$, and $\Delta\sigma_{zz}$) during this

type of a small deformation probe as:

$$\mathcal{C}_{11} = \frac{\Delta\sigma_{xx}}{\Delta\varepsilon_{xx}} \tag{4.36}$$

$$\mathcal{C}_{12} = \frac{\Delta\sigma_{yy}}{\Delta\varepsilon_{xx}} \tag{4.37}$$

$$\mathcal{C}_{13} = \frac{\Delta\sigma_{zz}}{\Delta\varepsilon_{xx}} \tag{4.38}$$

$\mathcal{C}_{33}$ can be calculated from $\Delta\sigma_{zz}$ during a small deformation probe where a small value of $\Delta\varepsilon_{zz}$ is applied under $\Delta\varepsilon_{xx} = \Delta\varepsilon_{yy} = 0$:

$$\mathcal{C}_{33} = \frac{\Delta\sigma_{zz}}{\Delta\varepsilon_{zz}} \tag{4.39}$$

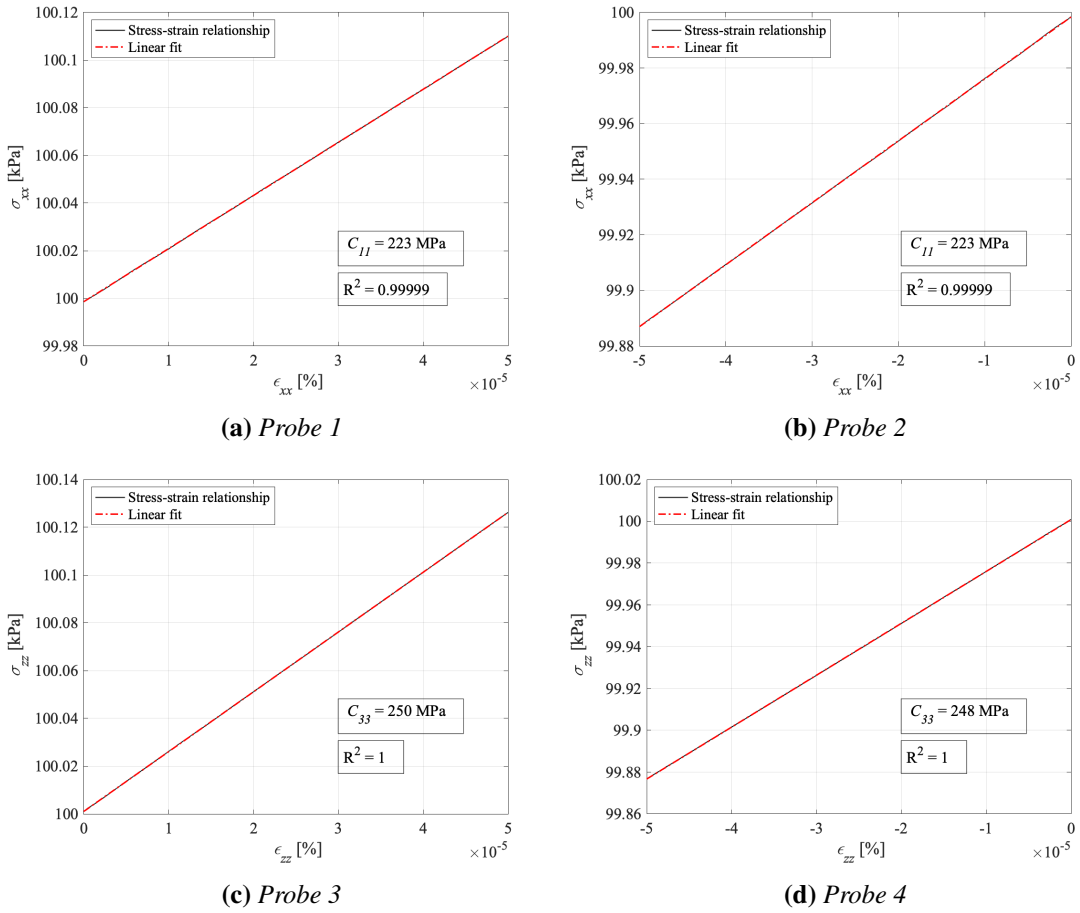
If the sample remains in the elastic regime during a strain probe, forward loading ($\Delta\varepsilon < 0$) and unloading ($\Delta\varepsilon > 0$) should give no difference in the moduli (Recchia et al., 2020). DEM simulation results by Recchia et al. (2020), comparing the moduli obtained from loading and unloading, suggest that the elastic regime of monodisperse DEM spherical assemblies with $G_{\mathrm{p}} = 29$ GPa and ν_{p} = 0.20 should be within $|\Delta\varepsilon| < 1 \times 10^{-4}\%$.

Small strain probe simulations

The following four types of small deformation probes were applied to the samples in the current study:

- $\Delta\varepsilon_{xx} > 0, \Delta\varepsilon_{yy} = \Delta\varepsilon_{zz} = 0$ (***Probe 1***)
- $\Delta\varepsilon_{xx} < 0, \Delta\varepsilon_{yy} = \Delta\varepsilon_{zz} = 0$ (***Probe 2***)
- $\Delta\varepsilon_{zz} > 0, \Delta\varepsilon_{xx} = \Delta\varepsilon_{yy} = 0$ (***Probe 3***)
- $\Delta\varepsilon_{zz} < 0, \Delta\varepsilon_{xx} = \Delta\varepsilon_{yy} = 0$ (***Probe 4***)

Following Magnanimo et al. (2008), the interparticle friction value was increased to $\mu_{\mathrm{fric}} = 0.45$ while simulating the application of a strain increment. A constant strain rate of either 0.1 %/s or -0.1 %/s was applied until a maximum absolute strain of $< 5 \times 10^{-5}\%$ was achieved. The stress-strain responses from $|\varepsilon| = 0.2 \times 10^{-5}\%$ to $|\varepsilon| = 5.0 \times 10^{-5}\%$ were used to calculate $\mathcal{C}_{11}$, $\mathcal{C}_{12}$, $\mathcal{C}_{13}$, and $\mathcal{C}_{33}$ following Eq. (4.36) - Eq. (4.39). The relationships between ε_{xx} and σ_{xx} during *Probes 1* and *2* and the relationships between ε_{zz} and σ_{zz} during *Probes 3* and *4* of a highly anisotropic *TCUL* sample ($e = 0.690$; $\overline{Z} = 4.74$; $a = 0.15$; $\sigma_{\mathrm{iso}} = 100$ kPa) are shown with linear fitting lines in Fig. 4.3. As shown in Fig. 4.3, the R^2 values are $\approx$ 1.0, which indicates that the stress-strain relationships



(a) *Probe 1* **(b)** *Probe 2*

(c) *Probe 3* **(d)** *Probe 4*

Figure 4.3: Stress-strain relationships during probes after Morimoto, O'Sullivan and Taborda (2022) (permission obtained from American Society of Civil Engineers).

during the probes are effectively linear. The values of $\mathcal{C}_{11}$, $\mathcal{C}_{12}$, $\mathcal{C}_{13}$, and $\mathcal{C}_{33}$ were obtained from the loading and unloading simulations were compared and differences between the moduli were confirmed to be small, which is also shown in Fig. 4.3. In the study by Recchia et al. (2020), the maximum absolute difference between $\mathcal{C}_{33}$ and $\mathcal{C}_{11}$ in the elastic regime is approximately 10 % and that of $\mathcal{C}_{13}$ is around 30 %. In this study, a maximum absolute difference between $\mathcal{C}_{33}$, $\mathcal{C}_{11}$, $\mathcal{C}_{12}$ and $\mathcal{C}_{13}$ was 8.57%, which is comparable to those by Recchia et al. (2020). The averaged values of the moduli obtained from the loading and unloading simulations were used to calculate E_z and E_x following Eq. (4.34) and Eq. (4.35). The E_z and E_x values of the samples are shown in Fig. 4.4, where noticeable anisotropy in Young's modulus of *TEUL* samples can be seen.

A complementary study using a larger sample consisting of 41,444 particles was conducted to demonstrate that 21,217 particles are sufficient. An *IC* sample which has a similar e value to one of the *IC* samples was produced using 41,444 particles. Sample properties ($\overline{Z}$, a, E_{zz}, k^*_{zz}/k_f) were measured and compared with an equivalent *IC* sample with 21,217 particles as Table 4.2. The difference between the two samples were very small.

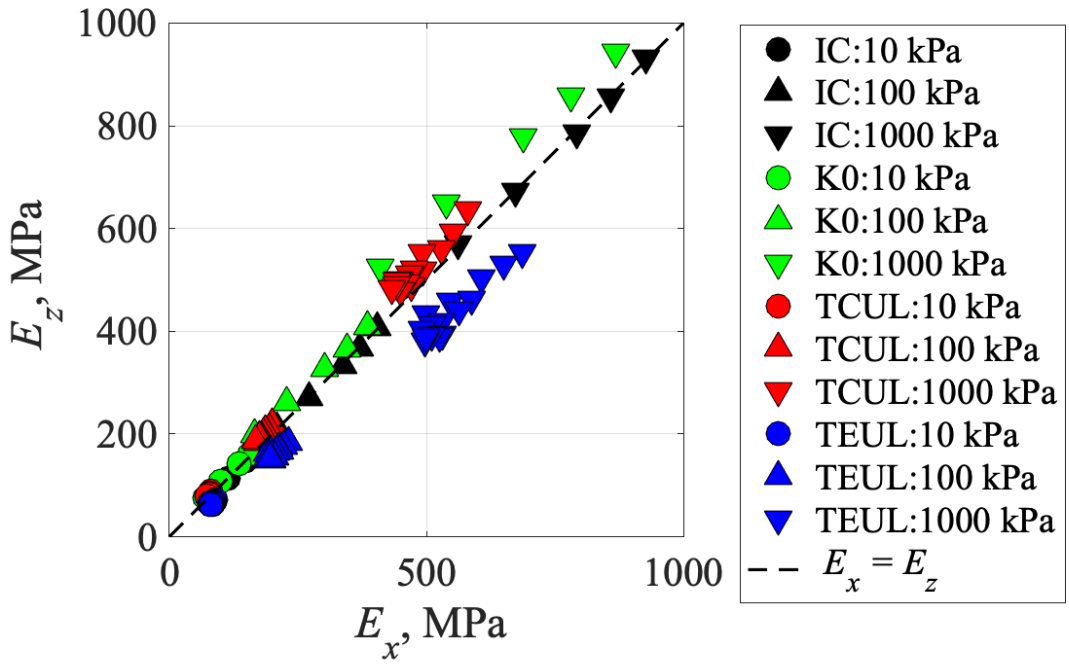


Figure 4.4: E_z and E_x values of the samples after Morimoto, O'Sullivan and Taborda (2022) (permission obtained from American Society of Civil Engineers).

4.3.3 Heat Transfer Simulations

DEM model overview

To measure the ETC of the samples, a heat pipe network model which uses the modified BOB model (Dai, Hanaor & Gan, 2019) was implemented in `LAMMPS`. The detail of the thermal DEM and validation of the code are provided in Chapter 3.

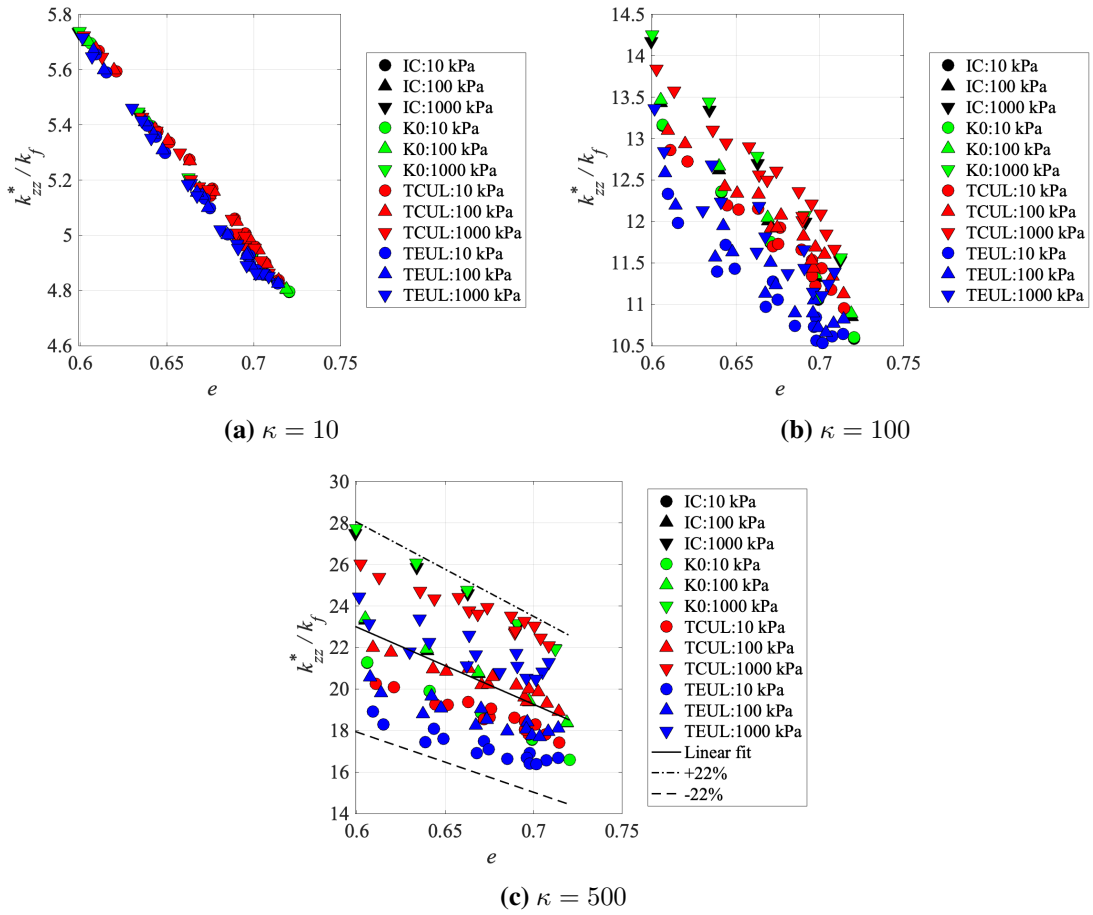
Heat transfer simulation procedure

When the effective thermal conductivity of a sample is measured, the effect of the rearrangement and thermal expansion of the particles must be minimised; otherwise, the effective thermal conductivity of the sample is dependent on the temperature gradient applied to the sample. Therefore, the positions of the particles were fixed and the thermal expansion of the particles was neglected during the heat transfer simulation. All the particles had an initial temperature of 273 K. To measure the ETC in a certain direction, i, the temperatures of opposite boundaries ($T_{\mathrm{i},0}$ and $T_{\mathrm{i},1}$) perpendicular to the i-axis were set to be 274 K and 273 K, respectively, and maintained constant during the heat transfer simulation. The temperature difference between the top and bottom of the sample was $274 - 273 = 1$ [K]; however, the magnitude of the temperature difference did not affect the effective thermal conductivity values obtained since the rearrangement and the thermal expansion of the particles were not simulated. The simulation continued until a steady state was attained. The ETC of the sample (k^*_{ii}) in the i-direction was calculated using the rate of heat at the steady state (H_{steady}):

$$k^*_{ii} = H_{\mathrm{steady}} \frac{L_i}{A_i(T_{\mathrm{i},0} - T_{\mathrm{i},1})} \ . \tag{4.40}$$

where A_i and L_i are the cross-sectional area and the length of the sample along the i-direction, respectively. The ratio of the solid to pore fluid conductivities, κ, was varied in a parametric study considering κ = 10, 30, 50, 100, 150, 300, and 500 to represent various combinations of solid particles and pore fluid. The range of κ values considered by Dai, Hanaor and Gan (2019) (κ = 10 to 1000), Cheng, Yu and Zulli (1999) (κ = 10 to 3000) and Yun and Evans (2010) (κ = 1.89 to 120) informed this choice of parameters. It is useful to consider typical κ values of soil as an example of granular materials with non-metalic solid particles. The κ value of a saturated soil ranges from 3.09 to 12.9 with $k_{\mathrm{s}} = 1.85$ to 7.70 W/(m·K) (Horai, 1971; Brigaud & Vasseur, 1989) and $k_{\mathrm{f}} = 0.5984$ W/(m·K) at 20 °C (Lide, 2004). The κ value of a dry soil is between 70.6 and 294 with $k_{\mathrm{f}} = 0.0262$ W/(m·K) at 27 °C (Lide, 2004). κ may reach around 500 for Al_2O_3-air mixtures which are common in a packed bed energy storage (Anderson et al., 2015).

ETC values



(a) $\kappa = 10$ **(b)** $\kappa = 100$

(c) $\kappa = 500$

Figure 4.5: Relationship between k^*_{zz}/k_f and e after Morimoto, O'Sullivan and Taborda (2022) (permission obtained from American Society of Civil Engineers).

The results of the heat transfer simulations are summarized in Fig. 4.5 in terms of the relationship between the void ratio and the ETC of the samples for (a) $\kappa = 10$, (b) $\kappa = 100$, and (c) $\kappa = 500$. The ETC values were normalised by k_f, the thermal conductivity of the pore fluid. One expects that $k^*_{ii}/k_\mathrm{f} \to 1$ for $e \to \infty$ and $k^*_{ii}/k_\mathrm{f} \to \kappa$ for $e \to 0$. For the lowest κ value considered ($\kappa = 10$), the void ratio and the ETC of appear to have a unique, almost linear relationship. However, for the larger κ values of 100 and 500, where an increase in contact areas between particles has a significant effect on the overall ETC, the data exhibit significant scatter. The best fit line obtained using regression is shown for $\kappa = 500$, and the data deviate from the line by up to $\pm 22\%$, showing that a relatively simple relationship between e and kappa exists only when κ is very low (e.g. $\kappa = 10$).

4.4 Exploring the link between the ETC and Packing Characterisitcs, Elastic Moduli and Stress Level

The analytical model presented in Section 4.2 indicated a link between the ETC and E, σ_{iso} and e. The data generated in the DEM simulations allow an empirical exploration of this link.

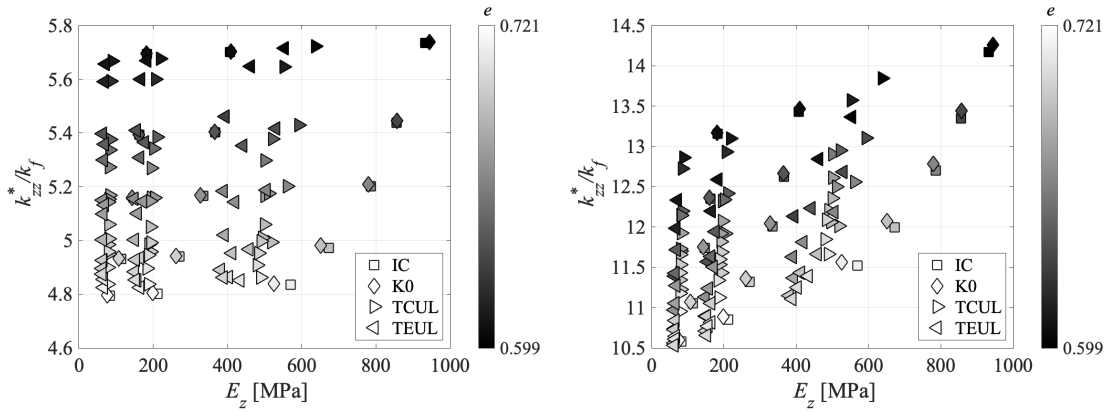
4.4.1 Young's Modulus and ETC

Fig. 4.6 presents plots of k^*_{zz}/k_{f} against E_z for samples with (a) $\kappa = 10$, (b) $\kappa = 100$, and (c) $\kappa = 500$. The relationship between E_x and k^*_{xx} for $\kappa = 500$ is presented in Fig. 4.6(d). The grayscales of the symbols on Fig. 4.6 give the values of e for the samples; a darker color indicates a denser sample (i.e. a lower e). The symbol shape indicates the sample type. In contrast to Fig. 4.5, for a given sample type, there appears to be a clearer correlation between E_z and k^*_{zz} or E_x and k^*_{xx}. This correlation is more evident for samples with a higher κ value, where the contribution of conduction through contact areas to the overall ETC is more important than in samples with a lower κ value. These data support the hypothesis that predicting the ETC or the variation in ETC using Young's moduli data is possible, particularly for higher κ values. Fig. 4.6 also indicates that for similar values of E_i, a lower void ratio gives a higher k^*_{ii} value for various κ values.

To explore further the validity of the hypothesis proposed on the basis of the analytical model, for the *IC* samples the Young's moduli predicted by Eq. (4.5) (E_{EMT}) data were determined using the e, $\overline{Z}$, G_{p}, ν_{p} and σ_{iso} values from the DEM simulations. These values of E_{EMT} are plotted against the Young's moduli measured in small deformation probes (E_{DEM}) in Fig. 4.7(a). As previous studies have shown (Makse et al., 1999; Khalili et al., 2017), the E_{EMT} values are significantly larger than the E_{DEM} values. However, as shown on Fig. 4.7(b), the ratio of E_{EMT} to a reference E_{EMT} (E_{EMTref}) reasonably agrees with the ratio of E_{DEM} to a reference E_{DEM} (E_{DEMref}) as La Ragione and Magnanimo (2012) suggested. Here the sample with the medium e value ($e = 0.6690$) and $\sigma_{\text{iso}} = 100$ kPa was chosen as the reference sample.

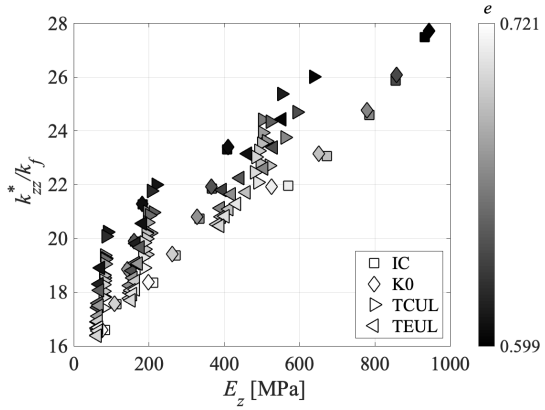
4.4.2 Effective Thermal Conductivity

Using the analytical model, it has been shown that k^*_{ij} can be divided into two components, namely $k^{\beta*}_{ij}$ and k^{h*}_{ij}. The analytical k^*_{ij} adopting a uniform temperature gradient (Eq. (4.12)) and the k^*_{ij} from the boundary heat rate (Eq. (4.40)) differ by less than 10%. $k^{\beta*}_{ij}$ is dependent on the number of contacts and the contact radii in the sample and so it is related to the Young's modulus and the stresses within the sample as shown in Eq. (4.19) and

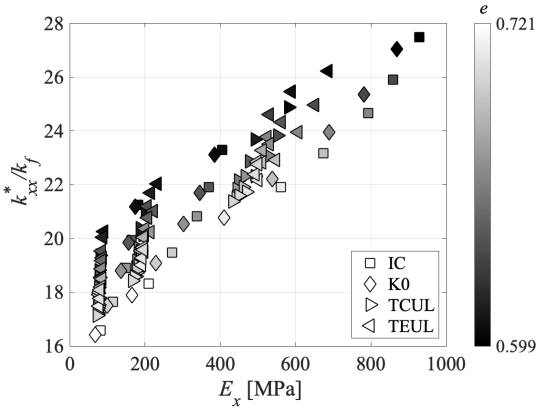


(a) $\kappa = 10$ (z-direction)

(b) $\kappa = 100$ (z-direction)

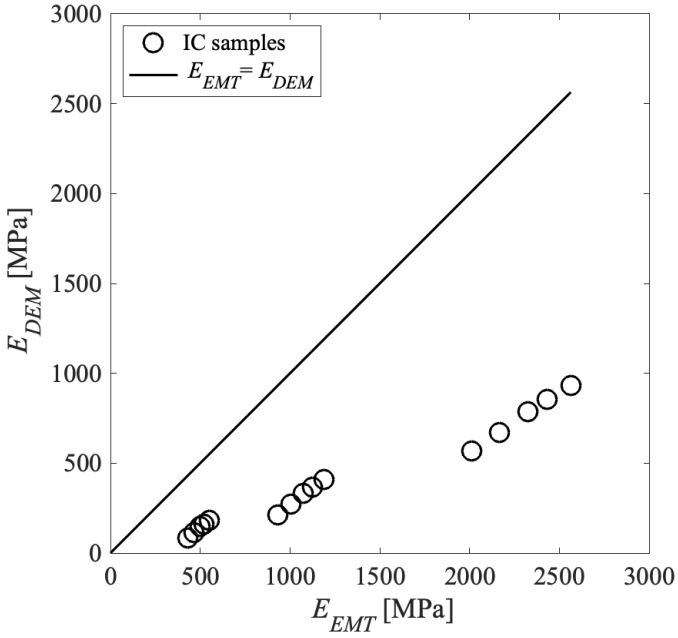


(c) $\kappa = 500$ (z-direction)

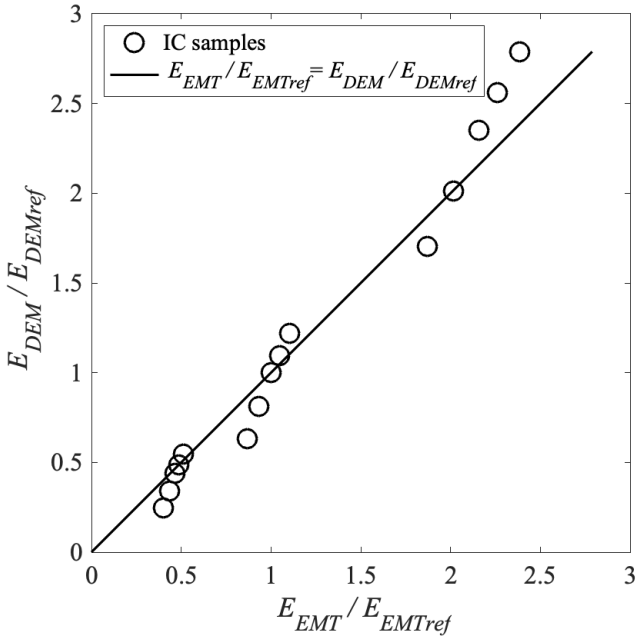


(d) $\kappa = 500$ (x-direction)

Figure 4.6: Relationship between k^*_{ii}/k_f and E_i after Morimoto, O'Sullivan and Taborda (2022) (permission obtained from American Society of Civil Engineers). Grayscale gives the values of e so that a darker color indicates a denser. The symbol shape indicates the sample type.

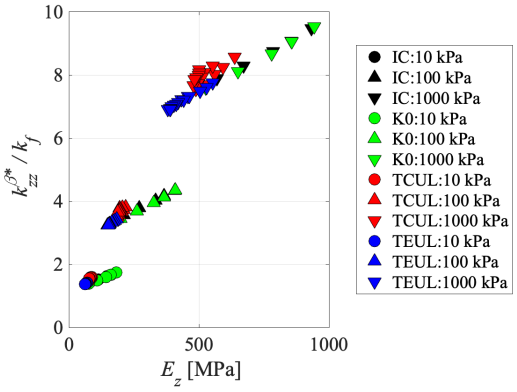


(a) E_{DEM} and E_{EMT}

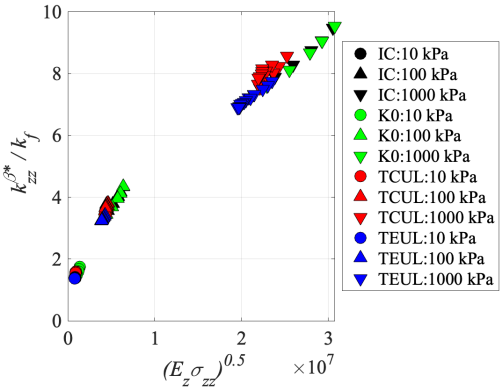


(b) $E_{\mathrm{DEM}}/E_{\mathrm{DEMref}}$ and $E_{\mathrm{EMT}}/E_{\mathrm{EMTref}}$

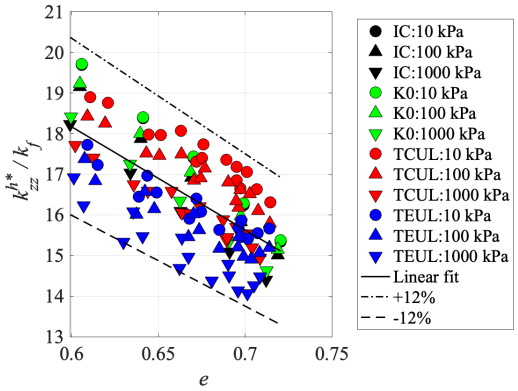
Figure 4.7: E_{DEM} and E_{EMT} after Morimoto, O'Sullivan and Taborda (2022) (permission obtained from American Society of Civil Engineers)



(a) $k_{zz}^{\beta*}$ and E_z



(b) $k_{zz}^{\beta*}$ and $E_z^{0.5}\sigma_{zz}^{0.5}$



(c) k_{zz}^{h*} and e

Figure 4.8: Plots regarding $k_{ij}^{\beta*}$ and k_{ij}^{h*} ($\kappa = 500$) after Morimoto, O'Sullivan and Taborda (2022) (permission obtained from American Society of Civil Engineers). The symbol shape indicates the stress level. The symbol color indicates the sample type.

Eq. (4.23). On the other hand, k_{ij}^{h*} is dependent on the distribution of the gap distance (h) values for the sample, which is correlated to e.

Fig. 4.8 (a) is a plot of $k_{zz}^{\beta*}/k_{\mathrm{f}}$ against E_z and it appears that, for a given value of σ_{zz} (indicated by the shape of the marker), E_z and $k_{zz}^{\beta*}$ have a nearly unique relationship (i.e. independent of the sample type). However, it is also clear from 13(a) that the effect of σ_{zz} on this relationship is substantial. As shown in Eq. (4.19), for a small σ_{zz}, which gives small contact radii, $k_{zz}^{\beta*}$ is proportional to $E_z^{0.5}\sigma_z^{0.5}$. The variation in $k_{zz}^{\beta*}/k_{\mathrm{f}}$ with $E_z^{0.5}\sigma_z^{0.5}$ is shown in Fig. 4.8 (b). The relationship is unique for the data in this study.

Fig. 4.8 (c) plots $k_{zz}^{h*}/k_{\mathrm{f}}$ against e and includes the best fit straight line. There is substantial scatter, though it is less evident than for the relationship between k_{zz}^{*} and e (Fig. 4.5 (c)), as shown by the maximum deviations from the best-fit line.

4.4.3 Proposed Expression Relating the ETC to Young's Modulus and Void Ratio

Any method to indirectly predict the ETC or the variation in ETC should be based on parameters that can be measured in experiments. Experimental measurement of $\overline{Z}$ is only possible using sophisticated 3D image analysis of datasets obtained from micro computed tomography e.g. Fonseca et al. (2013). Consequently, here we explore the potential to use the sample Young's moduli and void ratio values to estimate the corresponding ETC.

Informed by the analytical study and regression analyses of the DEM-generated data, the following equation gives a good fit to the ETC data for the DEM samples considered here:

$$\frac{k^*_{ii}}{k^*_{\text{ref}}} = \left(\frac{E_i}{E_{\text{ref}}}\right)^{\omega_{\text{E}}} \left(\frac{1+e}{1+e_{\text{ref}}}\right)^{\omega_{\text{e}}} \tag{4.41}$$

where k^*_{ref}, E_{ref}, and e_{ref} are the effective thermal conductivity, Young's modulus, and the void ratio of a reference sample and ω_{E} and ω_{e} are two empirical fitting parameters. The reference sample used here was the *IC* sample with $\sigma_{\text{iso}} = 100$ kPa and $\mu_{\text{fric}} = 0.10$ during isotropic compression as this had a void ratio that was close to the mean void ratio for all the samples; however, additional analyses showed that the reference sample chosen has little influence on the results. According to the analytical study, for small κ values, $k^{\beta*}_{ii}$ is expected to be very small, and so the effects of neglecting σ_{ii} in the expression are expected to be small.

To calibrate the empirical parameters, ω_{e} and ω_{E}, nonlinear least square regression was used employing `MATLAB` (MathWorks, 2020). The resulting ω_{E} and ω_{e} values are given in Table 4.3. The R^2 values are higher than 0.9461 for all the κ values, which demonstrates a good applicability for a wide range of κ values. The best fit ω_{E} value increased with increasing κ, which can be attributed to the larger effect of conductance through contact areas on the overall ETC for a higher κ. On the other hand, the best fit ω_{e} value was less sensitive to the κ value than the best fit ω_{E} value, with $2.2705 < \omega_{\text{e}} < 2.5586$. A comparison between the predicted and actual $\frac{k^*_{ii}}{k^*_{\text{ref}}}$ is presented in Fig. 4.9 for κ = 10, 100, and 500. As shown in Table 4.3 and Fig. 4.9, reasonably accurate results were obtained from the E and e values. It should be noted that the k^*_{ii} values of all the samples (*IC*, K_0, *TCUL*, and *TEUL*) can be predicted only using the Young's modulus in the same direction, E_i, even though the analytical study considered only isotropic samples under an isotropic stress state.

Practically, k_{ref}, E_{ref} and e_{ref} can be obtained experimentally from the same sample using commonly used techniques, such as thermal needle probe to measure k_{ref}, small strain probes or bender element tests to determine E_{ref}, and measuring the weight and the volume

Table 4.3: ω_{E}, ω_{e} and R^2 after Morimoto, O'Sullivan and Taborda (2022) (permission obtained from American Society of Civil Engineers).

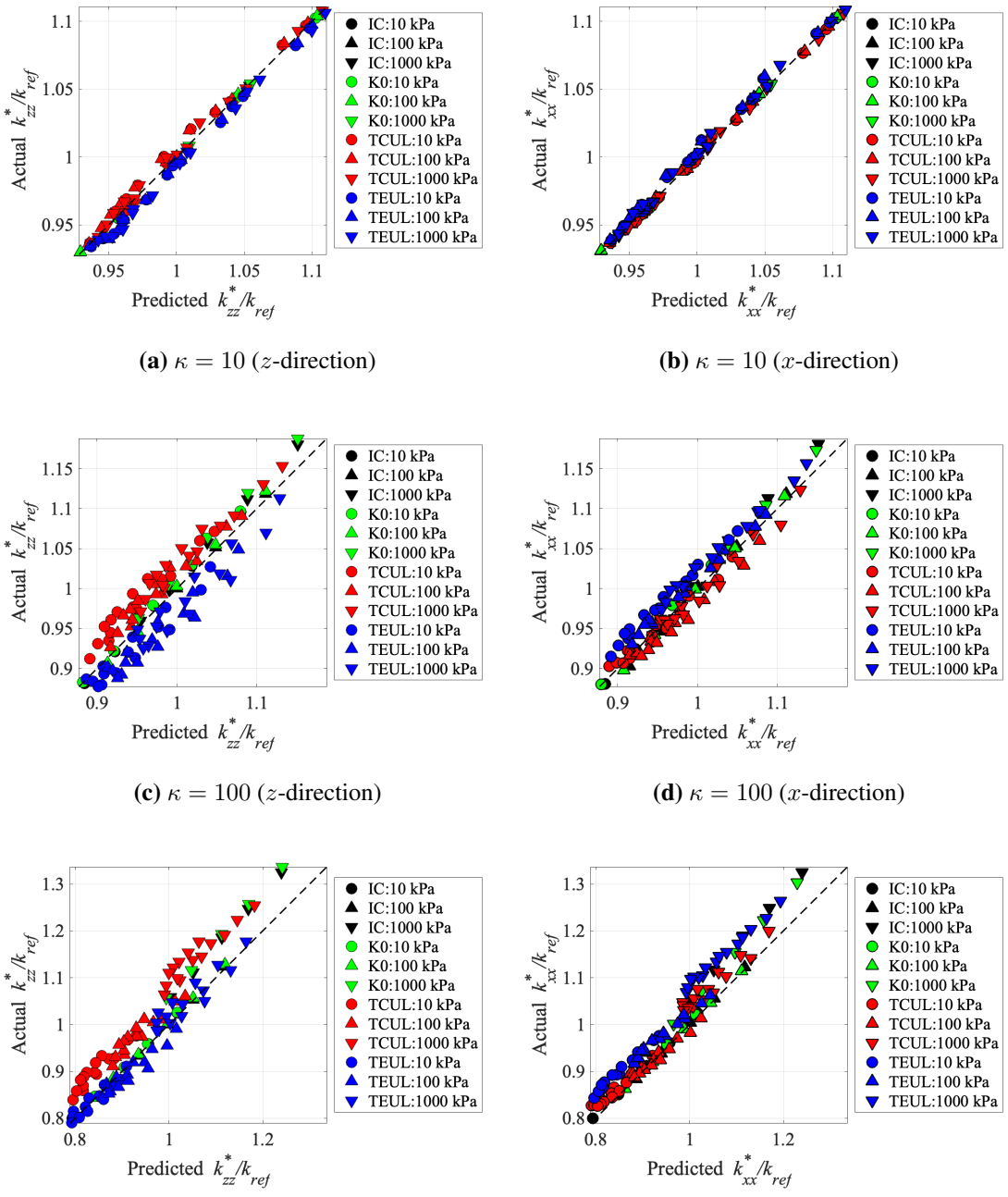
κ	Best fit ω_{E}	Best fit ω_{e}	R^2
10	-0.0010	2.5177	0.9967
30	0.0077	2.5556	0.9708
50	0.0154	2.5586	0.9563
100	0.0331	2.5117	0.9461
150	0.0474	2.4655	0.9473
300	0.0802	2.3718	0.9570
500	0.1154	2.2705	0.9664

of the sample to get e_{ref}. The accuracy of the model does not depend on the stress state, the fabric anisotropy, and the density of the samples, and so for example an oedometer with a thermal needle and bender elements installed can be used to get reference data.

4.5 Summary

This chapter has combined analytical modelling and analysis of DEM data to explore the relationships between the ETC and Young's modulus to establish a new approach to indirectly measure the ETC of granular media. Both studies adopted a heat pipe network model to apply Fourier's law for discrete elements. In order to model the effective heat conductance of discrete spheres and the gap fluid between them, the analytical model by Batchelor and O'Brien (1977) (BOB model) was employed for both analytical and DEM studies, and an excellent agreement with particle-scale FEM results was shown. The analytical study showed that the ETC of a granular medium can be related to its packing characteristics, namely e, $\overline{Z}$ and r_{c}/R, by assuming a uniform temperature gradient within the granular medium. Subsequently, the analytical study provided a relationship between the Young's modulus and the packing characteristics using Effective Medium Theory. Combining these two relationships, the novel analytical study developed in this chapter demonstrated that a component of the ETC, $k_{ii}^{\beta*}$ can be correlated with the Young's modulus and the stress level. The analytical study also suggested that the other components of the ETC, k_{ii}^{h*}, can be linked to the e value of the medium.

The complementary DEM study was carried out to support the findings in the analytical study. The packing characteristics and the stress state of virtual DEM samples were varied by subjecting the samples to different stress paths (*IC*, K_0, *TCUL*, and *TEUL*). To obtain the small strain Young's moduli of the samples, small strain probes were conducted. The ETC values of the DEM samples were measured using the heat pipe network model and the modified BOB model, which were implemented into `LAMMPS` and verified in Chapter 3.



(a) $\kappa = 10$ (z-direction)

(b) $\kappa = 10$ (x-direction)

(c) $\kappa = 100$ (z-direction)

(d) $\kappa = 100$ (x-direction)

(e) $\kappa = 500$ (z-direction)

(f) $\kappa = 500$ (x-direction)

Figure 4.9: Actual and predicted k^*_{ii}/k_{ref} values after Morimoto, O'Sullivan and Taborda (2022) (permission obtained from American Society of Civil Engineers). The symbol shape indicates the stress level. The symbol color indicates the sample type.

These simulation results showed that for a small κ, the relationship between e and the ETC of the samples was nearly unique. Conversely, for a higher κ, the correlation between E_i and k_{ii}^* is more evident, which demonstrates that the consideration of E_i and e enhances the prediction of k_{ii}^*. The dependency of $k_{ii}^{\beta *}$ on E_i and σ_{ii} and the dependency of k_{ii}^{h*} on e, which were suggested in the analytical study, were shown by detailed analysis of the DEM data.

Based on the analytical study and the DEM study, this contribution has suggested a new method predicting the ratio of k_{ii}^* to the ETC of a reference sample, k_{ref}^*, using the ratios of the Young's modulus and the void ratio to those of the reference sample (E_i/E_{ref} and $(1+e)/(1+e_{\text{ref}})$). The parameters can be calibrated easily and the predictions showed excellent agreement with the DEM results. The indirect measurement method of the ETC proposed in this study may contribute to a variety of engineering fields by reducing the costs associated with the measurement of ETC of granular materials with a simple procedure that can achieve reasonable accuracy. Consideration of polydispersity, fluid flow, particle shape and three-phase granular materials remains for future work.

CHAPTER 5

THERMAL STRESS IN GRANULAR MATERIALS

5.1 Background

Granular materials are encountered in various industrial and engineering fields. Granular materials are often subjected to heating / temperature change due to various internal and external factors such as chemical/nuclear reactions, proximity to geothermal structures such as energy piles, use of packed-bed thermal energy storage, heat application in industrial processes, and daily/seasonal temperature variations. Materials, in general, experience thermal expansion when their temperature increases. Under constrained conditions, this thermal expansion can induce significant increments in stress, which may have serious consequences (e.g. buckling of rails during hot summer periods). The application of thermal cycles to granular media are also of interest since cyclic changes in stresses induced by such loadings lead to volume change as demonstrated in previous studies (Chen et al., 2006; Vargas & McCarthy, 2007; Zhao et al., 2017; Iliev et al., 2019). Nonetheless, there has been only limited consideration of thermal stresses in granular materials while thermal stresses in continuum materials have been well discussed in the scientific literature.

The behaviour of granular materials is difficult to predict as they are formed of discrete particles that move relative to each other. The Discrete Element Method (Cundall & Strack, 1979) has emerged as a valuable tool to investigate the behaviour of granular materials. One drawback of DEM is its high computational cost. Furthermore, any user of DEM must also have access to DEM software and the skills required to run high-quality simulations. An alternative is to use Effective Medium Theory (EMT). Using EMT, Walton (1987) has introduced statistical approximations to estimate bulk properties of granular materials analytically as introduced in Section 4.2. While EMT has known limitations,

an analytical formula which estimates thermal stresses in granular materials is useful to enable overall understanding and to verify numerical models, including DEM models. Here, thermally-induced stresses in granular materials were analytically estimated developing a new expression based on EMT, where several simplifications are made. To assess the validity of the assumptions made, DEM simulations considering different packings of monodisperse particles where the radii of the particles were increased to model the thermal expansion of the particles were carried out. By comparing the responses predicted by the analytical and numerical models, the advantages and limitations of the analytical approach are critically assessed. Finally, this chapter proposes a method to correct the analytical model using the DEM data.

5.2 Analytical model

5.2.1 Analytical estimate of stress

Rothenburg and Bathurst (1989) amongst others have predicted the isotropic stress (σ_{iso}) in a monodisperse, isotropic granular material from the contact density (m_v), the mean distance between the centres of contacting particles ($\overline{\Delta}$), and the mean normal contact force ($\overline{F}$) as:

$$\sigma_{\text{iso}} \approx \frac{m_v \overline{\Delta F}}{3} \tag{5.1}$$

If the granular material consists of monodisperse particles with radius, R, then

$$\overline{\Delta} \approx 2R \tag{5.2}$$

$$m_v = \frac{N_{\text{p}} \overline{Z}}{2V} = \frac{\overline{Z}}{\frac{8}{3}\pi(1+e)R^3} \tag{5.3}$$

where N_{p} is the number of particles considered, and $\overline{Z}$, V and e are the mean coordination number, the volume and the void ratio of the sample, respectively. The void ratio is related to the solid fraction (ϕ) as $e = \phi/(1-\phi)$. Using Eqs. (5.2) and (5.3), Eq. (5.1) can be rewritten as:

$$\sigma_{\text{iso}} \approx \frac{\overline{ZF}}{4\pi(1+e)R^2} \tag{5.4}$$

5.2.2 Increment in contact force

According to the simplified Hertzian contact model, at temperature T the normal contact force (F_T) between two identical smooth particles with radius R_T, shear modulus,G_p, and Poisson's ratio ν_p, is:

$$F_T = \frac{2\sqrt{2}}{3}\frac{G_\mathrm{p}}{1-\nu_\mathrm{p}}{R_T}^{1/2}{\delta_T}^{3/2} \tag{5.5}$$

$$\delta_T = 2R_T - \Delta_T \tag{5.6}$$

where Δ_T is the distance between the centres of the two particles and δ_T is the contact deformation (overlap). If the temperature of the two particles increases to $T + \Delta T$ while the centres of the two particles remain fixed in space (Fig. 5.1(a)), following the model described in Section 2.4, R and δ increase due to the thermal expansion of the particles:

$$R_{T+\Delta T} = R_T(1+\alpha_\mathrm{L})\Delta T \equiv R_T{\alpha_\mathrm{L}}^* \tag{5.7}$$

$$\delta_{T+\Delta T} = \delta_T + 2R_T\alpha_\mathrm{L}\Delta T \tag{5.8}$$

where α_L is the particles' linear thermal expansion coefficient and ${\alpha_\mathrm{L}}^*$ is defined as

$${\alpha_\mathrm{L}}^* = (1+\alpha_\mathrm{L})\Delta T \tag{5.9}$$

Consequently, referring to Fig. 5.1(b), the contact force between particles increases to:

$$F_{T+\Delta T} = \frac{2\sqrt{2}}{3}\frac{G_\mathrm{p}}{1-\nu_\mathrm{p}}R_T^{\frac{1}{2}}{\alpha_\mathrm{L}}^{*\frac{1}{2}}(\delta_T + 2R_T\alpha_\mathrm{L}\Delta T)^{\frac{3}{2}} \tag{5.10}$$

5.2.3 Analtyical estimation of stress increase

To derive an analytical estimation for the isotropic stress induced in a granular medium by heating, two assumptions are made: (1) the change in $\overline{Z}$ due to a temperature change from T to $T + \Delta T$ is negligible, and (2) the increment in $\overline{F}$ due to the temperature change follows Eq. (5.10). The validity of these assumptions will be assessed using DEM data later. Then, the isotropic stress after the increment in temperature is estimated to be:

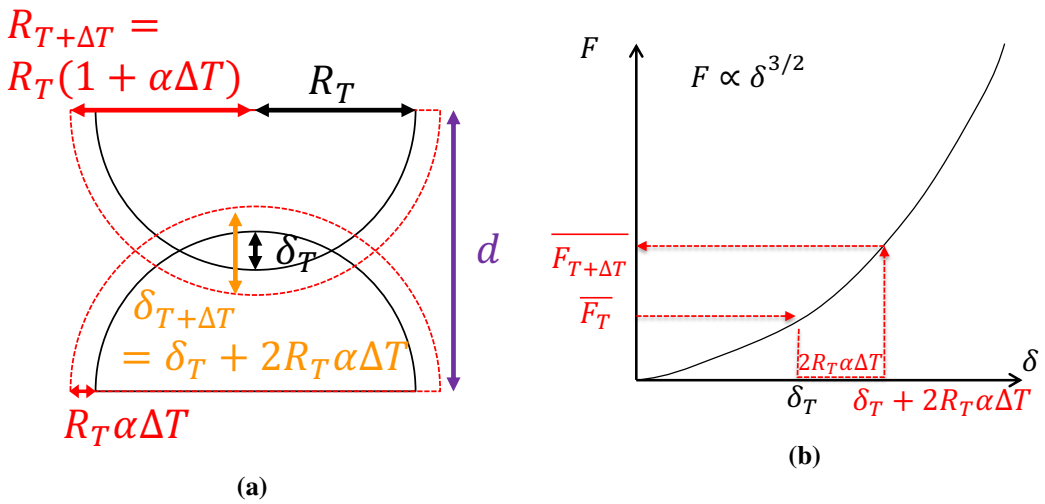


Figure 5.1: Schematic illustrations of a change in (a) the contact overlap δ and (b) the contact force F after a temperature change from T to $T + \Delta T$.

$$\sigma_{\mathrm{iso},T+\Delta T} \approx \frac{\overline{Z}_T \left[\frac{2\sqrt{2}}{3}\frac{G_\mathrm{p}}{1-\nu_\mathrm{p}} R_T^{\frac{1}{2}} {\alpha_\mathrm{L}}^{*\frac{1}{2}} (\overline{\delta_T} + 2R_T\alpha_\mathrm{L}\Delta T)^{\frac{3}{2}}\right]}{4\pi(1+e_T)R_T^2} \tag{5.11}$$

where $\overline{\delta_T}$ is the mean value of δ_T in the material, which can be estimated from Eqs. (5.4) and (5.5) to be:

$$\overline{\delta_T} \approx R_T \left(3\sqrt{2}\pi \frac{1-\nu_\mathrm{p}}{G_\mathrm{p}} \frac{1+e_T}{\overline{Z}_T} \sigma_{\mathrm{iso},T}\right)^{\frac{2}{3}} \tag{5.12}$$

A material variable, $\mathcal{M}$, and a packing variable $\mathcal{P}$, are defined as:

$$\mathcal{M} = \frac{G_\mathrm{p}}{1-\nu_\mathrm{p}} \tag{5.13}$$

$$\mathcal{P} = \frac{\overline{Z}_T}{1+e_T} \tag{5.14}$$

Thus an analytical equation which expresses $\sigma_{\mathrm{iso},T+\Delta T}$ as a function of the material properties ($\mathcal{M}$ and α_L) and initial conditions ($\sigma_{\mathrm{iso},T}$ and $\mathcal{P}$), is obtained:

$$\sigma_{\mathrm{iso},T+\Delta T} \approx \frac{\sqrt{2}}{6\pi}\mathcal{M}\mathcal{P}{\alpha_\mathrm{L}}^{*\frac{1}{2}} \left(\left(\frac{3\sqrt{2}\pi}{\mathcal{M}\mathcal{P}}\sigma_{\mathrm{iso},T}\right)^{\frac{2}{3}} + 2\alpha_\mathrm{L}\Delta T\right)^{\frac{3}{2}} \tag{5.15}$$

5.3 DEM simulation approach

DEM simulations were conducted to examine the validity of Eq. (5.15). A modified version of LAMMPS detailed in Section 4.3 was used. Two regular packings, a Face Centred Cubic (FCC) packing and a Simple Cubic (SC) packing with different $\sigma_{\text{iso},T}$ values, as well as various monodisperse random packings with different e_T and $\sigma_{\text{iso},T}$ values were considered in a parametric study. The simulation parameters are summarised in Table 5.1; the material properties of particles are those typical of glass beads that are often used in fundamental laboratory studies. In general, the FCC packing has a much higher coordination number than that of random packings and the SC packing is much looser than random packings. In addition, the rearrangement of particles does not take place in such regular packings under an isotropic stress condition due to the symmetry and periodicity of the regular packings. Consequently, the behaviour of such regular packings is expected to be different from realistic random packings. Nonetheless, these regular packings were still useful to be considered to verify Eq. (5.15).

5.3.1 Sample generation

Each cubic sample used was enclosed by periodic boundaries. For the two regular packings, the particle positions were analytically generated so that the particles were initially very close, but not overlapping. To obtain isotropic and homogeneous samples in the case of the random packings, the particle positions were incrementally randomly generated in a cubic domain whose side length is 20 mm. Particle overlap was not allowed and particles were added one by one until a void ratio of 2.0 was reached. There were 5093 uniformly sized spheres in the simulations of the random packings.

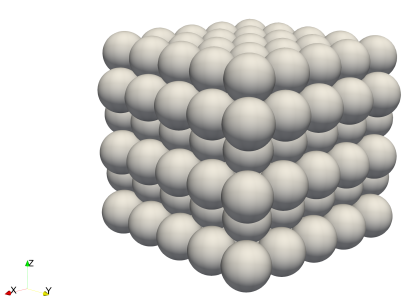
5.3.2 Isotropic compression

Each packing was compressed until the isotropic stress (σ_{iso}) reached 1 kPa with a maximum strain rate of 1%/s. Viscous damping with a damping coefficient of 0.10 was activated to reduce the kinetic energy of the particles while maintaining $\sigma_{\text{iso}} = 1$ kPa. Then, σ_{iso} was gradually increased with a maximum strain rate of 0.2%/s. Three σ_{iso} values, i.e. 10 kPa, 100 kPa, and 1000 kPa were considered.

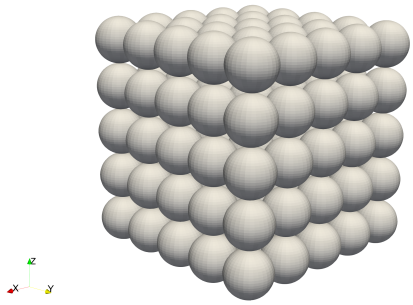
For the random packings, three inter-particle friction coefficient (μ_{fric}) values were applied during isotropic compression to achieve three samples with different e values. The packings were achieved using $\mu_{\text{fric}} = 0.01, 0.10, 0.34$ and denoted 'Dense', 'Medium', and 'Loose', respectively. The μ_{fric} value was set to be 0.0 during compression of the FCC and SC packings. Typical FCC, SC, and random packings after an isotropic compression are shown in Fig. 5.2.

Table 5.1: DEM simulation parameters. Reproduced from Morimoto, O'Sullivan and Taborda (2021), under the terms of the CC BY 4.0 license.

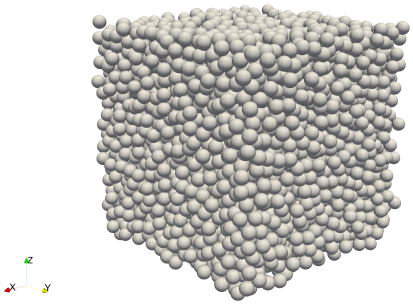
Samples	FCC	SC	Random
e	0.3505	0.9099	See Table 5.5
$\overline{Z}$	12	6	See Table 5.5
N_{p}	150	125	5093
Boundary	Periodic boundaries		
Particles	FCC	SC	Random
Contact model	Simplified Hertz-Mindlin model		
G_{p}	29 GPa		
ρ	2700 kg/m^3		
ν_{p}	0.20		
μ_{fric} (Isotropic compression)	0.0		0.01, 0.10, 0.34
μ_{fric} (Radius Expansion)	0.0		0.35
R	0.5 mm		
α_{L}	9×10^{-6} K^{-1}		
Simulations	FCC	SC	Random
σ_{iso}	10, 100, 1000 kPa		
ΔT	1, 10, 50 K		



(a) FCC packing



(b) SC packing



(c) Random packing

Figure 5.2: Typical samples

5.3.3 Radius expansion

After the isotropic compression procedure, the positions of the boundaries were fixed, and the particle radii were increased to simulate thermal expansion of the particles following Zhao et al. (2017). The increase in the particle radii took place within one time increment; simulations considering a gradual increase in the particle radii remain to be future work Three temperature increments (ΔT) of 1, 10, and 50 K were considered, and for each ΔT value, the expanded particle radii were calculated using an α_{L} value of 9.0×10^{-6} K^{-1}, which is a typical value for glass beads, following the model introduced in Section 2.4.

In the randomly packed samples two scenarios were considered after the radii were expanded. In the first case (denoted *'Fix'*), the positions of the particles were fixed, and the isotropic stress was measured immediately after the radius increase procedure. In the second case (denoted *'Release'*), particle movements were allowed with $\mu_{\mathrm{fric}} = 0.35$ and viscous damping (0.10), and the isotropic stress was measured after the stress value converged to a stable value. Only the *Fix* case was considered for the regular packings, as all the particles will be in a state of equilibrium even after the radius expansion procedure.

5.4 Comparison of analytical model and DEM results

As discussed in Section 5.2, several assumptions were introduced to obtain Eq. (5.15):

(i) The granular material is monodisperse.

(ii) The granular material is isotropic.

(iii) The material properties of the particles remain constant under a change in temperature.

(iv) The overlaps between the particles ($\overline{\delta}$) are neglected when calculating $\overline{\Delta}$ in Eq. (5.2).

(v) The change in $\overline{Z}$ due to a change in temperature is negligible.

(vi) The change in $\overline{F}$ due to a temperature change follows Eq. (5.10).

(vii) The positions of the particles are fixed.

Assumptions (i), (ii), and (iii) hold only for limited cases and in principle this EMT approach can be used to derive a more general expression. However, it is worth exploring the validity of the assumptions (iv) to (vii) before implementing this challenging generalisation. This section compares the analytical predictions with the DEM data for the samples considered here so that the errors induced by these assumptions can be examined. The validity of the assumptions for the regular packings, the *Fix* case, and the *Release* case is summarised in Table 5.2.

Table 5.2: Validity of assumptions

Assumptions	Regular packing	Random packing	
		Fix case	*Release* case
(i)	✓	✓ - in this study	
(ii)	✓	✓ - in this study	
(iii)	✓ - in this study		
(iv)	×	×	×
(v)	✓	×	×
(vi)	✓	×	×
(vii)	✓	✓	×
Maximum error observed	$< 0.1\%$	6.3 %	52.8%
$*$ ✓ . . . valid, × . . . invalid			

5.4.1 Regular packings

In a regular packing under an isotropic stress condition, where $\overline{Z}$ remains constant, the contact forces are always completely homogeneous, the particles are always in a state of equilibrium, and assumptions (v) to (vii) listed above apply. Only assumption (iv) might lead to a difference between analytical and DEM $\sigma_{\text{iso},T+\Delta T}$ values (Table 5.2).

The e_T and $\overline{Z}_T$ values used in Eqs. (5.14) and (5.15) were determined analytically. Referring to Tables 5.3 and 5.4, nearly perfect agreement was obtained between the analytical and DEM $\sigma_{\text{iso},T+\Delta T}$ values, confirming the validity of Eq. (5.15) for regular packings. Errors due to assumption (iv) are $\leq 0.1\%$ for the conditions considered in this study. These errors will increase when 'soft' granular materials with a low G_{p} are considered.

5.4.2 Random packings

This chapter considers the validity of Eq. (5.15) for random packings, where, in contrast to the regular packings, assumptions (v) to (vii) do not hold true. As outlined in Section 5.2, two simulation cases, namely *Fix* and *Release*, were considered. The e_T and $\overline{Z}_T$ values of the random packings considered in this study are summarised in Table 5.5. Analytical $\sigma_{\text{iso},T+\Delta T}$ values for the random packings were calculated using these values and compared with DEM $\sigma_{\text{iso},T+\Delta T}$ values (for both the *Fix* and *Release* cases) in Fig. 5.3 for the middle stress level considered (100 kPa). Both the analytical model and DEM data provide the same useful insight that, for a given ΔT, $\Delta\sigma_{\text{iso},\Delta T}$ increases with reducing e.

Fix case

Table 5.3: Analytical $\sigma_{\text{iso},T+\Delta T}$ values for the regular packings. Reproduced from Morimoto, O'Sullivan and Taborda (2021), under the terms of the CC BY 4.0 license.

		$\sigma_{\text{iso},T}$ [kPa]		
Packing	ΔT	10	100	1000
FCC	0	10.0	100.0	1000.0
	1	15.2	110.7	1022.7
	10	87.4	221.3	1234.0
	50	714.0	952.2	2320.1
SC	0	10.0	100.0	1000.0
	1	12.5	105.3	1011.3
	10	42.4	156.7	1115.0
	50	274.7	455.1	1614.7

Table 5.4: DEM $\sigma_{\text{iso},T+\Delta T}$ values for the regular packings. Reproduced from Morimoto, O'Sullivan and Taborda (2021), under the terms of the CC BY 4.0 license.

		$\sigma_{\text{iso},T}$ [kPa]		
Packing	ΔT	10	100	1000
FCC	0	10.0	100.0	1000.0
	1	15.2	110.7	1022.7
	10	87.4	221.4	1234.2
	50	714.0	952.4	2321.3
SC	0	10.0	100.0	999.9
	1	12.5	105.3	1011.2
	10	42.4	156.7	1115.1
	50	274.8	455.3	1615.7

Table 5.5: e_T and $\overline{Z}_T$ values of the random packings. Reproduced from Morimoto, O'Sullivan and Taborda (2021), under the terms of the CC BY 4.0 license.

		$\sigma_{\text{iso},T}$ [kPa]		
		10	100	1000
Dense	e_T	0.5749	0.5738	0.5689
	$\overline{Z}_T$	5.774	5.895	6.148
Medium	e_T	0.6498	0.6485	0.6428
	$\overline{Z}_T$	5.096	5.268	5.533
Loose	e_T	0.7176	0.7161	0.7096
	$\overline{Z}_T$	4.097	4.321	4.701

Table 5.6: Differences in $\Delta\sigma_{\text{iso},\Delta T}$ values between the analytical model and the DEM result (*Fix* case). Reproduced from Morimoto, O'Sullivan and Taborda (2021), under the terms of the CC BY 4.0 license.

		$\sigma_{\text{iso},T}$ [kPa]		
	ΔT	10	100	1000
Dense	1	5.2%	6.0%	6.3%
	10	2.2%	4.5%	5.8%
	50	-0.2%	1.8%	4.4%
Medium	1	4.3%	4.9%	5.0%
	10	1.7%	3.6%	4.6%
	50	-0.9%	1.3%	3.4%
Loose	1	4.1%	4.4%	4.3%
	10	1.3%	3.0%	3.8%
	50	-2.5%	0.2%	2.5%

In the *Fix* case, where particle movement is prohibited, assumption (vii) is enforced in the DEM model. The differences between the analytical- and DEM-generated data, given in Table 5.6, can be calculated by

$$\mathcal{E}_{\Delta\sigma_{\text{iso},\Delta T}} = \frac{\Delta\sigma_{\text{iso},\Delta T}^{\text{Model}} - \Delta\sigma_{\text{iso},\Delta T}^{\text{DEM}}}{\Delta\sigma_{\text{iso},\Delta T}^{\text{DEM}}} \tag{5.16}$$

A positive value of $\mathcal{E}_{\Delta\sigma_{\text{iso},\Delta T}}$ indicates an analytical result that is higher than the corresponding DEM result. As the errors due to assumption (iv) are found to be very small from the study using the regular packings, the errors shown in Table 5.6 are attributed to assumptions (v) and (vi) listed in Table 5.2. The $\overline{Z}$ value after a temperature increment is summarised in Table 5.7. In the case of a small temperature increment (e.g. $\Delta T = 1$ K), where the increase in $\overline{Z}$ is small, the differences are < 6.3%, and they can be attributed to ignoring the heterogeneity in the contact forces (assumption (vi)). As ΔT increased, the differences decreased because the errors due to assumption (vi) are counteracted by ignoring the increase in $\overline{Z}$ (assumption (v)) which leads to underestimation of $\sigma_{\text{iso},T+\Delta T}$.

Release case

In general, if the radii of particles in a random packing are increased, the particles do not remain in static equilibrium. This is true even if the changes in radii take place simultaneously, the rearrangements are due to the non-linearity of the contact stiffness, the sliding contacts and the generation of new contacts. These particle movements lead to a redistribution of the contact forces (or a displacement of the particles) and reduction in the overall stress. The differences between the predictions of $\Delta\sigma_{\text{iso},\Delta T}$ for analytical

Table 5.7: $\overline{Z}_{T+\Delta T}$ from the DEM result (*Fix* case).

		$\overline{Z}_{T+\Delta T}$			$\Delta\overline{Z}_{\Delta T}/\overline{Z}_T$		
		$\sigma_{\mathrm{iso},T}$ [kPa]			$\sigma_{\mathrm{iso},T}$ [kPa]		
	ΔT	10	100	1000	10	100	1000
Dense	0	5.774	5.895	6.148			
	1	5.784	5.906	6.154	0.2%	0.2%	0.1%
	10	5.814	5.925	6.166	0.7%	0.5%	0.3%
	50	5.894	5.984	6.190	2.1%	1.5%	0.7%
Medium	0	5.096	5.268	5.533			
	1	5.118	5.285	5.554	0.4%	0.3%	0.4%
	10	5.160	5.306	5.561	1.3%	0.7%	0.5%
	50	5.278	5.374	5.590	3.6%	2.0%	1.0%
Loose	0	4.097	4.321	4.701			
	1	4.128	4.373	4.765	0.7%	1.2%	1.4%
	10	4.208	4.414	4.774	2.7%	2.2%	1.6%
	50	4.389	4.523	4.829	7.1%	4.7%	2.7%

and DEM data are shown in Table 5.8. The $\overline{Z}$ value after a temperature increment is summarised in Table 5.9, which shows that a change in $\overline{Z}$ is not significant for all cases. In all cases considered, the analytical approach overestimated $\sigma_{\mathrm{iso},T+\Delta T}$ because the stress reduction was neglected (assumption (vii)). The differences increased with increasing ΔT and reducing sample density; both of these factors increase the likelihood of particle movements occurring. While the errors for dense and medium packings were within 20%, Eq. (5.15) is clearly not reliable for the loosest sample considered.

5.5 Improving the analytical model using DEM results

As discussed in Section 5.4, among assumptions (iv) to (vii), assumption (vii) is attributed to the discrepancy between Eq. (5.15) and the DEM result. The effect of particle displacements needs to be considered to improve the efficacy of the analytical model. When the temperature of a sample increased from T to $T + \Delta T$, the displacement vector of particle $p1$ can be expressed as:

$$\Delta\mathbf{x}_{p1,\Delta T} = \mathbf{x}_{p1,T+\Delta T} - \mathbf{x}_{p1,T} \tag{5.17}$$

where $\mathbf{x}_{p1,T}$ is the position of particle $p1$ at temperature T. The collective movement of particles in a sample can be quantified by the mean value of the magnitude of $\Delta\mathbf{x}_{\Delta T}$, which is denoted as $\overline{\|\Delta\mathbf{x}_{\Delta T}\|}$. The difference between the analytical model and DEM

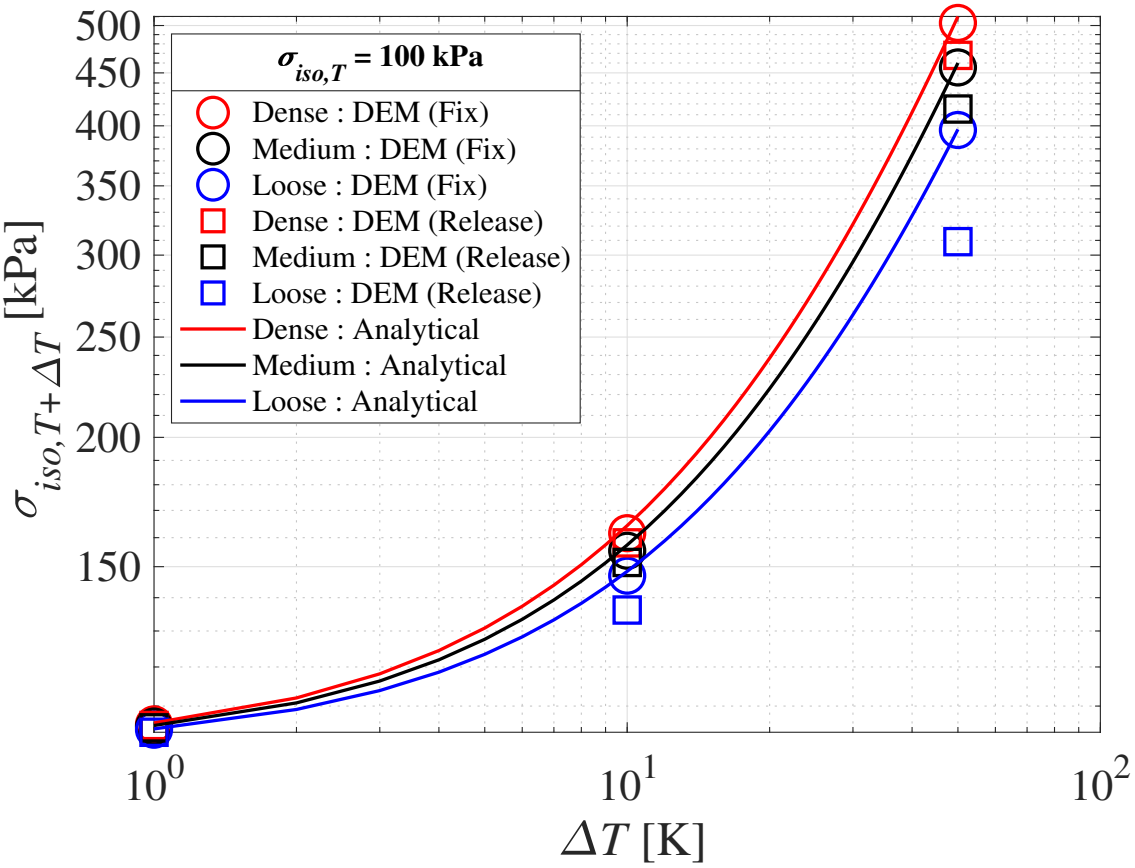
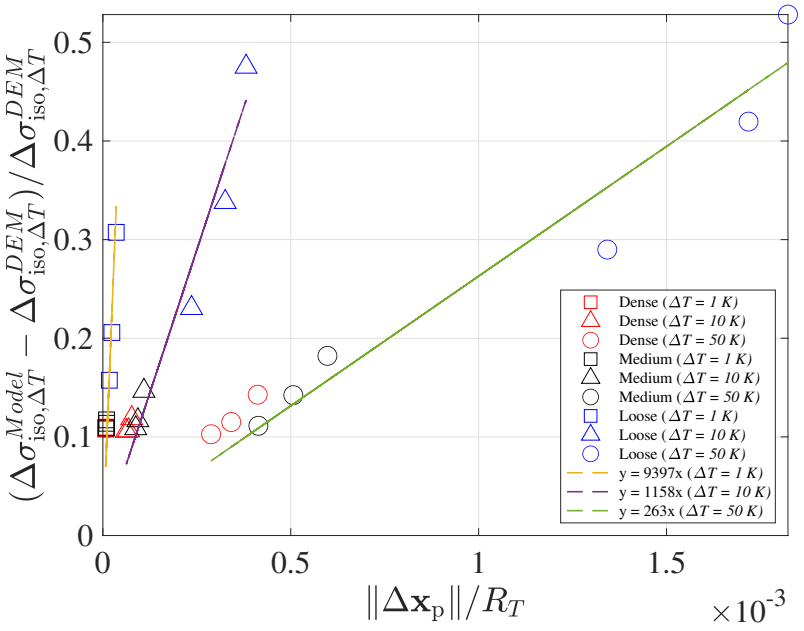


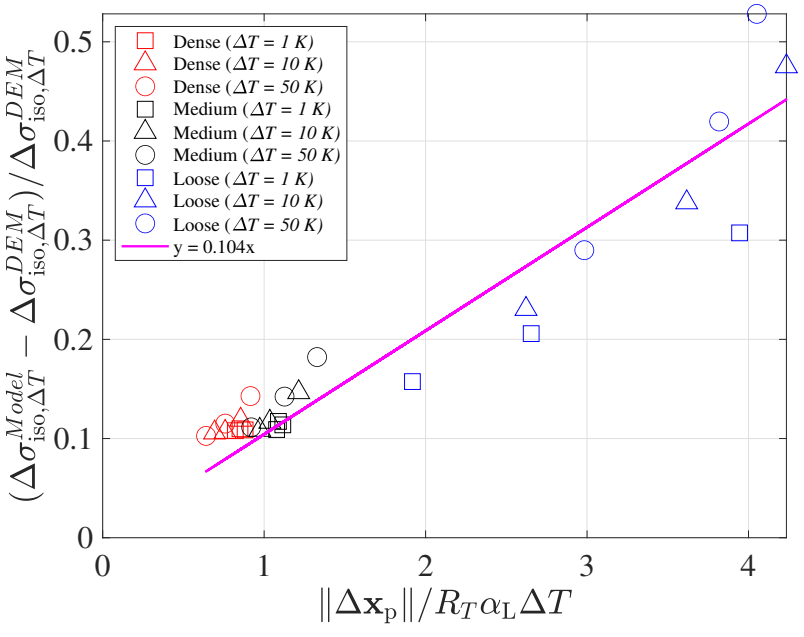
Figure 5.3: Comparison between Analytical and DEM $\sigma_{\mathrm{iso},T+\Delta T}$ values ($\sigma_{\mathrm{iso},T}$ = 100 kPa). Reproduced from Morimoto, O'Sullivan and Taborda (2021), under the terms of the CC BY 4.0 license.

Table 5.8: Differences in $\Delta\sigma_{\mathrm{iso},\Delta T}$ values between the analytical model and the DEM result (*Release case*). Reproduced from Morimoto, O'Sullivan and Taborda (2021), under the terms of the CC BY 4.0 license.

		$\sigma_{\mathrm{iso},T}$ [kPa]		
	ΔT	10	100	1000
Dense	1	10.9%	11.0%	10.8%
	10	11.9%	10.7%	10.6%
	50	14.3%	11.5%	10.3%
Medium	1	11.7%	11.4%	10.9%
	10	14.7%	11.7%	10.9%
	50	18.2%	14.2%	11.1%
Loose	1	30.7%	20.6%	15.7%
	10	47.5%	33.8%	23.1%
	50	52.8%	42.0%	29.0%



(a)



(b)

Figure 5.4: Error in $\Delta\sigma_{\mathrm{iso},\Delta T}$ versus normalised mean particle displacement. (a) normalised by particle radius R_T. (b) normalised by $R_T\alpha_\mathrm{L}\Delta T$.

Table 5.9: $\overline{Z}_{T+\Delta T}$ from the DEM result (*Release* case).

		$\overline{Z}_{T+\Delta T}$			$\Delta\overline{Z}_{\Delta T}/\overline{Z}_T$		
		$\sigma_{\mathrm{iso},T}$ [kPa]			$\sigma_{\mathrm{iso},T}$ [kPa]		
	ΔT	10	100	1000	10	100	1000
Dense	0	5.774	5.895	6.148			
	1	5.777	5.894	6.134	0.1%	0.0%	-0.2%
	10	5.810	5.908	6.142	0.6%	0.2%	-0.1%
	50	5.895	5.978	6.172	2.1%	1.4%	0.4%
Medium	0	5.096	5.268	5.533			
	1	5.096	5.251	5.517	0.0%	-0.3%	-0.3%
	10	5.142	5.271	5.523	0.9%	0.1%	-0.2%
	50	5.278	5.363	5.558	3.6%	1.8%	0.5%
Loose	0	4.097	4.321	4.701			
	1	4.091	4.300	4.675	-0.1%	-0.5%	-0.5%
	10	4.157	4.333	4.689	1.5%	0.3%	-0.3%
	50	4.322	4.441	4.764	5.5%	2.8%	1.3%

result defined in Eq. (5.16) was plotted against the normalised $\overline{\|\Delta\mathbf{x}_{\Delta T}\|}$ value in Fig. 5.4. In Fig. 5.4(a), the $\overline{\|\Delta\mathbf{x}_{\Delta T}\|}$ values were normalised by the particle radius (R_T). As shown in Fig. 5.4(a), for a given, identical ΔT value, the data points from the packings with a variety of e_T values can be regressed by a linear function:

$$\mathcal{E}_{\Delta\sigma_{\mathrm{iso},\Delta T}} = X_1 \frac{\overline{\|\Delta\mathbf{x}_{\Delta T}\|}}{R_T} \tag{5.18}$$

$X_1 = 9397$ for $\Delta T = 1$ K, $X_1 = 1158$ for $\Delta T = 10$ K, and $X_1 = 263$ for $\Delta T = 50$ K, which indicates that C_1 is inversely proportional to ΔT. Following the observation, $\overline{\|\Delta\mathbf{x}_{\Delta T}\|}$ was normalised by $R_T\alpha_{\mathrm{L}}\Delta T$ (i.e. the change in particle radii after a temperature change) and is plotted with $\mathcal{E}_{\Delta\sigma_{\mathrm{iso},\Delta T}}$ in Fig. 5.4(b). Fig. 5.4(b) indicates that the particle movement can be related to the packing characteristics. A nearly linear relationship between $\overline{\|\Delta\mathbf{x}_{\Delta T}\|}/R_T\alpha_{\mathrm{L}}\Delta T$ and $\mathcal{E}_{\Delta\sigma_{\mathrm{iso},\Delta T}}$ is obtained and the following relationship was obtained after LSQ fitting:

$$\mathcal{E}_{\Delta\sigma_{\mathrm{iso},\Delta T}} = 0.104 \frac{\overline{\|\Delta\mathbf{x}_{\Delta T}\|}}{R_T\alpha_{\mathrm{L}}\Delta T} \tag{5.19}$$

Eq. (5.19) can be used to correct the error arising from the simplification made in Eq. (5.15); however, $\overline{\|\Delta\mathbf{x}_{\Delta T}\|}$ needs to be estimated using the packing characteristics at the initial state. A possible idea is that the displacement of the particles can be related to the stability

(or redundancy) of the packing and thus the packing variable $\mathcal{P} = \overline{Z}_T/(1+e_T)$, which expresses the density of the contacts in the sample, could be used. To seek the possibility of predicting $\overline{\|\Delta\mathbf{x}_{\Delta T}\|}$ from $\mathcal{P}$, two types of normalised $\overline{\|\Delta\mathbf{x}_{\Delta T}\|}$ values were plotted against the $\mathcal{P}$ in Fig. 5.5. In Fig. 5.5(a), the $\overline{\|\Delta\mathbf{x}_{\Delta T}\|}$ was normalised by R_T similarly to Fig. 5.4(a), which indicates that ΔT needs to be considered to find a unique relationship between the mean particle displacement and the packing variable. Fig. 5.5(b) is a similar plot but $\overline{\|\Delta\mathbf{x}_{\Delta T}\|}$ is normalised by the change in the particle radius, $R_T\alpha_{\mathrm{L}}\Delta T$. A roughly unique relationship between $\mathcal{P}$ and $\overline{\|\Delta\mathbf{x}_{\Delta T}\|}/R_T\alpha_{\mathrm{L}}\Delta T$ is found in Fig. 5.5(b), which can be formulated as:

$$\frac{\overline{\|\Delta\mathbf{x}_{\Delta T}\|}}{R_T\alpha_{\mathrm{L}}\Delta T} = \exp(-1.15\mathcal{P} + 4.01) \tag{5.20}$$

Combining Eq. (5.19) and Eq. (5.20),

$$\mathcal{E}_{\Delta\sigma_{\mathrm{iso},\Delta T}}(\mathcal{P}) = 0.104\exp(-1.15\mathcal{P} + 4.01) \tag{5.21}$$

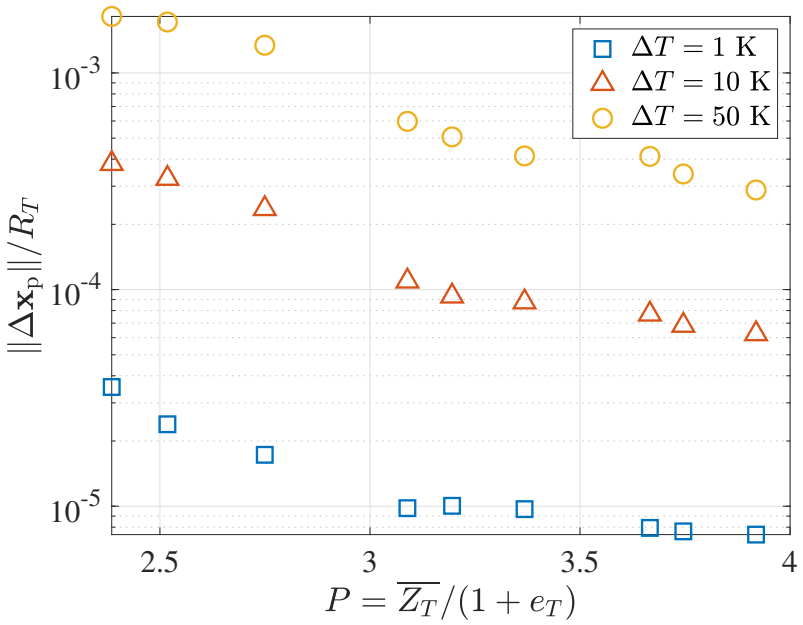
Using Eq. (5.21), the analytical model can be corrected by:

$$\sigma_{\mathrm{iso},T+\Delta T} = \sigma_{\mathrm{iso},T} + \frac{\sigma^{\text{analytical}}_{\mathrm{iso},T+\Delta T} - \sigma_{\mathrm{iso},T}}{\mathcal{E}_{\Delta\sigma_{\mathrm{iso},\Delta T}} + 1} = \sigma_{\mathrm{iso},T} + \frac{\sigma^{\text{analytical}}_{\mathrm{iso},T+\Delta T} - \sigma_{\mathrm{iso},T}}{0.104\exp(-1.15\mathcal{P} + 4.01) + 1} \tag{5.22}$$

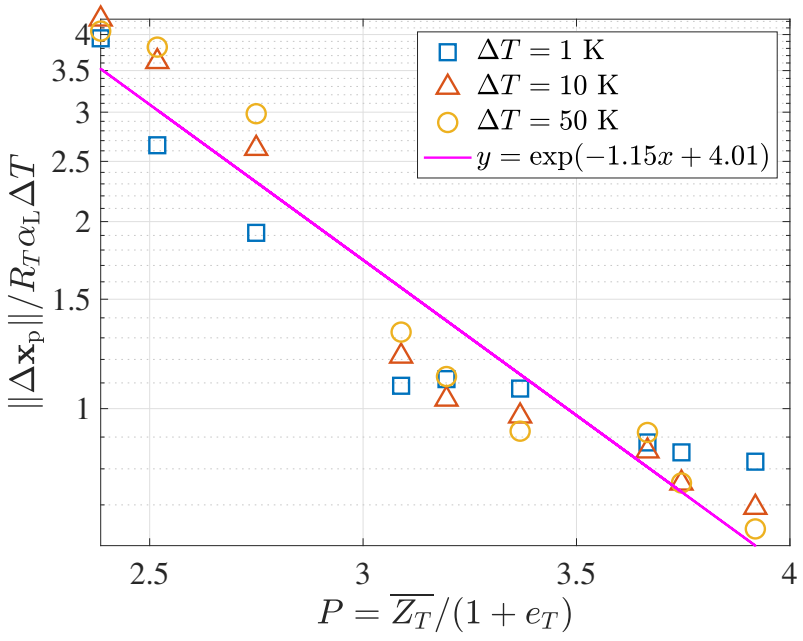
where $\sigma^{\text{analytical}}_{\mathrm{iso},T+\Delta T}$ is the analytical thermal stress calculated by Eq. (5.15) and $\sigma_{\mathrm{iso},T}$ is the thermal stress obtained from the DEM simulation. Corrected analytical $\sigma_{\mathrm{iso},T+\Delta T}$ values for the random packings were compared with DEM $\sigma_{\mathrm{iso},T+\Delta T}$ values (*Release* cases) in Fig. 5.6 for $\sigma_{\mathrm{iso},T} = 100$ kPa. In addition, the differences between the predictions of $\Delta\sigma_{\mathrm{iso},\Delta T}$ from the corrected analytical model and DEM data are shown in Table 5.10. Referring to Fig. 5.6 and Table 5.10, the accuracy of the analytical model can be improved by introducing the correction term (Eq. (5.21)), which is based on the packing variable $\mathcal{P}$ and three fitting parameters. The maximum error obtained for the cases considered in this study was 11.6% after the correction.

5.6 Summary

This chapter has presented an analytical expression to predict thermally-induced stress increments in isotropic monodisperse granular materials (Section 5.2). Data generated using the new expression were compared with complementary data generated from DEM simulations (Section 5.4). The analytical expression achieved very good predictions for



(a)



(b)

Figure 5.5: Normalised mean particle displacement versus the packing variable $\mathcal{P}$. (a) normalised by particle radius R_T. (b) normalised by $R_T\alpha_\mathrm{L}\Delta T$.

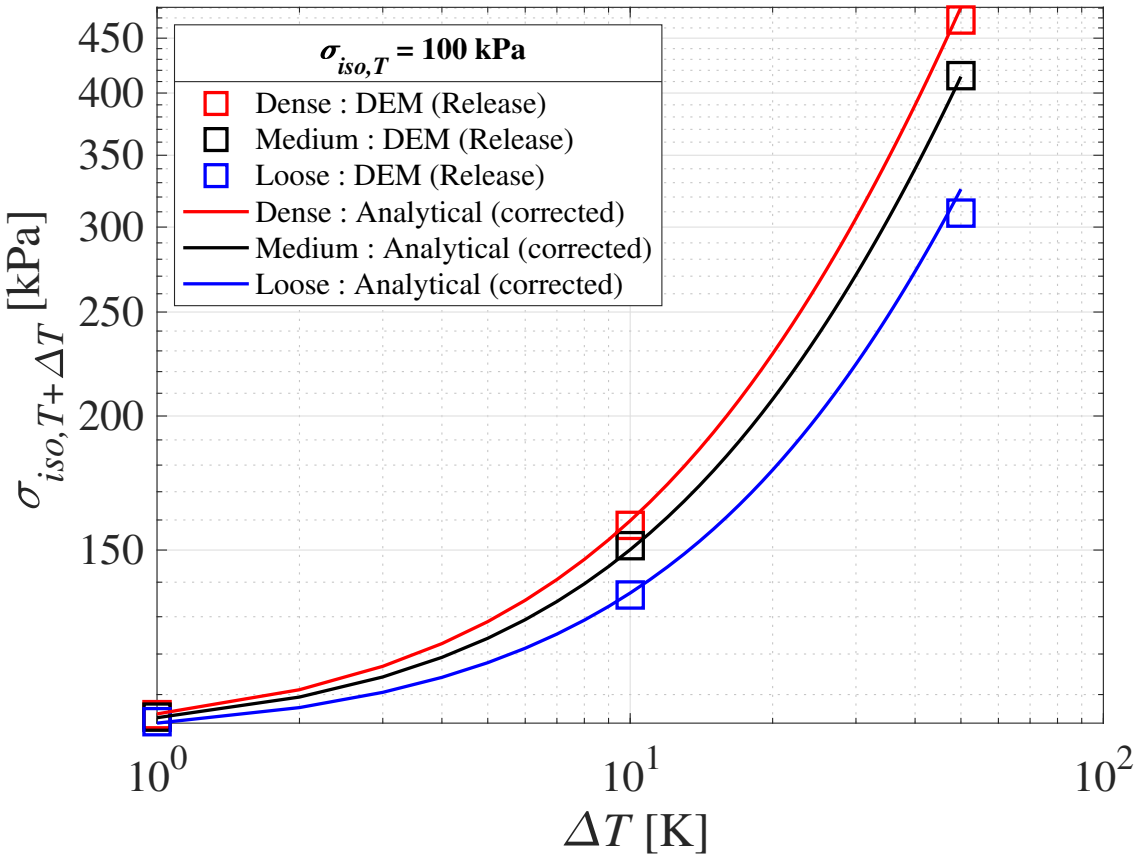


Figure 5.6: Comparison between corrected analytical and DEM $\sigma_{\mathrm{iso},T+\Delta T}$ values ($\sigma_{\mathrm{iso},T}$ = 100 kPa).

Table 5.10: Differences in $\Delta\sigma_{\mathrm{iso},\Delta T}$ values between the corrected analytical model and the DEM result (*Release* case).

		$\sigma_{\mathrm{iso},T}$ [kPa]		
	ΔT	10	100	1000
Dense	1	2.2%	3.0%	4.2%
	10	3.2%	2.7%	4.0%
	50	5.4%	3.5%	3.7%
Medium	1	-4.0%	-2.8%	-0.9%
	10	-1.5%	-2.5%	-0.9%
	50	1.5%	-0.3%	-0.7%
Loose	1	-4.5%	-8.4%	-6.9%
	10	7.7%	1.6%	-1.0%
	50	11.6%	7.8%	3.8%

regular packings and good predictions for random packings where particle movements are fixed. For random packings where particle movements are allowed, the relative error in stress increments was $< 20\%$, which is remarkable considering that the analytical model was developed without any fitting from the DEM data. However, the analytical expression was shown to be ineffective in the case of loose random packings where particle movements are allowed.

To correct the errors, the mean particle displacement normalised by a particle radius increment was analysed and shown to be related to the discrepancy between the analytical model and the DEM data. This chapter showed that such mean particle displacement can be estimated from the packing variable $\mathcal{P}$, which expresses the redundancy of the system. Finally, this chapter proposes a corrected analytical model, whose correction term only depends on $\mathcal{P}$. The corrected analytical model agrees well with the DEM results with a maximum error of 11.6%. The result indicates that the stress change due to the particle rearrangement can be related to the initial packing characteristics; namely e and $\overline{Z}$.

This chapter also indicates an interesting perspective of thermo-mechanical behaviour of granular materials. Even for isotropic granular materials, a change in the temperature introduces a displacement of the particles, which was observed as the difference between the analytical model and the DEM result in this chapter as this chapter considered the stationary boundary condition. If stress-control boundary conditions are applied, these particle displacements could result in a change in the volume of the granular sample. The next chapter focuses on such a volume change of granular materials induced by cyclic temperature variations.

CHAPTER 6

EFFECT OF CYCLIC TEMPERATURE VARIATIONS ON GRANULAR MATERIALS

6.1 Background

Granular materials subject to cyclic temperature variations are encountered in various engineering fields including soils around thermo-active piles, packed bed energy storage, and food grains in a silo subject to seasonal temperature variations. A number of laboratory experiments (Chen et al., 2006; Ng, Wang & Zhou, 2016) have shown that this type of cyclic temperature variation induces a volume change in granular materials, which may need to be accounted for in engineering design of management of systems involving granular materials.

However, the fundamental mechanisms underlying the volume change behaviour of granular materials subject ot cyclic temperature change are not fully understood. A thermal DEM such as the option introduced in Section 3.2 can be a powerful tool to explore such fundamental mechanisms. Studies by Zhao et al. (2017) and Suo et al. (2021) have considered the response of granular materials under a stationary boundary condition subjected to cyclic temperature change; however, such a boundary condition is rarely encountered in practice since aby container holding a granular medium is also subjected to thermal expansion and contraction. A study by Coulibaly, Shah and Rotta Loria (2020) conducted thermal cycle simulations under an oedometoric condition; however, such an oedometric condition leads to the change in the horizontal stress, and thus, it is very difficult to isolate the effect of temperature variations from the change in the stress state. In addition, in a thermal oedometer experiment, the metal container also expands/contracts; thus, it is impossible to compare such DEM results with previous laboratory experiment results.

Table 6.1: Particle size distribution (PSD).

Hostun sand (Azeiteiro et al., 2017)	
Grain size (mm)	% finer
0.844	100.0
0.422	88.2
0.251	8.4
0.150	0.6
0.074	0.0

In this chapter, a novel study simulating granular media subjected to thermal cycles under an isotropic stress condition is presented. A major advantage of employing such a simulation condition is that the stress state is constant and the pure thermal behaviour of granular materials can be monitored. Another advantage is that it is possible to compare the DEM results with experimental results using a thermal triaxial apparatus such as Ng, Wang and Zhou (2016) and the temperature-controlled triaxial MKII cell, which is under development at Imperial College London (Bortolotto, Taborda & O'Sullivan, 2021).

6.2 Methodology

6.2.1 Model parameters

In this chapter, the thermal DEM framework introduced in Section 3.2 was used. The PSD was determined by the following procedures. To generate a continuous curve the particle size data of the PSD of Hostun sand reported by Azeiteiro et al. (2017) were extracted (Table 6.1). The discrete particle size data were interpolated by a logistic function following Evans et al. (2009) and Yun and Evans (2010) as shown in Fig. 6.1.

The material properties of typical Aluminum-Borosilicate glass beads saturated by water were used. Assuming that the surface of glass beads is smooth, the simplified Hertz-Mindlin contact model was used. The shear modulus and Poisson's ratio of the particles (G_p and ν_p) were set to be 32 GPa, and 0.22 following Barreto (2009). The friction coefficient of the particles (μ_fric) was set to be 0.325 following Barreto (2009) during the transient heat transfer and the triaxial preshearing simulations, while the μ_fric value was varied to achieve a variety of e values during the isotropic compression simulations. The thermal conductivities of the particles and the fluid (k_s and k_f) were 1.127 and 0.596, which gives a thermal conductivity ratio (κ) of 1.89. For this κ value, the conduction through the gap fluid cannot be neglected; thus, this Batchelor and O'Brien (1977) (BOB) model, introduced in Section 2.2.3, was employed. The parameter χ used in the modified BOB model (Eq. (2.23)) was calibrated from the experimental effective thermal conductivity

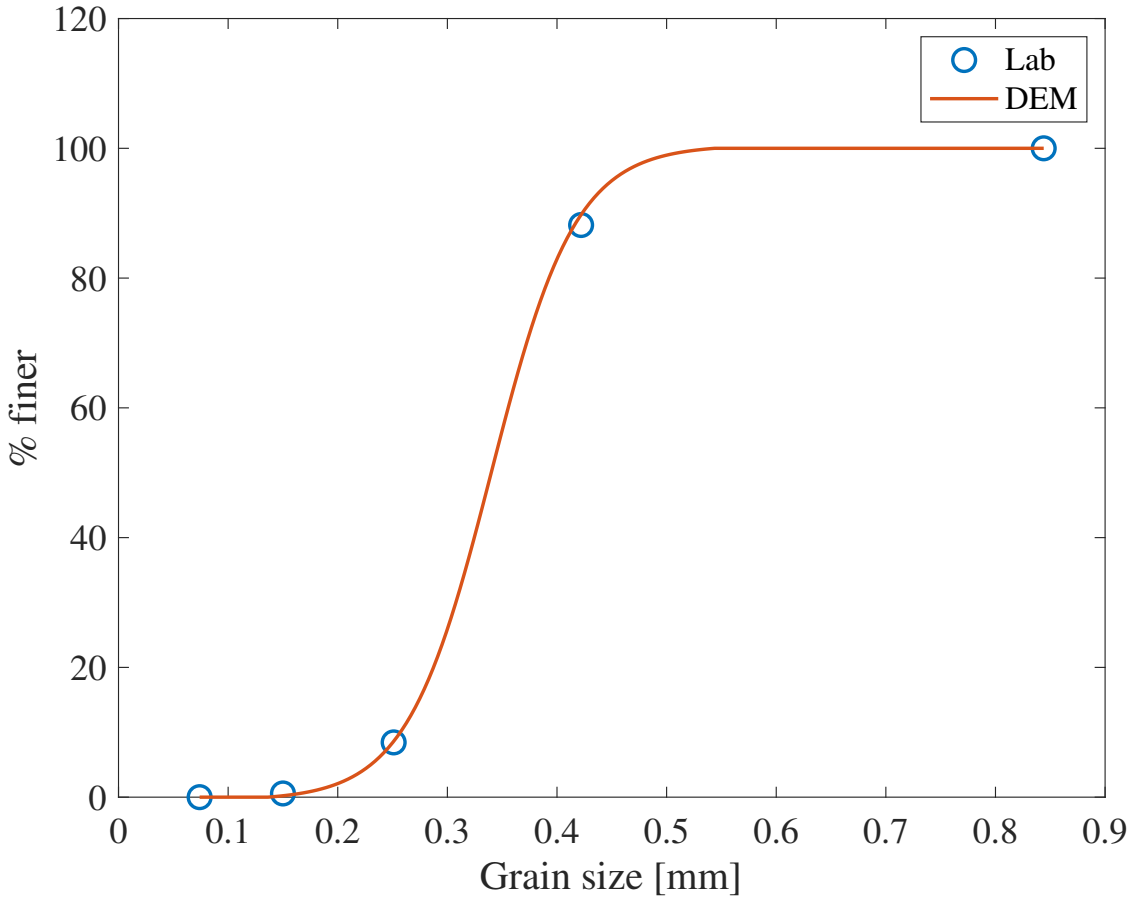


Figure 6.1: Particle size distribution (PSD).

value for a glass beads-water mixture reported by Yun and Evans (2010) and determined to be 0.85. The linear thermal expansion coefficient of the particles was set to be 5.13×10^{-6} K^{-1}. The thermal expansion of the fluid can be neglected under a drained condition.

The densities of glass beads and water (ρ_s and ρ_f) are 2590 kg/m^3 and 1000 kg/m^3 and the specific heats of glass beads and water (c_s and c_f) are 750 (J·kg)/K and 4200 (J·kg)/K. The density of the particles in the simulation was set to be 2590 kg/m^3 so that the mechanical behaviour of the particles is similar to the reality. The specific heat of the particles was modified to simulate a realistic transient heat transfer phenomenon by the following procedures. In order to obtain the same time scale as reality, the heat capacity of the system in the simulation has to be identical to that in reality. Thus, the specific heat of the particles in the DEM simulation (c_s^{DEM}) is related to the real material properties as:

$$\rho_s c_s^{DEM} V_s = \rho_s c_s V_s + \rho_f c_f V_f \tag{6.1}$$

$$c_s^{DEM} = c_s + \frac{\rho_f}{\rho_s} c_f e \tag{6.2}$$

In the transient heat transfer simulations using a thermal DEM, the void ratio range was between 0.55 and 0.65; however, this value includes the loosening existing near the walls, which can be neglected in a laboratory. Thus, a slightly dense value was employed for the calculation of c_s^{DEM}. $c_s^{DEM} = 1680$, which is corresponding to $e \approx 0.575$ in Eq. (6.2), was chosen.

6.2.2 Simulation procedure

The thermal DEM simulations had several steps: (1) Isotropic compression under periodic boundary conditions, (2) Isotropic compression under mixed boundary conditions, (3) Triaxial compression and unloading, (4) Transient heat transfer. A rectangular simulation domain was considered for thermal DEM simulations throughout the simulation.

Isotropic compression under periodic boundary conditions

In a transient heat transfer simulation, a pair of walls is considered to apply a constant temperature boundary condition; however, an isotropic compression under periodic boundary conditions is useful to ensure the homogeneity of the sample.

7503 non-overlapping spheres were generated under a rectangular box enclosed by periodic walls following the approach used in Section 5.3. The ratio of the domain lengths in three directions was 1:1:1.5, where a slightly longer sample length for the direction where a pair of walls was introduced in the later stage was considered to reduce boundary effects.

An isotropic stress was gradually increased ($0 \rightarrow 1 \rightarrow 2 \rightarrow 4 \rightarrow \ldots$ kPa) by moving the position of the periodic boundaries. Two target isotropic stresses, 100 kPa and 500 kPa, and two friction coefficient values, 0.01 and 0.32, were considered during this stage.

Isotropic compression under mixed boundary conditions

After completing the first step, the periodic boundary orthogonal to the z-direction was replaced by a pair of rigid walls, which did not touch any particle initially. Contacts between particles over the removed periodic boundary were lost; thus, the stress decreased to 0 kPa. To reduce the movement of the particles, a viscous damping of 0.10 was considered. After confirming the movement of the particles terminated, the pair of the walls was moved slowly until a vertical stress of 1 kPa was achieved while the viscous damping was removed. Following that, the stresses were isotropically and gradually increased by controlling the position of the pair of the walls and the periodic boundaries ($1 \rightarrow 2 \rightarrow 4 \rightarrow \ldots$ kPa) until the target isotropic stress was achieved. The same friction coefficient as used in the first step was adopted here.

Triaxial compression and unloading

The steps described above created nearly isotropic samples; however, in a laboratory experiment it is very difficult to create an isotropic sample. An air pluviation method has been often employed in laboratory experiments e.g. Ng, Wang and Zhou (2016), which results in an anisotropic sample that is stiffer in the vertical (axial) loading direction than in the horizontal loading direction. Similar to Section 4.3.1, the "pre-shearing" method by Wei and Wang (2017) was employed to increase the anisotropy of the DEM samples. The friction coefficient was set to be 0.325, which is considered to be the friction coefficient of the glass beads and triaxial compression was applied to the samples until a target axial strain was achieved. After that, triaxial extension was applied until the axial stress of the sample reached the initial axial stress. This procedure created a sample with an anisotropic fabric but under an isotropic stress state. The anisotropy of the sample was quantified by the anisotropy degree a introduced in Eq. (4.29). The properties of the samples and the simulation parameters set to obtain the samples are summarised in Table 6.2.

Transient heat transfer

The samples prepared by the procedure described above were subjected to cyclic variations in the temperature. The initial temperature of a sample was considered to be 293 K. To increase the temperature of the sample, a constant temperature boundary condition at $T = 353$ K was applied to the pair of the walls orthogonal to the z-direction, which results in a temperature rise of 60 K in the sample. A typical temperature distribution in a sample during a transient heat transfer simulation is shown in Fig. 6.2. After the minimum value of the temperatures of the particles reached 352.4 K, a *'heating'* step was considered to

Table 6.2: Samples and simulation parameters.

Case ID	Simulation parameters			Packing characteristics		
	σ_{iso}	μ_{fric}	$\varepsilon_{\text{a}}^{\text{pre}}$	e	$\overline{Z}$	a
ISO-100-L	100	0.32	0%	0.642	3.688	0.001
ISO-100-D	100	0.01	0%	0.551	5.165	0.016
ANI3%-100-L	100	0.32	3%	0.642	3.574	0.132
ANI3%-500-L	500	0.32	3%	0.645	3.748	0.118
ANI3%-100-D	100	0.01	3%	0.566	3.615	0.170
ANI13%-100-L	100	0.32	13%	0.636	3.615	0.166
ANI1%-100-D	100	0.01	1%	0.556	3.762	0.143

be completed. A *'cooling'* step followed, where the temperature of the walls were set to be 293 K until the maximum particle temperature reached 293.6 K. These *heating* and *cooling* steps were repeated to apply cyclic temperature variations to the sample.

The sample had a length of approximately 7.5 mm and a *'heating'* or *'cooling'* cycle took 2 minutes in the real time scale. However, in a DEM simulation, a critical time increment is much smaller than the time required to reach a steady-state. According to the empirical method for calculating a critical time increment proposed by Otsubo, O'Sullivan and Shire (2017), a critical time increment for a sample with $\sigma_{\text{iso}} = 100$ kPa is approximately 8×10^{-8} second. Consequently, 1.5 billion timesteps were required for each half cycle. The simulations were computationally expensive, and a half cycle took around 7 days with 48 cores.

6.3 Sample homogeneity

In this study, rigid wall boundaries were applied in the axial direction. In such a case, a displacement and a heat flux is introduced to a sample from both of the rigid walls and extra care is needed to ensure that the response of the sample is representative. To examine sample homogeneity, the e, a, and the contact density (N_{c}/V) values of six slices from each sample were compared before and after thermal cycles following Huang et al. (2014b).

The results of sample slice analyses for ISO-100-L are shown in Fig. 6.3. Fig. 6.3(a) shows the e value of each slice before thermal cycles. Relatively high e value was observed near the rigid wall boundary; however, the other four slices have e values between 0.623 and 0.642, which indicate that the inner part of the sample was homogeneous. The two slices adjacent to the upper or bottom boundary will be denoted as 'outer slices' and the other four slices will be denoted as 'inner slices' hereinafter. After 8 thermal cycles (Fig. 6.3(b)), the change in the e value was very small and the homogeneity in the e of

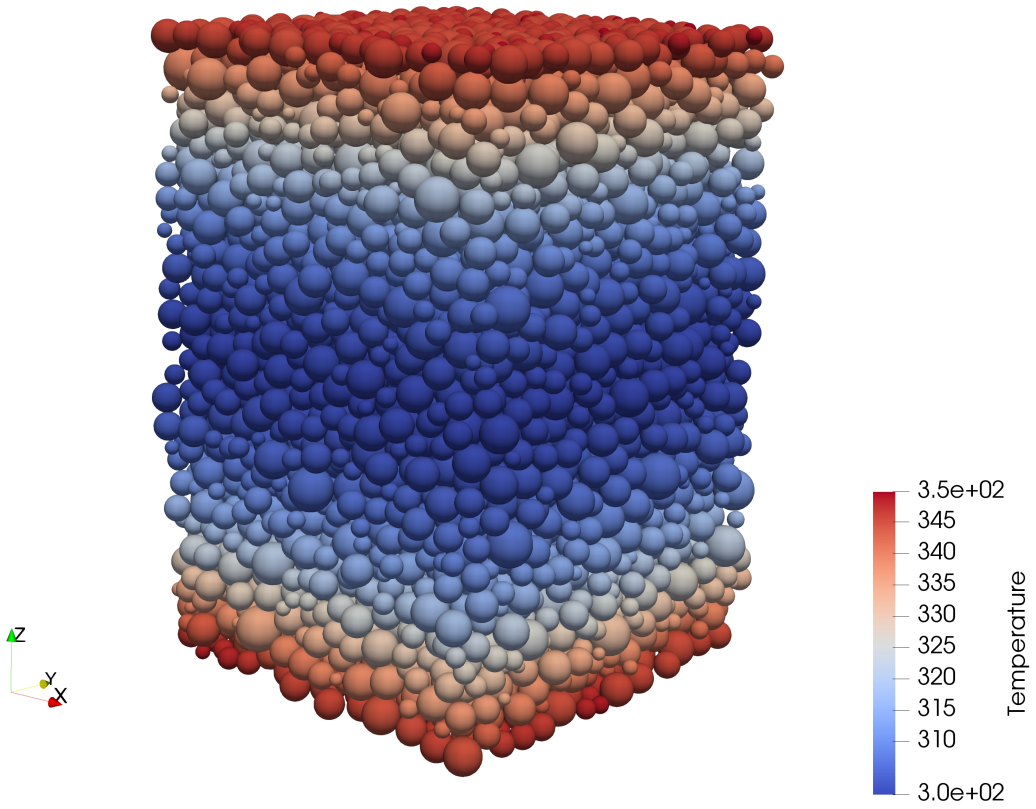


Figure 6.2: Temperature distribution in a sample during a transient heat transfer simulation.

the inner slices was maintained. Fig. 6.3(c) shows the a value of the six slices from the sample before thermal cycles. A slightly high a value was observed near a rigid wall boundary presumably because a contact between a wall and a particle was included for the calculation of the a. For the inner slices, the a was $< \pm 0.10$, which indicates the inner part of the sample is fairly isotropic. After eight thermal cycles (Fig. 6.3(d)), the a value of the inner part of the sample remains isotropic ($< \pm 0.10$). Fig. 6.3(e) and (f) show the distribution of the number of contacts in the slice divided by the slice volume, which can be related to the values of $\overline{Z}$, before and after thermal cycles. It can be seen that the N_{c}/V of the inner slices of the sample was homogeneous (between 73.306 and 76.403 according to Fig. 6.3(e)), and all decreased after eight thermal cycles (Fig. 6.3(f)).

A similar analysis was conducted for ISO-100-D as shown in Fig. 6.4. For slice e values, the e values of all the inner slices were slightly increased by 0.001 after 8 thermal cycles comparing Fig. 6.4(a) and (b). The a values of the inner slices were uniformly isotropic and N_{c}/V before and after thermal cycles (Fig. 6.4(c) and (d)). An interesting observation was made for the N_{c}/V values of the slices of the sample in Fig. 6.4(e) and (f), where the N_{c}/V value of each slice dropped significantly. The changes in N_{c}/V values of the inner slices were -16.7, -19.3, -18.6, and -18.1, with this decrease taking place homogeneously.

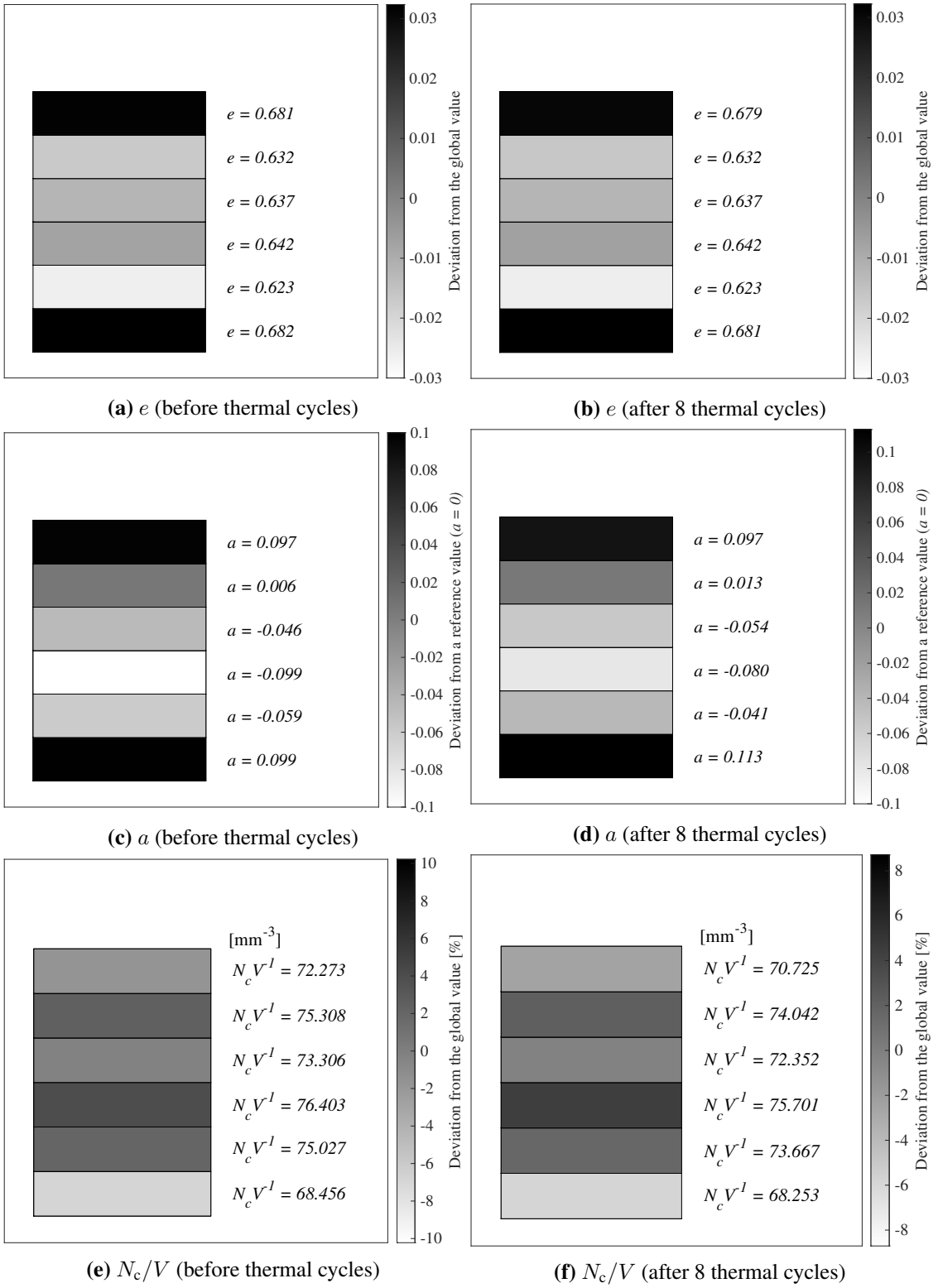
The sample slice analysis for two anisotropic samples, namely ANI3%-100-L and ANI3%-100-D, are shown in Fig. 6.5 and Fig. 6.6. In both cases, the e values of all the inner slices decreased by between 0.001 and 0.002, indicating that the contractive response of the inner slices was homogeneous (Fig. 6.5(a) and (b) and Fig. 6.6(a) and (b)). A decrease in the a values of the inner slices took place after eight thermal cycles for both of ANI3%-100-L (Fig. 6.5(c) and (d)) and ANI3%-100-D (Fig. 6.6(c) and (d)). For both cases, changes in the N_{c}/V values of the inner slices after eight thermal cycles were small compared to ones observed in ISO-100-D (Fig. 6.4(e) and (f)) and were $< \pm 2.2$. These results support that the sample preparation and heat transfer simulation procedures were rigorously conducted so that the overall response of the sample was representative.

6.4 Evolution of mechanical strain

6.4.1 Concept of mechanical strain

To quantify a contraction or dilation of a soil sample, a volumetric strain is conventionally used. The volumetric strain of a sample can be calculated by:

$$\varepsilon_{\mathrm{vol}} = \varepsilon_{11} + \varepsilon_{22} + \varepsilon_{33} \tag{6.3}$$



(a) e (before thermal cycles)

(b) e (after 8 thermal cycles)

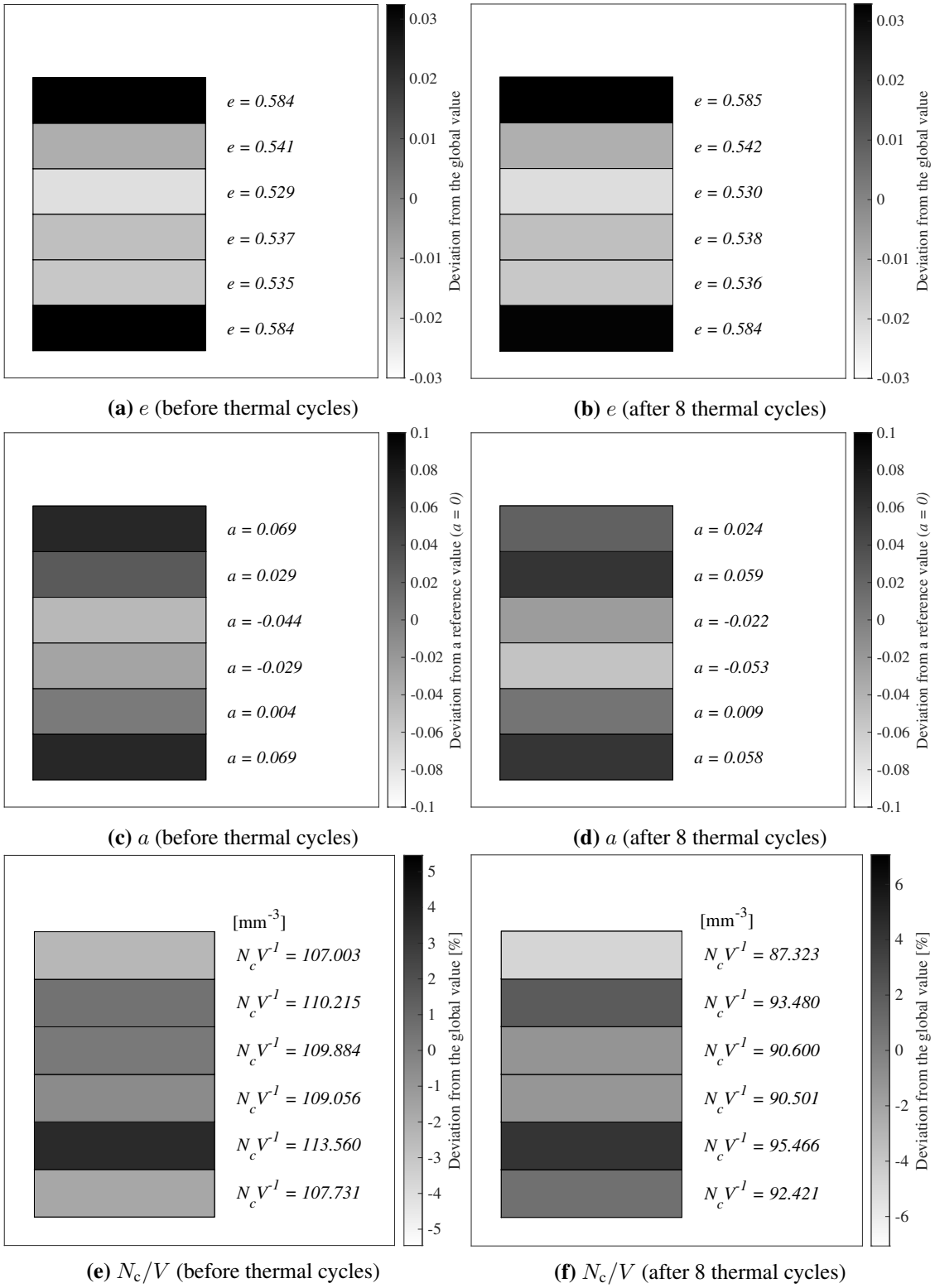
(c) a (before thermal cycles)

(d) a (after 8 thermal cycles)

(e) N_c/V (before thermal cycles)

(f) N_c/V (after 8 thermal cycles)

Figure 6.3: Sample homogeneity analysis of ISO-100-L.



(a) e (before thermal cycles)

(b) e (after 8 thermal cycles)

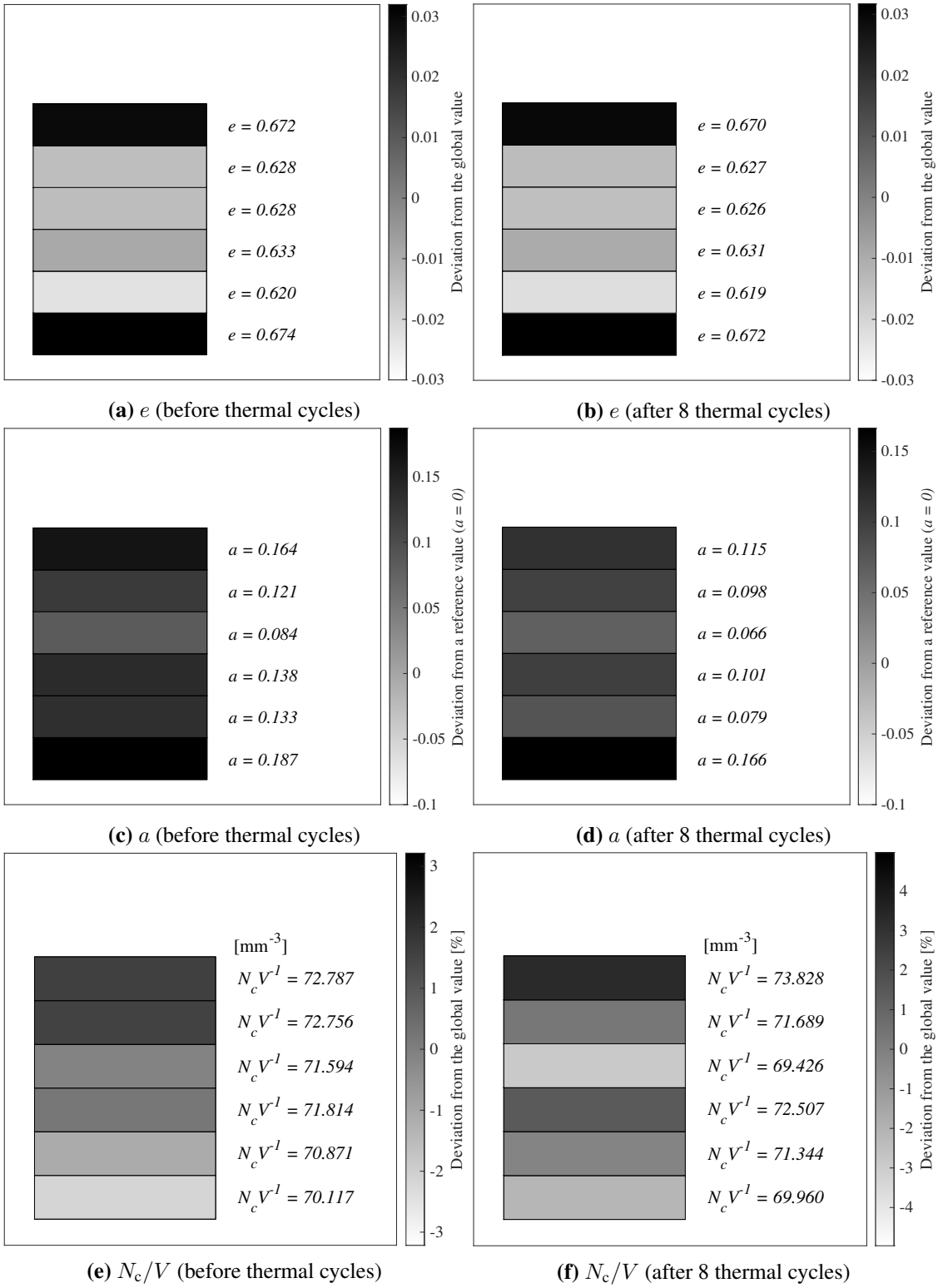
(c) a (before thermal cycles)

(d) a (after 8 thermal cycles)

(e) N_c/V (before thermal cycles)

(f) N_c/V (after 8 thermal cycles)

Figure 6.4: Sample homogeneity analysis of ISO-100-D.



(a) e (before thermal cycles)

(b) e (after 8 thermal cycles)

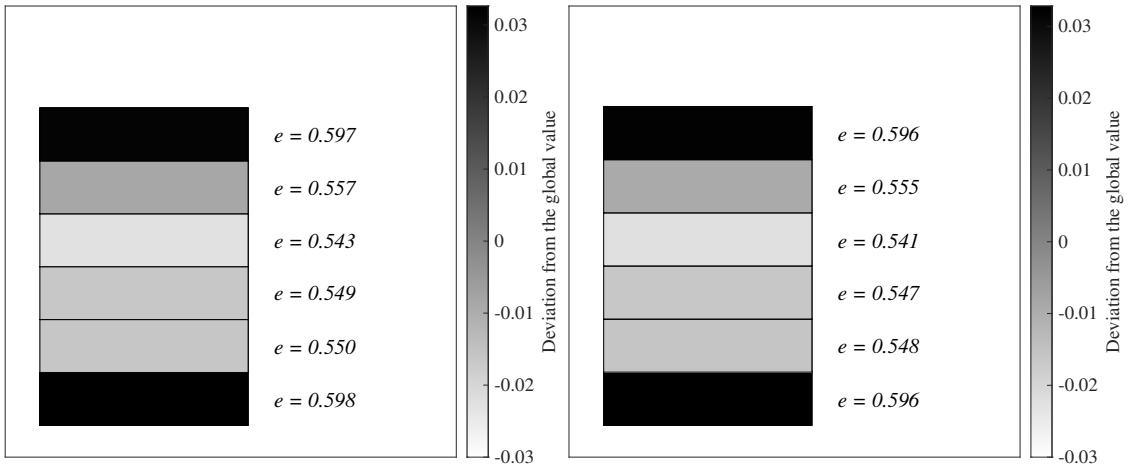
(c) a (before thermal cycles)

(d) a (after 8 thermal cycles)

(e) N_c/V (before thermal cycles)

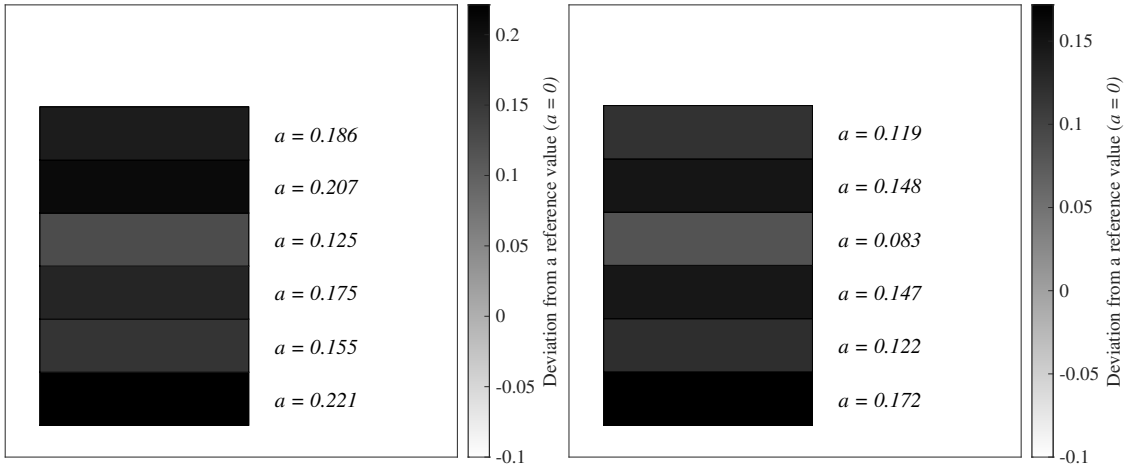
(f) N_c/V (after 8 thermal cycles)

Figure 6.5: Sample homogeneity analysis of ANI3%-100-L.



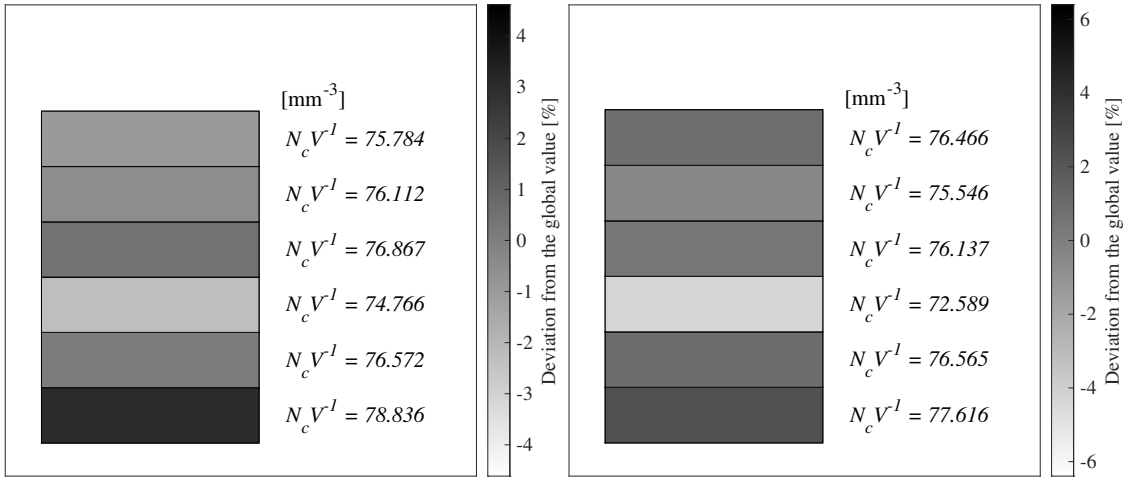
(a) e (before thermal cycles)

(b) e (after 8 thermal cycles)



(c) a (before thermal cycles)

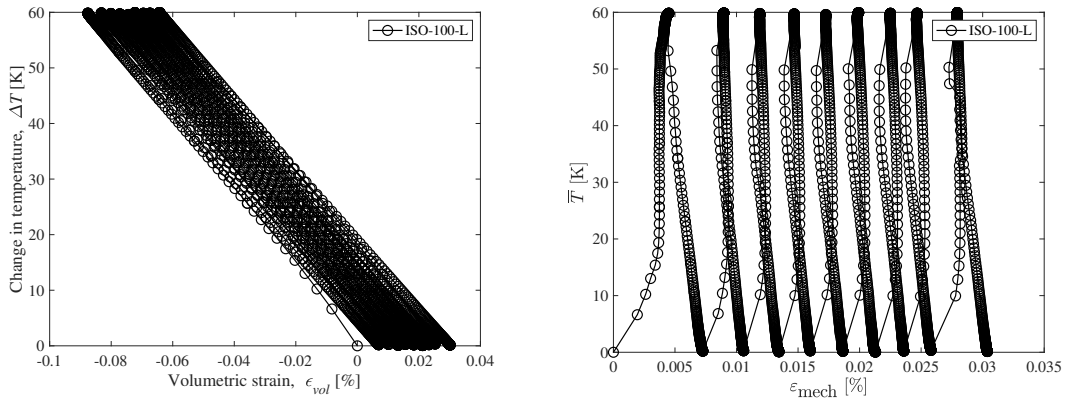
(d) a (after 8 thermal cycles)



(e) N_c/V (before thermal cycles)

(f) N_c/V (after 8 thermal cycles)

Figure 6.6: Sample homogeneity analysis of ANI3%-100-D.



(a) ΔT-ε_{vol} plot **(b)** ΔT-$\varepsilon_{\text{mech}}$ plot

Figure 6.7: Volume change behaviour of ISO-100-L due to thermal cycles.

where a positive ε_{vol} indicates a contraction of the sample and a negative ε_{vol} indicates a dilation of the sample following the sign convention used in soil mechanics. However, such a volumetric strain includes not only the rearrangement of the particles but also the thermal expansion of the particles. Bortolotto, Taborda and O'Sullivan (2021) has proposed the concept of the mechanical strain, which reflects only the rearrangement of the particles. Following Bortolotto, Taborda and O'Sullivan (2021), the mechanical strain of the sample can be calculated using the volumetric strain, the temperature change, and the linear thermal expansion coefficient of the particles as:

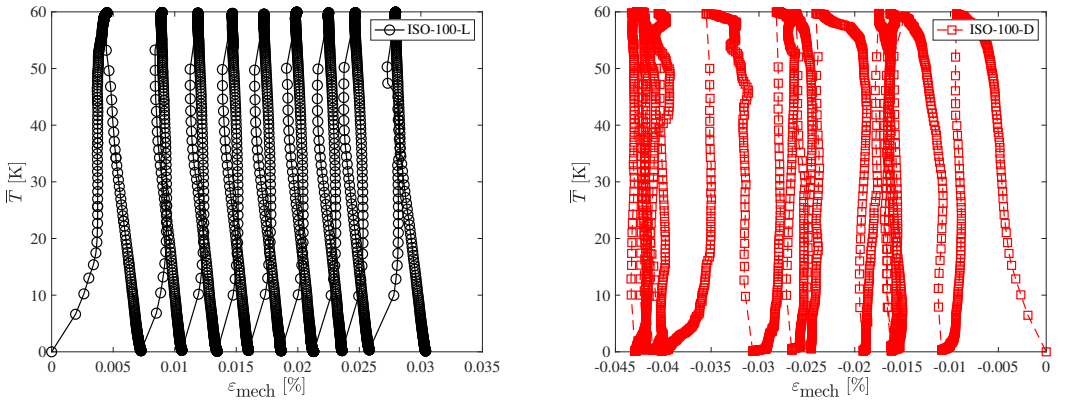
$$\varepsilon_{\text{mech}} = \varepsilon_{\text{vol}} + 3\alpha_{\text{L}}\Delta T \tag{6.4}$$

where a positive $\varepsilon_{\text{mech}}$ indicates a contraction of the sample. If there is no rearrangement of the particles ($\varepsilon_{\text{mech}} = 0$), the ε_{vol} is equivalent to the volume strain of the particles i.e. $\varepsilon_{\text{vol}} = -3\alpha_{\text{L}}\Delta T$.

A comparison between T-ε_{vol} plot and T-$\varepsilon_{\text{mech}}$ plot are shown for case ISO-100-L in Fig. 6.7. Fig. 6.7(a) shows that the sample repeats dilation-contraction cycles; however, Fig. 6.7(b) shows that particle rearrangement and mechanical strain takes place after both heating and cooling.

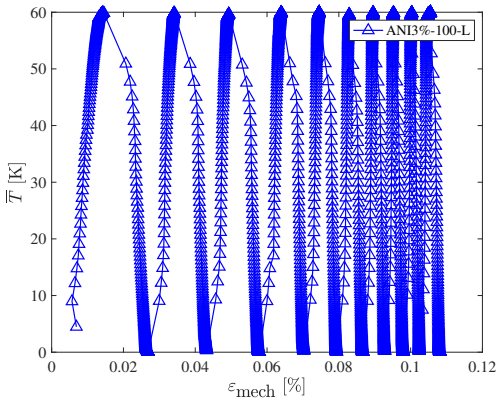
6.4.2 Effect of initial void ratio and anisotropic degree on mechanical strain evolution

It is important to compare numerical study results with experimental study results. Ng, Wang and Zhou (2016) conducted experiments on the behaviour of Toyoura sand subjected to cyclic temperature variations under an isotropic stress condition using a thermal triaxial apparatus. One of observations made by Ng, Wang and Zhou (2016) is that a loose sample

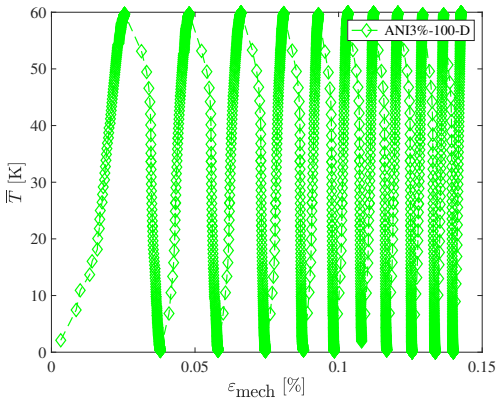


(a) ISO-100-L

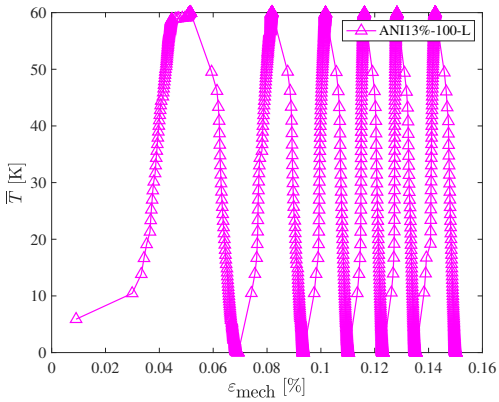
(b) ISO-100-D



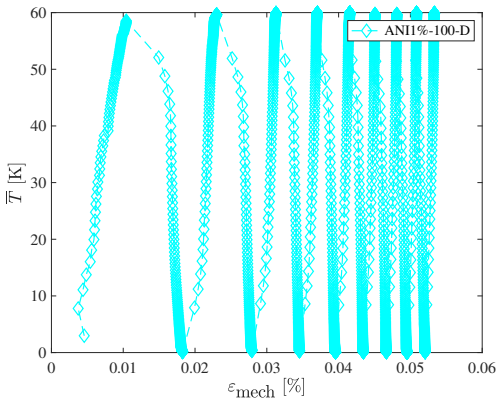
(c) ANI3%-100-L



(d) ANI3%-100-D



(e) ANI13%-100-L



(f) ANI1%-100-D

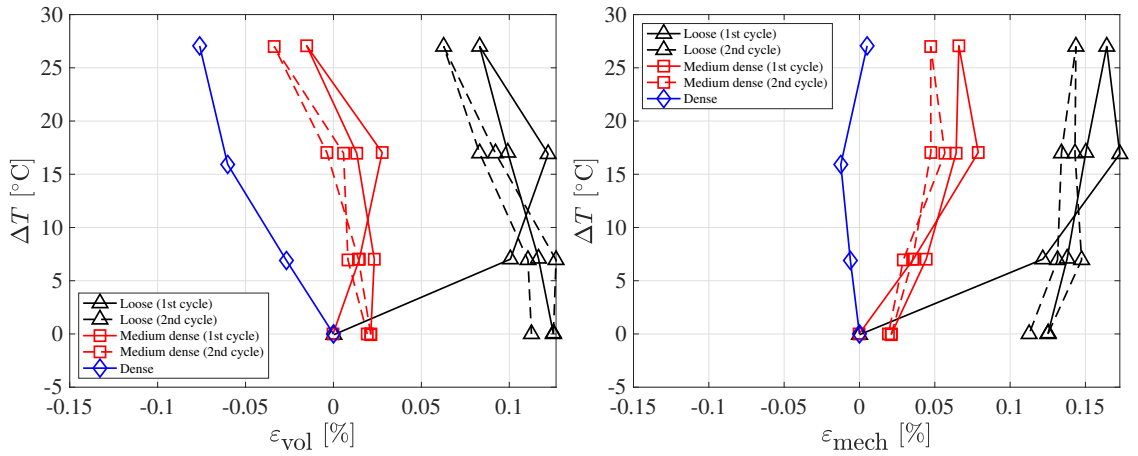
Figure 6.8: Evolution of $\varepsilon_{\text{mech}}$ of a sample with $\sigma_{\text{iso}} = 100$ kPa during temperature cycles.

showed contractive behaviour, a medium dense sample exhibited smaller contraction and a dense sample showed a volume expansion. Fig. 6.9(a) shows a ΔT-ε_{vol} plot of experiment results by Ng, Wang and Zhou (2016). Additionally, the mechanical strain values of Fig. 6.9(b) were calculated based on Eq. (6.4) using $\alpha_{\text{L}} = 1 \times 10^{-5}$ K^{-1}, which is the α_{L} value of sand particles reported by Agar (1984) and taking the volumetric strain measured by Ng, Wang and Zhou (2016). This reanalysis of these data shows that in fact the loose and medium dense samples had a decrease in $\varepsilon_{\text{mech}}$ (dilation) during the cooling steps. For the dense sample, there was almost zero $\varepsilon_{\text{mech}}$ during the heating steps.

$\varepsilon_{\text{mech}}$-$\Delta\overline{T}$ plots of all the DEM samples with $\sigma_{\text{iso}} = 100$ kPa are shown in Fig. 6.8. The evolution of $\varepsilon_{\text{mech}}$ per cycle is plotted in Fig. 6.10. A comparison between Fig. 6.8(a) and (b) indicates that for the isotropic samples, a loose sample (ISO-100-L) shows a more contractive behaviour than a dense sample (ISO-100-D) in the presented DEM analysis, which is in line with the observation made by Ng, Wang and Zhou (2016). However, ISO-100-D repeatedly showed a dilative behaviour for each cycle (Fig. 6.10), which was not observed by Ng, Wang and Zhou (2016). The increase in the $\varepsilon_{\text{mech}}$ value of ISO-100-L was much smaller (0.007% at the first cycle) than that of the loose sample reported in Ng, Wang and Zhou (2016) ($> 0.1\%$ at the first cycle).

One of reasons why a change in the $\varepsilon_{\text{mech}}$ value of ISO-100-L and ISO-100-D would be the lack of anisotropy, which usually exists in soil samples created by air pluviation. The $\varepsilon_{\text{mech}}$ value of two samples with the same pre-shearing strain of 3% but different initial void ratios are plotted against $\Delta\overline{T}$ in Fig. 6.8(c) and (d). ANI3%-100-D showed a contractive behaviour unlike ISO-100-D even though the two samples have a similar initial void ratio (Table 6.2). The difference between the volume change behaviours of ANI3%-100-D and ISO-100-D can be attributed to the difference in the degrees of anisotropy in the two samples. According to Fig. 6.10, the anisotropic sample showed a much more contractive behaviour than the isotropic sample with a similar void ratio; however, an increase in the $\varepsilon_{\text{mech}}$ value of these samples is still smaller than that of the loose sample reported by Ng, Wang and Zhou (2016). One of interesting observation is that ANI3%-100-D was slightly more contractive than ANI3%-100-L even though ANI3%-100-D is denser than ANI3%-100-L, which would be attributed to different a values.

To clarify the effect of the initial a value, a similar analysis was conducted for ANI13%-100-L (Fig. 6.8(e)), which had a similar initial a value to that of ANI3%-100-D, and ANI1%-100-D (Fig. 6.8(f)), which had a similar initial a value to that of ANI3%-100-L. ANI13%-100-L showed the most contractive behaviour among the samples considered in this study; however, the $\varepsilon_{\text{mech}}$ value after the first thermal cycle was still smaller than the experimental data. In the end, it may be attributed to particle shapes, particle breakage, and surface roughness, which were not considered in the present DEM study. The evolution in



(a) ΔT-ε_{vol} plot **(b)** ΔT-ε_{mech} plot

Figure 6.9: Volume change behaviour of Toyoura sand with a variety of void ratios due to thermal cycles after Ng, Wang and Zhou (2016).

the ε_{mech} value of ANI3%-100-L was faster than that of ANI1%-100-D; in addition, that of ANI13%-100-L was faster than ANI3%-100-D (Fig. 6.10). It can be concluded that a looser sample is more contractive than a denser one if the a values of the two samples are similar.

For each case except for ISO-100-D, an increase in the ε_{mech} value with increasing numbers of thermal cycles was not observed in the experimental results by Ng, Wang and Zhou (2016). Additional experimental and DEM studies would be necessary to clarify this point in future.

6.4.3 Effect of magnitude of isotropic stress

Another interesting observation made by Ng, Wang and Zhou (2016) is the effect of the magnitude of the isotropic stress. The thermal behaviour of loose Toyoura sand specimens subject to a different magnitude of isotropic stress obtained by Ng, Wang and Zhou (2016) was extracted and plotted in Fig. 6.11. Fig. 6.11 shows that a higher isotropic stress results in a higher volumetric strain (more contractive behaviour).

To establish if the thermal DEM can reproduce the experimeental observations, ANI3%-500-L, which has a similar e and a but a different magnitude of σ_{iso} from that of ANI3%-100-L was prepared. Fig. 6.12 compares the thermal behaviour of ANI3%-100-L and ANI3%-500-L. In contrast to the observation made by Ng, Wang and Zhou (2016), Fig. 6.12(a) and (b) show that a higher isotropic stress results in a less thermal strain. From the particle-scale perspective, this result can be explained by a higher mean coordination number of a sample with a higher isotropic stress. The different observation between the DEM and experimental results may be attributed to the neglect of particle crushing and surface roughness and the ideal particle shape used in the DEM simulations.

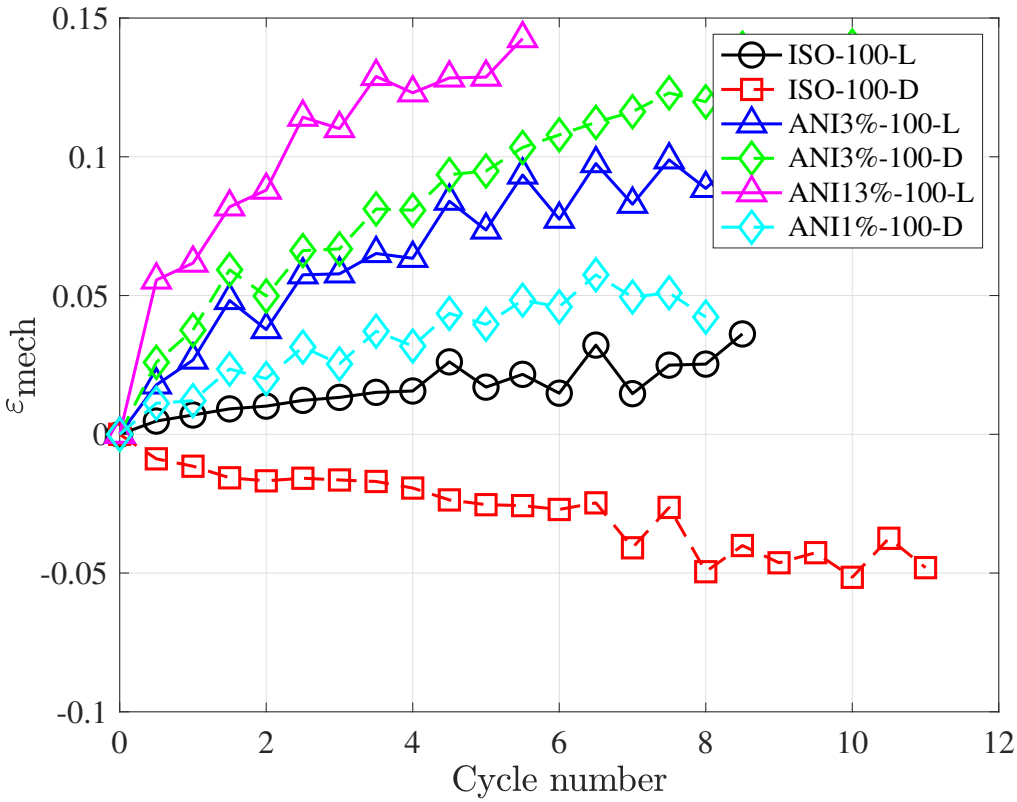
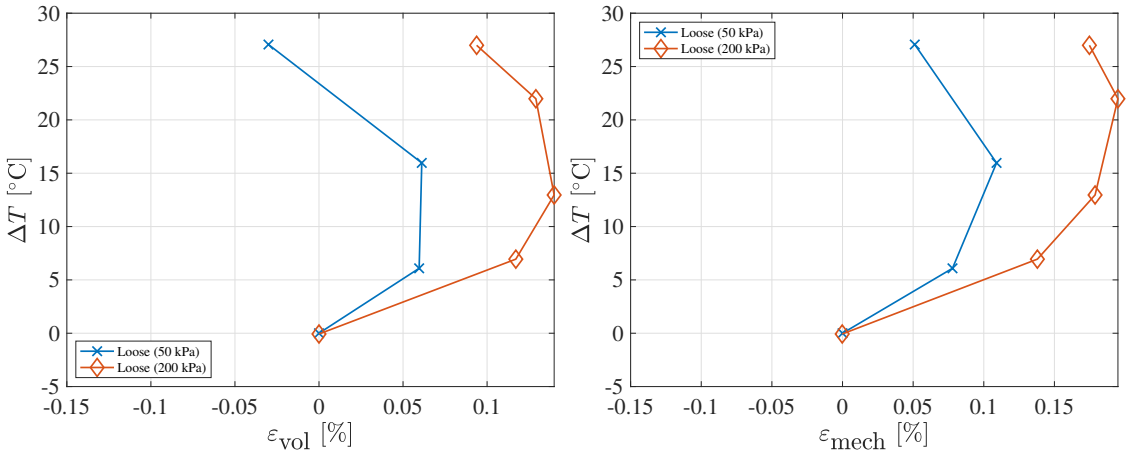
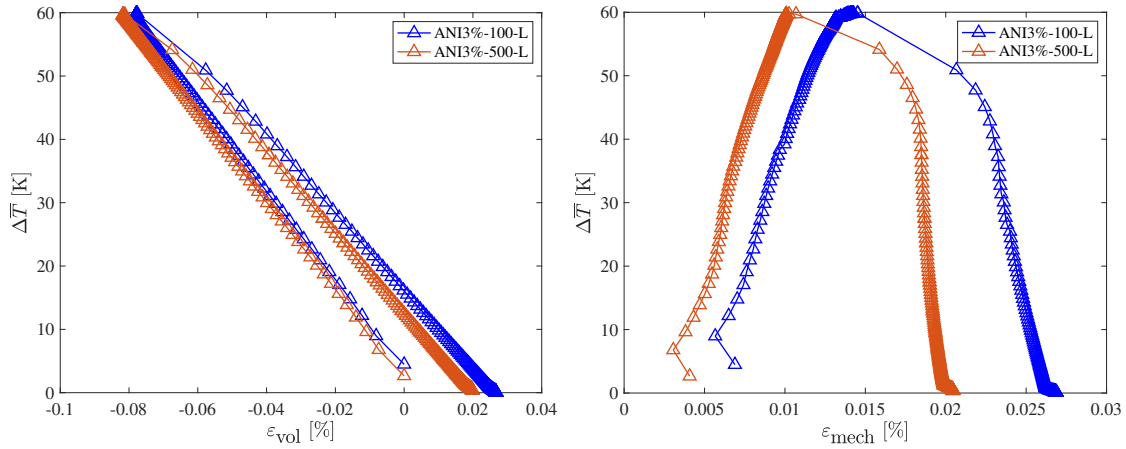


Figure 6.10: Evolution of the ε_{mech} values in samples with numbeer of temperature cycles.



(a) ΔT-ε_{vol} plot **(b)** ΔT-ε_{mech} plot

Figure 6.11: Volume change behaviour of loose Toyoura sand specimens with different σ_{iso} values due to thermal cycles after Ng, Wang and Zhou (2016).



(a) ΔT-$\varepsilon_{\mathrm{vol}}$ plot **(b)** ΔT-$\varepsilon_{\mathrm{mech}}$ plot

Figure 6.12: Volume change behaviour of loose DEM samples with different σ_{iso} values due to thermal cycles.

6.5 Evolution of packing characteristics due to thermal cycles

In this chapter, a change in several packing properties induced by thermal cycles is reported. Mean coordination number, $\overline{Z}$, is useful to evaluate the stability of a packing and is not always related to its e value as previously shown in Fig. 4.2. Fig. 6.13 shows the evolution of the $\overline{Z}$ value of each sample during thermal cycles. A sharp drop in the $\overline{Z}$ value of ISO-100-D was observed during the first heating cycle, and a gradual decrease in the $\overline{Z}$ value followed. $\overline{Z}$ can be related to the modulus of the sample as previously shown in Eq. (4.8); thus, the shear behaviour of a sample experienced thermal cycles could be an interesting future research topic. The other samples, however, showed no noticeable change in their $\overline{Z}$ value as shown in Fig. 6.13.

The evolution of the a values of the samples after each cycle is shown in Fig. 6.14. Isotropic samples (ISO-100-L and ISO-100-D) remained to be isotropic after > 8 thermal cycles; on the other hand, the a value of anisotropic samples constantly decreased. The accumulation of the $\varepsilon_{\mathrm{mech}}$ may be associated with such a decrease in the a value; however, microscopical investigation of the samples remains to be a future study to prove the hypothesis.

6.6 Summary

This chapter has presented DEM simulation results modelling granular materials subjected to cyclic temperature variations at a constant isotropic stress condition. The simulation results were compared with a previous laboratory study result by Ng, Wang and Zhou (2016) which applied cyclic temperature variations to Toyoura sand using triaxial apparatus.

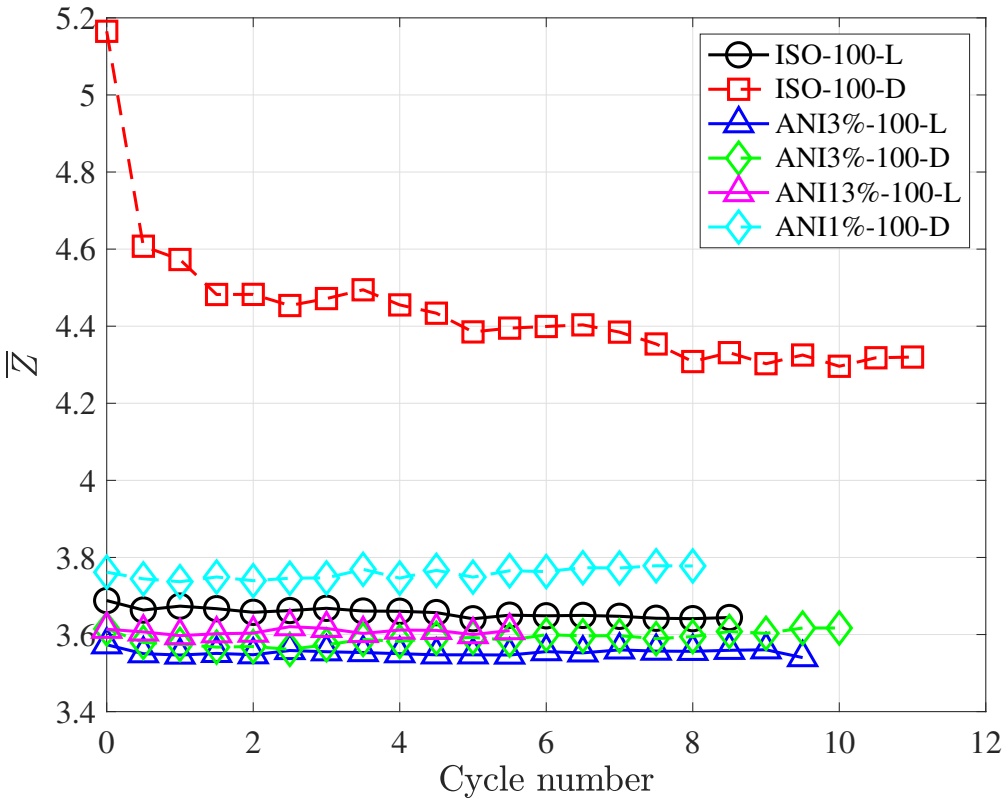


Figure 6.13: Evolution of the $\overline{Z}$ values in sampleswith number of temperature cycles.

Detailed analysis on the slices of the samples showed that the thermo-mechanical response of the samples was homogeneous. The volume strain of the samples was corrected using the thermal expansion coefficient of the particles and the temperature increment, with which the sample volume change associated with particle rearrangement was clearly isolated from the sample volume change associated with particle expansion. A looser sample shows a more contractive behaviour as reported by Ng, Wang and Zhou (2016); however, the sample anisotropy had a measurable impact on the thermal contraction of the sample. In each case, the mechanical strain continuously developed.

Some basic particle-scale analyses were carried out. The change in the mean coordination number ($\overline{Z}$) was not significant except for the dense and isotropic packing, which exhibited thermal dilation. For the anisotropic samples, the degree of anisotropy (a) decreased after each cycle. A more detailed analysis would be needed to explore the fundamental behaviour underlying the volume change of the granular materials in future: for example, a particle-scale strain analysis using 'local' strain proposed by Bagi (1996) and Bagi (2006).

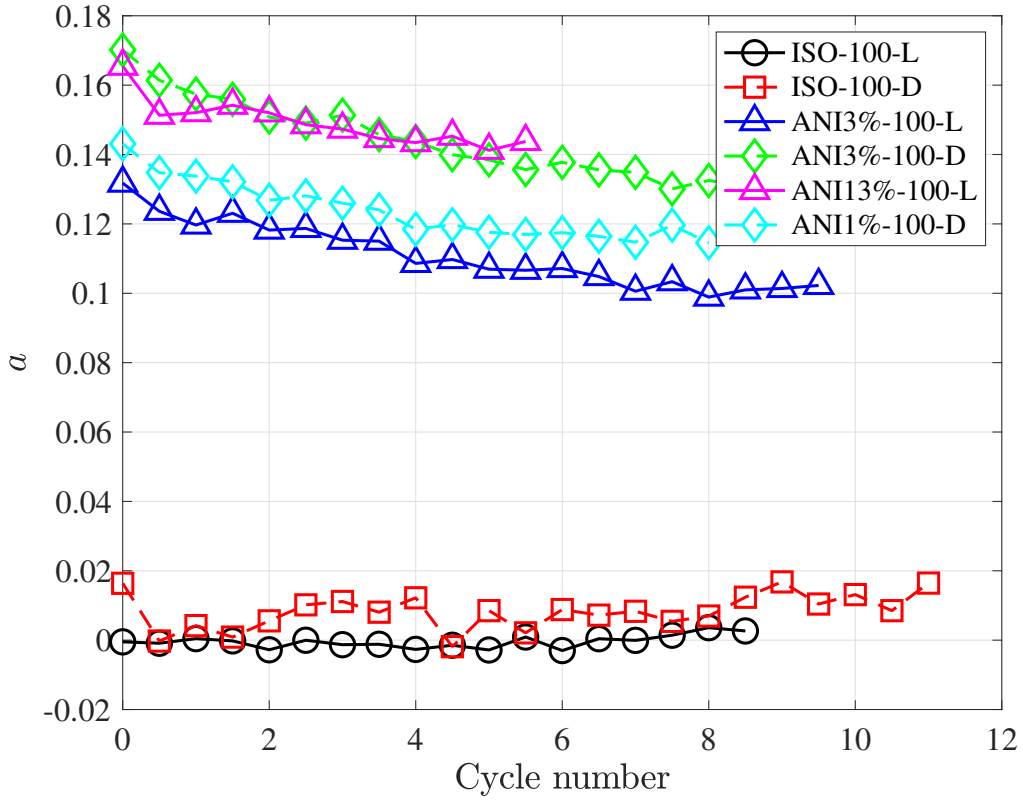


Figure 6.14: Evolution of the a values in samples with number of temperature cycles.

– PART II –

ANALYSES OF SYSTEM RESPONSES WITH PORE FLUIDS FLOWING

CHAPTER 7

LITERATURE REVIEW

7.1 Introduction

This section summarises how the behaviour of fluid can be mathematically formulated and how the interaction between solid particles and fluid can be modelled. In this thesis, only incompressible laminar flow of a Newtonian fluid is considered with a view towards geotechnical engineering. Also the velocity of particles is assumed to be negligibly small compared to the velocity of fluid i.e. no movement of particle is considered. The viscous dissipation and the effect of the gravity are also neglected in this thesis.

Section 7.2 reviews the continuity, momentum, and energy transport equations for an incompressible Newtonian fluid. Section 7.2 shows some key dimensionless (non-dimensional) numbers, which can be derived from the equations reviewed in Section 7.2 and useful to analyse the fluid flow behaviour. Section 7.4 discusses a variety of computational fluid dynamics methods to solve or model the fluid flow.

7.2 Governing equations of incompressible viscous fluid flow

The flow of an incompressible viscous fluid is governed by well-established continuity, momentum, and energy transport equations (Batchelor, 1967; White, 2009).

$$\text{Continuity} : \nabla \cdot \mathbf{u} = 0 \tag{7.1}$$

$$\text{Momentum} : \rho \frac{\mathrm{D}\mathbf{u}}{\mathrm{D}t} \equiv \rho \left(\frac{\partial \mathbf{u}}{\partial t} + \mathbf{u} \cdot \nabla \mathbf{u} \right) = -\nabla p + \mu \nabla^2 \mathbf{u} \tag{7.2}$$

$$\text{Energy transport} : \frac{\mathrm{D}T}{\mathrm{D}t} \equiv \frac{\partial T}{\partial t} + \mathbf{u} \cdot \nabla T = \alpha_{\text{dif}} \nabla^2 T \tag{7.3}$$

where $\mathbf{u}$ is the velocity, ρ is the density, p is the pressure, μ is the dynamic viscosity, T is the temperature, α_{dif} is the thermal diffusivity, and $\frac{\mathrm{D}}{\mathrm{D}t}$ is the material derivative. Eq. (7.3) is also called as "advection-diffusion equation" because it considers two mechanisms of heat transfer; advection and diffusion, namely.

$$\frac{\partial T}{\partial t} = \underbrace{-\mathbf{u} \cdot \nabla T}_{\text{Advection}} + \underbrace{\alpha_{\text{dif}} \nabla^2 T}_{\text{Diffusion}} \tag{7.4}$$

In this thesis, advection refers to the heat transfer phenomena where there is a simultaneous transfer of heat and movement of material. This thesis does not use the term "convection" to avoid confusion.

7.3 Analysis of fluid flow behaviour using dimensionless numbers

7.3.1 Reynolds number

The momentum equation (Eq. (7.2)) can be non-dimensionalised using

$$\mathbf{u} = u_0 \hat{\mathbf{u}} \tag{7.5}$$

$$t = t_0 \hat{t} \tag{7.6}$$

$$t_0 = \mathcal{L}/u_0 \tag{7.7}$$

$$\nabla = \mathcal{L}^{-1} \hat{\nabla} \tag{7.8}$$

$$p = \rho u_0^2 \hat{p} \tag{7.9}$$

Substituting Eqs. (7.5) to (7.9) to Eq. (7.2),

$$\rho \frac{u_0}{\mathcal{L}/u_0} \frac{\mathrm{D}\hat{\mathbf{u}}}{\mathrm{D}\hat{t}} = -\frac{\rho u_0^2}{\mathcal{L}} \hat{\nabla} \hat{p} + \frac{\mu u_0}{\mathcal{L}^2} \hat{\nabla}^2 \hat{\mathbf{u}} \tag{7.10}$$

Multiplying Eq. (7.10) by $\mathcal{L}/\rho u_0^2$,

$$\frac{\mathrm{D}\hat{\mathbf{u}}}{\mathrm{D}\hat{t}} = -\hat{\nabla} \hat{p} + \frac{\mu}{\rho u_0 \mathcal{L}} \hat{\nabla}^2 \hat{\mathbf{u}} \tag{7.11}$$

Now the Reynolds number, Re, is defined as

$$Re = \frac{\rho u_0 \mathcal{L}}{\mu} \tag{7.12}$$

Combining Eqs. (7.11) and (7.12),

$$\frac{\mathrm{D}\hat{\mathbf{u}}}{\mathrm{D}\hat{t}} = -\hat{\nabla} \hat{p} + \frac{1}{Re} \hat{\nabla}^2 \hat{\mathbf{u}} \tag{7.13}$$

For $Re \to \infty$, the viscous term becomes negligible.

7.3.2 Peclet number

The advection diffusion equation can be non-dimensionalied using Eqs. (7.5) to (7.8) and

$$T = T_0 \hat{T} \tag{7.14}$$

Substituting Eqs. (7.5) to (7.8) and (7.14) to Eq. (7.3),

$$\frac{T_0}{\mathcal{L}/u_0} \frac{\mathrm{D}\hat{T}}{\mathrm{D}\hat{t}} = \frac{\alpha_{\text{dif}} T_0}{\mathcal{L}^2} \hat{\nabla}^2 \hat{T} \tag{7.15}$$

Multiplying Eq. (7.15) by $T_0 u_0/\mathcal{L}$,

$$\frac{\mathrm{D}\hat{T}}{\mathrm{D}\hat{t}} = \frac{\alpha_{\text{dif}}}{u_0 \mathcal{L}} \hat{\nabla}^2 \hat{T} \tag{7.16}$$

Now defining the Peclet number (Pc) as

$$Pc = \frac{u_0 \mathcal{L}}{\alpha_{\text{dif}}} \tag{7.17}$$

Combining Eqs. (7.16) and (7.17),

Table 7.1: Typical values for Prandtl numbers (Coulson et al., 1999)

Material	Pr
Mercury	0.02
Oxygen	0.63
Air	0.71
Ammonia (gas)	1.38
Water	5 - 10
n-Butanol	50
Light oil	600
Glycerol	1000
Polymer melts	10000

$$\frac{\mathrm{D}\hat{T}}{\mathrm{D}\hat{t}} = \frac{1}{Pc}\hat{\nabla}^2\hat{T} \tag{7.18}$$

For $Pc \to \infty$, the conductive (diffusive) heat transfer becomes negligible.

7.3.3 Prandtl number

Prandtl number, Pr, is a dimensionless number representing the ratio of the momentum diffusivity to the thermal diffusivity of the fluid.

$$Pr = \frac{\text{Momentum diffusivity}}{\text{Thermal diffusivity}} = \frac{\nu_{\text{vis}}}{\alpha_{\text{dif}}} = \frac{\mu/\rho}{k/\rho c} = \frac{c\mu}{k} \tag{7.19}$$

The product of the Reynolds number and Prandtl number is equal to Peclet number as

$$RePr = \frac{\rho u \mathcal{L}}{\mu} \cdot \frac{\mu/\rho}{\alpha_{\text{dif}}} = \frac{u\mathcal{L}}{\alpha_{\text{dif}}} = Pc \tag{7.20}$$

Typical values for Prandtl numbers are summarised in Table 7.1.

7.3.4 Characteristic length

The Reynolds and Peclet numbers have a term $\mathcal{L}$, which is chosen according to the system of interest. For a system where a single sphere is immersed in fluid flow, the diameter of the sphere has been used as the characteristic length (Ranz & Marshall, 1952; Whitaker, 1972). For monodisperse packed granular media, Ergun (1952) used the diameter of particles; however, if there is polydispersity in granular media, it is not straightforward to define the characteristic length. van der Hoef, van Sint Annaland and Kuipers (2004)

defined the characteristic length in bi-disperse granular media as the average diameter. Yang et al. (2010) used the hydraulic diameter, which is defined using the ratio of the fluid phase volume to the solid surface area, as the characteristic length in monodisperse and polydisperse granular media. There are many other definitions; however, in general the characteristic length has been chosen empirically and thus there is poor understanding in the physical meaning of the choice in the characteristic length.

7.4 Numerical simulations of fluid flow through granular materials

Practically, a computer is used to solve these partial differential equations and a computational technique to solve the equations is often called as Computational Fluid Dynamics (CFD) in general. If some particles are immersed in a fluid, which is always the case for granular materials in reality, there are several CFD approaches to obtain the velocity, pressure and temperature fields in the fluid domain, which can be roughly classified into fully-resolved CFD, coarse-grid CFD, and Pore Network Model (PNM) based on the grid size (Fig. 7.1).

7.4.1 Fully-resolved CFD

A CFD method whose fluid grid is sufficiently fine such that the flow field around a particle is fully resolved is called as a fully-resolved CFD. If the grid is fine and appropriately shaped and the numerical schemes are appropriately chosen, an accurate flow field can be obtained. The momentum and energy exchanges between a fluid cell and a particle surface adjacent to the fluid cell arise from boundary conditions set at the particle surface. Types of boundary conditions depend on the numerical method chosen to solve Eqs. (7.1) to (7.3). The numerical method to solve Eqs. (7.1) to (7.3), which include the Finite Volume Method with a body-fit mesh (Nijemeisland & Dixon, 2001; Calis et al., 2001; Romkes et al., 2003; Yang et al., 2010) and an Immersed Boundary Method (Uhlmann, 2005; Tavassoli, Peters & Kuipers, 2015; Knight et al., 2020). The Lattice Boltzmann Method (LBM) (Ladd, 1994; van der Hoef, Beetstra & Kuipers, 2005; Beetstra, van der Hoef & Kuipers, 2007) can be also used where a LBM solves an approximate Boltzmann equation which is equivalent to Eqs. (7.1) and (7.2) (Krüger et al., 2017). A comprehensive review of fully-resolved CFD methods particularly focusing on heat transfer in granular materials is provided in Deen et al. (2014). A fully-resolved CFD is more accurate but at the same time computationally more expensive than the other two methods as it directly solves Eqs. (7.1) to (7.3).

7.4.2 Coarse-grid CFD

Coarse-grid CFD has a grid size larger than a particle size (Fig. 7.1(a)). In a coarse-grid CFD, the momentum exchange term between a fluid cell and particles in the cell is added in the momentum equation (Tsuji, Kawaguchi & Tanaka, 1993; Xu & Yu, 1997). The momentum exchange between the fluid and the particles has been empirically modelled by several studies (Ergun, 1952; Di Felice, 1994; Tenneti, Garg & Subramaniam, 2011; Tang et al., 2015) as summarised in Knight et al. (2020). These models are often based on the porosity (n) and the Reynolds number (Re).

Shimizu (2006) added the energy exchange term for the energy transport equation equation (Eq. (7.3)), which corresponds to the conductive heat conduction between a particle and fluid (particle-fluid heat conduction). This energy exchange between the fluid cell and the particles in the fluid cell is calculated based on an analytical or empirical correlation such as those found in studies Ranz and Marshall (1952), Whitaker (1972), Gunn (1978) and Tavassoli, Peters and Kuipers (2015) (a comprehensive summary is available in Peng, Doroodchi and Moghtaderi (2020)).

A coarse-grid CFD has the lowest computational cost among the three methods introduced in this section. However, the momentum and energy exchanges are calculated using empirical models only based on the packing density; thus, the accuracy of predicting fluid-particle interaction phenomenon at a particle scale with this type of a CFD method is necessarily limited.

7.4.3 Pore Network Model

A PNM, or Pore-scale Finite Volume (PFV) model (Caulk et al., 2020), descretises the fluid domain into pores which are connected together with a pipe for fluid flow is considered between two adjacent pores. A Delaunay triangulation is often used for the domain discretisation (Bryant & Blunt, 1992; Chareyre et al., 2012; Catalano, Chareyre & Barthélemy, 2014). An optimisation technique, such as merging pores (Sufian et al., 2019), is sometimes used. In a PNM, the momentum exchange between a pore and surrounding particles is made based on the conductance of a fluid pipe connecting adjacent pores. An important difference from coarse-grid CFD is that this conductance can be determined from the geometry of the fluid pipe. Several conductance models have been proposed (Bryant & Blunt, 1992; Chareyre et al., 2012); however, an accurate and efficient model for conductance has not been proposed yet (Rong, Dong & Yu, 2020).

Recently Caulk and Bruno (2019) and Caulk et al. (2020) proposed a PNM considering the energy transport equation. Similar to a coarse-grid CFD, they modelled the conductive heat transfer between a particle and fluid based on an empirical model by Tavassoli, Peters

and Kuipers (2015) because modelling the conductive heat transfer between a particle and fluid using geometric information of pore connections has not been proposed unlike the momentum exchange term.

PNMs have significant potential to be an accurate and efficient CFD method for fluid flow in granular materials. Chareyre et al. (2012) noted that Their PNM is a million times faster than their fully-resolved CFD based on a Finite Volume method. However, issues regarding PNMs are difficulties in deriving accurate conductance and particle-fluid heat conduction model.

7.4.4 Coupling DEM with CFD

To consider the effect of the fluid flow on particles in a granular medium, the DEM can be coupled with a CFD (refer to Section 7.4.4 for an overview of CFD modelling options). This section discusses how the fluid motion can be additionally taken into account in the DEM.

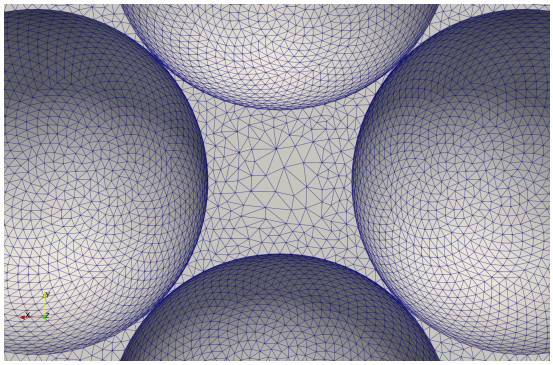
CFD methods to simulate fluid flow through granular particles using are discussed in Section 7.4.4. To consider the movement of particles resulting from fluid flow, the momentum exchange term (fluid-particle interaction force) is added in Eq. (2.28). The energy exchange between fluid and a particle is considered in a heat pipe network model. Such CFD-DEM coupled methods are proposed for all the three types of CFD methods reviewed in Section 7.4.4.

- Coarse-grid CFD (Shimizu, 2006; Kloss et al., 2012)
- PNM (Caulk & Bruno, 2019; Caulk et al., 2020)
- Fully-resolved CFD (Feng, Han & Owen, 2010; Kloss et al., 2012; Deen et al., 2014)

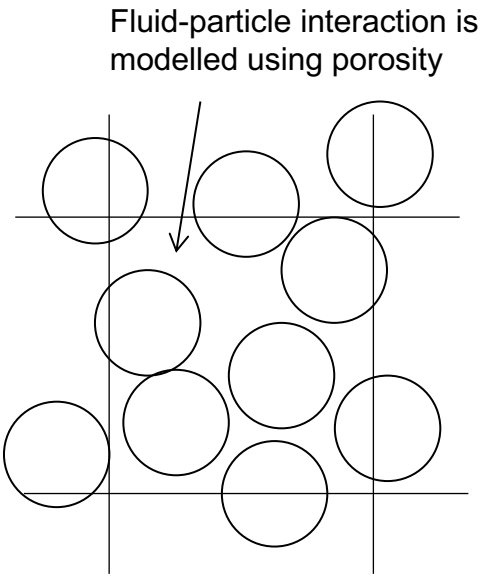
It is essential to accurately model fluid-particle interaction force and heat transfer between particles and fluid if Coarse-grid CFD or PNM is used as a CFD.

7.5 Summary

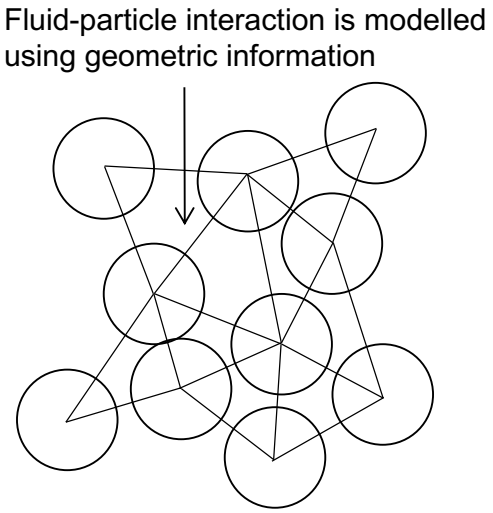
This chapter has reviewed the governing equations of incompressible Newtonian fluid flow (Section 7.2), dimensionless numbers to analyse the fluid flow (Section 7.3) and the numerical methods to simulate the fluid flow (Section 7.4). Section 7.3 highlighted that the choice of the characterisic length in the context of granular materials has been empirical. Section 7.4 reviewed three CFD methods; fully-resolved CFD, coarse-grid CFD and PNM. The fully-resolved CFD is computationally very expensive and it is practically impossible to simulate the movement of particles and the fluid flow by coupling with DEM.



(a) Fully-resolved CFD



(b) Coarse-grid CFD (2D)



(c) PNM (2D)

Figure 7.1: Schematic illustration of the three types of CFD methods to simulate fluid flow through particles

The coarse-grid CFD is a computationally efficient option; however, the accuracy of the coarse-grid CFD is limited because it only uses the packing density and the Reynolds number, which are not enough to represent the complex flow field existing in a granular medium. The PNM is also computationally much cheaper than the fully-resolved CFD and can consider the complex pore-scale geometry existing in a granular medium. However, it was also acknowledged that mechanical and thermal interactions between the fluid and the particles have not been accurately modeled yet.

Considering the literature reviewed in this chapter, the latter part of this thesis focuses on accurately modelling the pore fluid flow behaviour and heat transfer in granular materials with pore fluid flowing by means of PNM. Fully-resolved CFD simulations are conducted to develop the fluid flow and heat transfer models in the PNM. The advantage of the PNM over the coarse-grid CFD is also clarified with the developed data. This thesis also proposes a more physical choice of the characteristic length in a granular medium using the analogy between the fluid flow in a granular medium and in a pipe.

CHAPTER 8

MODELLING FLUID FLOW THROUGH GRANULAR MATERIALS USING PNM AND FVM

8.1 Introduction

This chapter documents the development of an efficient and accurate model for fluid flow through granular materials, which was developed to simulate advective heat transfer in granular materials and will also contribute to future studies on the fundamental mechanisms underlying hydro-mechanical behaviours of soils e.g. suffusion, liquefaction, partially-drained shear. To study fluid-particle interactions, a number of CFD-DEM frameworks have been proposed. As reviewed in Chapter 2, such frameworks can be classified into three types: (1) Coarse-grid CFD, (2) PNM, and (3) fully-resolved CFD based on the mesh size. This chapter specifically considers a PNM. The limitation of existing local conductance models for PNMs is discussed in Section 8.2. To address the shortcomings of existing models, novel local conductance models are proposed using three types of regular packings, SC, BCC, and FCC in Section 8.3. This chapter also presents the development of fully-resolved CFD dataset for randomly packed spheres (Section 8.4), which is used for the validation of the developed PNM in terms of local flow rates, permeability and fluid-particle interaction force (Sections 8.5 and 8.6). Finally, Section 8.6 examines the existing empirical method to predict fluid-particle interaction force on particles, which is used in coarse-grid CFD-DEM frameworks.

8.2 Pore Network Models (PNMs)

It's challenging to develop an accurate PNM for granular media with varying packing densities and particle size distributions. Moreover, while PNMs present a computationally attractive option for modelling flow through granular materials, their accuracy is limited by the simplifications made to model the local conductance. To contextualize the contribution made in this chapter, Section 8.2.1 describes the overall PNM simulation process, while Section 8.2.2 reviews existing local conductance models and proposes some new models.

8.2.1 Domain discretisation and local flow calculation in PNM

To construct a PNM of a granular packing the pore space must firstly be discretized into individual pores. This study follows Chareyre et al. (2012) and uses a 3D weighted Delaunay triangulation where the particle centroids are the tetrahedra vertices. Each tetrahedron in the resulting tessellation defines an individual pore (Fig. 8.1(a)). The Voronoi diagram is the dual of the Delaunay tessellation and the weighting which is applied to each vertex (here the weights are equal to the square of the particle radii), prevents any Voronoi vertex from lying within a particle.

A schematic illustration of a two-dimensional PNM is shown in Fig. 8.1(b). Chareyre et al. (2012) considered the Voronoi vertices to be the nodes in the PNM; this contrasts with many previous studies who took the pore centroids to be the nodes (Sholokhova, Kim & Lindquist, 2009; Sufian et al., 2019). For each pair of connected pores, Chareyre et al. (2012) defined the pore throat (network edge) to be the domain enclosed by the pore centres and the surfaces of the particles common the two pores (the face particles). In a PNM, the individual pore pressures are defined at the PNM nodes, e.g. p_a in pore a. Flow occurs through the network edges that connect these nodes, e.g. Q_{ab} occurs from pore a to pore b.

To simulate fluid transport between pores, a mass balance equation is considered for each pore assuming steady laminar and incompressible flow:

$$\sum_{i=1}^{4} Q_{ab_i} = 0 \tag{8.1}$$

where Q_{ab_i} is the volumetric flow rate (in $[m^3 s^{-1}]$) from pore a to pore b_i, and b_i are the (four) pores adjacent to pore a. Assuming laminar flow between any two connecting pores, a and b, Q_{ab} is related to p_a and p_b by application of Darcy's law:

$$Q_{ab} = g_{ab}(p_a - p_b) \tag{8.2}$$

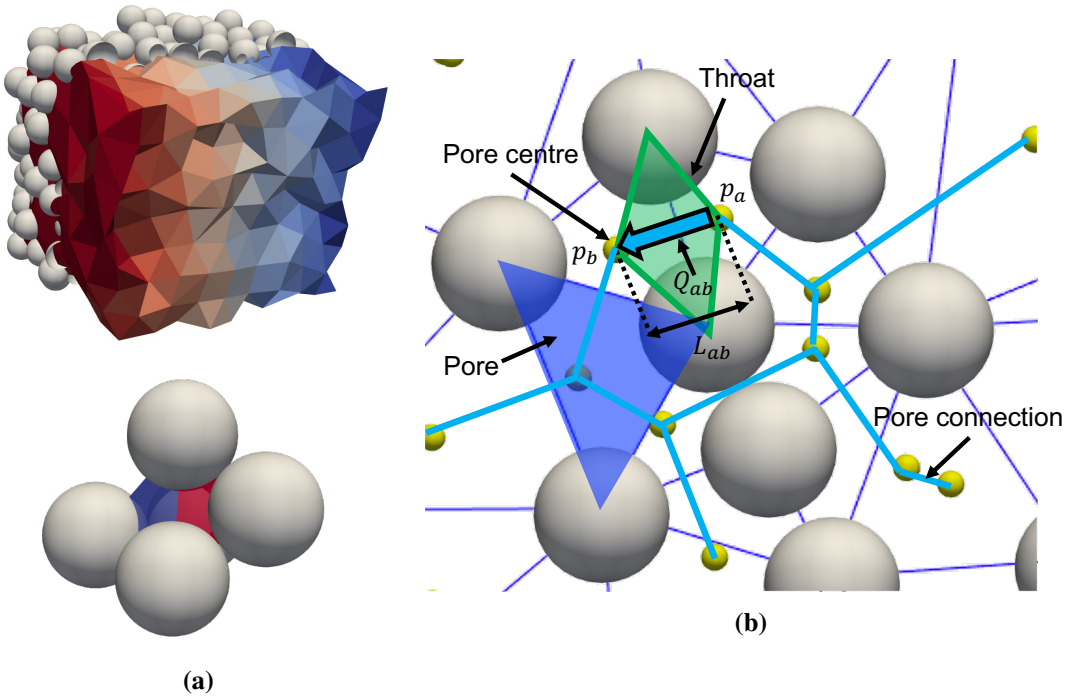


Figure 8.1: Schematic illustration of the PNM framework. (a) 3D schematic illustrations of fluid domain discretization using the weighted Delaunay triangulation (b) 2D schematic illustration of definition of pores, throats, pore centres and two adjacent pores. The yellow spheres mark the location of the nodes, the turquoise blue lines are the edges of the network, i.e. the pore connections. p_a and p_b are the pressures at pore a and b, respectively, Q_{ab} is the volume flow rate from pore a to pore b and L_{ab} is the length of throat ab. Reproduced from Morimoto et al. (2022), under the terms of the CC BY 4.0 license.

where g_{ab} is the hydraulic conductance (in $[m^3 Pa^{-1} s^{-1}]$) of the throat connecting pores a and b. While this model can be extended to consider flow characterised by high Reynolds number (Re)(e.g. Wu, Hou and Yu (2019) and Wu et al. (2021)) by including an inertia term in Eq. (8.2), the studies presented herein are restricted to low values of Re. The intrinsic conductance of throat ab, which is independent of the fluid dynamic viscosity μ_{f}, is denoted as $\mathcal{G}_{ab}$ (in $[m^3]$) in this study. $\mathcal{G}_{ab}$ and g_{ab} are related via the fluid dynamic viscosity:

$$\mathcal{G}_{ab} = \mu_{\mathrm{f}} g_{ab} \tag{8.3}$$

Eq. (8.1) holds for every pore, and so a system of N_{pore} linear simultaneous equations (where N_{pore} is the total number of the pores) must be solved to determine the pressures ($p_1, p_2, \ldots, p_{N_{\mathrm{pore}}}$). Following Eq. (8.1) - Eq. (8.3), the $\mathcal{G}_{ab}$ values characterising the throats in the system determine the Q_{ab} values of the throats, meaning that accurate modelling of $\mathcal{G}_{ab}$ is critical for the performance of the PNM. Calculation of $\mathcal{G}_{ab}$ depends only on the geometry of throat ab, as discussed in Section 8.2.2 below.

8.2.2 Local intrinsic conductance model in PNM

Most of the existing conductance models that have been documented in the literature are based upon the Hagen-Poiseuille equation, which gives the intrinsic conductance of a pipe as:

$$\mathcal{G} = \frac{\alpha \pi r^4}{L} = \frac{\Gamma}{L} \tag{8.4}$$

with:

$$\Gamma = \alpha \pi r^4 \tag{8.5}$$

where r is the pipe radius, L is the pipe length, and α is a geometric factor which reflects the pipe shape ($\alpha = 1/8$ for a cylindrical pipe). In a PNM, the distance between the nodes of pores a and b (L_{ab}), shown in Fig. 8.1(b), is taken to be the pipe length L. However, the definitions of r and α are not immediately apparent since the topology of pore throats is complex even in the case of monodisperse spheres. The efficacy of the more widely adopted r and α values, which are outlined below, is considered in this study. A useful analysis of various available expressions for conductance is given in Rong, Dong and Yu (2020).

Fluid area model (FA model)

This model simply calculates r from the throat face fluid area A_{f} (defined in Fig. 8.2(a)):

$$\Gamma = \alpha_{\mathrm{FA}} \frac{{A_{\mathrm{f}}}^2}{\pi} \tag{8.6}$$

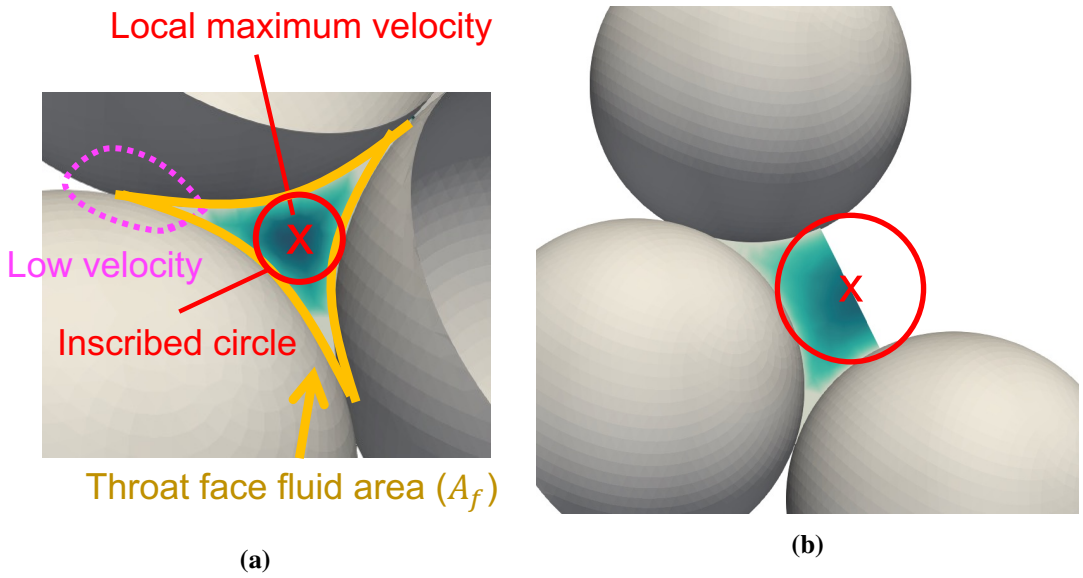


Figure 8.2: Schematic illustration of throat face geometries with a definition of an inscribed circle. (a) Closed throat face. (b) Throat face with a large open edge. Reproduced from Morimoto et al. (2022), under the terms of the CC BY 4.0 license.

where $\alpha_{\text{FA}} = 1/8$, i.e. assuming a circular pipe shape (i.e. a pipe that is circular in cross-section).

Effective radius model (ER model)

Assuming a no-slip boundary condition applies when the fluid is in contact with solid surfaces, the velocity distribution across a throat face depends on the throat face shape (Fig. 8.2). A throat face completely enclosed by particles, as in Fig. 8.2(a), has a relatively large low-velocity region. In contrast, the throat face shown in Fig. 8.2(b) has a large open edge and a higher proportion of the face area transmits relatively fast fluid flow. Bryant and Blunt (1992) defined an effective radius (r_{eff}) as $r_{\text{eff}} = (r_{\text{ic}} + r_{\text{eq}})/2$, where $r_{\text{eq}} = \sqrt{A_{\text{f}}/\pi}$ and r_{ic} is the radius of the inscribed circle defined by the three particles defining the throat face (illustrated in Fig. 8.2) so that

$$\Gamma = \alpha_{\text{ER}} \pi {r_{\text{eff}}}^4 \tag{8.7}$$

where $\alpha_{\text{ER}} = 1/8$ for a circular pipe.

Hydraulic radius model (HR model)

Chareyre et al. (2012) observed that the *ER* model tends to underpredict the permeability and so they defined the hydraulic radius, r_{h}, to be the ratio of Θ_{ab} to the solid surface area (γ_{ab}) of throat ab:

$$r_{\mathrm{h}} = \frac{\Theta_{ab}}{\gamma_{ab}} = \frac{\Theta_{ab}}{\sum_{m=1}^{3} \gamma_{m,ab}} \tag{8.8}$$

where $\gamma_{m,ab}$ is the surface area of the part of particle m touching throat ab (illustrated in Fig. 8.3). Referring to Fig. 8.3, the volume of throat ab (Θ_{ab}) is the sum of the volumes of the two tetrahedra defined by pore centres and the centroids of the face three particles. The volume of the fluid in the throat (Θ_{ab}) is given by subtracting the volumes of the intersection of the face particles with the throat volume from V_{ab}. For a pipe with a circular cross-section,

$$r_{\mathrm{h}} = \frac{\pi r^2 L}{2\pi r L} = \frac{r}{2} \tag{8.9}$$

Chareyre et al. (2012) suggested using the throat face area A_{f} and r_{h} to calculate Γ:

$$\Gamma = 4\alpha_{\mathrm{HR}} A_{\mathrm{f}} {r_{\mathrm{h}}}^2 \tag{8.10}$$

While Chareyre et al. (2012) suggest taking $\alpha_{\mathrm{HR}} = 1/8$, Sweijen et al. (2018) suggest that the α_{HR} value should be calibrated to capture the global permeability of the particle assembly.

HR4 model

The *HR* model includes A_{f}, which, as shown in Fig. 8.2, may not effectively characterise the throat geometry. The *HR4* model, which is introduced in the current study, uses only r_{h} i.e.:

$$\Gamma = 16\alpha_{\mathrm{HR4}} {r_{\mathrm{h}}}^4 \tag{8.11}$$

where $\alpha_{\mathrm{HR4}} = 1/8$ for a circular pipe.

ER-HR model

A new *ER-HR* model, inspired by the models proposed by Bryant and Blunt (1992) and Chareyre et al. (2012) is also considered here, where $\pi {r_{\mathrm{eff}}}^2$ is used in lieu of A_{f} in Eq. (8.10):

$$\Gamma = 4\alpha_{\text{ER-HR}} \pi {r_{\mathrm{eff}}}^2 {r_{\mathrm{h}}}^2 \tag{8.12}$$

where $\alpha_{\text{ER-HR}} = 1/8$ for a circular pipe.

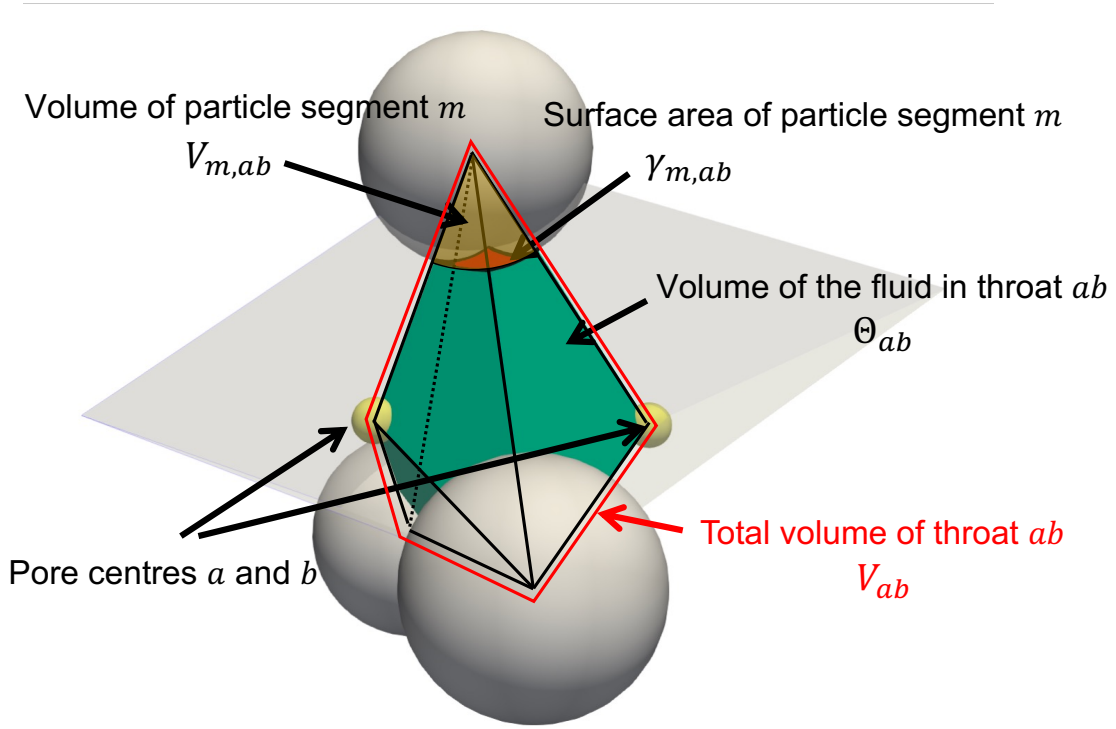


Figure 8.3: Schematic illustration of the total volume of throat ab (V_{ab}), the volume of the fluid in throat ab (Θ_{ab}) and the surface area ($\gamma_{m,ab}$) and the volume ($V_{m,ab}$) of sphere segment m. Reproduced from Morimoto et al. (2022), under the terms of the CC BY 4.0 license.

There are other models, which are not considered here. For example, Patzek and Silin (2001) and Mason and Morrow (1991) adopted a shape factor defined from the perimeter and the area of a throat face; this shape factor is conceptually similar to the hydraulic radius. The pore-throat-pore model proposed by van der Linden et al. (2018) was not considered as it does not perform well without merging Delaunay cells (Sufian et al., 2019). Rong, Dong and Yu (2020) proposed a method to calculate the radius r in Eq. (8.4) by conducting a CFD simulation of flow through each throat face geometry, following Thompson and Fogler (1997); however, this method is computationally expensive and was therefore not considered in this study. Thompson and Fogler (1997) proposed correcting the conductance of a tube by analytically determining the conductance of a hyperbolic Venturi; this method was not employed here because determining the curvature of the Venturi is challenging in the case of polydisperse granular materials.

8.2.3 Calculation of fluid-particle interaction force in a PNM

The fluid-particle interaction force can be decomposed into the pressure gradient force, arising from the pressure normal to the particle surface and the viscous drag force, arising from shear stresses on the particle surface. Chareyre et al. (2012) proposed that the pressure gradient force vector on particle m at throat ab ($\mathbf{F}^{\mathrm{p}}{}_{m,ab}$) can be calculated as:

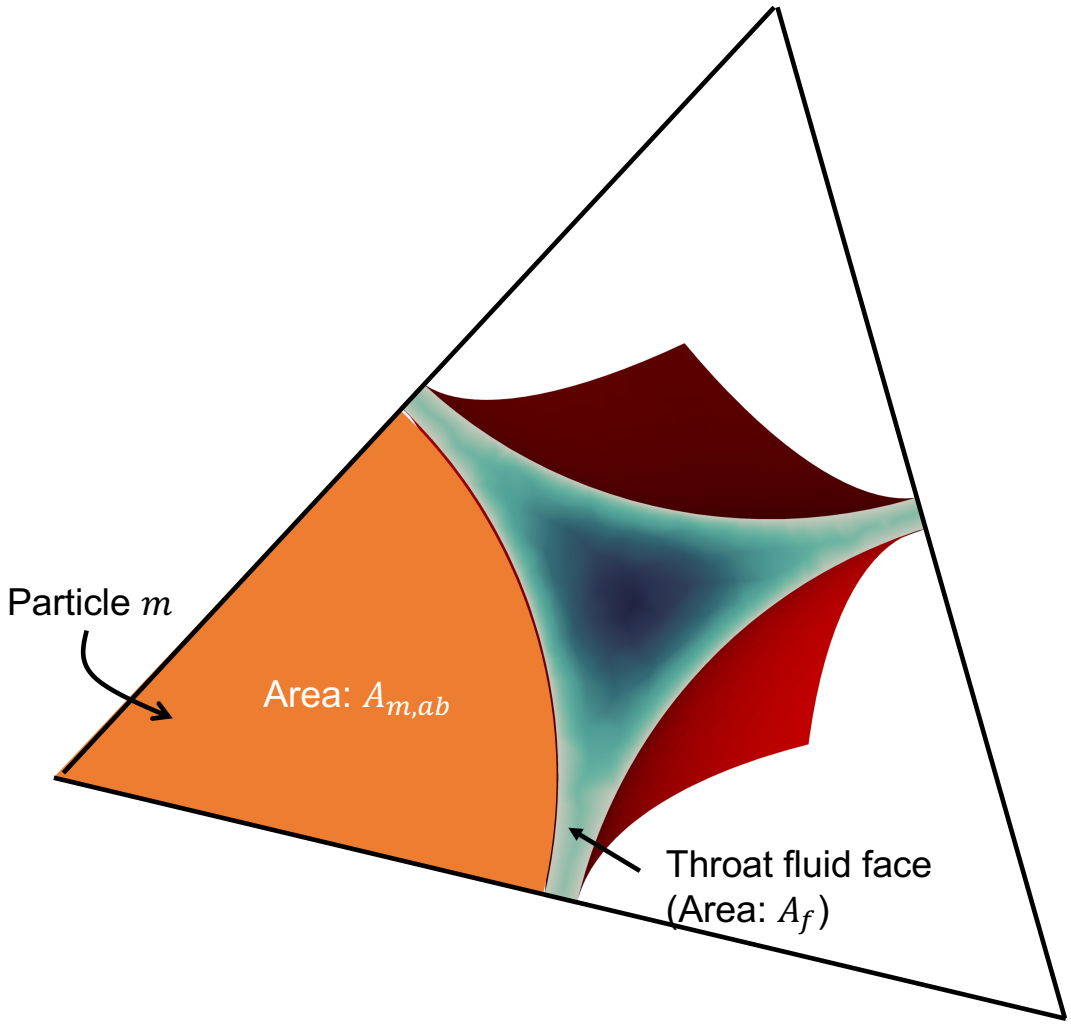


Figure 8.4: Schematic illustration of $A_{m,ab}$ and A_{f}.

$$\mathbf{F}^{\mathrm{p}}{}_{m,ab} = A_{m,ab}(p_a - p_b)\mathbf{n_{ab}} \tag{8.13}$$

where $A_{m,ab}$ is the area of the union of particle m (illustrated in Fig. 8.4) and the throat face and $\mathbf{n_{ab}}$ is the unit vector normal to the throat face and pointing from pore node a to pore node b. Chareyre et al. (2012) proposed calculating the viscous drag force on each individual particle, m, that defines throat ab as:

$$\mathbf{F}^{\mathrm{d}}_{m,ab} = \frac{\gamma_{m,ab}}{\sum_{k=1}^{3}\gamma_{k,ab}} \sum_{k=1}^{3} F^{\mathrm{d}}{}_{k,ab} \tag{8.14}$$

where $\gamma_{m,ab}$ is the surface area of particle m within the throat ab and the total viscous force $\sum_{k=1}^{3} F^{\mathrm{d}}{}_{k,ab}$ is calculated by:

$$\sum_{k=1}^{3} {F^{\mathrm{d}}}_{k,ab} = A_{\mathrm{f}}(p_a - p_b)\mathbf{n_{ab}} \tag{8.15}$$

where A_{f} is the throat fluid face area.

The total fluid-particle interaction force acting on particle m is the sum of the pressure and viscous forces i.e.:

$$\mathbf{F}_m^{f\to p} = \mathbf{F}_m^p + \mathbf{F}_m^d = \sum_{ab} (\mathbf{F}^{\mathrm{p}}{}_{m,ab} + \mathbf{F}^{\mathrm{d}}_{m,ab}) \tag{8.16}$$

8.3 Analytical study to estimate the Γ and α values of throats in regular packing of uniform spheres

The accuracy of the local conductance model depends on the choice of the radius of the pipe representing the throat (r) and the shape factor α. This section back-analyses data from an analytical study by Zick and Homsy (1982) to estimate the Γ and α values of throats in three regular (lattice) packings of uniform spheres, i.e. SC, BCC, and FCC (Fig. 8.5). These regular packings enable a constrained study of the conductance models, as only one type of local pore topology exists in each packing. The global permeability data considered are outlined in Section 8.3.1, and the Γ values are related to these data in Section 8.3.2. The α values derived from this dataset are then presented in Section 8.3.3.

8.3.1 Global permeability of regular packing

Zick and Homsy (1982) used a Galerkin method to study laminar flow around uniform spheres on lattice packings with SC, BCC and FCC configurations. They systematically varied the packing density of the systems they considered and provided a set of data in terms of the drag coefficient, c_{d}, which is given by:

$$c_{\mathrm{d}} = \frac{F}{6\pi\mu_{\mathrm{f}} R u_{\text{inlet}}} = \frac{F}{3\pi\mu_{\mathrm{f}} D u_{\text{inlet}}} \tag{8.17}$$

where R is the particle radius, D is the particle diameter, u_{inlet} is the inlet velocity, and F is the drag force acting on the particle. The denominator is the well-known Stokes drag force (F^{Stokes}) for a particle immersed in a slow flow.

$$F^{\text{Stokes}} = 6\pi\mu_{\mathrm{f}} R u_{\text{inlet}} = 3\pi\mu_{\mathrm{f}} D u_{\text{inlet}} \tag{8.18}$$

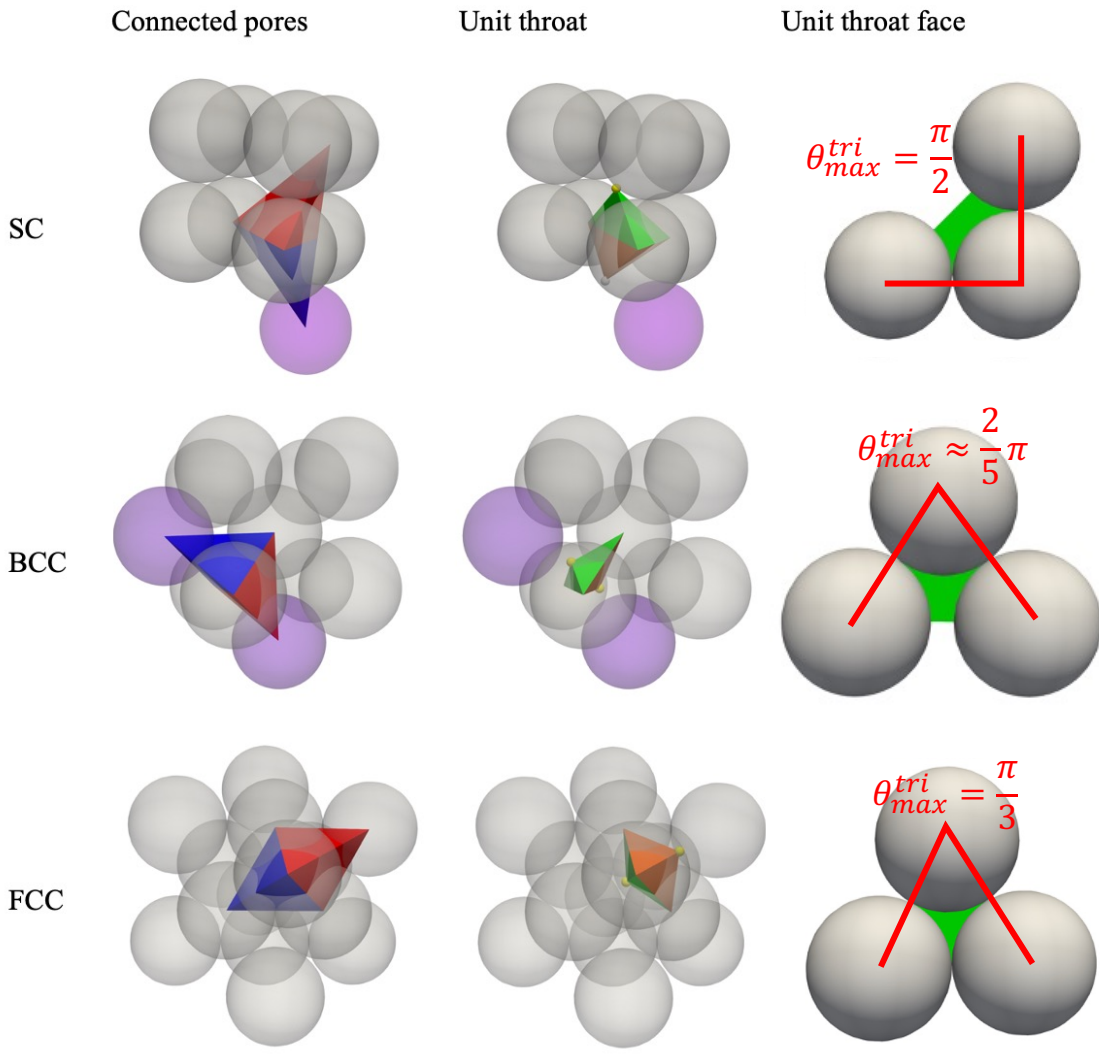


Figure 8.5: Schematic illustration of connected pores, unit throats, and unit throat faces in SC, BCC, FCC packings. Reproduced from Morimoto et al. (2022), under the terms of the CC BY 4.0 license.

These c_{d} values can be related to the pressure gradient ($\Delta p/L$) across the packing following Zick and Homsy (1982):

$$\frac{\Delta p}{L} = -\frac{9}{2}\frac{\mu_{\mathrm{f}}}{R^2}\frac{1}{e+1}c_{\mathrm{d}}u_{\mathrm{inlet}} \tag{8.19}$$

Using Darcy's law the analytical global permeability of a regular packing, $k_{\mathrm{h,RP}}$, can be related to c_{d} as:

$$k_{\mathrm{h,RP}} = \left|\frac{\mu_{\mathrm{f}}u_{\mathrm{inlet}}}{\frac{\Delta p}{L}}\right| = \frac{2R^2}{9c_{\mathrm{d}}}(e+1) \tag{8.20}$$

8.3.2 Back-calculation of Γ

Using the data provided in Zick and Homsy (1982) the intrinsic local conductance between two adjacent pores was estimated from the global permeability data following an approach previously adopted to relate the local thermal conductivity to the global thermal conductivity in heat pipe network models (e.g. El Shamy, De Leon and Wells (2013)). The average volume flow rate in the i-direction, ($\overline{Q_i}$) $[m^3 s^{-1}]$ can be expressed as:

$$\overline{Q_i} = \frac{1}{L}\sum_{fp=1}^{N_{\mathrm{pore}}} {Q^{fp}}_i L^{fp} \tag{8.21}$$

where L is the length of the system, N_{pore} is the number of the pipes in the system, and ${Q^{fp}}_i$ is the volume flow rate in pipe fp in the i direction, and L^{fp} is the length of pipe fp. Following Darcy's law and referring to Eq. (8.2)-Eq. (8.4),

$${Q^{fp}}_i = -\frac{\Gamma_{ab}^{fp}}{\mu_{\mathrm{f}}}{n^{fp}}_i\frac{\partial p}{\partial x_i} = -\frac{\Gamma_{ab}^{fp}}{\mu_{\mathrm{f}}}{n^{fp}}_i\frac{\Delta p^{fp}}{L^{fp}} \tag{8.22}$$

where Γ_{ab}^{fp} is the Γ value of pipe fp connecting pores a and b, n^{fp} is the normal unit vector expressing the direction of pipe fp, and Δp^{fp} is the pressure drop through pipe fp. In the case of a lattice system, assuming that the pressure gradient within the system is uniform,

$$\Delta p^{fp} = L^{fp}{n^{fp}}_j\frac{\partial p}{\partial x_j} \tag{8.23}$$

where $\frac{\partial p}{\partial x_j}$ is the pressure gradient in direction j. Substituting Eqs. (8.22) and (8.23) to Eq. (8.21),

$$\overline{Q_i} = -\left[\frac{1}{L}\sum_{fp=1}^{N_{\text{pore}}} \frac{\Gamma_{ab}^{fp}}{\mu_{\text{f}}} n^{fp}{}_i n^{fp}{}_j L^{fp}\right] \frac{\partial p}{\partial x_j} \tag{8.24}$$

Dividing by cross-sectional area of the system,

$$u_i = -\left[\frac{1}{V}\sum_{fp=1}^{N_{\text{pore}}} \frac{\Gamma_{ab}^{fp}}{\mu_{\text{f}}} n^{fp}{}_i n^{fp}{}_j L^{fp}\right] \frac{\partial p}{\partial x_j} \tag{8.25}$$

Thus, the intrinsic permeability tensor of the system is:

$$k_{\text{h},ij} = \frac{1}{V}\sum_{fp=1}^{N_{\text{pore}}} \Gamma_{ab}^{fp} n^{fp}{}_i n^{fp}{}_j L^{fp} \tag{8.26}$$

Each lattice configuration has only one type of throat as shown in Fig. 8.5; thus, each lattice type and packing density has a unique Γ_{ab}^{fp} and L^{fp} value, denoted here as Γ^{RP} and L^{RP}. The diagonal terms of the permeability tensor in Eq. (8.26), $k_{\text{h,diag}}$ ($= k_{\text{h},xx} = k_{\text{h},yy} = k_{\text{h},zz}$), are equal to the analytical global permeability $k_{\text{h,RP}}$ in Eq. (8.20); therefore,

$$k_{\text{h,RP}} = \Gamma^{\text{RP}} \frac{L^{RP}}{V} \sum_{fp=1}^{N_{\text{pore}}} n^{fp}{}_x n^{fp}{}_x \tag{8.27}$$

Eq. (8.27) enables back-calculation of the Γ^{RP} value from the global permeability $k_{\text{h,RP}}$. Verification of this approach to determine the Γ values was carried out using fully resolved CFD data and is documented in Appendix C.

SC packing

The unit cell for the SC packing consists of 6 throats with the same topology. Assuming the lattice is aligned with the Cartesian axes, the unit vector normal to the throat face is $(|n_x|, |n_y|, |n_z|)$=$(1, 0, 0)$, $(0, 1, 0)$ or $(0, 0, 1)$, and there are two throats with each unit vector in each unit cell. Denoting the length of the unit cell as l, the volume of the cell is l^3 and the length of the throat L^{RP} is l. Following Eq. (8.27),

$$k_{\text{h,RP}} = \Gamma^{\text{RP}} \frac{l}{l^3}(2 \times 1 \times 1) = \frac{2\Gamma^{\text{RP}}}{l^2} \tag{8.28}$$

Taking advantage of the symmetry of the packing, we can calculate the volume of the throat and the sum of the solid angles of the particles within the throat as:

$$V_{\text{throat}} = \frac{\text{Volume of unit cell}}{\text{Number of throats}} = \frac{l^3}{6} \tag{8.29}$$

$$\Omega_{\text{throat}} = \frac{4\pi \times \text{Number of spheres}}{\text{Number of throats}} = \frac{4\pi \times 1}{6} = \frac{2}{3}\pi \tag{8.30}$$

Note that the solid angle of a sphere is 4π and there is a sphere in the unit cell of the SC packing and so r_{h} can be calculated once the solid angle within the throat is obtained as:

$$r_{\text{h}} = \frac{\text{Total volume of the throat} - \text{Solid volume}}{\text{Solid surface area}} = \frac{V_{\text{throat}} - \frac{1}{3}\Omega_{\text{throat}}R^3}{\Omega_{\text{throat}}R^2} \tag{8.31}$$

A_{f} and r_{eff} can be easily obtained from the face geometry.

BCC packing

The unit cell for the BCC packing consists of 24 throats with the same topology. The unit vector normal to the throat face is $(|n_x|, |n_y|, |n_z|)$=$(\frac{1}{\sqrt{2}}, \frac{1}{\sqrt{2}}, 0)$, $(\frac{1}{\sqrt{2}}, 0, \frac{1}{\sqrt{2}})$ or $(0, \frac{1}{\sqrt{2}}, \frac{1}{\sqrt{2}})$, and each of these unit vectors is associated with 8 throats. Just as for the SC packing,

$$k_{\text{h,RP}} = \Gamma^{\text{RP}} \frac{\frac{\sqrt{2}}{4}l}{l^3}(16 \times \frac{1}{\sqrt{2}} \times \frac{1}{\sqrt{2}}) = \frac{2\sqrt{2}\Gamma^{\text{RP}}}{l^2} \tag{8.32}$$

$$V_{\text{throat}} = \frac{l^3}{24} \tag{8.33}$$

$$\Omega_{\text{throat}} = \frac{4\pi \times 2}{24} = \frac{1}{3}\pi \tag{8.34}$$

FCC packing

The unit cell of the FCC packing consists of 32 throats with the same topology. The unit vector normal to the throat face is $(|n_x|, |n_y|, |n_z|) = (\frac{1}{\sqrt{3}}, \frac{1}{\sqrt{3}}, \frac{1}{\sqrt{3}})$. Thus,

$$k_{\text{h,RP}} = \Gamma^{\text{RP}} \frac{\frac{\sqrt{3}}{4}l}{l^3}(32 \times \frac{1}{\sqrt{3}} \times \frac{1}{\sqrt{3}}) = \frac{8}{\sqrt{3}}\frac{\Gamma^{\text{RP}}}{l^2} \tag{8.35}$$

$$V_{\text{throat}} = \frac{l^3}{32} \tag{8.36}$$

$$\Omega_{\text{throat}} = \frac{4\pi \times 4}{32} = \frac{1}{2}\pi \tag{8.37}$$

8.3.3 Variation in shape factor α with packing density for lattice packings

Once the Γ values are obtained, the shape factor α defined in Eq. (8.4) can be determined. For example, the α value for the *FA* model (α_{FA}) is given as:

$$\alpha_{\text{FA}} = \frac{\pi \Gamma^{\text{RP}}}{{A_{\text{f}}}^2} \tag{8.38}$$

α was calculated for a range of void ratios, for each of the regular lattice packings considered by Zick and Homsy (1982) (i.e. SC, BCC and FCC), and using the models outlined in Eqs. (8.6), (8.7) and (8.10) to (8.12) (*FA*, *ER*, *HR*, *HR4* and *ER-HR* models). The minimum void ratios considered for the SC, BCC, and FCC packings were 0.910, 0.470, and 0.361, respectively. In Fig. 8.6, the calculated α values were plotted against void ratio e; for these packings the local void ratio of the throat (e^*) is identical to the void ratio of the packing itself, global void ratio (e).

Referring to Fig. 8.6, for the FCC and BCC packings, the back-calculated α_{FA} values are relatively similar over the range of e values considered here (i.e. $0.11 < \alpha_{\text{FA}} < 0.18$). However, the α_{FA} values obtained for the SC packing are much larger than those for the FCC and BCC packings. This result shows that the accuracy of any model that uses the throat face fluid area, A_{f}, depends on both packing type and density. On the other hand, the *ER* model which employs the corrected throat face fluid area seems to be less sensitive to geometrical changes as the α_{ER} values for all the packings are between 0.22 – 0.32. These values are larger than the $\alpha = 1/8$ predicted by the Hagen-Poiseuille equation because the throat cross-sectional area becomes larger towards the end of the throat.

For all the models containing r_{h} (i.e. *HR*, *HR4* and *ER-HR*), the back-calculated values of α have been found to decrease as the packing density reduces (i.e. as the void ratio increases); this does not support the use of a constant α as proposed in Chareyre et al. (2012). In models that include A_{f} term, i.e. the *FA* and *HR* models, there is a large difference between the α values for the SC and BCC packings, i.e. the α values depend upon both fabric and void ratio.

In a lattice packing, the local void ratio of the throat (e^*) is identical to the global void ratio (e). Based on these analyses of the regular, lattice packings, an expression that relates the optimal α value for a throat to the void ratio of the throat is introduced (denoted as the $\alpha_{\text{XX}}(e^*)$ model, hereinafter, where the subscript XX denotes the model type, i.e. *HR*, *HR4* or *ER-HR*). In Fig. 8.6, the data show that the that α-e^* relationships for the three lattice packings are almost identical for the *HR4* and *ER-HR* models. The α data are available for a wider range of e^* values in comparison to the BCC data and so these FCC data were

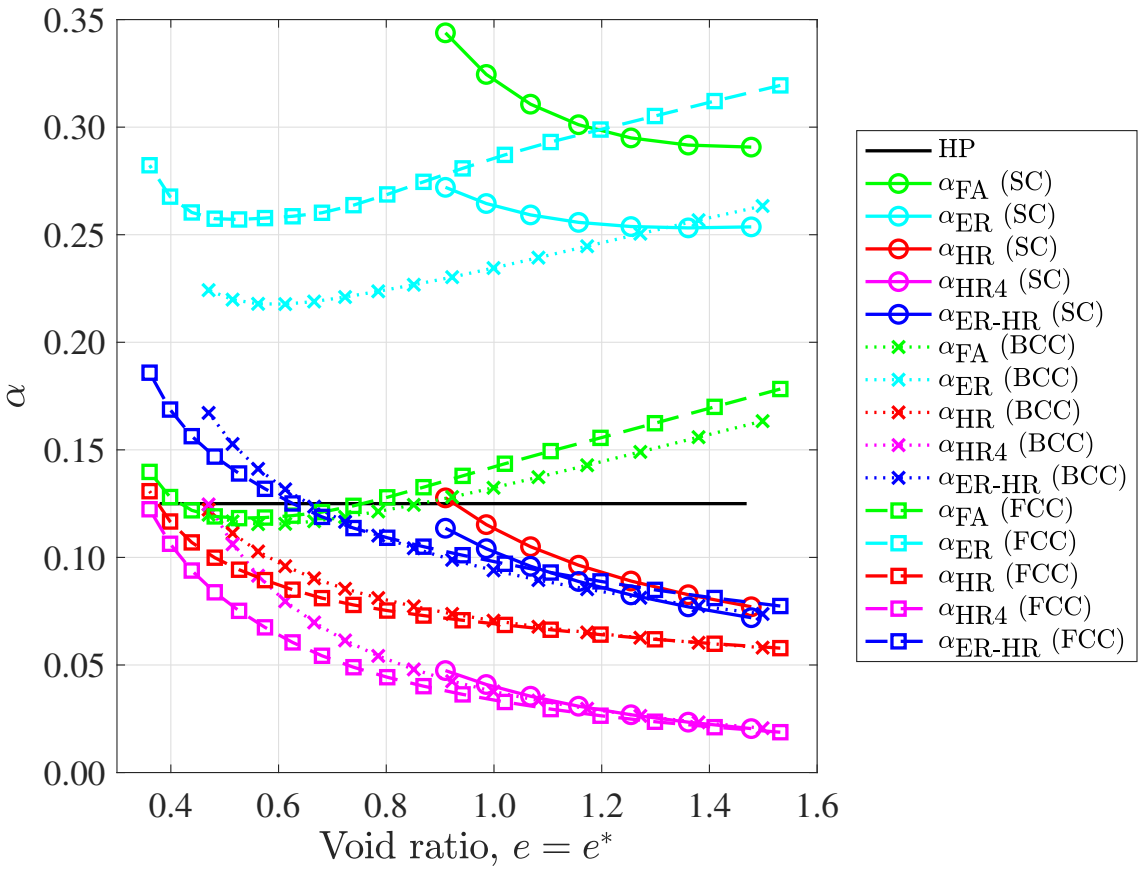


Figure 8.6: Schematic illustration of connected pores, unit throats, and unit throat faces in SC, BCC, FCC packings. Reproduced from Morimoto et al. (2022), under the terms of the CC BY 4.0 license.

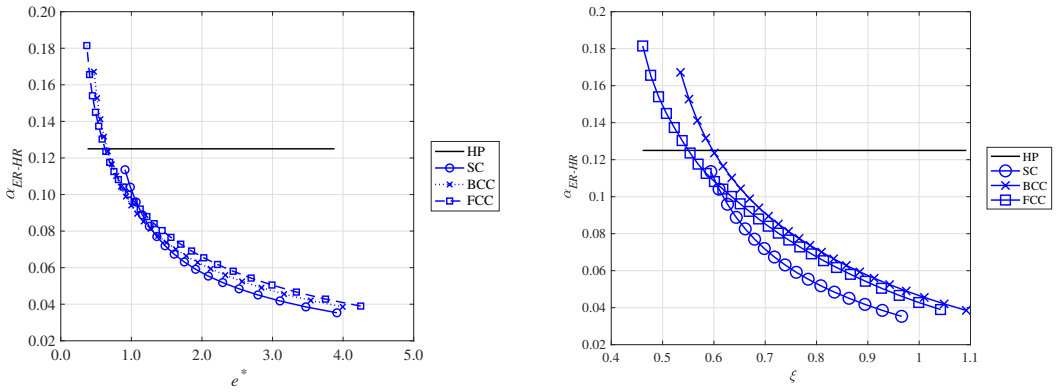


Figure 8.7: Back-calculated α values for a variety of packings and void ratios. (a) α vs e^*. (b) α vs ξ. Reproduced from Morimoto et al. (2022), under the terms of the CC BY 4.0 license.

used to develop new cubic equations for α for use with the *HR*, *HR4* and *ER-HR* models as follows:

$$\alpha_{\text{HR}}(e^*) = 0.555\left(\frac{1}{1+e^*}\right)^3 - 0.565\left(\frac{1}{1+e^*}\right)^2 + 0.279\left(\frac{1}{1+e^*}\right) \tag{8.39}$$

$$\alpha_{\text{HR4}}(e^*) = 0.510\left(\frac{1}{1+e^*}\right)^3 - 0.249\left(\frac{1}{1+e^*}\right)^2 + 0.062\left(\frac{1}{1+e^*}\right) \tag{8.40}$$

$$\alpha_{\text{ER-HR}}(e^*) = 0.510\left(\frac{1}{1+e^*}\right)^3 - 0.441\left(\frac{1}{1+e^*}\right)^2 + 0.286\left(\frac{1}{1+e^*}\right) \tag{8.41}$$

Another method of modelling $\alpha_{\text{ER-HR}}$ uses $\xi = \Theta_{ab}{}^{\frac{1}{3}}/\gamma_{ab}{}^{\frac{1}{2}}$, the non-dimensional fluid volume – solid surface ratio, instead of e^*. In this case, the results with the three different packings also fall on a unique line. The result with the FCC packings can be approximated using the following function:

$$\alpha_{\text{ER-HR}}(\xi) = \frac{0.0302}{\xi^2} + \frac{0.0156}{\xi^2} \tag{8.42}$$

The advantage of using this definition of packing density is most significant when bimodal packings are considered, which will be demonstrated later with results.

8.4 PNM and CFD models to assess applicability of new conductance expressions to randomly packed assemblies of spheres

This section assesses the applicability of the new expressions for α (Eqs. (8.39) to (8.42)) in the context of more general packing configurations. The expressions were implemented in a new PNM, as described in Section 8.4.1. The PNM simulations were conducted following Section 8.4.2. CFD simulations were carried out as outlined in Section 8.4.3 to back calculate α and enable a direct comparison with the new PNM in terms of global permeability.

8.4.1 PNM Implementation

The PNM used here was implemented in C++ using appropriate external libraries. The weighted Delaunay triangulation was conducted using `TetGen` (Si, 2015) following Sufian et al. (2019). The geometric parameters, A_{f}, r_{eff}, and r_{h}, are calculated using the positions and radii of the particles. The spherical surface area γ_Ω and the volume V_Ω of a sphere segment with a solid angle Ω are calculated using the sphere radius R:

$$\gamma_\Omega = \Omega R^2 \tag{8.43}$$

$$V_\Omega = \frac{1}{3}\Omega R^3 \tag{8.44}$$

where $\Omega = 4\pi$ for a sphere. Following Eq. (8.8), the hydraulic radius of a throat is then:

$$r_{\text{h}} = \frac{V_{ab} - \sum_{m=1}^{3} V_{m,ab}}{\sum_{m=1}^{3} \gamma_{m,ab}} = \frac{V_{ab} - \sum_{m=1}^{3} \frac{1}{3}\Omega_{m,ab} {R_m}^3}{\sum_{m=1}^{3} \Omega_{m,ab} {R_m}^2} \tag{8.45}$$

where V_{ab} is the total volume of the throat ab, which can be calculated easily, and $\gamma_{m,ab}$ and $V_{m,ab}$ are the spherical surface area and the volume of the segment of particle k which define the throat (Fig. 8.3). The algorithm proposed by Van Oosterom and Strackee (1983) was used to calculate Ω; this is similar to the implementation in `YADE` (Smilauer et al., 2021). The set of N_{pore} linear equations defined by Eq. (8.1) were solved using `PETSc`, a linear equation solver (Balay et al., 1997; Balay et al., 2019). A direct method based on *LU* decomposition was chosen for robustness since the time for solving the equations is trivial (< 0.1 sec for max. 629 particles).

8.4.2 PNM simulations

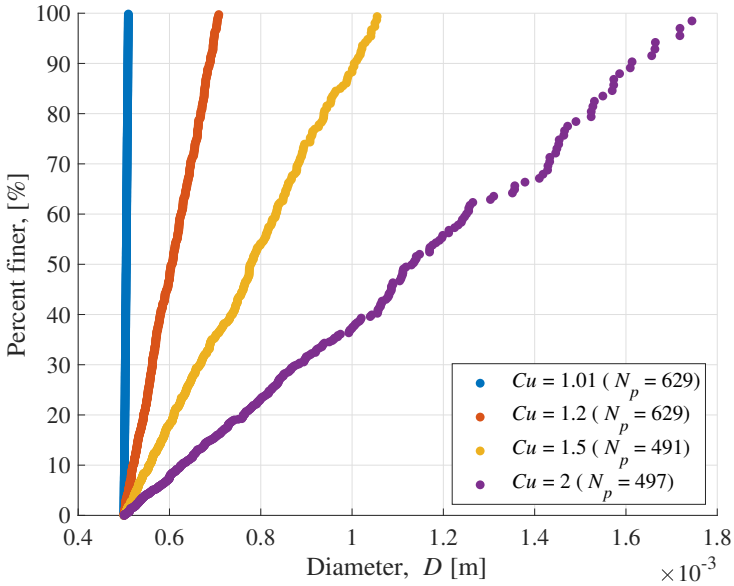
Data for randomly packed spheres generated by Knight et al. (2020) using DEM were used as input for the PNM analyses presented here. The DEM simulations were conducted with periodic boundary conditions along all three cartesian axes directions. Two types of PSD, linear and bimodal, were considered (Fig. 8.8). In all cases, the minimum particle diameter was 0.5 mm. For the linear PSDs, the coefficient of uniformity (Cu) was varied from 1.01 to 2.0. For the bimodal PSDs, the ratio of the coarse particle diameter to the fine particle diameter (SR) and the ratio of the volume of fine particles to the total volume of particles (FC) were varied ($SR = 2.0, 4.0$; $FC = 0.10, 0.35$). The numbers of fine particles ($N_{\mathrm{p}}^{\mathrm{F}}$) and coarse particles ($N_{\mathrm{p}}^{\mathrm{C}}$) were varied to achieve the target FC. The range of void ratios considered was between 0.468 and 1.525 for linearly graded samples and between 0.35 and 0.77 for bimodal samples, where the void ratio was varied by simulating isotropic compression. Solid fraction (ϕ) and void ratio (e) data are included in Table 8.1 and Table 8.2.

Overall flow in the z-direction was considered, and particles crossing the top maximum (z_{max}) and bottom (z_{min}) boundaries were copied to the opposite z boundary following the procedure adopted by Knight et al. (2020) and Sufian et al. (2019). When partitioning the void space, the two boundaries orthogonal to the z-direction at z_{min} and z_{max} were considered to be spheres, with a radius much larger than the sample length along z following Chareyre et al. (2012). For the weighted Delaunay triangulation adopted here, the centre of the pores including these large spheres representing the boundaries lay approximately on the relevant boundary. Constant pressure boundary conditions were considered with 1 [Pa] and 0 [Pa] applied at z_{min} and z_{max}, respectively. This constant pressure boundary condition was applied by setting the pressure of the pores including one of the large boundary spheres to the relevant boundary pressure value. In the x- and y-directions, periodic boundaries were used. Details on the implementation of the periodic boundaries are provided in Appendix D.

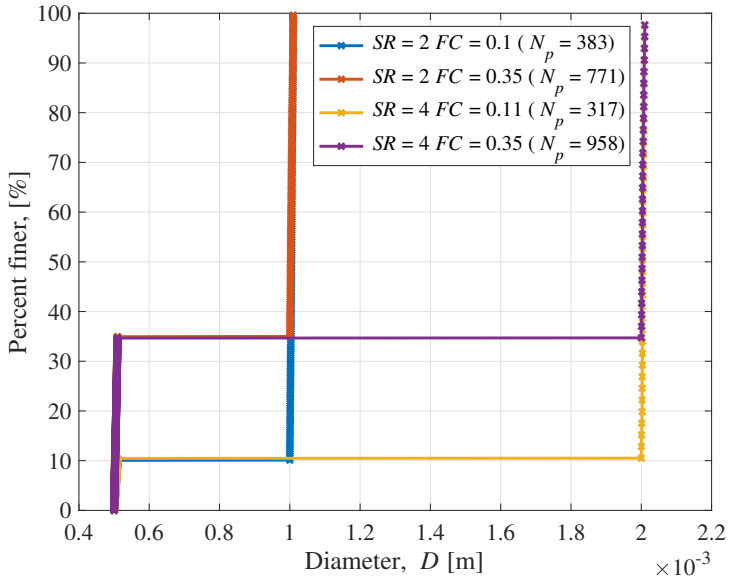
The $\alpha(e^*)$ models introduced in Section 8.3.3 were implemented in the PNM. Referring to Eq. (8.44), the e^* value of throat ab in a random packing can be calculated using the total volume of the throat ab (V_{ab}), the solid angle $\Omega_{m,ab}$ and the radius R_m of each particle m that defines the throat ab:

$$e^* = \frac{\text{Volume of the fluid phase in the throat}}{\text{Volume of thee solid phase in th throat}} = \frac{V_{ab}}{\sum_{m=1}^{3} \frac{1}{3}\Omega_{m,ab}{R_m}^3} - 1 \tag{8.46}$$

After conducting a flow simulation, the inlet flow velocity ($u_{\mathrm{inlet,PNM}}$) was calculated by summing up the total volumetric flow rate through the z_{min} and z_{max} boundary pores



(a) Linear graded PSD. Reproduced from Morimoto et al. (2022), under the terms of the CC BY 4.0 license.



(b) Bimodal PSD

Figure 8.8: PSD considered in this study for OF simulations using random packings.

Table 8.1: Linear graded samples used in OF and PNM simulations

Cu	SR	N_{p}	ϕ	e
1.01	1.02	629	0.396	1.525
			0.460	1.174
			0.519	0.927
			0.567	0.764
			0.621	0.610
			0.651	0.536
1.20	1.42	629	0.396	1.525
			0.460	1.174
			0.518	0.931
			0.567	0.764
			0.620	0.613
			0.643	0.555
1.50	2.11	491	0.408	1.451
			0.460	1.174
			0.519	0.927
			0.568	0.761
			0.621	0.610
			0.654	0.529
2.00	3.48	497	0.398	1.513
			0.449	1.227
			0.522	0.916
			0.571	0.751
			0.624	0.603
			0.681	0.468

Table 8.2: Bimodal samples used in OF and PNM simulations

SR	FC	N_{p}	$N_{\mathrm{p}}^{\mathrm{F}}$	$N_{\mathrm{p}}^{\mathrm{C}}$	ϕ	e
2.0	0.10	383	180	203	0.621	0.610
					0.656	0.524
	0.35	771	624	147	0.622	0.608
					0.673	0.486
4.0	0.11	317	279	38	0.645	0.550
					0.685	0.460
	0.35	958	930	28	0.651	0.536
					0.740	0.351

following Chareyre et al. (2012) and Sufian et al. (2019). The intrinsic permeability of the sample (in $[m^2]$) is then:

$$k_{\mathrm{h}} = \frac{u_{\mathrm{inlet,PNM}} A}{\mu_{\mathrm{f}}} \frac{\Delta p}{L} \tag{8.47}$$

where Δp is the pressure difference applied to the sample, and A and L are the cross-sectional area and the length of the sample, respectively.

8.4.3 OF simulation using random packings and post-processing

To validate the PNM, rigorously validated fully-resolved CFD simulation data were developed using `OpenFOAM` with a body-fit mesh generation technique (Knight, 2018; Knight et al., 2020; Knight, 2021). The unstructured mesh generation technique developed by Knight (2018), `MeshSpherePacking` (MSP), results in a mesh that fits to the surface of spheres in a cubic space with periodic boundaries.

The mesh generated by MSP was converted into the `polyMesh` format, which is a basic mesh format for `OpenFOAM`. In `OpenFOAM`, `SimpleFOAM`, an incompressible steady-state solver, was used to solve the continuity and momentum equations (Weller et al., 1998). For all the cases considered here periodic boundary conditions were applied in the x- and y-directions. A constant pressure boundary with a kinematic pressure value of 0 $[m^2 s^{-2}]$ was applied at the z_{max} boundary and a constant inlet velocity boundary with a velocity value of $(0, 0, u_{\mathrm{inlet}})$ was considered at z_{min} where u_{inlet} is the inlet velocity. A no-slip boundary condition was applied at the surface of each particle, i.e. the velocity of the fluid was set to zero at the surface of each particle. The initial velocity field within each mesh element was also set to be $(0, 0, u_{\mathrm{inlet}})$ and numerical iterations were conducted until the relative variations in the pressure and the velocity between two successive iterations were $< 1 \times 10^{-3}\%$. The pressure field and the velocity field were output for post-processing.

The MSP-OpenFOAM framework was validated by considering FCC packings of uniform spheres and by comparing the results in terms of drag coefficient (c_{d}) values with data from the study by Zick and Homsy (1982). This approach to the validation of the CFD technique in terms of c_{d} follows those adopted in previous studies (Knight et al., 2020; Zhao & O'Sullivan, 2022). The validation confirms that the adopted approach can correctly capture permeability and fluid-particle interactions given an adequate resolution of discretization.Hereinafter, we denote a fully-resolved CFD simulation using `OpenFOAM` as an OF simulation.

In the OF simulations of the FCC packing, 5 layers of 2 particles were considered as shown in Fig. 8.9(a). If the distance between the particle centroids is Δ, the diameter of the

particles, D, was varied from 0.8Δ to Δ, to give $0.350 < e < 1.637$, where e is the void ratio. The positions and diameters of the particles were input to MSP. The ratio of D to the mesh length (ds_c), which is illustrated in Fig. 8.9(b), was varied from 20 to 50 to examine the effect of element size on the data generated. The fluid-particle interaction force on the central particle was exported from `OpenFOAM` using the built-in function `forces`, which calculates the pressure gradient force vector $\mathbf{F}^{\mathrm{p}}$ and the viscous drag force vector $\mathbf{F}^{\mathrm{d}}$ as:

$$\mathbf{F}^{\mathrm{p}} = \sum_k \rho_k \mathbf{s}_k p_k \tag{8.48}$$

$$\mathbf{F}^{\mathrm{d}} = \sum_k \mathbf{s}_k \mu_{\mathrm{f}} \sigma_{\mathrm{dev}} \tag{8.49}$$

where $\mathbf{s}_k$ is the face area vector at face k representing the particle surface and σ_{dev} is the deviatoric stress tensor. The fluid-particle interaction force $\mathbf{F}^{f\to p}$ is the summation of $\mathbf{F}^{\mathrm{p}}$ and $\mathbf{F}^{\mathrm{d}}$. The c_{d} value was calculated following Eq. (8.17) using the magnitude of the calculated $\mathbf{F}^{f\to p}$. The OF simulation results are compared with the Zick and Homsy data in Fig. 8.10. With $D/ds_c = 20$, the OF simulation underestimated c_{d} for the denser packings, however for $D/ds_c = 30$, the error is $\leq 12\%$ for a wide range of void ratios ($0.350 < e < 1.637$). Following Eq. (8.20), accurately predicting c_{d} is equivalent to accurately predicting the permeability. The relative error is relatively small considering the large range of void ratio values and similar to the error level documented in previous studies e.g. Knight et al. (2020). Thus $D/ds_c = 30$ was also used for the detailed analyses presented here. For a random packing, ds_c was taken as $D_{\mathrm{min}}/30$, where D_{min} is the minimum particle diameter. Note that the conductance models developed in this study are based on the analytical data by Zick and Homsy (1982) and therefore do not depend on the mesh quality of the OF simulations.

The same random packings considered in the PNM (Section 8.4.2) were used as inputs to MSP for subsequent OF simulations. A typical OF model indicating local velocity data is shown in Fig. 8.11. As in the PNM, any sphere crossing the periodic boundaries at z_{max} or z_{min} boundary was copied to the opposite boundary. After copying the particles, the mesh for the packings was generated using MSP and an OF simulation followed.

The "true" Γ value of the throats in random packings was calculated usig the following procedure. The weighted Delaunay triangulation information, namely the IDs of particles defining pores, the Voronoi vertices of pores and pore connections, was output from the PNM. To obtain the "true" Γ value of each throat, the volumetric flow rate vector through the throat face (in $[(m^3s^{-1}, m^3s^{-1}, m^3s^{-1})]$) and the pressure gradient within the throat was interpolated using `ParaView` (Ahrens, Geveci & Law, 2005). The mesh geometry,

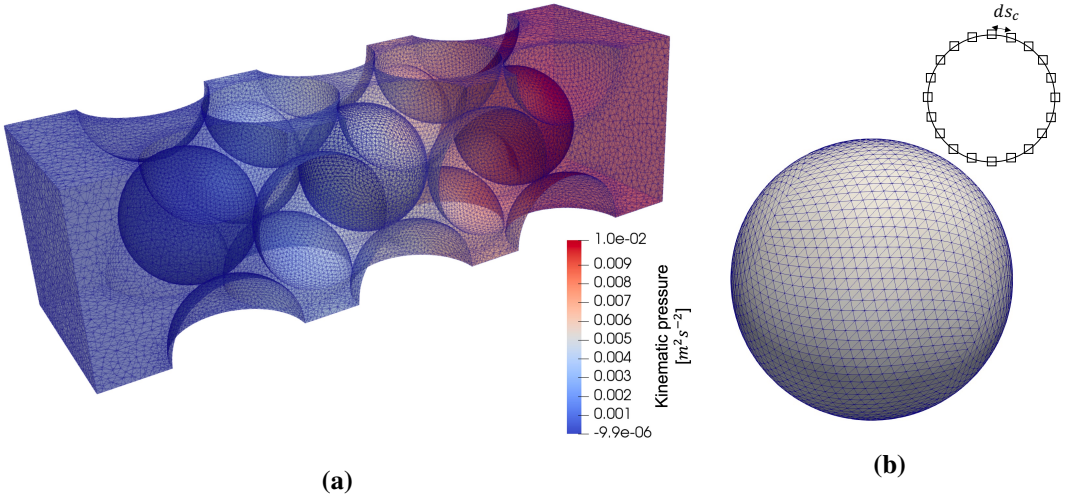


Figure 8.9: Schematic illustration of OF simulations using FCC packings for validation. (a) The geometry of an FCC model and the pressure distribution (b) Mesh seeds on a sphere surface ($D_{\min}/30$) and the definition of ds_c. Reproduced from Morimoto et al. (2022), under the terms of the CC BY 4.0 license.

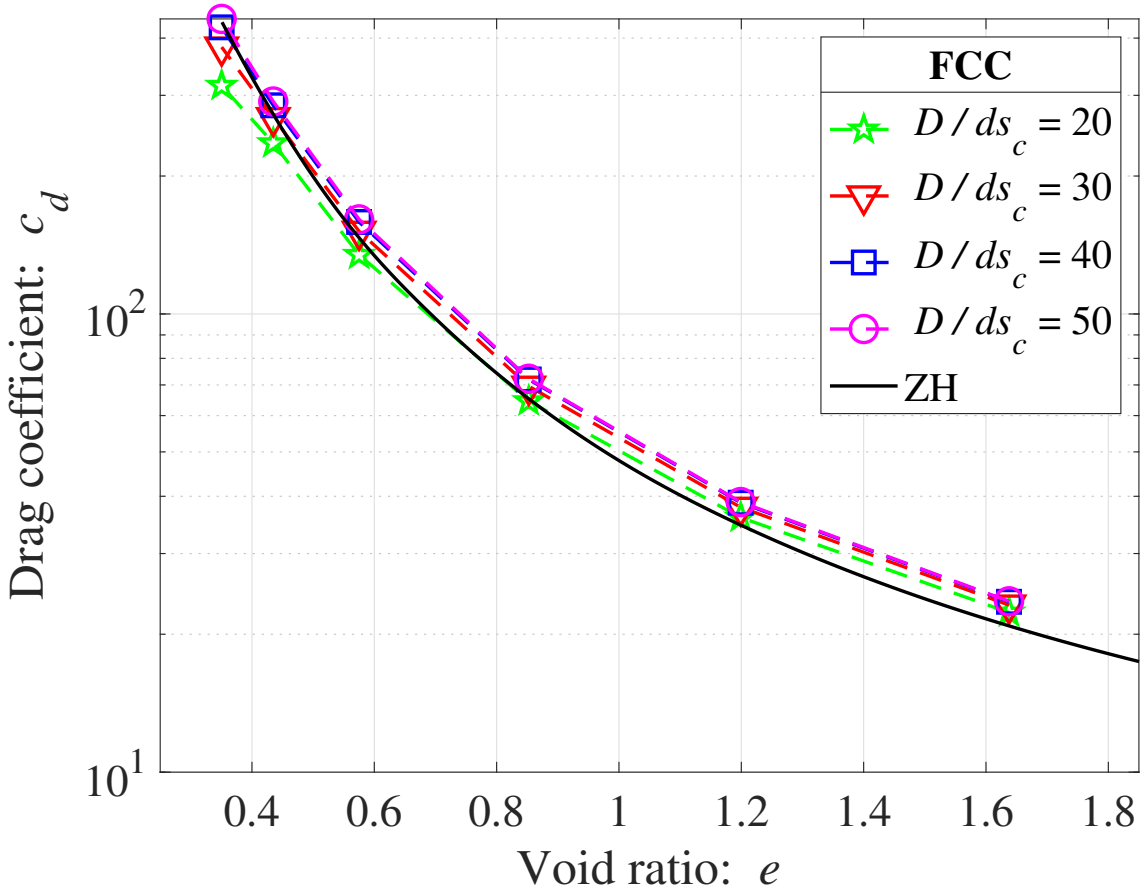


Figure 8.10: Validation of OF study results in terms of c_{d} versus e using FCC packings. Reproduced from Morimoto et al. (2022), under the terms of the CC BY 4.0 license.

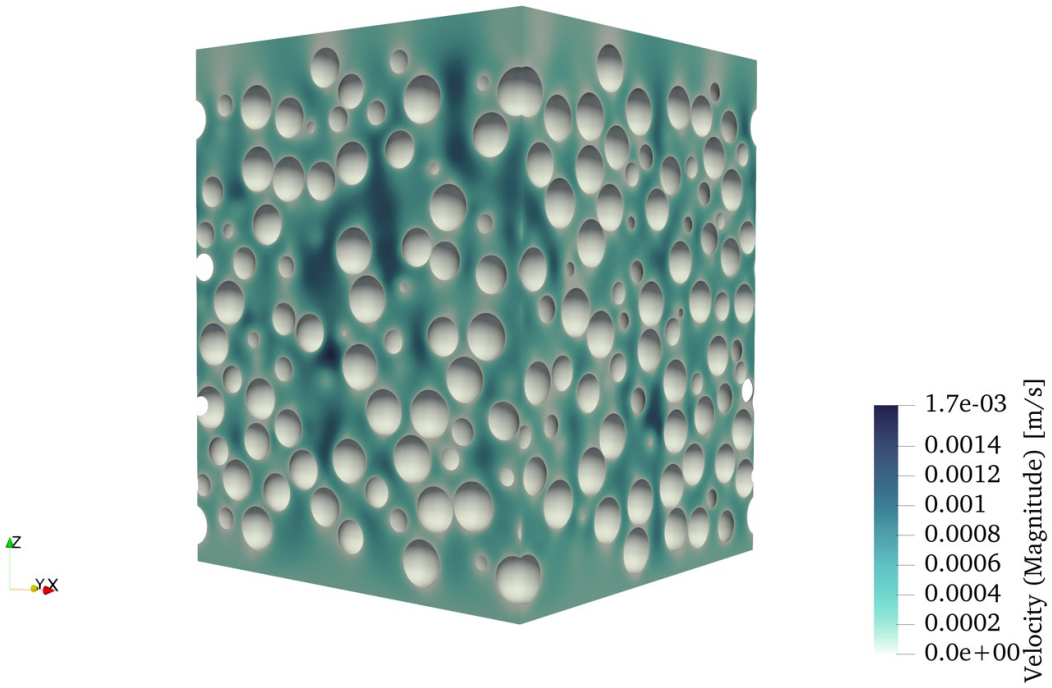


Figure 8.11: Geometry of a random packing OF model with a flow velocity field ($Cu = 1.01$, $e = 1.525$). Reproduced from Morimoto et al. (2022), under the terms of the CC BY 4.0 license.

flow field, and pressure field were output from `OpenFOAM` in the `vtk` format. The mesh on the throat face was extracted from the `vtk` file using the `clip` and `slice` functions in `ParaView` and the total volume flow rate vector through the meshes was interpolated using the `integrateVariables` function. The pressures at pore centres a and b (p_a and p_b) were interpolated using the `ProbeLocation` function. For each pore connection, the volume flow rate vector and the pressures at the centres of the connected pores (p_a and p_b in Eq. (8.2)) are available. The magnitude of the volume flow rate vector was used for Q_{ab} in Eq. (8.2) and the "true" Γ_{ab} value was back-calculated, using Eqs. (8.39) to (8.41):

$$\Gamma_{ab} = \frac{Q_{ab} L_{ab}}{p_a - p_b} \mu_{\mathrm{f}} \tag{8.50}$$

Faces crossing a periodic boundary, which account for at most 20% of the total number of faces, were not considered in the detailed analysis due to a technical difficulty associated with interpolating the volume flow rate through such faces.

The particle-fluid interaction force vector $\mathbf{F}^{f \to p}$ on each particle was extracted using the built-in function `forces` in OpenFOAM similarly to the validation study. The $\mathbf{F}^{f \to p}$ values on the particles crossing the periodic boundaries at z_{max} and z_{min} were not considered in this study as the flow around the particles is not fully-developed.

8.4.4 Empirical calculation of fluid-particle interaction force

In a coarse-grid CFD-DEM model, unlike the case where coupling is achieved using fully-resolved CFD or a PNM, the local pressure gradient field of the fluid surrounding each particle cannot be obtained, with the fluid-particle interaction force being calculated using an empirical drag coefficient. To calculate the fluid-particle interaction force on particle m in a coarse-grid CFD, this force, $\mathbf{F}_m^{f\rightarrow p,CG}$, is split into the "coarse-grid" pressure gradient force ($\mathbf{F}_m^{p,CG}$) and the "coarse-grid" viscous drag force ($\mathbf{F}_m^{d,CG}$).

$$\mathbf{F}_m^{f\rightarrow p,CG} = \mathbf{F}_m^{p,CG} + \mathbf{F}_m^{d,CG} \tag{8.51}$$

$\mathbf{F}_m^{p,CG}$ can be related to the pressure gradient field of the coarse grid cell (∇p) and the volume of the particle m (V_m):

$$\mathbf{F}_m^{p,CG} = -V_m \nabla p \tag{8.52}$$

In this study, the $\mathbf{F}_m^{p,CG}$ is referred to as the "coarse-grid" pressure gradient force since this definition ignores the variability of the direction of the local pressure drop. It is not equivalent to the pressure gradient forces obtained from a fully-resolved CFD or a PNM in this study.

The other force term in $\mathbf{F}_m^{d,CG}$ is determined using an empirical expression such as those proposed by Ergun (1952), Di Felice (1994), Tenneti, Garg and Subramaniam (2011), and Tang et al. (2015). These models give expressions for the "normalised" viscous drag force defined as:

$$\overline{\mathbf{F}_m^{d,CG}} = \frac{\mathbf{F}_m^{d,CG}}{F_m^{\text{Stokes}}} \tag{8.53}$$

where the Stokes force F^{Stokes} is defined in Eq. (8.18). Most of the empirical expressions relate $\overline{\mathbf{F}_m^{d,CG}}$ to the packing density and the Reynolds number (Re). For example, Ergun (1952)'s empirical relation reads:

$$\overline{F^{\text{d},CG,Ergun}} = \frac{150\phi + 1.75Re}{18(1-\phi)^2} \tag{8.54}$$

Even though the term F_m^{Stokes} includes the particle diameter, previous fully-resolved CFD simulations (van der Hoef, Beetstra & Kuipers, 2005; Beetstra, van der Hoef & Kuipers, 2007; Sarkar, van der Hoef & Kuipers, 2009; Knight et al., 2020) suggest that the normalised viscous drag force includes the effect of the particle size. While, the Ergun (1952)

expression does not consider any particle size effect, van der Hoef, Beetstra and Kuipers (2005) have proposed a function relating the viscous drag force on a particle in polydisperse sample to a normalised viscous drag force on a particle in monodisperse sample with the same solid fraction (ϕ):

$$\mathbf{F}_m^{d,CG} = [y_m + 0.064{y_m}^3]\overline{F^{d,CG}}(\phi, Re)F^{\text{Stokes}}\frac{\mathbf{u}_{\text{inlet}}}{\|\mathbf{u}_{\text{inlet}}\|} \tag{8.55}$$

where

$$x_m = \frac{V_m}{\sum_{k=1}^{N_\text{p}} V_k}, y_m = \frac{D_m}{\langle D\rangle}, \langle D\rangle = \left[\sum_{k=1}^{N_\text{p}} \frac{x_k}{D_k}\right] \tag{8.56}$$

where D_m is the diameter of particle k. The efficacy of the expressions was confirmed for bi-modal and polydisperse samples using the LBM data obtained by van der Hoef, Beetstra and Kuipers (2005), Beetstra, van der Hoef and Kuipers (2007), and Sarkar, van der Hoef and Kuipers (2009). Here, $\mathbf{F}_m^{d,CG}$ is used to deote the "coarse-grid" viscous drag force because van der Hoef, Beetstra and Kuipers (2005) obtained $\mathbf{F}_m^{d,CG}$ by multiplying the total fluid-particle interaction force vector $\mathbf{F}^{f\to p}$ obtained from their LBM simulation by $1-\phi$ ($\mathbf{F}_m^{d,CG} = (1-\phi)\mathbf{F}^{f\to p}$), thus $\mathbf{F}_m^{d,CG}$ is not equivalent to the viscous drag force obtained by integrating the shear force on the surface of the particle.

As discussed above, both $\mathbf{F}^\text{p}$ and $\mathbf{F}_m^{p,CG}$ and $\mathbf{F}^\text{d}$ and $\mathbf{F}_m^{d,CG}$ conceptually differ; therefore, this study compares the total fluid-particle interaction force ($\mathbf{F}^\text{p} + \mathbf{F}^\text{d}$ or $\mathbf{F}_m^{p,CG} + \mathbf{F}_m^{d,CG}$) obtained from the OF simulation, PNM simulations with a variety of local conductance models, and empirical force calculation. In this study, the magnitude of $\mathbf{F}_m^{p,CG}$ (Eq. (8.52)) was calculated using the pressure drop over the sample (Δp) in the flow direction obtained from the OF simulation and the sample length (L) as:

$$\|\mathbf{F}_m^{p,CG}\| = V_m\frac{\Delta p}{L} \tag{8.57}$$

The magnitude of $\mathbf{F}_m^{d,CG}$ was obtained following Eqs. (8.53) to (8.56); namely,

$$\|\mathbf{F}_m^{d,CG}\| = [y_m + 0.064{y_m}^3]\overline{F^{d,CG,Ergun}}(\phi, Re)[3\pi\mu_\text{f}D_m u_\text{OF}] \tag{8.58}$$

where u_OF is the inlet velocity specified in the OF simulation. The magnitude of the total fluid-particle interaction force is the summation of $\|\mathbf{F}_m^{p,CG}\|$ and $\|\mathbf{F}_m^{d,CG}\|$, and then normalised fluid-particle interaction force is defined as:

$$\overline{\mathbf{F}_m^{f\to p,CG}} = \frac{\|\mathbf{F}_m^{p,CG}\| + \|\mathbf{F}_m^{d,CG}\|}{3\pi\mu_{\mathrm{f}} D_m u_{\mathrm{OF}}} \tag{8.59}$$

8.5 Analysis of PNM performance for randomly packed spheres

8.5.1 Analysis of local flow direction

The direction of flow between a pair of adjacent pores in a PNM is assumed to be parallel to the vector from the centre of a pore to the centre of the other connected pore. Hitherto the validity of this assumption has not been thoroughly investigated. The pore centre locations determine the flow direction in the PNM, and two definitions were considered here; (1) use of Voronoi vertices following Chareyre et al. (2012) (denoted as the *VV* method) and (2) use of the centroids of the pore cells e.g. Sufian et al. (2019) (denoted as the *CC* method). Where the *VV* method is used, the vector is always normal to the throat face.

If the angle between the PNM flow vector and the OF flow vector through a face is $\theta^{\mathbf{q}}$ ($0 \leq \theta^{\mathbf{q}} \leq \pi/2$) (Fig. 8.12), the PNM correctly predicts the flow direction at the throat if $\theta^{\mathbf{q}} = 0$, while $\theta^{\mathbf{q}} \neq 0$ indicates a discrepancy. The distributions of $\theta^{\mathbf{q}}$ in two random packings ($e = 1.525$ and 0.536 with $Cu = 1.01$) obtained using the *VV* and *CC* methods are shown in Fig. 8.13. For the dilute packing ($e = 1.525$, Fig. 8.13(a)) neither method correctly captures the flow direction. A typical throat whose flow direction is not accurately predicted by the PNM is shown in Fig. 8.14. In these cases, the three face particles do not form a closed loop and the largest gap in the loop is orthogonal to the flow direction. For a dense packing ($e = 0.536$, Fig. 8.13 (b)), the *VV* method exhibited a good performance, with an obvious peak in the distribution of $\theta^{\mathbf{q}}$ at $\theta^{\mathbf{q}} = 0$. However, the *CC* method still does not effectively capture the flow direction.

A tabular summary of the analysis of the $\theta^{\mathbf{q}}$ values for all the packings considered is provided in Table 8.3. ${\theta^{\mathbf{q}}}_{peak}$ is defined as the $\theta^{\mathbf{q}}$ value which has the most data points considering a histogram with 32 bins ($(n-1)\pi/64 \leq \theta^{\mathbf{q}} \leq n\pi/64$). The mean $\theta^{\mathbf{q}}$ values (${\theta^{\mathbf{q}}}_{mean}$), the standard deviations ($SD_{\theta^{\mathbf{q}}}$) and the proportion of $\theta^{\mathbf{q}}$ values with $\theta^{\mathbf{q}} \leq \pi/4$ (denoted as $\Pi(\theta^{\mathbf{q}} \leq \pi/4)$) are also shown. In all cases, the *VV* approach has a superior performance based on all the accuracy measures (${\theta^{\mathbf{q}}}_{peak}$, ${\theta^{\mathbf{q}}}_{mean}$, and $\Pi(\theta^{\mathbf{q}} \leq \pi/4)$) when compared with the *CC* approach. Where the *VV* approach is used, $\Pi(\theta^{\mathbf{q}} \leq \pi/4)$ values of up to 75% are attained, however this decreases with reducing sample density (i.e. increasing void ratio). In general, while these data indicate that the denser samples are better suited to simulations using a PNM, with the *VV* method being the preferable approach, the results suggest that flow in a dilute system should not be simulated using

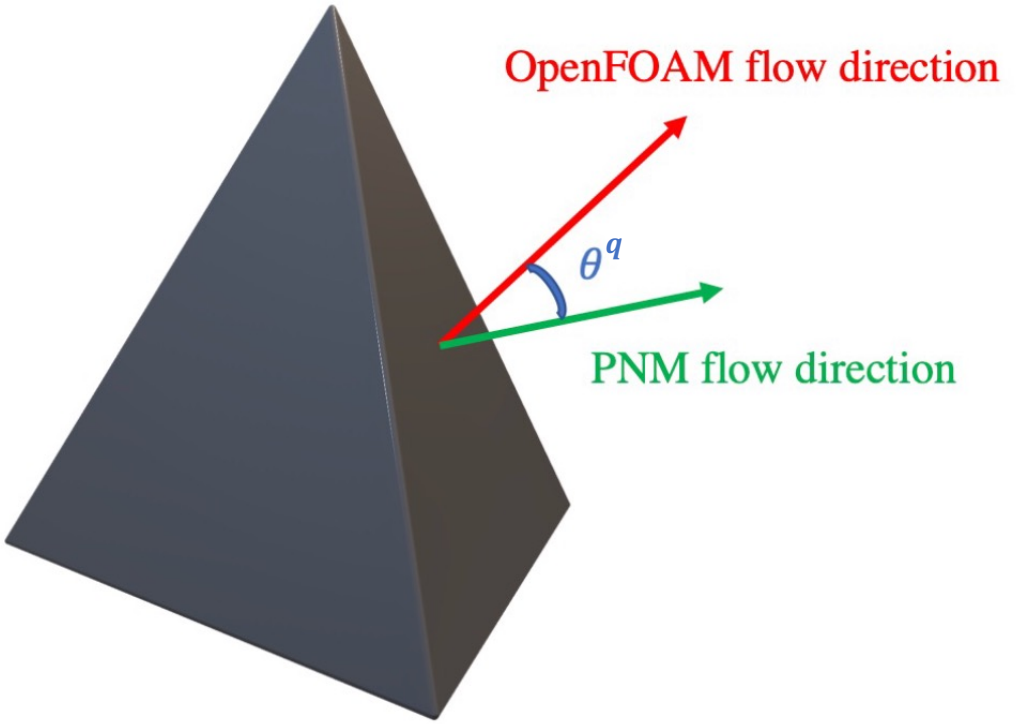
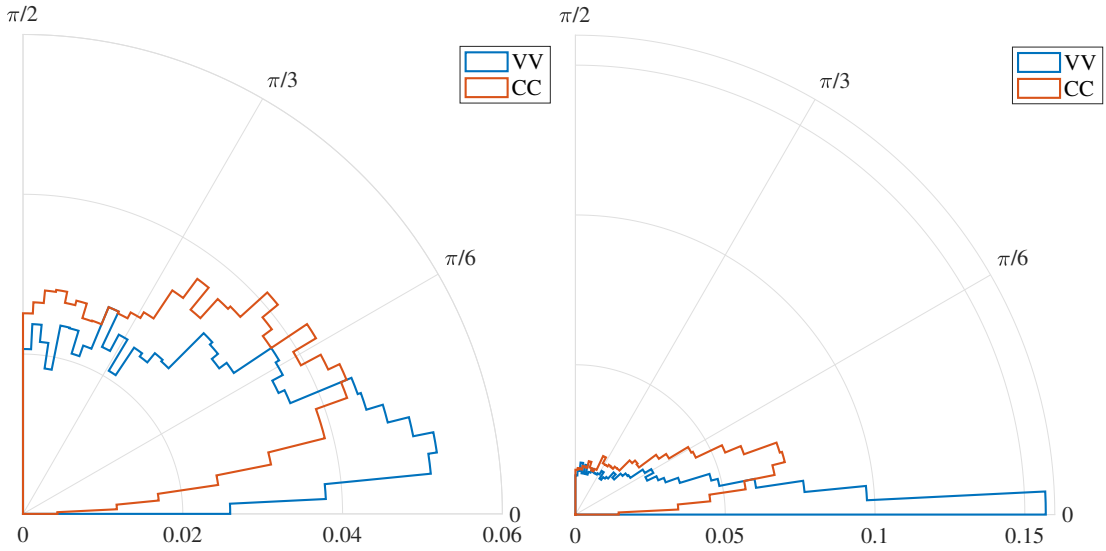


Figure 8.12: Schematic illustration on the definition of $\theta^{\mathbf{q}}$. Reproduced from Morimoto et al. (2022), under the terms of the CC BY 4.0 license.



(a) $Cu = 1.01$, $e = 1.525$. **(b)** $Cu = 1.01$, $e = 0.536$.

Figure 8.13: Distribution of $\theta^{\mathbf{q}}$. Reproduced from Morimoto et al. (2022), under the terms of the CC BY 4.0 license.

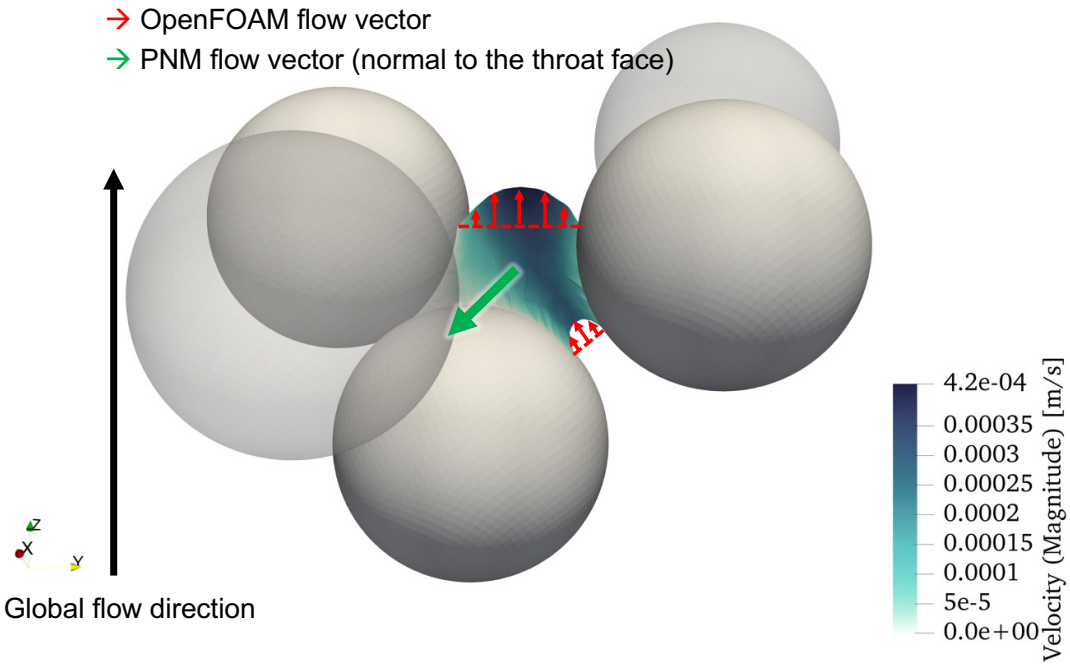


Figure 8.14: An example of faces whose flow direction a PNM failed to capture. Face geometry was transformed based on the OF flow vector, which shows that the flow is not normal to the throat face. Reproduced from Morimoto et al. (2022), under the terms of the CC BY 4.0 license.

a PNM. Based on these analyses, hereinafter we only consider the *VV* approach and packed granular systems which are dense enough to transmit forces. To get an indication of the likely range of relevant void ratios we considered some prior studies: in their DEM simulations of isotropically compressed spheres, Shire and O'Sullivan (2016) found that $0.558 < e < 0.714$ for $Cu = 1.2$ and $0.467 < e < 0.555$ for $Cu = 2.0$; for monodispersed spheres ($Cu = 1.0$), Song, Wang and Makse (2008) stated that e_{max} is approximately 0.82 if an infinite friction coefficient is considered and e_{min} is approximately 0.58; for natural sands, higher e_{min} and e_{max} values are observed due to the rolling resistance that arises at contacts between non-spherical particles e.g. Nevada sand ($Cu = 1.8$; $e_{\text{max}} = 0.850$; $e_{\text{min}} = 0.570$), Ticino sand ($Cu = 1.5$; $e_{\text{max}} = 0.990$; $e_{\text{min}} = 0.574$) (Cho, Dodds & Santamarina, 2006). Considering these studies, we restrict consideration to packings with $e < 0.80$ hereinafter.

Fig. 8.15(a) compares the local flow rates (Q^*) for each edge normalized by the global flow rate (Q) obtained from an OF simulation and a PNM simulation using the *HR* model for the assembly with $Cu = 1.01$ and $e = 0.536$. Each data point is coloured by the edge $\theta^{\mathbf{q}}$ value. The ratio of the PNM data to the OF data tends to decrease as $\theta^{\mathbf{q}}$ increases. For a high $\theta^{\mathbf{q}}$, the pressure gradient at the throat is not orthogonal to the throat face and the PNM tends to underestimate the pressure gradient and thus the volumetric flow rate. Fig. 8.15(b)

Table 8.3: Tabular summary of distributions of $\theta^{\mathfrak{q}}$ values for various packings.

Cu	e	*VV* (Voronoi vertex approach)				*CC* (Cell centroid approach)			
		$\theta^{\mathfrak{q}}{}_{\text{peak}}$ [rad]	$\theta^{\mathfrak{q}}{}_{\text{mean}}$ [rad]	$SD_{\theta^{\mathfrak{q}}}$ [rad]	$\Pi(\theta^{\mathfrak{q}} \leq \frac{\pi}{4})$ [%]	$\theta^{\mathfrak{q}}{}_{\text{peak}}$ [rad]	$\theta^{\mathfrak{q}}{}_{\text{mean}}$ [rad]	$SD_{\theta^{\mathfrak{q}}}$ [rad]	$\Pi(\theta^{\mathfrak{q}} \leq \frac{\pi}{4})$ [%]
1.01	1.525	0.15	0.67	0.44	62.5	0.39	0.78	0.41	53.3
	1.174	0.15	0.63	0.44	65.2	0.44	0.74	0.41	57.4
	0.927	0.15	0.60	0.45	67.0	0.29	0.69	0.41	61.9
	0.764	0.05	0.56	0.44	70.0	0.25	0.65	0.41	65.7
	0.610	0.00	0.51	0.45	73.4	0.29	0.61	0.41	69.4
	0.536	0.00	0.48	0.45	75.1	0.25	0.59	0.41	71.3
1.2	1.525	0.10	0.66	0.44	63.2	0.34	0.79	0.41	53.0
	1.174	0.10	0.61	0.44	66.8	0.39	0.75	0.41	56.6
	0.931	0.10	0.58	0.45	68.8	0.39	0.72	0.41	60.4
	0.764	0.00	0.55	0.45	70.7	0.34	0.68	0.41	63.4
	0.613	0.00	0.51	0.46	72.9	0.20	0.63	0.42	67.7
	0.555	0.00	0.49	0.45	74.7	0.25	0.60	0.41	70.5
1.5	1.451	0.10	0.65	0.44	62.8	0.59	0.79	0.40	52.9
	1.174	0.15	0.62	0.45	65.3	0.44	0.76	0.41	56.4
	0.927	0.05	0.59	0.45	68.5	0.44	0.72	0.40	59.8
	0.761	0.05	0.56	0.45	70.7	0.29	0.69	0.41	63.0
	0.610	0.00	0.52	0.46	72.0	0.29	0.63	0.42	66.8
	0.529	0.00	0.48	0.45	74.5	0.20	0.61	0.41	69.5
2.0	1.513	0.20	0.69	0.44	60.1	0.44	0.81	0.41	49.9
	1.227	0.20	0.65	0.45	62.3	0.39	0.79	0.41	52.4
	0.916	0.05	0.61	0.45	66.2	0.29	0.75	0.41	56.6
	0.751	0.05	0.59	0.46	67.6	0.34	0.71	0.42	61.0
	0.603	0.00	0.56	0.46	70.3	0.29	0.67	0.42	64.4
	0.468	0.00	0.48	0.46	74.8	0.25	0.60	0.42	69.8

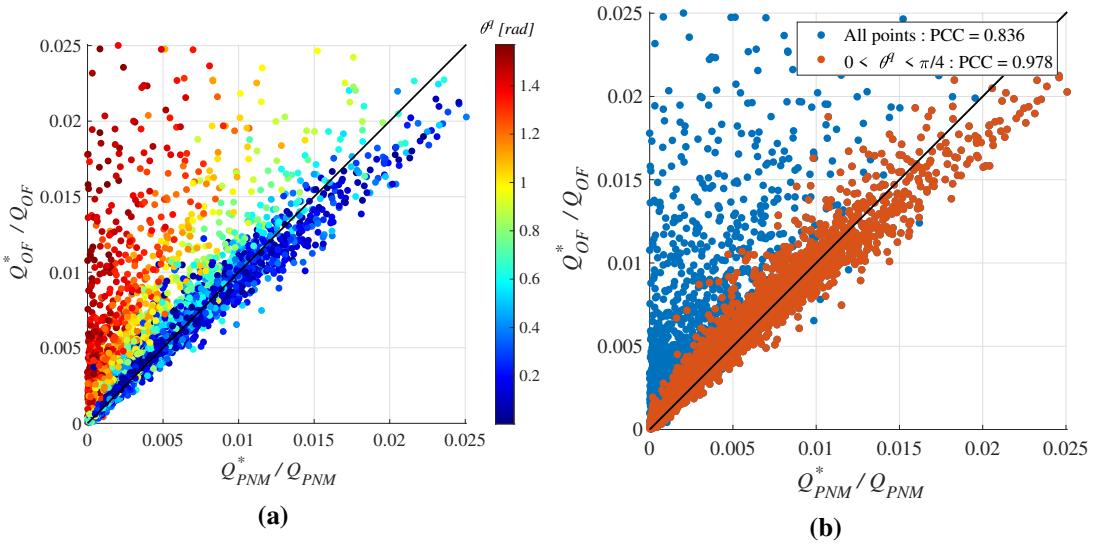


Figure 8.15: Comparison of normalized local volume flow rate (in $[m^3 s^{-1}]$) between OF and PNM (*HR* model with $\alpha_{\text{HR}} = 1/8$) for a packing with $Cu = 1.01$ and $e = 0.536$. (a) Coloured by $\theta^{\mathbf{q}}$ values. (b) Markers with $0 < \theta^{\mathbf{q}} < \pi/4$ are highlighted. Reproduced from Morimoto et al. (2022), under the terms of the CC BY 4.0 license.

considers the same data as in Fig. 8.15(a) but a binary approach was used to isolate data points with $\theta^{\mathbf{q}} \leq \pi/4$. Following Sufian et al. (2019), the correlation between the OF and PNM Q^* values was quantified using Pearson correlation coefficient values for all data and for data with $\theta^{\mathbf{q}} \leq \pi/4$. With $\theta^{\mathbf{q}} \leq \pi/4$, the correlation between normalized flow rate in PNM and OF was confirmed with a Pearson coefficient of 0.978. For all data, the Pearson coefficient decreased to 0.836; however, this is better than either of the models proposed by Sufian et al. (2019). The improvement in accuracy can be attributed to use of the *VV* approach instead of the *CC* approach. In short, the PNM shows a good performance for flow when the $\theta^{\mathbf{q}}$ value is close to zero and the proportion of edges with a $\theta^{\mathbf{q}}$ which is close to zero is the key determinant of the validity of a PNM framework.

8.5.2 α values in monodisperse packing

In Section 8.3.3, we developed an expression for α as a function of e^* or ξ, using three types of regular packings. However, in random packings, the geometry of the throats is much more heterogeneous than in regular packings. Here we consider the applicability of the developed model to random packings. Exploiting the OF simulation data, "true" α values for each conductance model introduced in Section 8.2.2, except for the *FA* model, were back-calculated adopting the approach used in the analytical study described in Section 8.3.3. Only throats whose $\theta^{\mathbf{q}}$ value is smaller than $\pi/4$ were considered in this section, so that we only considered the throats where a PNM approach can reasonably capture the flow direction, as there is limited value in assessing conductance models for

local topologies that cannot be reasonably approximated by a pair of nodes connected by an edge.

Fig. 8.16 shows relationships between the α value obtained in OF and the local void ratio (e^*) for each throat in the specimen with $Cu = 1.01$ and $e = 0.764$ for the ***ER***, ***HR***, ***HR4***, and ***ER-HR*** models. The α values calculated using the Zick and Homsy (1982) dataset for SC, BCC, and FCC packings are also plotted. Each data point is coloured based on the maximum angle of the throat face ($\theta^{\text{tri}}_{\text{max}}$) (defined in Fig. 8.5) to assess the sensitivity to changes in the face geometry. For each of the ***HR***, ***HR4***, and ***ER-HR*** models, non-linear least squares (LSQ) fitting was employed assuming that the optimal α value takes the following form:

$$\alpha^{LSQ}_{\text{XX}}(e^*) = X_1\left(\frac{1}{1+e^*}\right)^3 + X_2\left(\frac{1}{1+e^*}\right)^2 + X_3\left(\frac{1}{1+e^*}\right) \tag{8.60}$$

and the best fit curves obtained are included in Fig. 8.16(b-d). The X_1, X_2, and X_3 obtained by LSQ curve fitting (Eq. (8.60)) to the OF data are presented in Table 8.4. The Pearson's correlation coefficients (PCC) obtained by comparing predictions by the analytical models (Eq. (8.39) – Eq. (8.41)) or LSQ fit (Eq. (8.60)) and the OF data are also shown in the legends in Fig. 8.16(b-d).

There is a large scatter and no clear trend between α and e^* for the ***ER*** model (Fig. 8.16(a)); however, as shown in Fig. 8.16(b–d), for the ***HR***, ***HR4***, and ***ER-HR*** models, which all contain a r_{h} term, the α value back-calculated from the OF simulations decreases as e^* increases. These data do not support the constant α approach proposed in Chareyre et al. (2012) and agree with the observations made in the analytical study above (Fig. 8.6). In Fig. 8.16 (b-d), the results for the ***HR*** model (Fig. 8.16(b)) show a relatively large scatter. In effect, considering the colour of the data points, this scatter can be attributed to the oversimplification arising from using the A_{f} term to represent the face geometry as discussed in Section 8.3.3. On the other hand, the results for the ***HR4*** and ***ER-HR*** models exhibit less scatter, which support using these models with $\alpha(e^*)$ models for random packings. For the ***HR4*** and ***ER-HR*** models, the overall trend of the analytical $\alpha_{\text{XX}}(e^*)$ model and the LSQ curve agree well and there is a very small difference between the PCC values of the analytical model and LSQ fit.

Fig. 8.17 plots $\alpha_{\text{ER-HR}}$ against ξ, instead of e^*, to assess the performance of the $\alpha_{\text{ER-HR}}(\xi)$ model introduced in Eq. (8.42). The $\alpha_{\text{ER-HR}}$ value from the OF simulations has a negative correlation with ξ and the $\alpha - \xi$ relationship obtained from the analytical study captures the trend well. The PCC value for the $\alpha_{\text{ER-HR}}(\xi)$ model ($PCC = 0.782$) is slightly lower than those for the $\alpha_{\text{ER-HR}}(e^*)$ ($PCC = 0.822$) and $\alpha_{\text{HR4}}(e^*)$ ($PCC = 0.839$) models but better than that of $\alpha_{\text{HR}}(e^*)$ ($PCC = 0.458$).

Table 8.4: Tabular summary of X_1, X_2 and X_3 values in Eq. (8.60) for a variety of packings.

		HR			*HR4*			*ER-HR*		
Cu	e	X_1	X_2	X_3	X_1	X_2	X_3	X_1	X_2	X_3
	0.764	-0.212	0.186	0.134	0.102	0.064	0.146	0.288	-0.010	0.020
1.01	0.61	-0.140	0.102	0.165	0.142	0.051	0.138	0.509	-0.260	0.094
	0.536	-0.097	0.119	0.158	0.412	-0.196	0.202	0.842	-0.596	0.187
	0.764	-0.849	0.869	-0.034	-0.051	0.211	0.114	-0.115	0.415	-0.088
1.2	0.613	-0.626	0.653	0.020	0.033	0.138	0.128	0.165	0.135	-0.016
	0.555	-0.405	0.467	0.062	0.183	0.034	0.146	0.556	-0.269	0.093
	0.761	-0.822	0.838	-0.028	-0.182	0.334	0.081	-0.116	0.414	-0.091
1.5	0.61	-0.520	0.480	0.081	-0.039	0.169	0.130	0.157	0.108	-0.002
	0.529	-0.548	0.624	0.017	0.033	0.185	0.101	0.528	-0.257	0.090
	0.751	-0.423	0.371	0.098	0.035	0.037	0.167	0.057	0.189	-0.030
2.0	0.603	-0.226	0.151	0.162	0.091	-0.029	0.190	0.288	-0.044	0.030
	0.468	-0.172	0.145	0.160	0.164	-0.044	0.182	0.697	-0.490	0.156

For the densest packing with $Cu = 1.01$ ($e = 0.536$), a similar result is obtained as shown in Fig. 8.18 ($\alpha - e^*$ relationship) and Fig. 8.19 ($\alpha - \xi$ relationship).

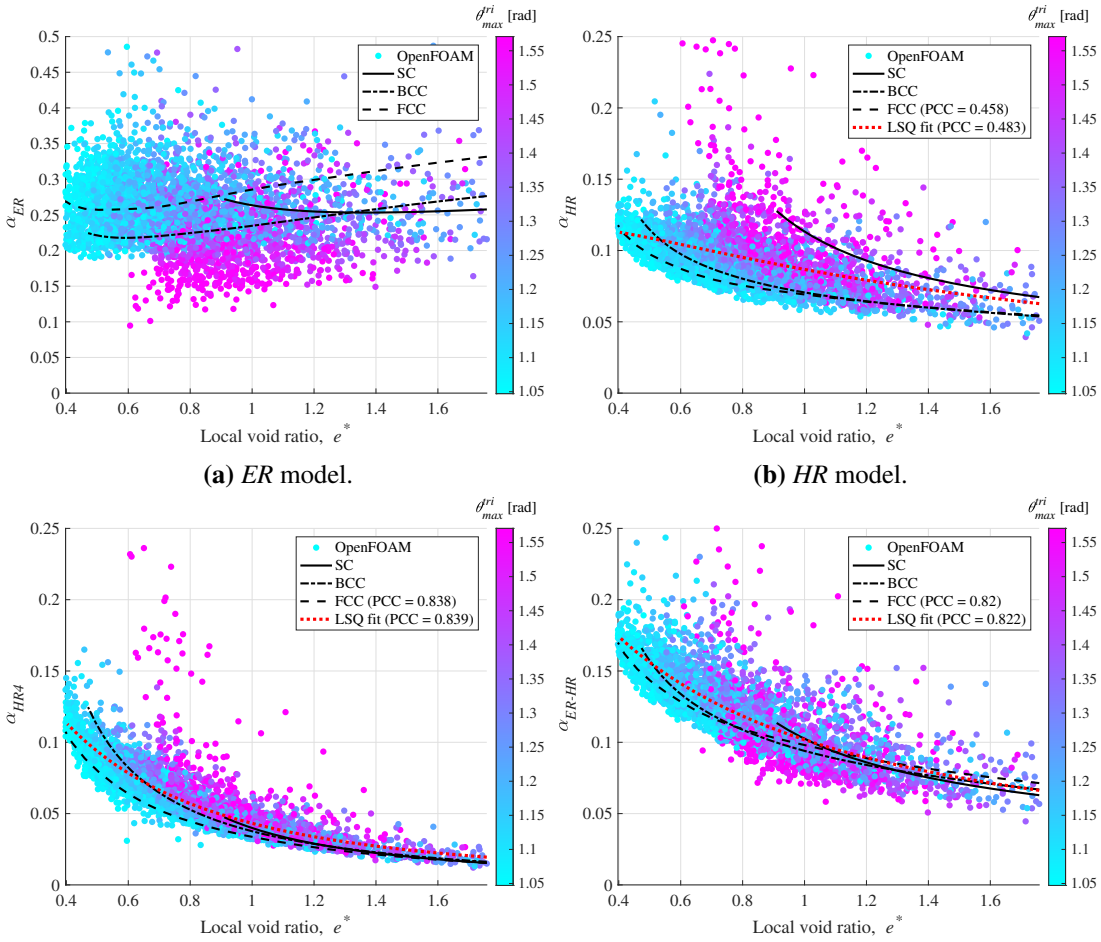
More detailed analysis to understand the poor performance of the *ER* model, was carried out using Fig. 8.20, where each marker for the *ER* model is coloured based on the normalized throat length defined as L_{ab}/r_{eff} instead of $\theta^{\text{tri}}_{\text{max}}$. The results show that the *ER* model is sensitive to the throat length. This length dependency arises because the throat cross-sectional area varies along the throat length so that if the length of the throat increases, the cross-sectional area at the end of the throat also increases.

8.5.3 α values in linearly graded packing

The analyses of the lattice configurations could not consider the effects of polydispersity. To understand the influence of polydispersity on the proposed $\alpha(e^*)$ model, the packings with $Cu = 2.00$, the most polydisperse cases amongst the linearly graded samples considered in this study, were considered. The resulting data are presented in Fig. 8.21 (α versus e^*) - Fig. 8.22 (α versus ξ) for $e = 0.751$ and Fig. 8.23 (α versus e^*) - Fig. 8.24 (α versus ξ) for $e = 0.468$. For both cases, the prediction of α values made by the proposed $\alpha(e^*)$ or $\alpha(\xi)$ expressions capture the general trend where the *HR4* and *ER-HR* models are used.

Fig. 8.25 is the same plot as Fig. 8.23(a) but each data point is coloured based on L_{ab}/r_{eff}. The sensitivity of the *ER* model to changes in the length of the throat is again evident.

A tabular summary of the PCC and R^2 values for both the analytical model (Eqs. (8.39) to (8.41)) and the LSQ best-fit equation is provided in Table 8.5. For the range of Cu and



(a) *ER* model. **(b)** *HR* model.

(c) *HR4* model. **(d)** *ER-HR* model.

Figure 8.16: Variation in α with e^*: comparison of an OF simulation and analytical models for $Cu = 1.01$ and $e = 0.764$. Marker colour gives the maximum angle of the throat face ($\theta^{\text{tri}}_{\text{max}}$). Reproduced from Morimoto et al. (2022), under the terms of the CC BY 4.0 license.

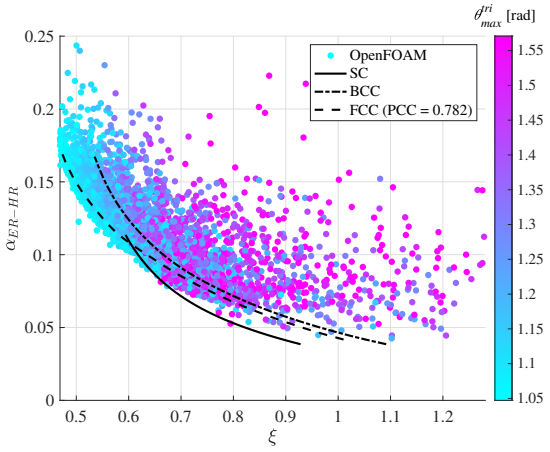
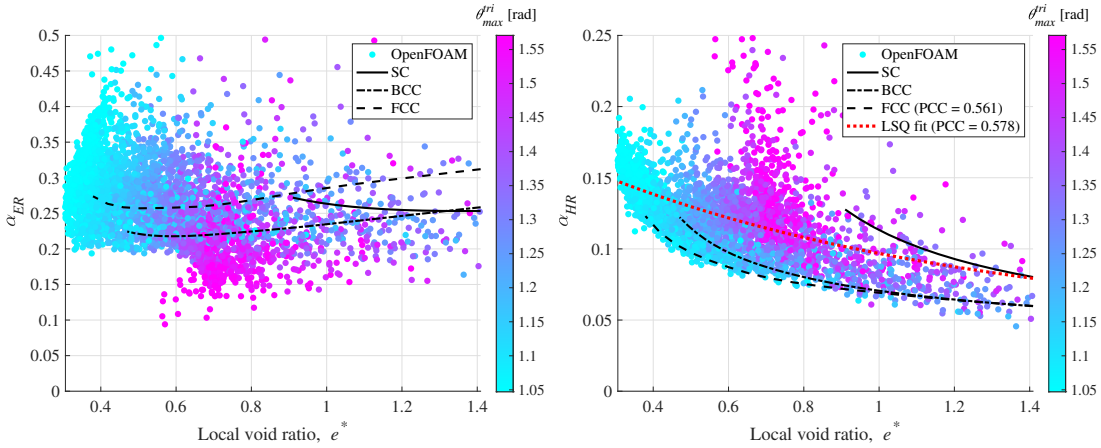
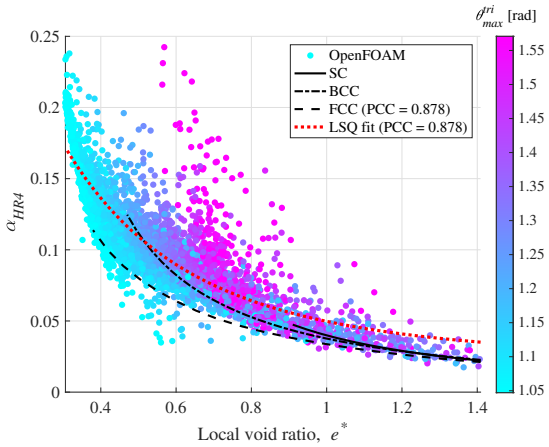


Figure 8.17: Variation in $\alpha_{\text{ER-HR}}$ with ξ: comparison of an OF simulation and analytical models for $Cu = 1.01$ and $e = 0.764$. Marker colour gives the maximum angle of the throat face ($\theta^{\text{tri}}_{\text{max}}$).

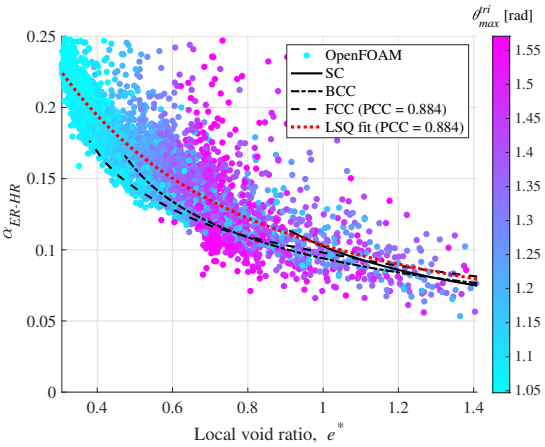


(a) *ER* model.

(b) *HR* model.



(c) *HR4* model.



(d) *ER-HR* model.

Figure 8.18: Variation in α with e^*: comparison of an OF simulation and analytical models for $Cu = 1.01$ and $e = 0.536$. Marker colour gives the maximum angle of the throat face ($\theta^{\text{tri}}_{\text{max}}$). Reproduced from Morimoto et al. (2022), under the terms of the CC BY 4.0 license.

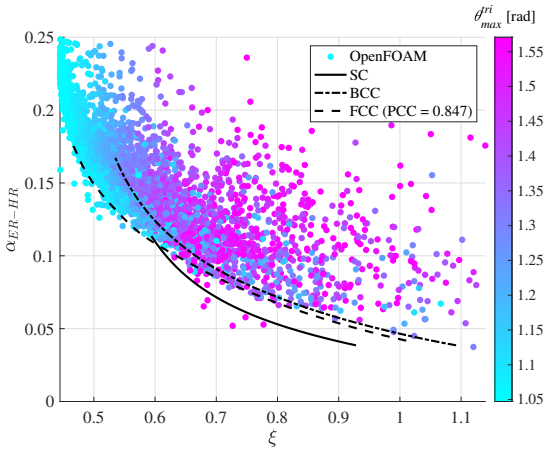


Figure 8.19: Variation in $\alpha_{\text{ER-HR}}$ with ξ: comparison of an OF simulation and analytical models for $Cu = 1.01$ and $e = 0.536$. Marker colour gives the maximum angle of the throat face ($\theta^{\text{tri}}_{\text{max}}$).

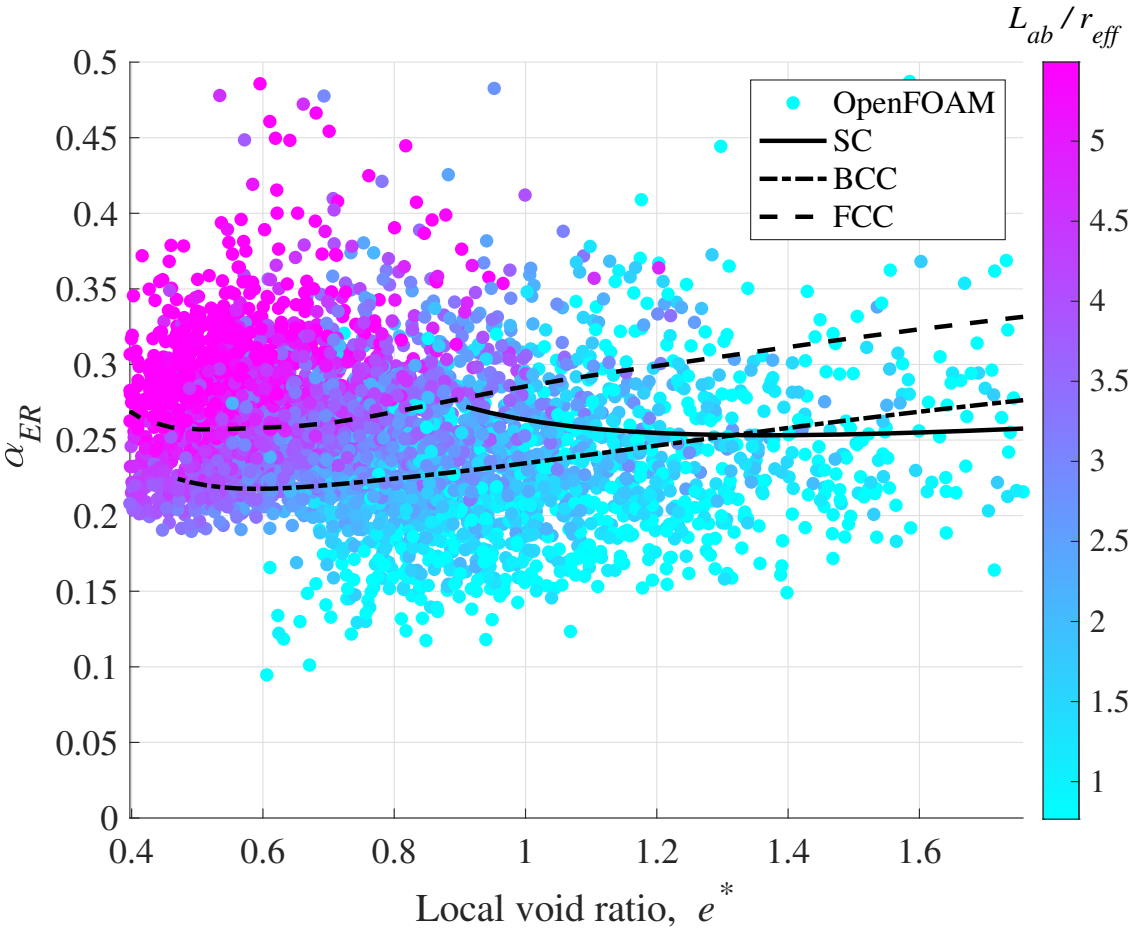
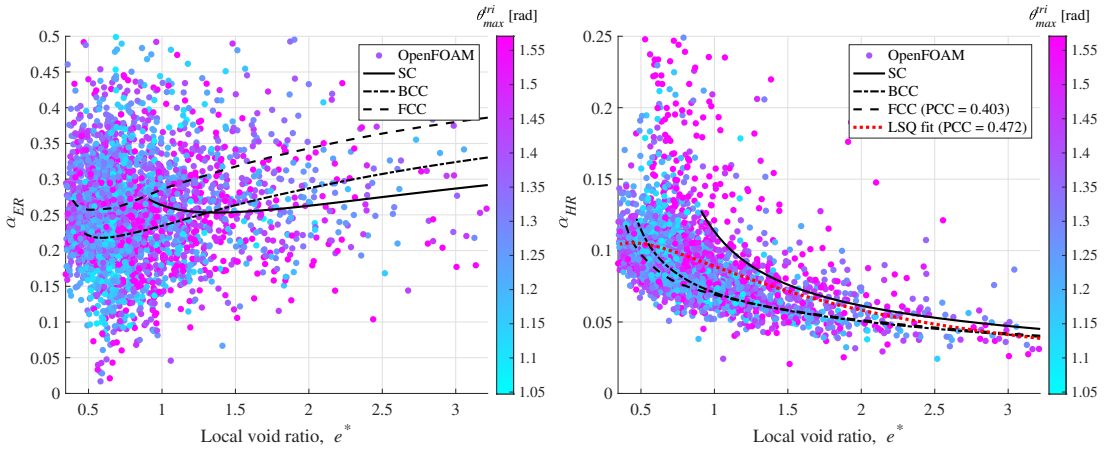
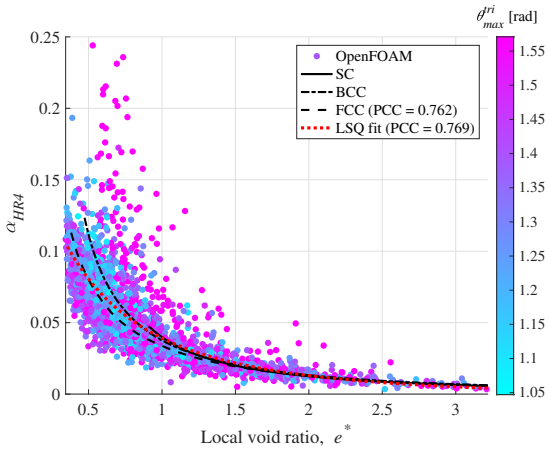


Figure 8.20: Variation in α_{ER} with e^*: comparison of an OF simulation and analytical models for $Cu = 1.01$ and $e = 0.764$. Marker colour gives the normalised throat length (L_{ab}/r_{eff}). Reproduced from Morimoto et al. (2022), under the terms of the CC BY 4.0 license.

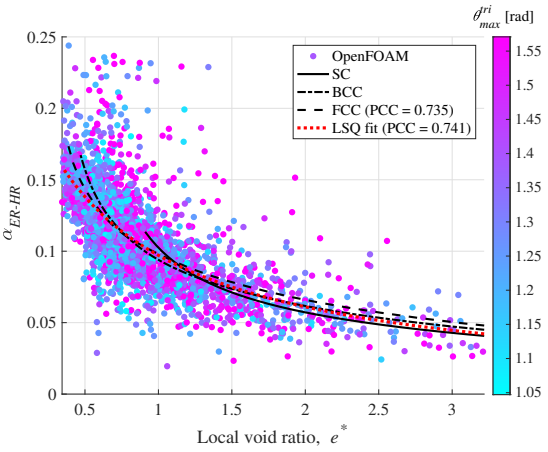


(a) *ER* model.

(b) *HR* model.



(c) *HR4* model.



(d) *ER-HR* model.

Figure 8.21: Variation in α with e^*: comparison of an OF simulation and analytical models for $Cu = 2.00$ and $e = 0.751$. Marker colour gives the maximum angle of the throat face ($\theta^{\text{tri}}_{\text{max}}$). Reproduced from Morimoto et al. (2022), under the terms of the CC BY 4.0 license.

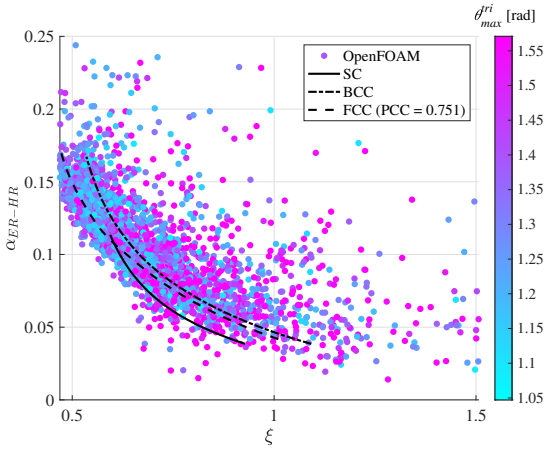
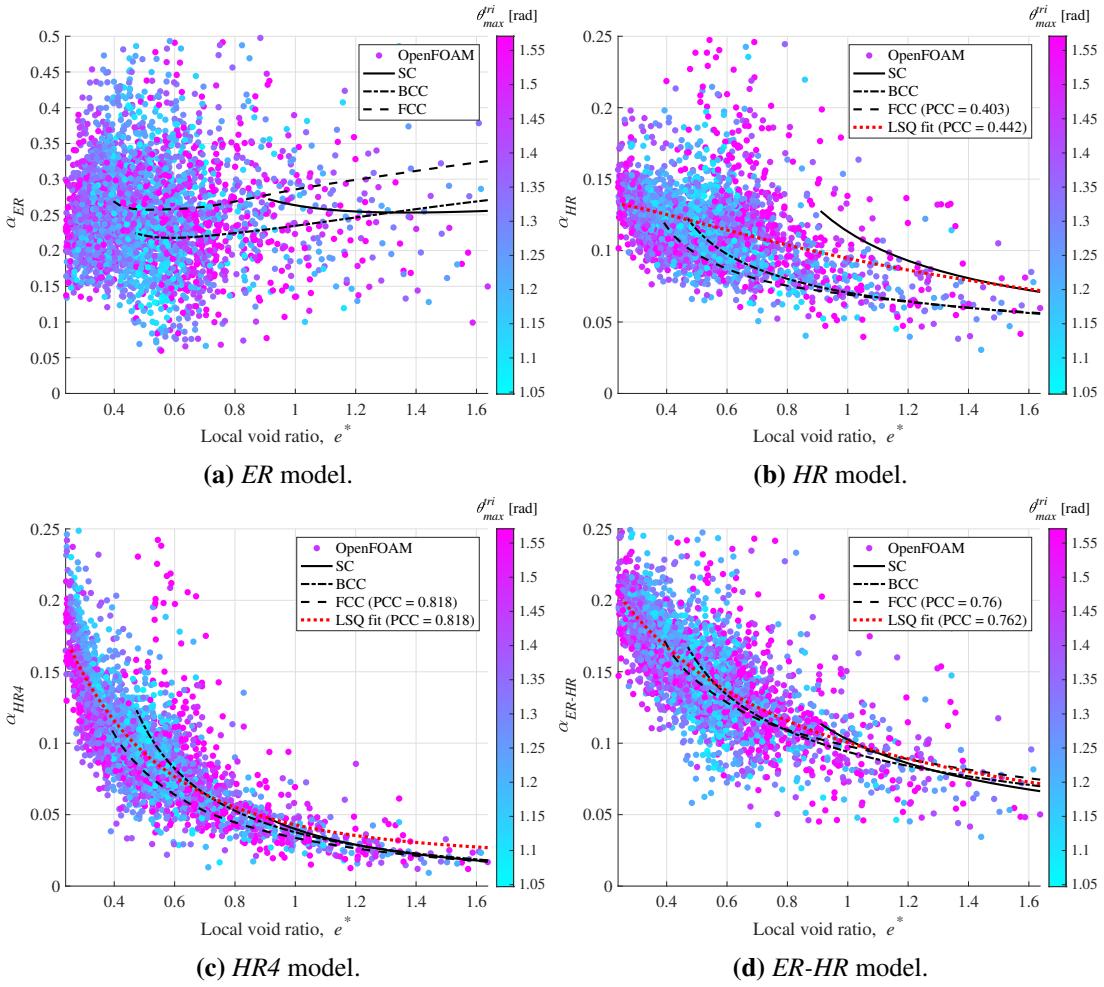


Figure 8.22: Variation of $\alpha_{\text{ER-HR}}$ with ξ: comparison of an OF simulation and analytical models for $Cu = 2.00$ and $e = 0.751$. Marker colour gives the maximum angle of the throat face ($\theta^{\text{tri}}_{\text{max}}$).



(a) *ER* model. **(b)** *HR* model.

(c) *HR4* model. **(d)** *ER-HR* model.

Figure 8.23: Variation in α with e^*: comparison of an OF simulation and analytical models for $Cu = 2.00$ and $e = 0.468$. Marker colour gives the maximum angle of the throat face ($\theta^{\text{tri}}_{\text{max}}$). Reproduced from Morimoto et al. (2022), under the terms of the CC BY 4.0 license.

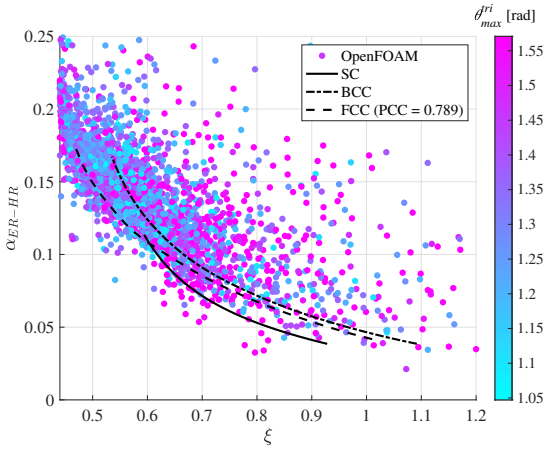


Figure 8.24: Variation in $\alpha_{\text{ER-HR}}$ with ξ: comparison of an OF simulation and analytical models for $Cu = 2.00$ and $e = 0.468$. Marker colour gives the maximum angle of the throat face ($\theta^{\text{tri}}_{\text{max}}$).

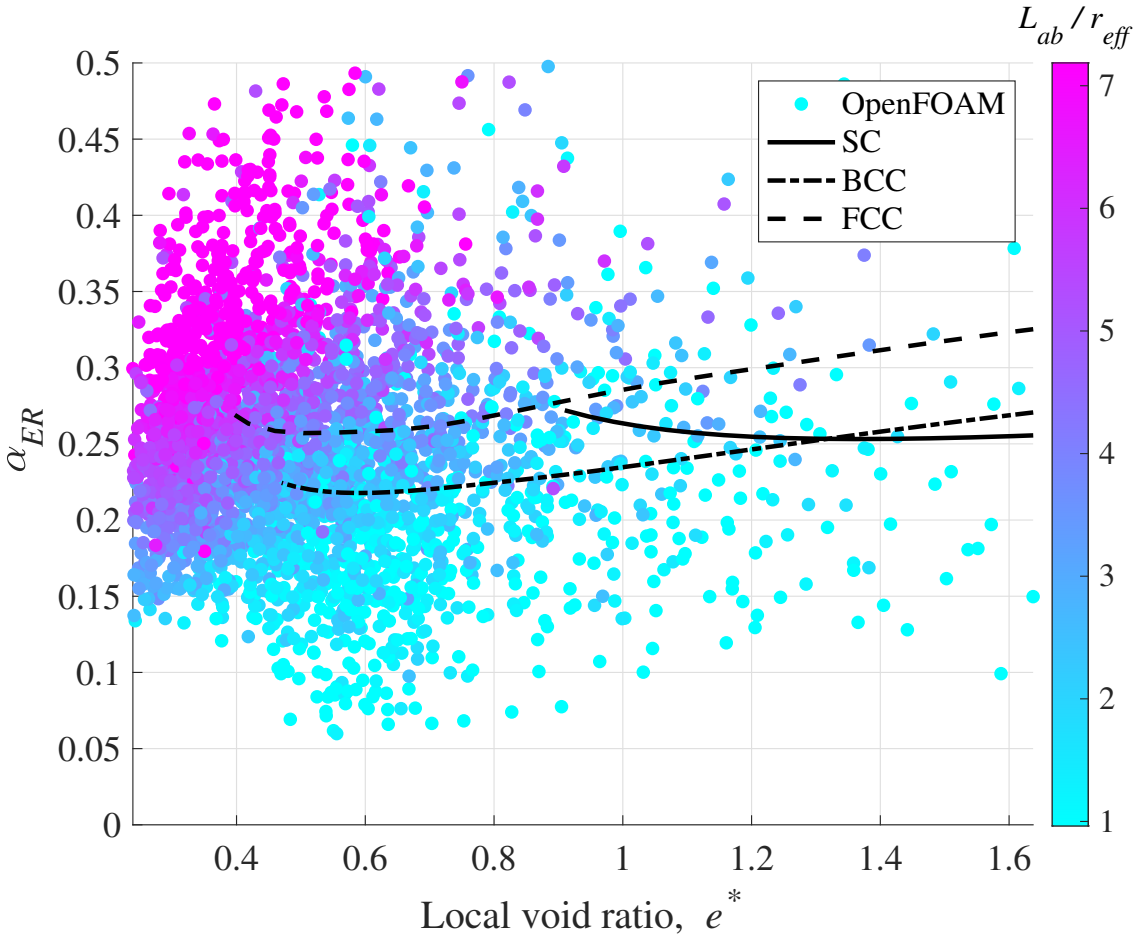


Figure 8.25: Variation in α_{ER} with e^*: comparison of an OF simulation and analytical models for $Cu = 2.00$ and $e = 0.468$. Marker colour gives the normalised throat length (L_{ab}/r_{eff}). Reproduced from Morimoto et al. (2022), under the terms of the CC BY 4.0 license.

e values considered here, the very small differences in the Pearson correlation coefficient (PCC) for ***HR4*** and ***ER-HR*** models between $\alpha(e^*)$ and $\alpha_{\text{XX}}^{LSQ}(e^*)$ show that the $\alpha(e^*)$ expressions capture the overall trend very well. Comparison of the R^2 values, however, shows that the $\alpha(e^*)$ expression gives some relatively large errors, which may be partially attributed to the errors existing in the OF data due to the compromised mesh size. The errors are smaller for the ***ER-HR*** model when $Cu = 1.01, 1.2, 1.5$, while the ***HR4*** model gave better R^2 values for $Cu = 2$. Overall, the proposed ***HR4*** and ***ER-HR*** models with the $\alpha(e^*)$ model can obtain results whose accuracy is comparable with the predictions using the LSQ best-fit to the OF data.

Table 8.5 includes the PCC and R^2 values for the $\alpha(\xi)$ model. The PCC values of the $\alpha(\xi)$ model is slightly lower (worse) than those of the $\alpha(e^*)$ model for $Cu = 1.01$ but better for $Cu = 2.00$.

8.5.4 α values in bimodal packing

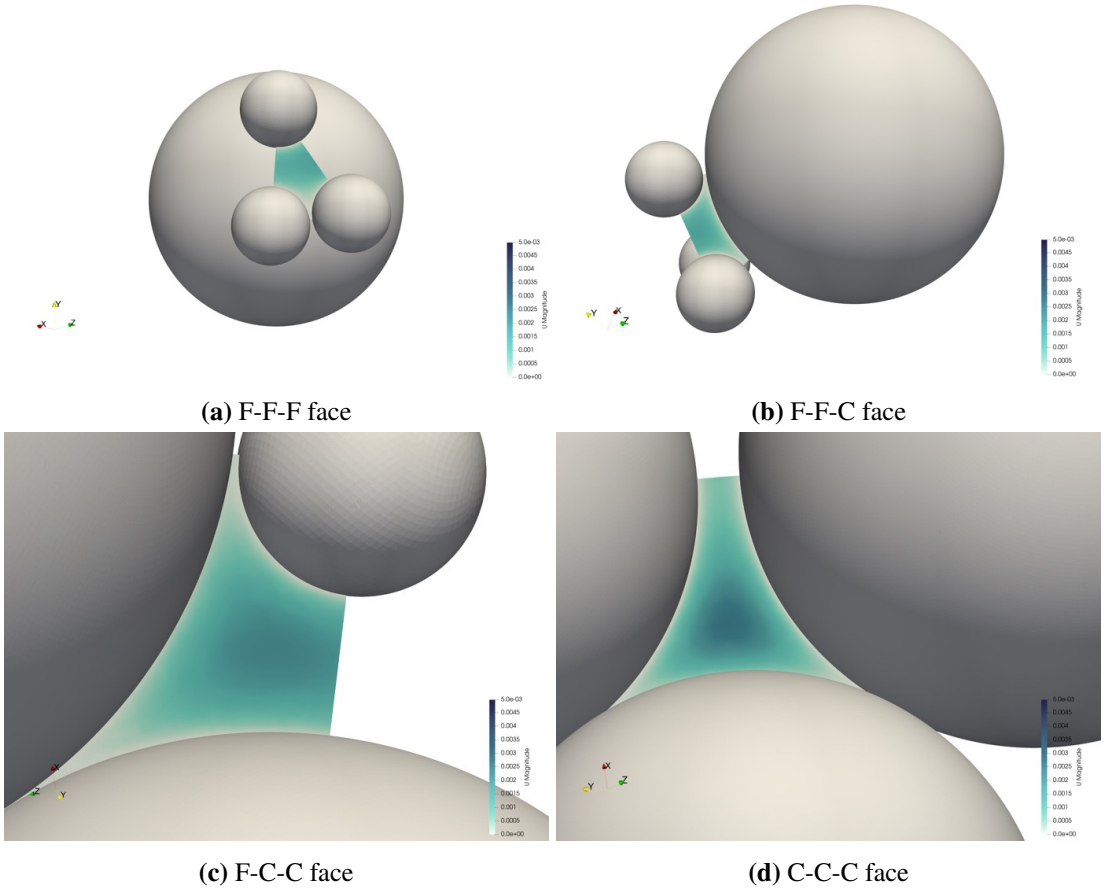
In a bimodal sample, the throat face consists of particles with significantly different radii however the $\alpha(e^*)$ and $\alpha(\xi)$ models were derived from regular packings, where the particle size is identical. If there are two particle radii (coarse and fine particles), there possible combinations of particles can define a throat: (1) Fine-Fine-Fine (F-F-F), (2) Fine-Fine-Coarse (F-F-C), (3) Fine-Coarse-Coarse (F-C-C), (4) Coarse-Coarse-Coarse (C-C-C) (see Fig. 8.26).

Fig. 8.27 gives the variation with e^* of the α_{HR4} and $\alpha_{\text{ER-HR}}$ values back-calculated from OF simulations for a gap-graded sample with $SR = 4.00$, $FC = 0.35$ and $e = 0.351$. Each data point corresponds to a throat and the points are coloured based on the throat type introduced above; these data clearly show that the $\alpha_{\text{HR4}}(e^*)$ and $\alpha_{\text{ER-HR}}(e^*)$ models overpredict α for the large F-F-C and F-C-C throats while these models accurately predict α for F-F-F throats. The $\alpha_{\text{ER-HR}}$-ξ relationship shown in Fig. 8.28, in turn, shows little discrepancy between data points for monodisperse throats and for polydisperse throats (F-F-C and F-C-C throats). The same observation was made for $SR = 4.00$, $FC = 0.11$ and $e = 0.550$ as shown in Fig. 8.29 and Fig. 8.30.

Considering an assembly with $SR = 4.0$, a F-F-C throat with $e^* = 0.307$ is shown in Fig. 8.31(a). The shape of throat face (fluid region) is very similar to that of the throat face in the densest SC packing which has a (much higher) $e^* = 0.910$ shown in Fig. 8.31(b). The $\alpha_{\text{ER-HR}}(e^*)$ value predicted from Eq. (8.41) for the throat in Fig. 8.31(a) is 0.1891. However, the back-calculated $\alpha_{\text{ER-HR}}$ value (0.133) is closer to $\alpha_{\text{ER-HR}}$ value of the densest SC packing (0.114). The overprediction in $\alpha_{\text{ER-HR}}$ is attributed to the large volume of solid phase coming from the large particle as indicated in Fig. 8.31(a). On the other hand, the ξ value of the densest SC packing is 0.594, and the throat shown in Fig. 8.31(a) has a similar

Table 8.5: Tabular summary of PCC and R^2 values of analytical and the LSQ best-fit to the OF data for various models.

		PCC							R^2						
		HR		*HR4*		*ER-HR*		*ER-HR*	*HR*		*HR4*		*ER-HR*		*ER-HR*
Cu	e	$\alpha(e^*)$	LSQ	$\alpha(e^*)$	LSQ	$\alpha(e^*)$	LSQ	$\alpha(\xi)$	$\alpha(e^*)$	LSQ	$\alpha(e^*)$	LSQ	$\alpha(e^*)$	LSQ	$\alpha(\xi)$
	0.764	0.458	0.483	0.838	0.839	0.820	0.822	0.782	-0.225	0.233	0.529	0.704	0.604	0.675	0.297
1.01	0.610	0.466	0.492	0.862	0.863	0.846	0.848	0.808	-0.395	0.242	0.501	0.744	0.631	0.718	0.343
	0.536	0.561	0.578	0.878	0.878	0.884	0.884	0.847	-0.738	0.335	0.296	0.772	0.449	0.781	0.036
	0.764	0.403	0.489	0.759	0.769	0.797	0.803	0.773	-0.283	0.239	0.440	0.591	0.586	0.644	0.340
1.2	0.613	0.371	0.444	0.815	0.818	0.817	0.820	0.802	-0.500	0.197	0.454	0.669	0.601	0.672	0.365
	0.555	0.481	0.520	0.849	0.849	0.853	0.854	0.832	-0.637	0.271	0.362	0.720	0.511	0.730	0.171
	0.761	0.383	0.469	0.735	0.746	0.769	0.778	0.756	-0.185	0.220	0.459	0.556	0.579	0.605	0.326
1.5	0.610	0.274	0.358	0.778	0.781	0.747	0.753	0.744	-0.400	0.128	0.484	0.610	0.539	0.567	0.330
	0.529	0.416	0.474	0.813	0.814	0.820	0.823	0.819	-0.476	0.225	0.437	0.662	0.585	0.678	0.299
	0.751	0.403	0.472	0.762	0.769	0.735	0.741	0.751	-0.024	0.223	0.564	0.591	0.522	0.549	0.354
2.0	0.603	0.346	0.403	0.800	0.801	0.728	0.733	0.759	-0.135	0.162	0.620	0.642	0.495	0.538	0.389
	0.468	0.403	0.442	0.818	0.818	0.760	0.762	0.789	-0.255	0.195	0.590	0.669	0.569	0.581	0.296



(a) F-F-F face **(b)** F-F-C face

(c) F-C-C face **(d)** C-C-C face

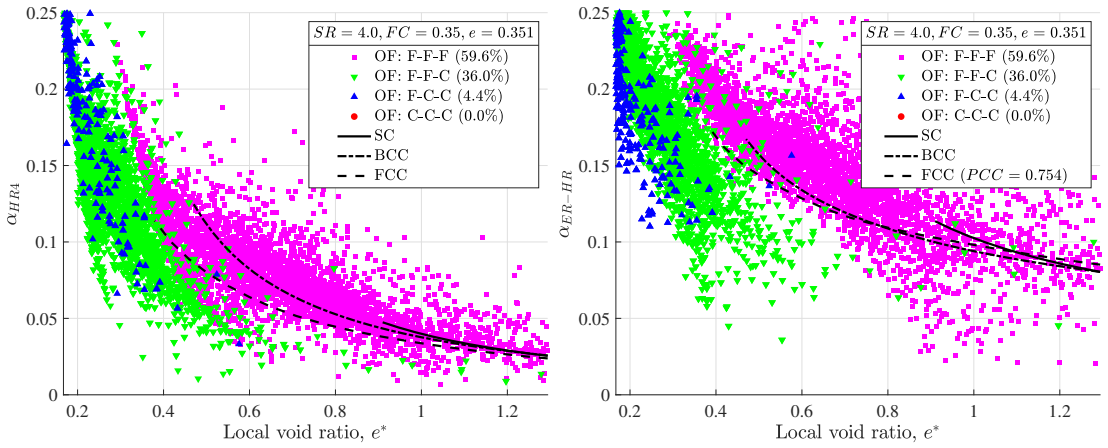
Figure 8.26: Four types of throat faces in a gap graded sphere packing with $SR = 4.0$.

value (0.612) and $\alpha_{\text{ER-HR}}(\xi)$. The relative error in comparison with the OF data is reduced from 42% when $\alpha_{\text{ER-HR}}(e^*)$ model is used to 20% with the $\alpha_{\text{ER-HR}}(\xi)$ model.

8.5.5 Global permeability prediction using developed models

The $\alpha(e^*)$ and $\alpha(\xi)$ expressions proposed as Eqs. (8.40) to (8.42) were used in a PNM and a simulation to obtain global permeability was conducted for each packing with a variety of e values and for each of selected models following the procedure outlined in Section 8.4.2. The *HR* model proposed by Chareyre et al. (2012) with a constant α_{HR} value of $1/8$ and the *HR4* and *ER-HR* models with $\alpha(e^*)$ were considered for the comparison.

Fig. 8.32(a) compares the global permeability values obtained by OF simulations and PNM simulations with three different models for linearly graded samples. The permeability values in Fig. 8.32(a) are summarised in Table 8.6. The $\alpha_{\text{HR4}}(e^*)$ and $\alpha_{\text{ER-HR}}(e^*)$ models capture the variation in permeability very well while the *HR* model with $\alpha_{\text{HR}} = 1/8$ noticeably overpredicts the global permeability. The relative error in the global permeabilities is plotted in Fig. 8.32(b). For both the $\alpha_{\text{HR4}}(e^*)$ and $\alpha_{\text{ER-HR}}(e^*)$ expressions the error is within $+/-15.2\%$ for a wide range of Cu and e. Fig. 8.33(a) is a similar plot but comparing the



(a) *HR4* model **(b)** *ER-HR* model

Figure 8.27: Variation in α with e^*: comparison of an OF simulation and analytical models for $SR = 4.00$, $FC = 0.35$ and $e = 0.351$. Marker colour gives the types of the throat face.

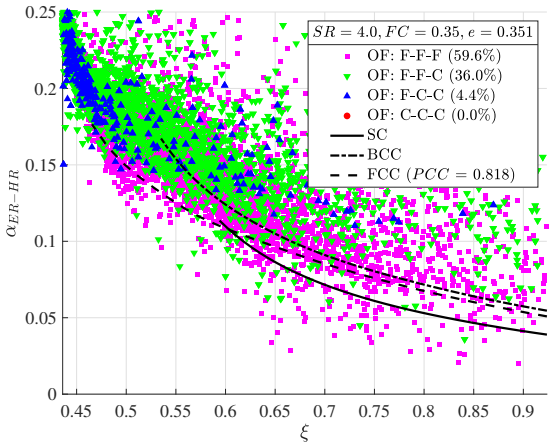
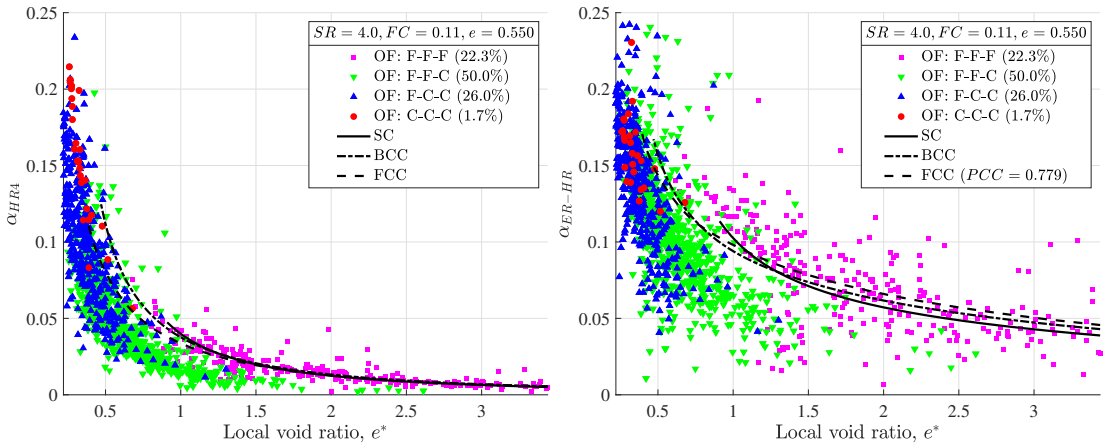


Figure 8.28: Variation in α with ξ: comparison of an OF simulation and analytical models for $SR = 4.00$, $FC = 0.35$ and $e = 0.351$. Marker colour gives the types of the throat face.



(a) *HR4* model **(b)** *ER-HR* model

Figure 8.29: Variation in α with e^*: comparison of an OF simulation and analytical models for $SR = 4.00$, $FC = 0.11$ and $e = 0.550$. Marker colour gives the types of the throat face.

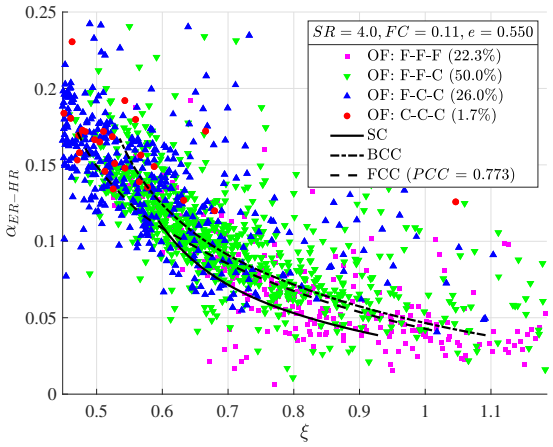
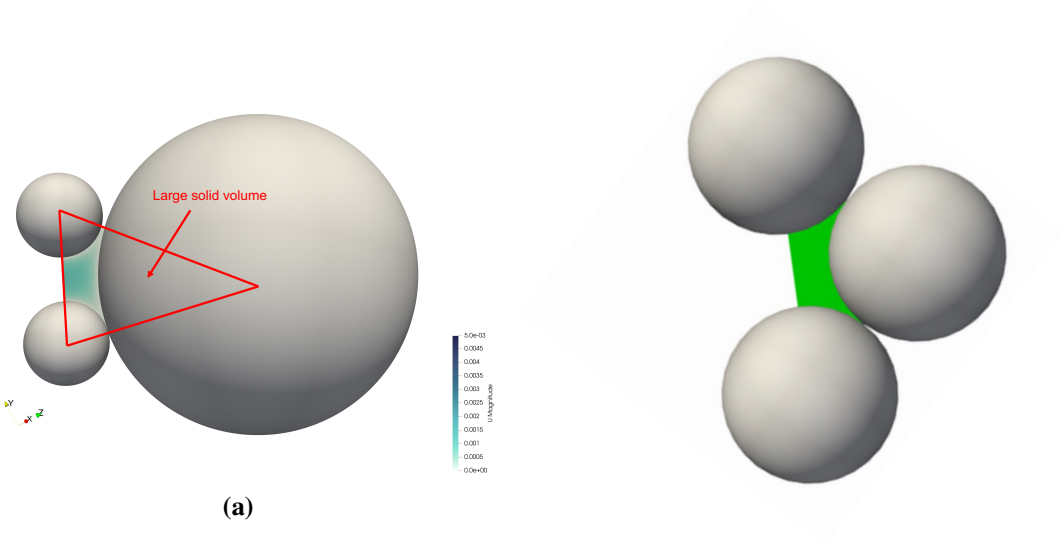


Figure 8.30: Variation in α with ξ: comparison of an OF simulation and analytical models for $SR = 4.00$, $FC = 0.11$ and $e = 0.550$. Marker colour gives the types of the throat face.



(a) **(b)**

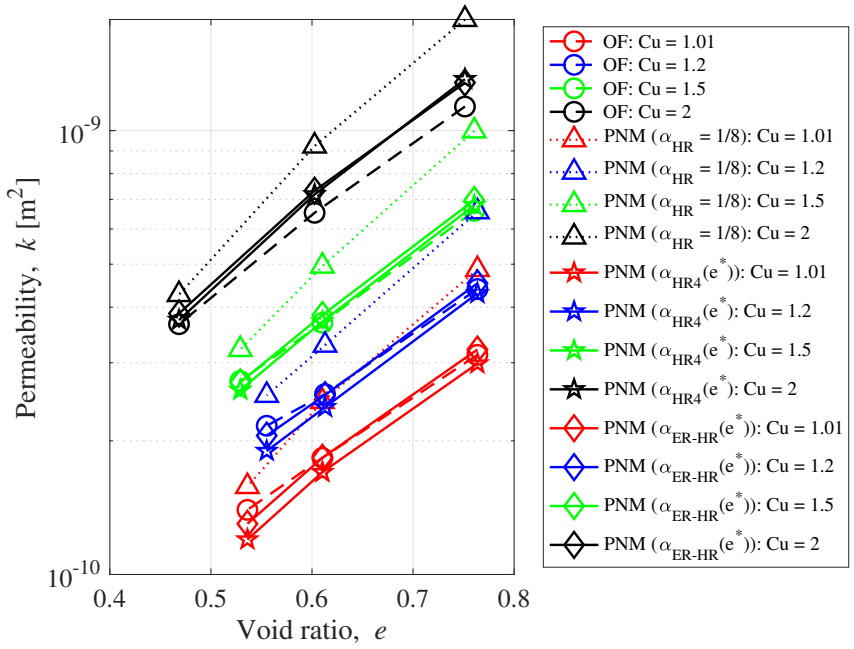
Figure 8.31: Two throat topologies which have a similar $\alpha_{\text{ER-HR}}$ value but a different e^* value. (a) one of F-F-C faces in the packing with $SR = 4.0$ ($\alpha_{\text{ER-HR}} = 0.133$, $e^* = 0.307$, $\xi = 0.612$). (b) a throat face of the densest SC packing ($\alpha_{\text{ER-HR}} = 0.114$, $e^* = 0.910$, $\xi = 0.594$).

$\alpha_{\text{ER-HR}}(e^*)$ and $\alpha_{\text{ER-HR}}(\xi)$ models. It can be seen that the $\alpha_{\text{ER-HR}}(\xi)$ model is as accurate as the $\alpha_{\text{ER-HR}}(e^*)$, where the maximum relative error was -10.7% (Fig. 8.33(b) and Table 8.6).

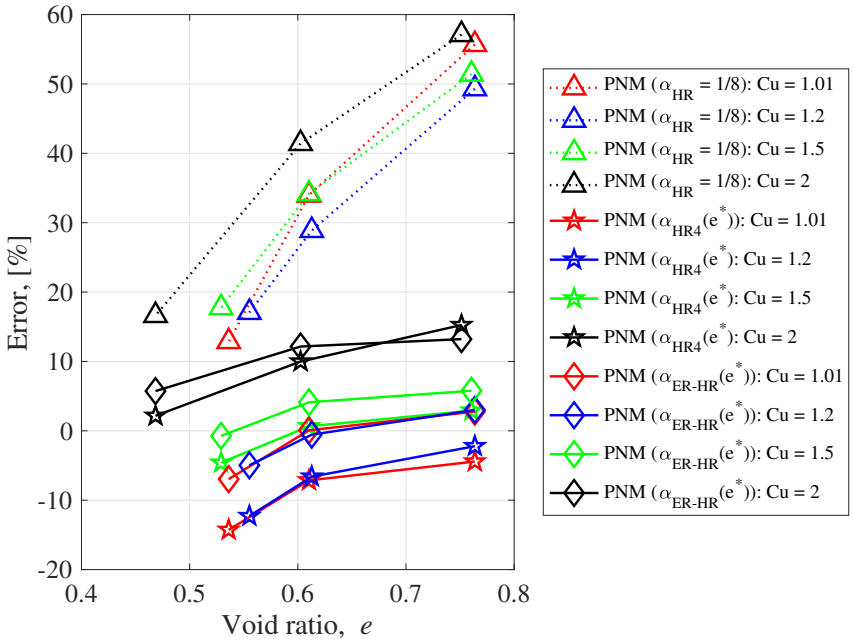
Fig. 8.34(a) shows a similar plot for the bimodal samples with $SR = 2$ (Fig. 8.34), where the global permeability values from OF and PNMs with the $\alpha_{\text{HR}} = 1/8$, the $\alpha_{\text{ER-HR}}(e^*)$, and the $\alpha_{\text{ER-HR}}(\xi)$ models are compared. Fig. 8.34(b) compares relative errors in global peremeability permeabilities from the OF results. The global premeability and relative error values are also summarised in Table 8.7. The results for $\alpha_{\text{HR4}}(e^*)$ are not shown in Fig. 8.34 for simplicity as $\alpha_{\text{HR4}}(e^*)$ and $\alpha_{\text{ER-HR}}(e^*)$ gave similar results as shown in Table 8.7. $\alpha_{\text{HR4}}(e^*)$, $\alpha_{\text{ER-HR}}(e^*)$ and $\alpha_{\text{ER-HR}}(\xi)$ have similary accuracy when compared to the OF benchmark data and outperformed the model by Chareyre et al. (2012) (the $\alpha_{\text{HR}} = 1/8$ model).

A similar plot is shown in Fig. 8.35 for the bimodal sample with $SR = 4$. Fig. 8.35(a) and (b) show that the $\alpha_{\text{ER-HR}}(e^*)$ model overpredicted the permeability due to the issue pointed out in Fig. 8.31. However, the $\alpha_{\text{ER-HR}}(\xi)$ model data were in good agreement with the OF data, which demonstrates the robustness of the $\alpha_{\text{ER-HR}}(\xi)$ model which can capture a change in polydispersity. The permeablity values and relative errors from OF and PNMs are summarised in Table 8.7.

For the linearly graded and bimodal samples considered in this study, the $\alpha_{\text{ER-HR}}(\xi)$ model gave a maximum error of 13% from the permeability values obtained from the OF simulations (Tables 8.6 and 8.7), while significantly reducing the simulation time. This result is significant because the $\alpha(\xi)$ model is developed without any input from OF

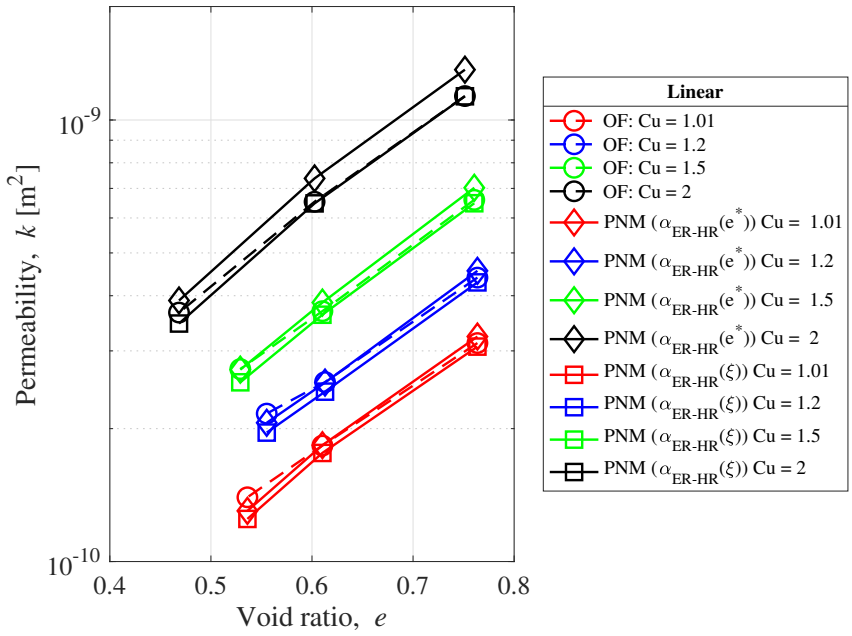


(a) k_h versus e

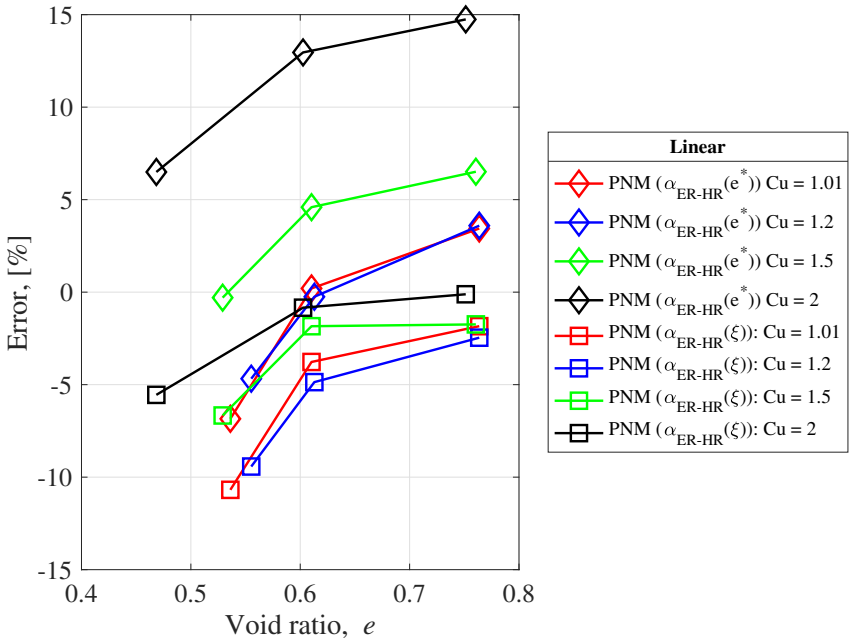


(b) Relative error in k_h values versus e

Figure 8.32: Variation in global permeabilities with e: comparison of an OF simulation and analytical models based on e^* for random dense linearly graded packings. Reproduced from Morimoto et al. (2022), under the terms of the CC BY 4.0 license.



(a) k_{h} versus e



(b) Relative error in k_{h} values versus e

Figure 8.33: Varaition in global permeabilities with e: comparison of an OF simulation and a PNM with the $\alpha_{\text{ER-HR}}(e^*)$ and $\alpha_{\text{ER-HR}}(\xi)$ for random dense linearly graded packings.

Table 8.6: The permeability values (in $[m^2]$) of a variety of linearly graded packings obtained from the OF and PNM simulations. The values in brackets are relative errors from the value obtained from the OF simulations.

			PNM			
Cu	e	OF	α_{HR}	$\alpha_{\text{HR4}}(e^*)$	$\alpha_{\text{ER-HR}}(e^*)$	$\alpha_{\text{ER-HR}}(\xi)$
1.01	0.764	3.13×10^{-10}	4.87×10^{-10}	2.99×10^{-10}	3.21×10^{-10}	3.07×10^{-10}
		(–)	(55.7%)	(-4.4%)	(2.8%)	(-1.84%)
	0.610	1.83×10^{-10}	2.45×10^{-10}	1.70×10^{-10}	1.83×10^{-10}	1.76×10^{-10}
		(–)	(34.0%)	(-7.1%)	(0.1%)	(-3.77%)
	0.536	1.40×10^{-10}	1.58×10^{-10}	1.20×10^{-10}	1.30×10^{-10}	1.25×10^{-10}
		(–)	(12.9%)	(-14.3%)	(-7.0%)	(-10.7%)
1.20	0.764	4.40×10^{-10}	6.56×10^{-10}	4.30×10^{-10}	4.53×10^{-10}	4.29×10^{-10}
		(–)	(49.3%)	(-2.2%)	(3.0%)	(-2.46%)
	0.613	2.55×10^{-10}	3.29×10^{-10}	2.38×10^{-10}	2.54×10^{-10}	2.43×10^{-10}
		(–)	(28.9%)	(-6.6%)	(-0.6%)	(-4.86%)
	0.555	2.16×10^{-10}	2.53×10^{-10}	1.90×10^{-10}	2.06×10^{-10}	1.96×10^{-10}
		(–)	(17.1%)	(-12.3%)	(-5.0%)	(-9.43%)
1.50	0.761	6.59×10^{-10}	9.98×10^{-10}	6.79×10^{-10}	6.97×10^{-10}	6.48×10^{-10}
		(–)	(51.4%)	(2.9%)	(5.8%)	(-1.74%)
	0.610	3.69×10^{-10}	4.95×10^{-10}	3.71×10^{-10}	3.84×10^{-10}	3.62×10^{-10}
		(–)	(34.2%)	(0.7%)	(4.1%)	(-1.84%)
	0.529	2.73×10^{-10}	3.21×10^{-10}	2.60×10^{-10}	2.71×10^{-10}	2.55×10^{-10}
		(–)	(17.7%)	(-4.6%)	(-0.7%)	(-6.67%)
2.00	0.751	1.13×10^{-9}	1.78×10^{-9}	1.31×10^{-9}	1.28×10^{-9}	1.13×10^{-9}
		(–)	(57.1%)	(15.2%)	(13.2%)	(-0.1%)
	0.603	6.53×10^{-10}	9.23×10^{-10}	7.18×10^{-10}	7.32×10^{-10}	6.47×10^{-10}
		(–)	(41.4%)	(10.0%)	(12.1%)	(-0.8%)
	0.468	3.66×10^{-10}	4.27×10^{-10}	3.74×10^{-10}	3.87×10^{-10}	3.46×10^{-10}
		(–)	(16.6%)	(2.2%)	(5.7%)	(-5.6%)

Table 8.7: The permeability values (in $[m^2]$) of a variety of bimodal packings obtained from the OF and PNM simulations. The values in brackets are relative errors from the value obtained from the OF simulations.

				PNM			
SR	FC	e	OF	α_{HR}	$\alpha_{\text{HR4}}(e^*)$	$\alpha_{\text{ER-HR}}(e^*)$	$\alpha_{\text{ER-HR}}(\xi)$
2	0.1	0.610	5.84×10^{-10}	7.53×10^{-10}	5.75×10^{-10}	6.06×10^{-10}	5.51×10^{-10}
			(-)	(28.9%)	(-1.6%)	(3.7%)	(-5.6%)
		0.524	4.15×10^{-10}	5.05×10^{-10}	4.06×10^{-10}	4.29×10^{-10}	3.92×10^{-10}
			(-)	(21.7%)	(-2.1%)	(3.4%)	(-5.4%)
	0.35	0.608	4.08×10^{-10}	5.35×10^{-10}	4.22×10^{-10}	4.32×10^{-10}	3.81×10^{-10}
			(-)	(31.3%)	(3.5%)	(5.9%)	(-6.6%)
		0.486	2.31×10^{-10}	2.64×10^{-10}	2.27×10^{-10}	2.36×10^{-10}	2.23×10^{-10}
			(-)	(14.6%)	(-1.5%)	(2.5%)	(-3.2%)
4	0.11	0.550	1.13×10^{-9}	1.87×10^{-9}	1.89×10^{-9}	1.58×10^{-9}	1.16×10^{-9}
			(-)	(65.2%)	(66.6%)	(39.6%)	(2.5%)
		0.460	7.09×10^{-10}	9.91×10^{-10}	1.04×10^{-9}	9.44×10^{-10}	7.05×10^{-10}
			(-)	(39.7%)	(46.9%)	(33.1%)	(-0.6%)
	0.35	0.536	4.58×10^{-10}	6.58×10^{-10}	6.20×10^{-10}	5.82×10^{-10}	4.41×10^{-10}
			(-)	(43.7%)	(35.4%)	(27.1%)	(-3.7%)
		0.351	1.74×10^{-10}	1.81×10^{-10}	1.88×10^{-10}	1.98×10^{-10}	1.51×10^{-10}
			(-)	(4.2%)	(8.6%)	(13.9%)	(-13.0%)

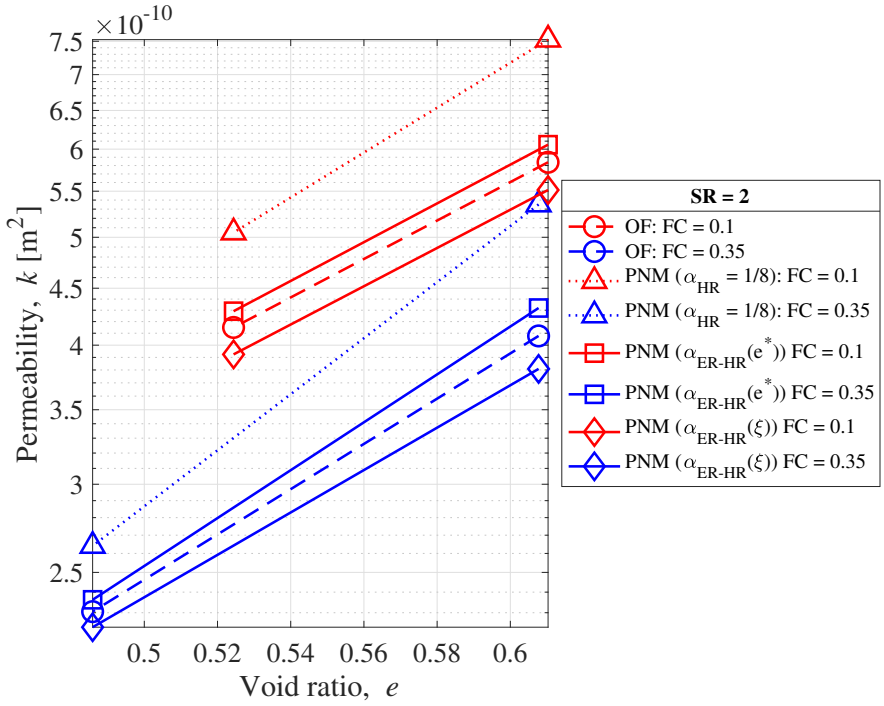
data and the result also supports a wide applicability of $\alpha_{\text{ER-HR}}(\xi)$ models without any calibration.

8.6 Fluid-particle interaction force vector from OF, a PNM and an empirical method

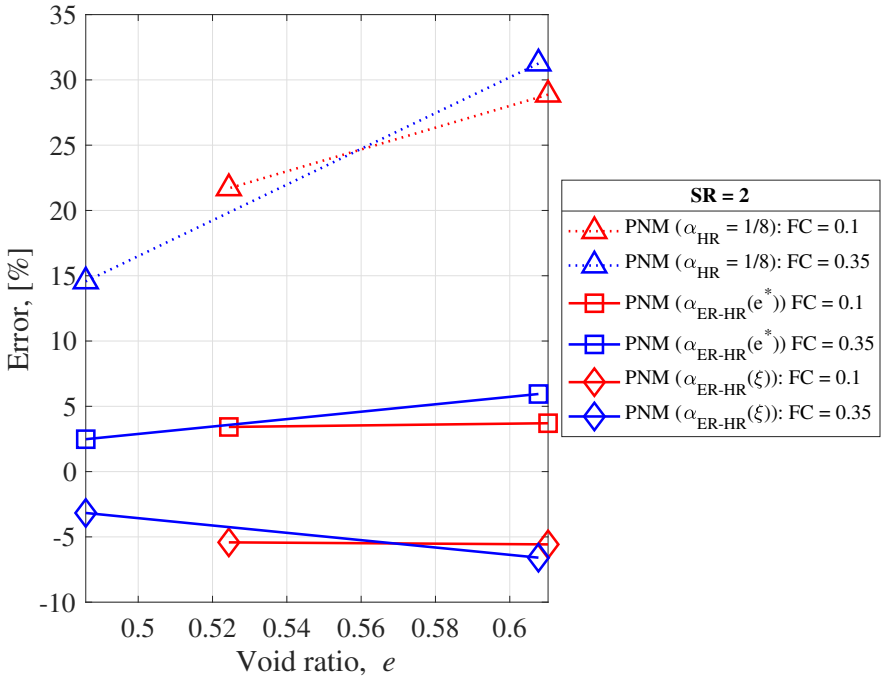
8.6.1 Fluid-particle interaction force magnitude from OF and a PNM with three types of local conductance models

To establish the ability of a PNM to accurately determine the magnitude of the fluid-particle interaction forces obtained from both a PNM and OF were normalised by Stokes drag force F^{Stokes} for a sphere. The normalised fluid-particle interaction force, the forces obtained using OF and PNM are denoted ($\overline{F_m^{f\to p,OF}}$) and ($\overline{F_m^{f\to p,PNM}}$) respectively and given by:

$$\overline{F_m^{f\to p,OF}} = \frac{\|\mathbf{F_m^{f\to p,OF}}\|}{3\pi\mu_{\text{f}}D_m u_{\text{inlet,OF}}} \tag{8.61}$$

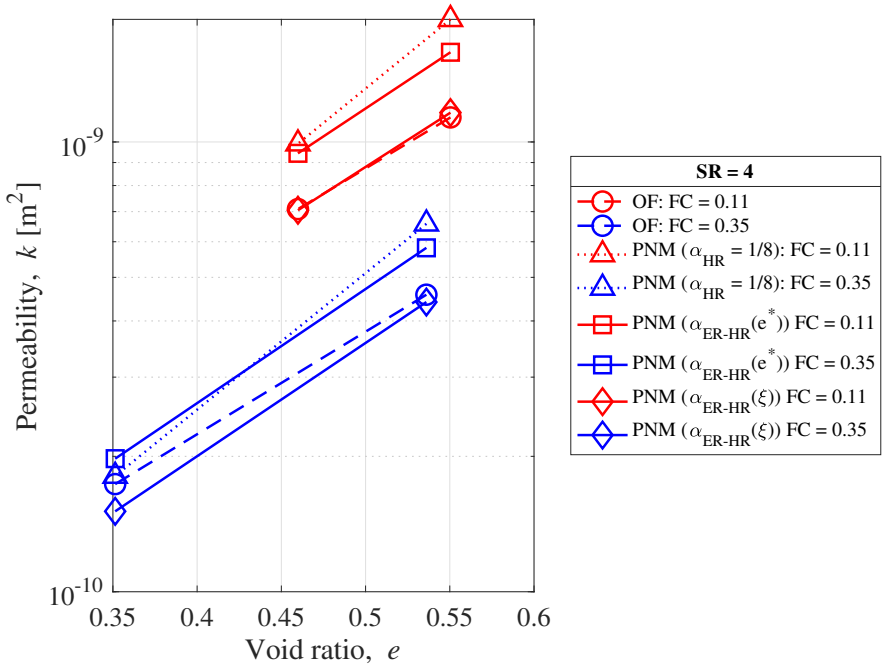


(a) k_h versus e

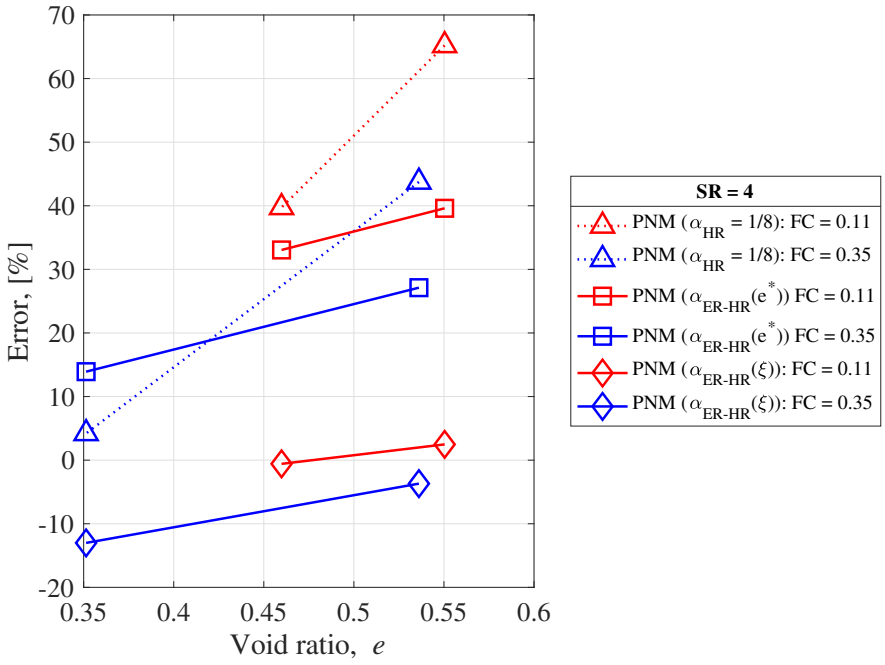


(b) Relative error in k_h values versus e

Figure 8.34: Comparison of global permeabilities between an OF simulation and a PNM with the *HR*, $\alpha_{\text{ER-HR}}(e^*)$, and $\alpha_{\text{ER-HR}}(\xi)$ models for random dense bimodal packings for $SR = 2$.

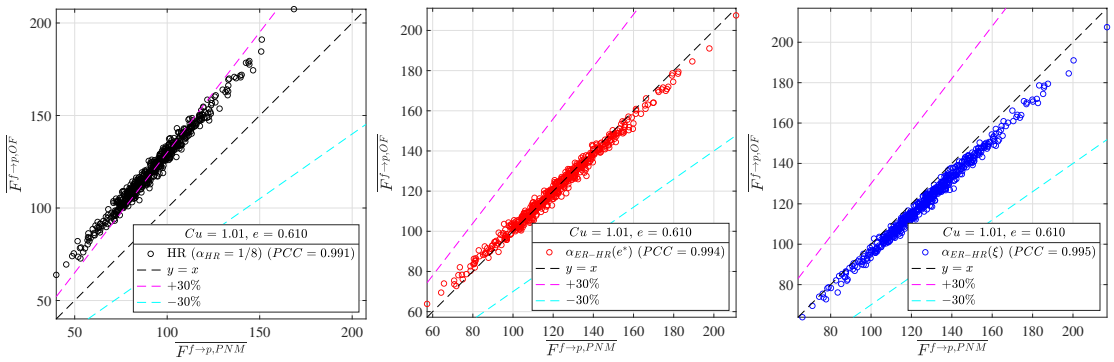


(a) k_h versus e



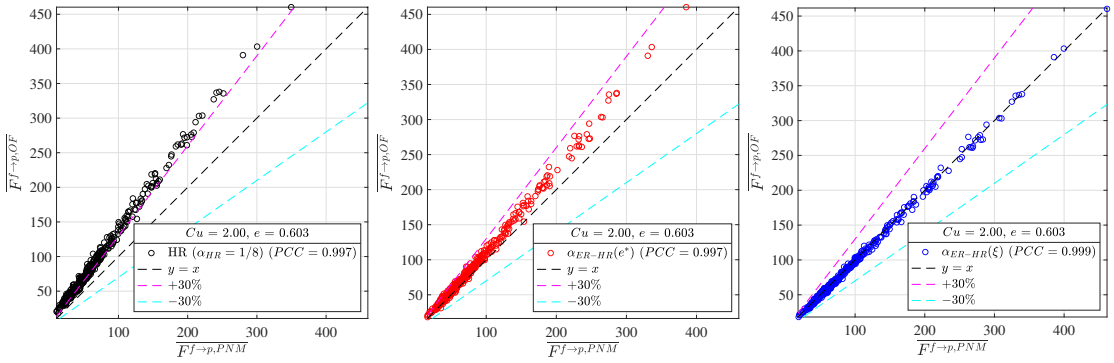
(b) Relative error in k_h values versus e

Figure 8.35: Comparison of global permeabilities between an OF simulation and a PNM with the *HR*, $\alpha_{\text{ER-HR}}(e^*)$, and $\alpha_{\text{ER-HR}}(\xi)$ models for random dense bimodal packings for $SR = 4$.



(a) *HR* model. **(b)** $\alpha_{\text{ER-HR}}(e^*)$. **(c)** $\alpha_{\text{ER-HR}}(\xi)$.

Figure 8.36: Comparison of the normalised drag force obtained from the OF and PNM simulations for linearly graded PSD with $Cu = 1.01$, $e = 0.610$.



(a) *HR* model. **(b)** $\alpha_{\text{ER-HR}}(e^*)$. **(c)** $\alpha_{\text{ER-HR}}(\xi)$.

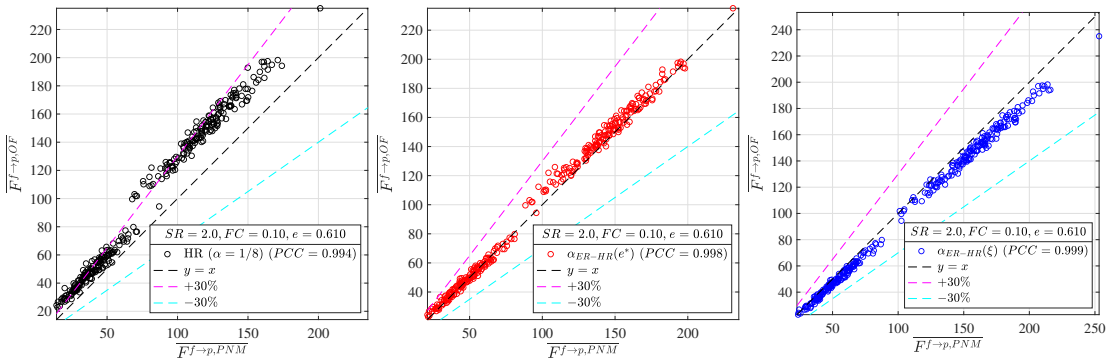
Figure 8.37: Comparison of the normalised drag force obtained from the OF and PNM simulations for linearly graded PSD with $Cu = 2.00$, $e = 0.603$.

$$\overline{F_m^{f\to p,PNM}} = \frac{\|\mathbf{F_m^{f\to p,PNM}}\|}{3\pi\mu_f D_m u_{\text{inlet,PNM}}} \tag{8.62}$$

where D_m is the diameter of particle m and u_{OF} is the inlet velocity in ms^{-1} (the calculation of $u_{\text{inlet,PNM}}$ is outlined in Section 8.4.2).

Fig. 8.36 compares normalised fluid-particle interaction forces acting on particles in packings with $Cu = 1.01$ and $e = 0.610$ obtained from OF and a PNM. Three PNM models are considered here, each using a different conductance model as follows: (a) the *HR* model by Chareyre et al. (2012), (b) the $\alpha_{\text{ER-HR}}(e^*)$ model, and (c) the $\alpha_{\text{ER-HR}}(\xi)$ model developed above. Both the data generated using the $\alpha_{\text{ER-HR}}(e^*)$ model and those generated using the $\alpha_{\text{ER-HR}}(\xi)$ are in good agreement with the OF data. Fig. 8.37 shows a similar comparison for $Cu = 2.00$ and $e = 0.603$, where the $\alpha_{\text{ER-HR}}(e^*)$ and $\alpha_{\text{ER-HR}}(\xi)$ models give excellent results, while the $\alpha_{\text{HR}} = 1/8$ model gives a large error for $e = 0.751$.

To compare the accuracy of a PNM for the three types of local conductance models, the relative error in the $\overline{F^{f\to p}}$ was calculated for each particle as



(a) *HR* model. **(b)** $\alpha_{\text{ER-HR}}(e^*)$. **(c)** $\alpha_{\text{ER-HR}}(\xi)$.

Figure 8.38: Comparison of the normalised drag force obtained from the OF and PNM simulations for bimodal PSD with $SR = 2$, $FC = 0.10$, $e = 0.610$.

$$\text{Relative error for particle } m = \frac{\overline{F_m^{f\to p,PNM}} - \overline{F_m^{f\to p,OF}}}{\overline{F_m^{f\to p,OF}}} \tag{8.63}$$

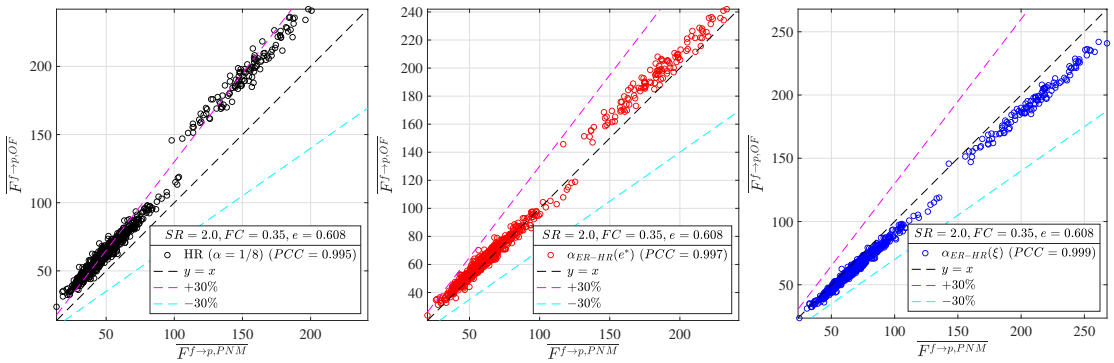
where a positive relative error value indicates that the PNM overpredicts the normalised fluid-particle interaction force. The mean value of the relative errors was calculated (shown in Table 8.8). In addition, the 2.5th percentile and the 97.5th percentile of the relative errors are presented in Table 8.8; which indicates the relative error in the $\overline{F^{f\to p}}$ for 95% of the particles is between these values. The HR model tends to underestimate the $\overline{F^{f\to p}}$ especially for looser packings, and the mean relative error can reach -37.1% for the linearly graded packings considered. On the other hand, the mean relative errors using the $\alpha_{\text{ER-HR}}(e^*)$ model are between -12.2% and 8.2% and the mean relative errors for the $\alpha_{\text{ER-HR}}(\xi)$ model are between 0.4% and 13.4%. 95% of the relative error values using the $\alpha_{\text{ER-HR}}(e^*)$ model between -25.1% and 12.6% and if the $\alpha_{\text{ER-HR}}(\xi)$ model is used, the values are from -9.5% to 18.6%. The results presented in Table 8.8 demonstrate the reliability of a PNM using either $\alpha_{\text{ER-HR}}(e^*)$ or $\alpha_{\text{ER-HR}}(\xi)$ for simulating fluid flow through a linearly graded sphere packing with $Cu = 1.01 - 2.00$.

For the gap graded samples with $SR = 2$, the normalised fluid-particle interaction forces obtained from a PNM with the three types of local conductance models are compared with those obtained from the OF in Fig. 8.38 and Fig. 8.39. In Fig. 8.38 and Fig. 8.39, there are two clusters as the coarse particles had a high normalised fluid-particle interaction force. In all the cases, the PNM with the $\alpha_{\text{ER-HR}}(e^*)$ model or $\alpha_{\text{ER-HR}}(\xi)$ can predict the drag coefficient on the particles accurately. The analysis of the relative error in $\overline{F^{f\to p}}$ is summarised in Table 8.9. For the PNM with the $\alpha_{\text{ER-HR}}(e^*)$ model or $\alpha_{\text{ER-HR}}(\xi)$, the mean relative error values are within ±10% and 95% of the relative error values are within ±20%.

Fluid-particle interaction forces acting on particles in gap graded samples with $SR = 4$ were calculated using the three types of local conductance models; namely *HR*, $\alpha_{\text{ER-HR}}(e^*)$,

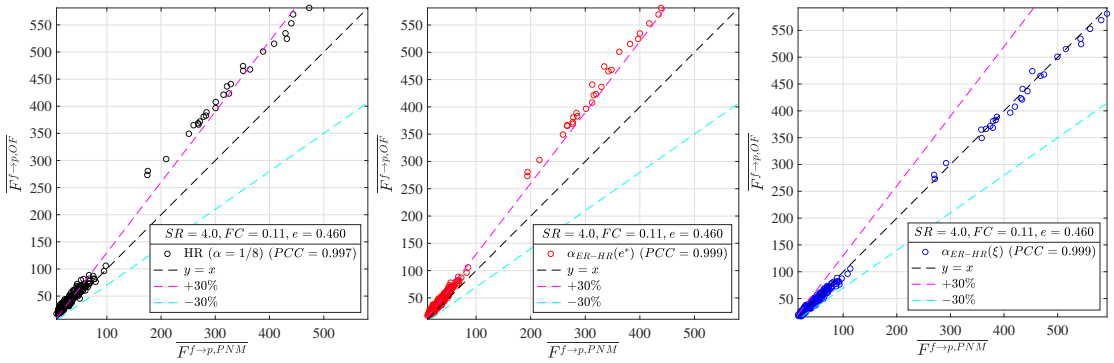
Table 8.8: Relative error analysis in the $\overline{F^{f\to p}}$ values between OF, PNMs, and empirical method for linearly graded samples.

Cu	e	PNM									Ergun		
		$\alpha_{\text{HR}} = 1/8$			$\alpha_{\text{ER-HR}}(e^*)$			$\alpha_{\text{ER-HR}}(\xi)$					
		Mean	2.5th	97.5th	Mean	2.5th	97.5th	Mean	2.5th	97.5th	Mean	2.5th	97.5th
1.01	0.764	-35.0	-41.9	-29.8	-3.1	-9.3	2.0	2.7	-1.5	6.1	-4.0	-29.9	34.9
	0.61	-24.0	-31.3	-18.4	0.1	-5.1	4.2	4.8	1.1	8.4	-2.1	-31.6	38.5
	0.536	-9.2	-18.4	-2.2	8.2	2.1	12.6	13.4	8.8	17.5	0.5	-29.6	44.7
1.20	0.764	-31.6	-39.6	-25.2	-2.6	-10.1	4.4	3.6	-2.0	8.7	-4.0	-32.5	39.2
	0.613	-20.9	-28.6	-15.0	0.8	-5.0	6.5	6.0	1.7	10.4	-2.5	-30.9	39.3
	0.555	-12.7	-21.6	-5.6	5.5	-1.0	10.9	11.5	6.4	16.1	1.2	-28.7	44.5
1.50	0.761	-33.0	-42.6	-26.3	-5.4	-14.4	2.1	2.9	-3.0	8.7	-3.4	-37.6	47.5
	0.61	-24.0	-32.4	-17.9	-3.1	-10.4	4.4	3.4	-1.5	9.3	-3.1	-33.9	40.5
	0.529	-12.4	-22.4	-4.2	2.0	-4.9	9.3	9.2	3.5	15.8	0.2	-31.5	51.5
2.00	0.751	-37.1	-49.9	-27.6	-12.2	-25.1	-1.6	0.4	-9.5	8.5	-4.1	-40.8	53.3
	0.603	-29.0	-42.6	-20.2	-9.6	-20.1	-0.3	2.3	-5.2	11.2	-1.4	-40.0	68.1
	0.468	-11.8	-21.9	0.2	-3.2	-12.0	7.2	8.4	1.3	18.6	-2.2	-33.4	38.4



(a) *HR* model. **(b)** $\alpha_{\text{ER-HR}}(e^*)$. **(c)** $\alpha_{\text{ER-HR}}(\xi)$.

Figure 8.39: Comparison of the normalised drag force obtained from the OF and PNM simulations for bimodal PSD with $SR = 2$, $FC = 0.35$, $e = 0.608$.



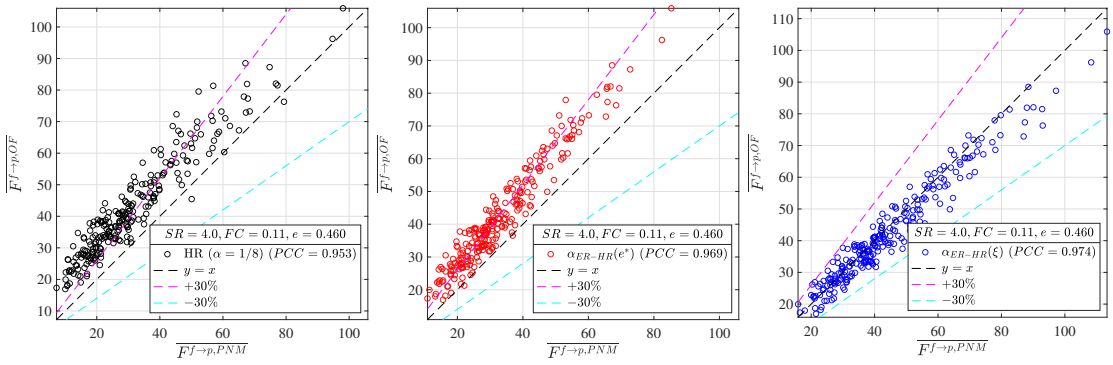
(a) *HR* model. **(b)** $\alpha_{\text{ER-HR}}(e^*)$. **(c)** $\alpha_{\text{ER-HR}}(\xi)$.

Figure 8.40: Comparison of the normalised drag force obtained from the OF and PNM simulations for bimodal PSD with $SR = 4$, $FC = 0.11$, $e = 0.460$.

and $\alpha_{\text{ER-HR}}(\xi)$ models. Fig. 8.40 shows the comparison the drag coefficients on all the particles in the sample with $SR = 4$, $FC = 0.11$, $e = 0.460$ predicted using these models with those obtained from the OF simulations. Fig. 8.41 is a similar plot but limited for fine particles. Considering Fig. 8.40(a) and (b) and Fig. 8.41(a) and (b), the *HR* and $\alpha_{\text{ER-HR}}(e^*)$ models give roughly 30% of errors for fine and coarse particles. Fig. 8.40(c) and Fig. 8.41(c) show that the $\alpha_{\text{ER-HR}}(\xi)$ model successfully address the problem and predicted the drag coefficient on the particles accurately. A similar comparison was made for $SR = 4$, $FC = 0.35$, $e = 0.536$ in Fig. 8.42 for all the particles and Fig. 8.43 for fine particles only, where the effectiveness of the $\alpha_{\text{ER-HR}}(\xi)$ model is clearly seen. The relative error analysis for $SR = 4$ is presented in Table 8.9. With the $\alpha_{\text{ER-HR}}(\xi)$ model, the mean relative error is within ±16% and the 95% of the relative error data are within ±25%.

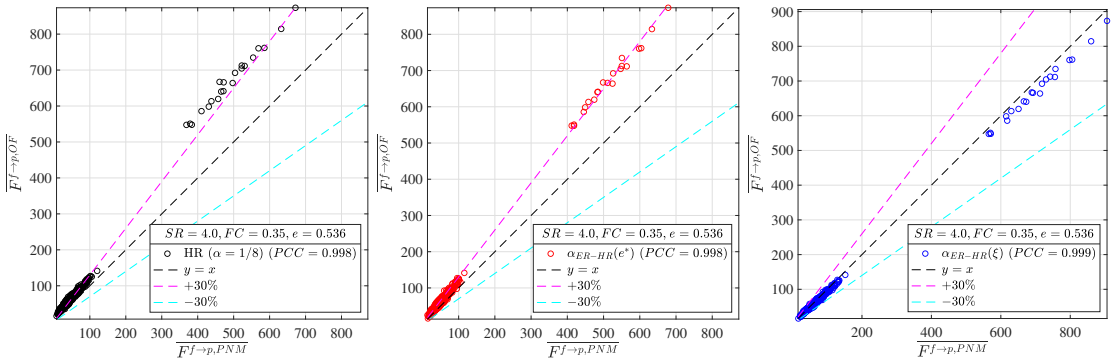
8.6.2 Comparison with an empirical method

Normalised fluid-particle interaction forces ($\overline{F^{f\to p}}$) obtained from OF, a PNM with the $\alpha_{\text{ER-HR}}(\xi)$ model, and the empirical method introduced in Section 8.4.4 are compared in



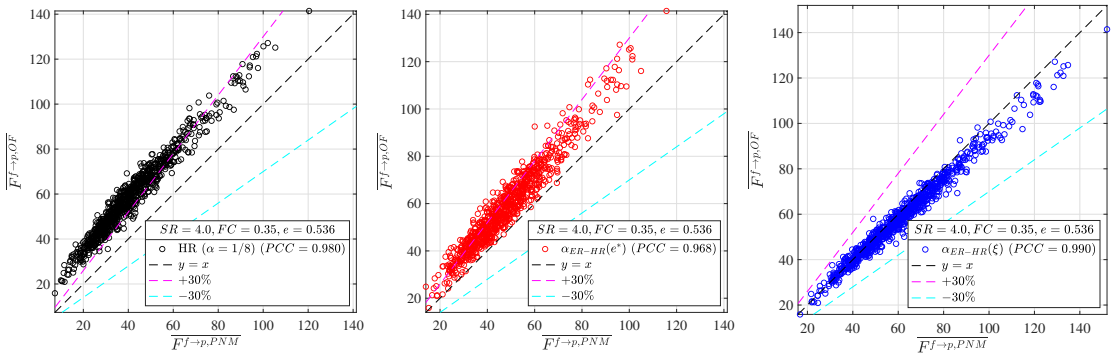
(a) *HR* model. **(b)** $\alpha_{\text{ER-HR}}(e^*)$. **(c)** $\alpha_{\text{ER-HR}}(\xi)$.

Figure 8.41: Comparison of the normalised drag force on fine particles obtained from the OF and PNM simulations for bimodal PSD with $SR = 4$, $FC = 0.11$, $e = 0.460$.



(a) *HR* model. **(b)** $\alpha_{\text{ER-HR}}(e^*)$. **(c)** $\alpha_{\text{ER-HR}}(\xi)$.

Figure 8.42: Comparison of the normalised drag force obtained from the OF and PNM simulations for bimodal PSD with $SR = 4$, $FC = 0.35$, $e = 0.536$.



(a) *HR* model. **(b)** $\alpha_{\text{ER-HR}}(e^*)$. **(c)** $\alpha_{\text{ER-HR}}(\xi)$.

Figure 8.43: Comparison of the normalised drag force on fine particles obtained from the OF and PNM simulations for bimodal PSD with $SR = 4$, $FC = 0.35$, $e = 0.536$.

Table 8.9: Relative error analysis in the $\overline{F^{f\to p}}$ values between OF, PNMs, and empirical method for bimodal samples.

SR	FC	e	PNM									Ergun		
			$\alpha_{\text{HR}} = 1/8$			$\alpha_{\text{ER-HR}}(e^*)$			$\alpha_{\text{ER-HR}}(\xi)$					
			Mean	2.5th	97.5th	Mean	2.5th	97.5th	Mean	2.5th	97.5th	Mean	2.5th	97.5th
2	0.1	0.61	-20.7	-34	-8.3	-2.4	-12.2	6.0	7.1	-0.3	15.5	-2.6	-38.3	57.9
		0.524	-14.7	-24.0	-3.8	-1.5	-9.0	8.2	8.0	1.8	16.4	-0.9	-34.3	55.5
	0.35	0.608	-22.3	-34.3	-12	-4.3	-14.3	6.5	8.3	0.8	15.7	1.5	-37.6	60.5
		0.486	-10.4	-22.5	-1.3	-0.4	-9.8	8.4	5.0	-1.6	11.7	1.5	-36.3	54.7
4	0.11	0.55	-39.4	-59.5	-20.3	-27.3	-44.8	-11.6	-0.9	-20.5	19.4	0.1	-50	91.5
		0.46	-28.5	-52.6	-5.5	-22.6	-41.0	-4.8	3.5	-16.5	24.4	3.6	-51.7	93.3
	0.35	0.536	-31.3	-48	-16.0	-18.7	-33.4	-5.0	4.0	-6.8	14.9	0.7	-49.8	76.6
		0.351	-3.5	-19.4	10.0	-8.2	-21.5	5.3	16.0	8.1	24.9	5.9	-33.8	70.4

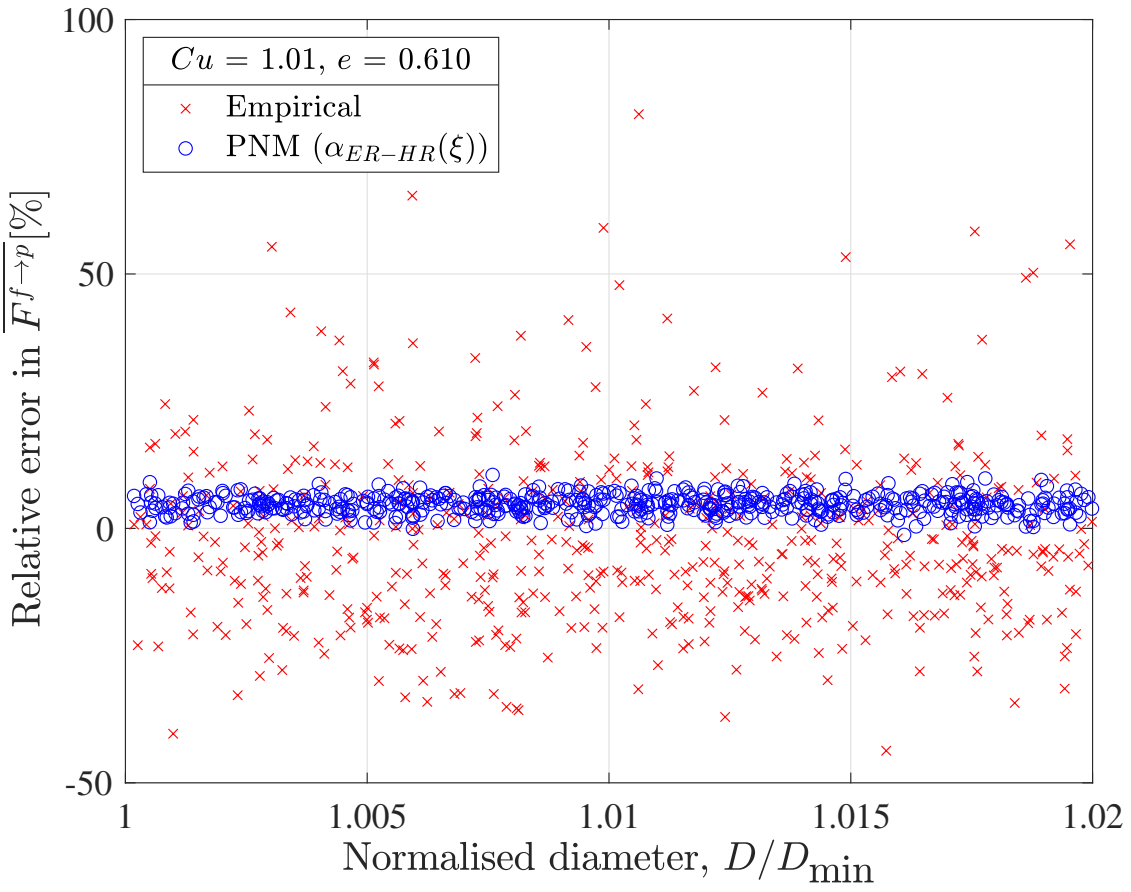


Figure 8.44: Relative error in normalised fluid-particle interaction force versus particle diameter normalised by D_{min} for the linearly graded random dense packing with $Cu = 1.01$, $e = 0.610$.

this section to explore the accuracy of the PNM-based approach relative to the commonly used unresolved DEM-CFD approach outlined Section 8.4.4. The relative errors in the $\overline{F^{f\to p}}$ values are plotted against the particle diameters normalised by the minimum diameter D_{min} for $Cu = 1.01$ and $e = 0.610$ (Fig. 8.44) and $Cu = 2.00$ and $e = 0.603$ (Fig. 8.45). As explained in Section 8.4.4, the empirical method only depends on the diameter of the particles; therefore, if the sample is monodisperse, the empirical method gives a constant fluid-particle interaction force value for every particle. However, the $\overline{F^{f\to p}}$ values obtained from the OF simulations are heterogeneous even in a monodisperse sample with $Cu = 1.01$, and consequently the empirical method gives large error values for some particles as can be seen in Fig. 8.44. As shown in Table 8.8, the 2.5th percentile and 97.5th percentile of the relative errors were -31.6% and 38.5%, respectively. On the other hand, this heterogeneity in the $\overline{F^{f\to p}}$ values can be captured by a PNM with the $\overline{F^{f\to p}}$ model as Fig. 8.44 and Table 8.8 show that most of relative errors are between 1.1% and 8.4%.

Fig. 8.45 shows a similar plot to Fig. 8.44 for a polydisperse system with $Cu = 2.0$ and $e = 0.603$. The empirical method gives large error values for small particles and the error value reached 100%. On the other hand, the relative error for the PNM with the $\alpha_{\text{ER-HR}}(\xi)$ model is mostly below ±10%.

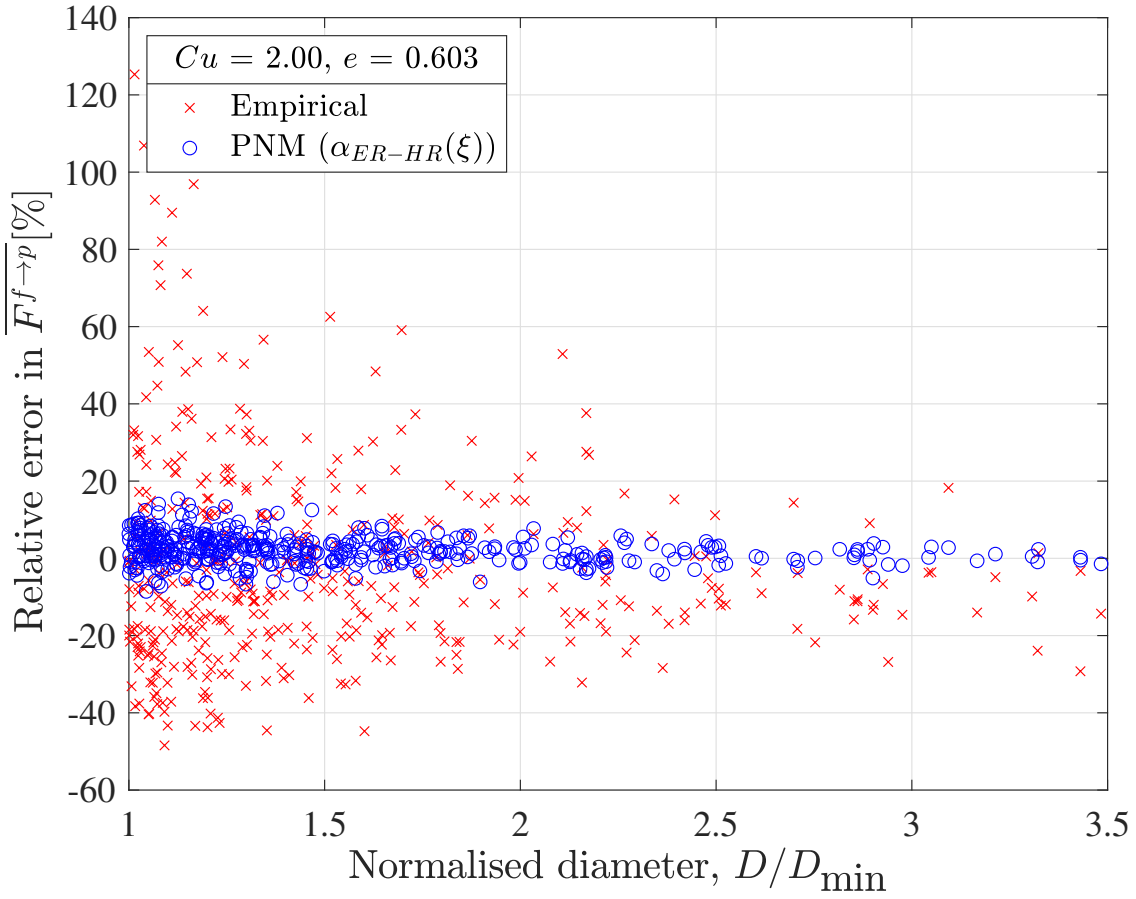


Figure 8.45: Relative error in normalised fluid-particle interaction force versus particle diameter normalised by D_{min} for the linearly graded random dense packing with $Cu = 2.00$, $e = 0.603$.

The analysis of the relative error values in the $\overline{F^{f\to p}}$ values obtained from the empirical method is presented in Table 8.8. The mean relative error values by the empirical method are within ±5%; however, the scatters observed in Fig. 8.44 and Fig. 8.45 are reflected as the large relative errors in the 2.5th and the 97.5th values.

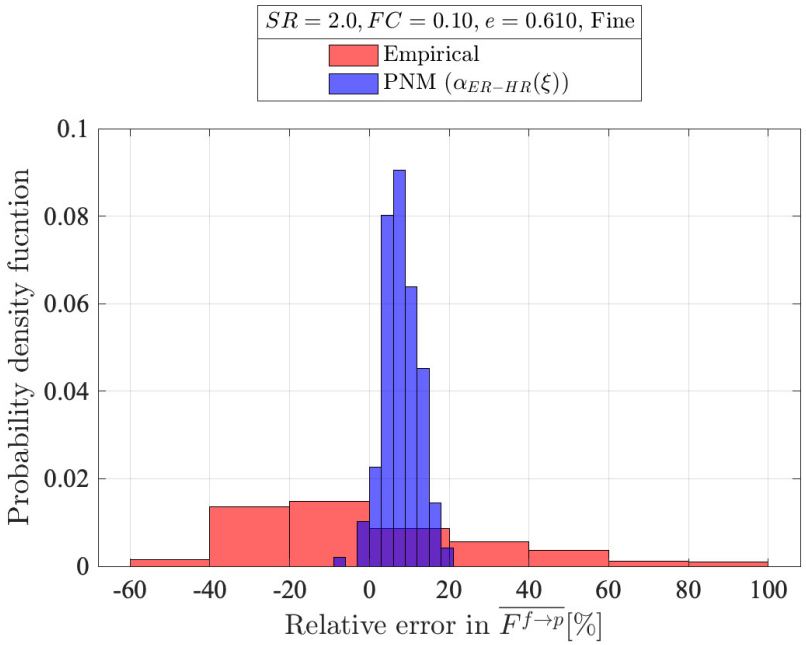
The performance of the empirical method and the PNM with the $\alpha_{\text{ER-HR}}(\xi)$ model was compared for the gap graded samples. Fig. 8.46 shows the probability density functions of the relative error values in $\overline{F^{f\to p}}$ for (a) fine particles and (b) coarse particles in the sample with $SR = 2$, $FC = 0.10$, and $e = 0.610$. Fig. 8.46(a) and (b) clearly show that the error range for the PNM with the $\alpha_{\text{ER-HR}}(\xi)$ is much narrower than that for the empirical method.

Similar plots were created for $SR = 4$, $FC = 0.11$, and $e = 0.460$ (Fig. 8.47). The prediction made by the PNM with the $\alpha_{\text{ER-HR}}(\xi)$ model is much more accurate than the prediction made by the empirical method. The empirical method tends to give a larger error for fine particles than for coarse particles, which questions the reliability of the coarse-grid CFD to simulate particle migration.

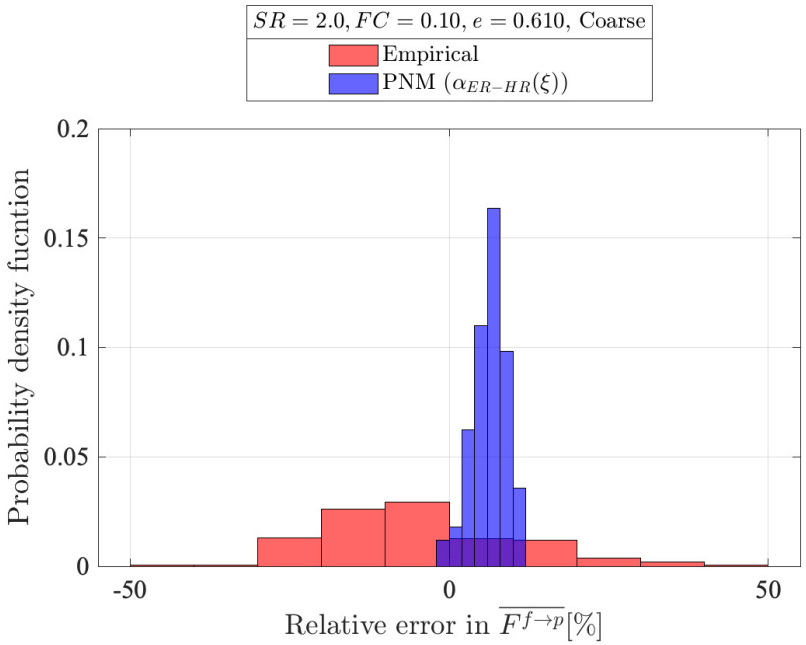
It is important to predict correctly both the magnitude and orientation of the fluid-particle interaction forces. The fluid-particle interaction force direction predicted by a coarse-grid approach coincides with the global flow direction (Eqs. (8.51) to (8.55)). On the other hand, as can be seen in Eqs. (8.13) to (8.16), a PNM gives not only the magnitude but also the direction of the fluid-particle interaction force, which can be a significant advantage over a coarse gird approach. To clarify it, the angle ($\theta^{\mathbf{F}}{}_{\text{PNM}}$) between the force vectors obtained from OF and PNM was analysed (defined in Fig. 8.48). Fig. 8.48 defines the angle between the force vector obtained from OF and the global flow direction ($\theta^{\mathbf{F}}{}_{\text{global}}$), which can be interpreted as the error in predicting the force direction by a coarse-grid approach. Fig. 8.49 shows that the direction of the fluid-particle interaction force does not always coincide with the global flow direction, which indicates the limitation of coarse-grid CFD-DEM approaches. On the other hand, a PNM with the $\alpha_{\text{ER-HR}}(\xi)$ model can predict the fluid-particle interaction force direction well, with most of the $\cos\theta^{\mathbf{F}}$ values being between 0.98 and 1 for both of (a) a linearly graded PSD with $Cu = 2.00$ and (b) a gap graded PSD with $SR = 4.0$.

8.7 Summary

This chapter compared three types of CFD techniques, namely a PNM, a fully-resolved CFD technique and a coarse-grid CFD under the condition where particle positions are fixed. Section 8.2 discussed the PNM simulation process and presented a variety of local conductance models, which determine the accuracy of a PNM. Section 8.3 outlined the development of local conductance models using three types of regular packings. The

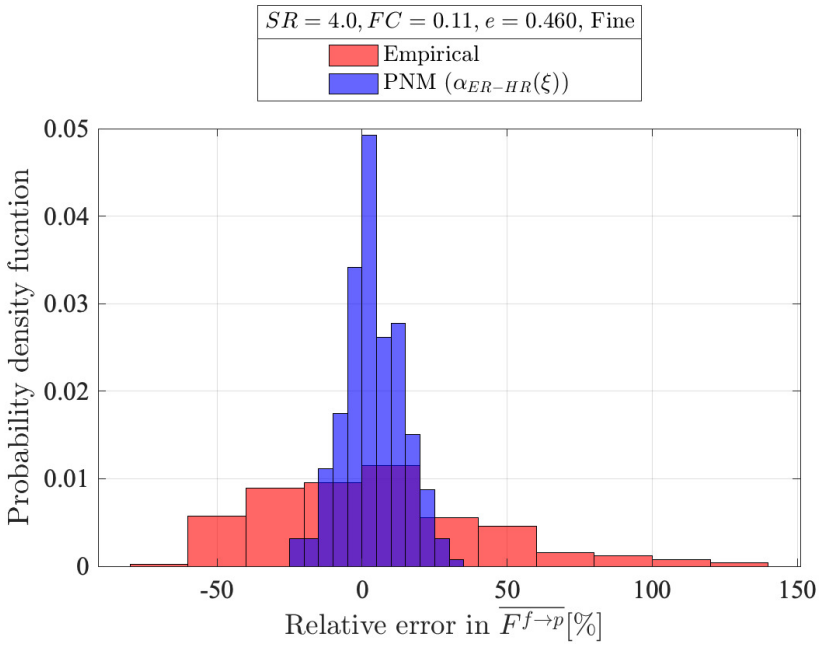


(a) Fine particles.

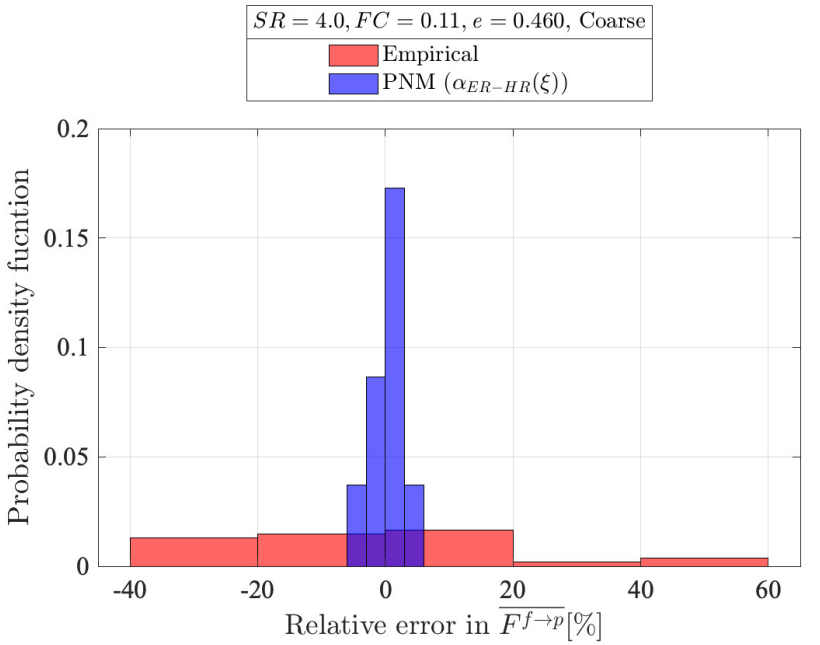


(b) Coarse particles.

Figure 8.46: Probability density function of relative error in $\overline{F^{f\to p}}$ for the bimodal random dense packing with $SR = 2$, $FC = 0.10$ and $e = 0.610$.



(a) Fine particles.



(b) Coarse particles.

Figure 8.47: Probability density function of relative error in $\overline{F^{f\to p}}$ for the bimodal random dense packing with $SR = 4$, $FC = 0.11$ and $e = 0.460$.

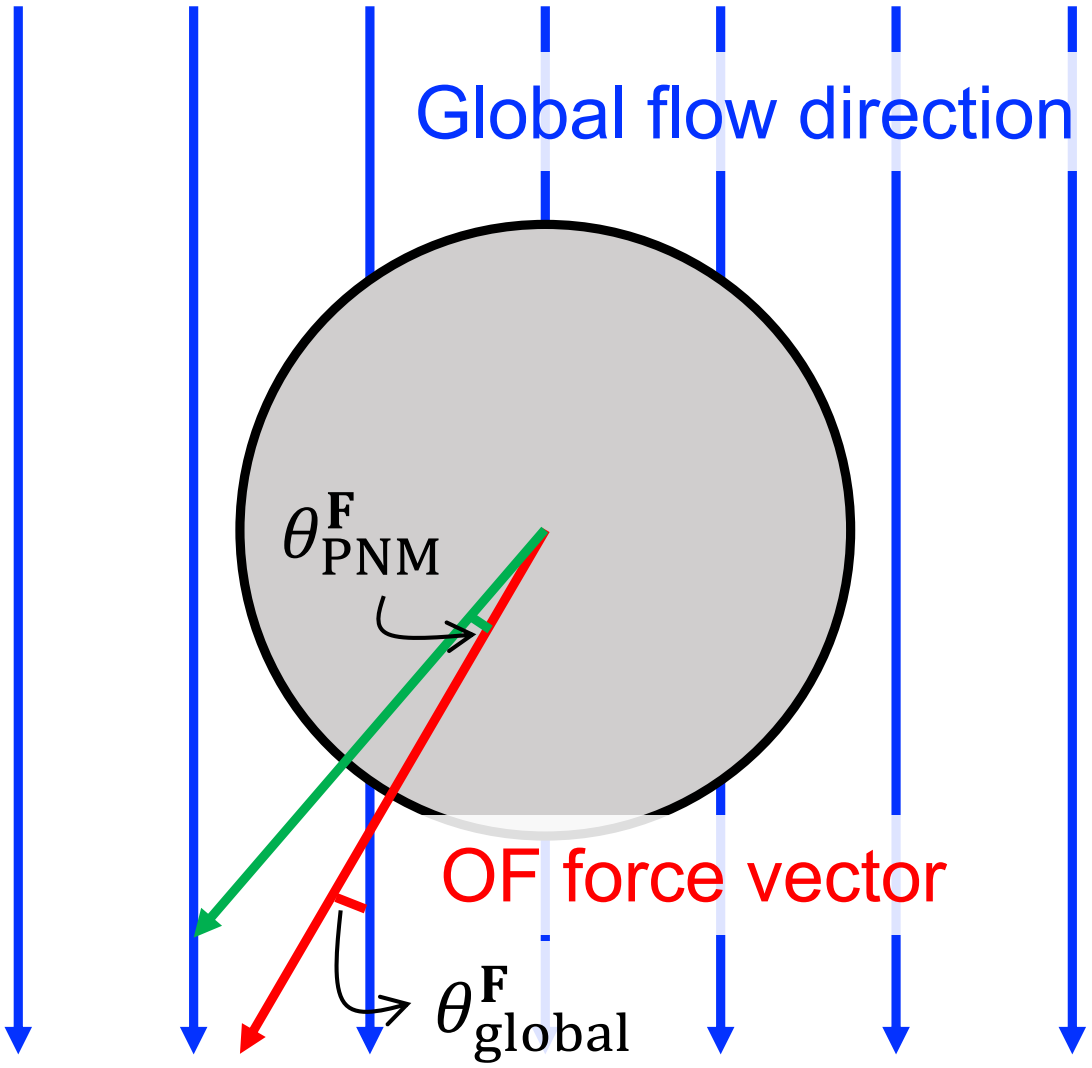
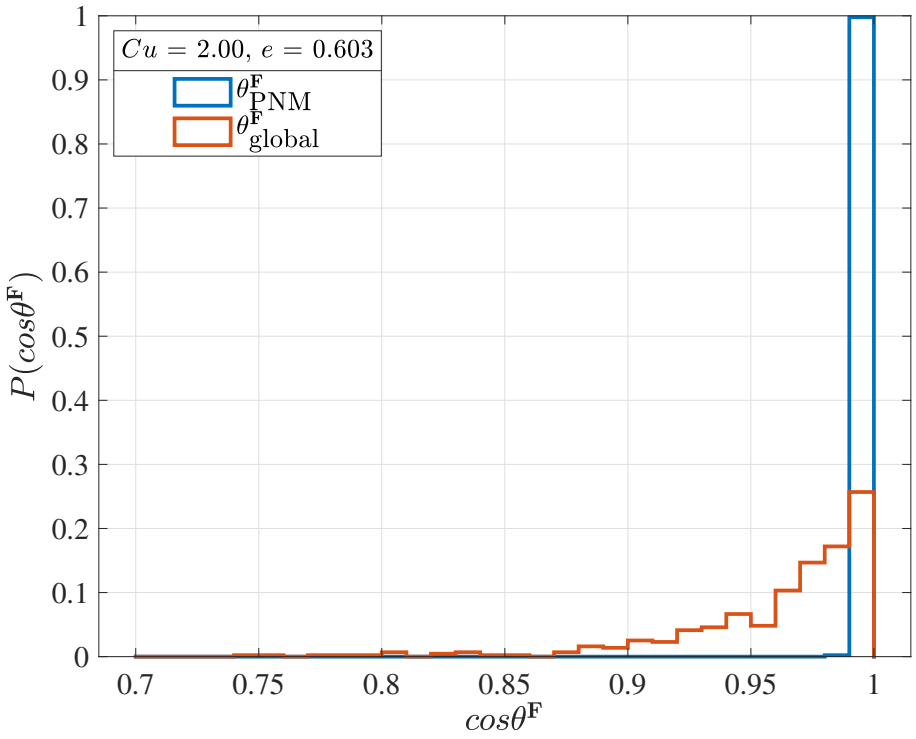
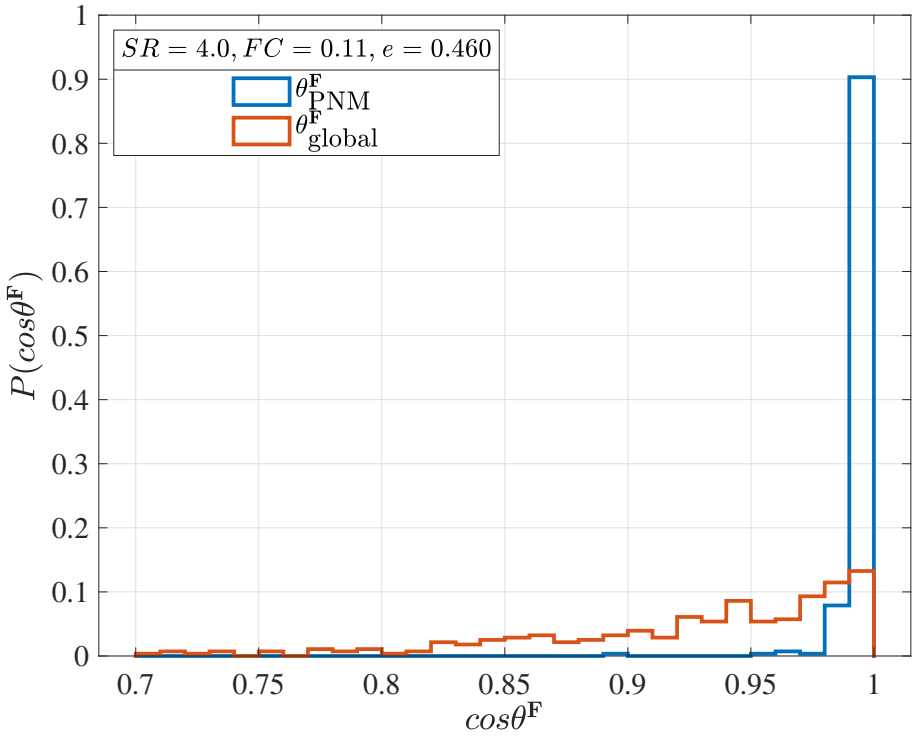


Figure 8.48: Schematic illustration on the definition of $\theta^{\mathbf{F}}{}_{\mathrm{PNM}}$ and $\theta^{\mathbf{F}}{}_{\mathrm{global}}$.



(a)



(b)

Figure 8.49: The probability distribution of $\cos\theta^{\mathbf{F}}$. For PNM, $\alpha_{\text{ER-HR}}(\xi)$ model was used. (a) Linearly graded PSD with $Cu = 2.00$ and $e = 0.603$ (b) Gap graded PSD with $SR = 4.0$, $FC = 0.11$, and $e = 0.11$.

methodology and implementation of a PNM, a fully-resolved CFD, and a coarse-grid CFD were explained in Section 8.4, and the results from the three methods were compared in Section 8.5 in terms of local and global flow rates and in Section 8.6 in terms of particle-fluid interaction force.

Section 8.2.1 gave the overall process of PNMs and describes how the choice of local conductance models determines the accuracy of the PNM. Section 8.2.2 reviewed existing and novel local conductance models. Section 8.2.3 showed the process of fluid-particle interaction force calculation developed by Chareyre et al. (2012).

The drag coefficient c_{d} values for each particle in three types of regular packings with a variety of packing densities are available from Zick and Homsy (1982) and the c_{d} values can be associated with the global permeability as shown in Section 8.3.1. From the global permeability values of the regular packings, the local conductance values can be back-calculated by taking advantage of the symmetry of the regular packings (Section 8.3.2). The back-calculated local conductance models of the packings were used to calculate the shape factor (α) value of the packings and the unique expressions of the α value for the three type of regular packings with a variety of e values were derived in Section 8.3.3.

Section 8.4 described the simulation procedure of the three types of the CFD techniques. Sections 8.4.1 and 8.4.2 outlined the detailed implementation and simulation procedure for a PNM. Section 8.4.4 explained the simulation and post-process procedures of the fully-resolved CFD simulations, which were conducted to assess the accuracy of a PNM with a variety of local conductance models and an empirical fluid-particle interaction force calculation used in a coarse-grid CFD. The process of the fluid-particle interaction force calculation is outlined in Section 8.4.4.

Section 8.5 compared a PNM with a variety of local conductance models and a fully-resolved CFD. Section 8.5.1 pointed out the limitation of a PNM framework itself when dilute packings are considered. Sections 8.5.2 to 8.5.4 compared a PNM with a variety of local conductance models and a fully-resolved CFD in terms of the local conductance values, and the novel $\alpha_{\text{ER-HR}}(\xi)$ model was the most robust local conductance model which is applicable for both of linearly graded and bimodal samples. Section 8.5.5 compared the global permeability k_{h} value and showed that a PNM with the $\alpha_{\text{ER-HR}}(\xi)$ model predicted the k_{h} values of the packings considered in this study with a relative error smaller than 13.0% without any calibration procedure.

Fluid-particle interaction force vectors obtained from a PNM with a variety of local conductance models, a fully-resolved CFD, and a coarse-grid CFD were compared in terms of the magnitude and the direction of the vectors in Section 8.6. Section 8.6.1 focused on the comparison between a PNM with a variety of local conductance models and a fully-

resolved CFD, and the accuracy of a PNM with the $\alpha_{\text{ER-HR}}(\xi)$ model was demonstrated. The heterogeneity in the magnitude and direction of the fluid-particle interaction force vector on a particle was observed from the fully-resolved CFD as shown in Sections 8.6.1 and 8.6.2; however, a coarse-grid CFD based on an empirical method cannot capture this heterogeneity as shown in Section 8.6.2 because the magnitude of the force vector is only based on the particle diameter and the direction of the force vector reflects only the global flow direction in such a method. On the other hand, a PNM with the $\alpha_{\text{ER-HR}}(\xi)$ model captures the heterogeneity of the flow field, and can predict the fluid-particle interaction force on 95% of the particles in the samples considered within an error of $+/-25\%$. In addition, the prediction of the direction of the fluid-particle interaction force made by a PNM with the $\alpha_{\text{ER-HR}}(\xi)$ model was found to be nearly perfect.

CHAPTER 9

PORE-SCALE MODELLING OF HEAT TRANSPORT DUE TO ADVECTION AND CONDUCTION

9.1 Introduction

There is a growing need to model heat transfer through soil and temperature effects on soil due to the rise in popularity of thermo-active geostructures. Chapters 3 to 6 discussed the scenario where the pore fluid is stagnant; however, if there is ground water flow, the contribution of the advective heat transfer needs to be taken into account. In addition, systems using packed bed energy storage circulate fluid to store or extract heat quickly. Therefore, a CFD-DEM framework considering heat transfer is beneficial for a number of practical applications.

PNMs have advantages in terms of accuracy (in comparison with unresolved CFD-DEM) and cost-efficiency (in comparison with fully resolved CFD-DEM) as discusseed in Chapter 8. Caulk et al. (2020) proposed a thermally-coupled PNM framework; however, their idea needs further refinement especially in terms of the model predicting the conductive heat transfer between the fluid and the particles (particle-fluid conduction hereinafter) they used since their model parameters are calculated considering only the global Reynolds number (Re) and the global solid fraction as proposed by Gunn (1978) and Tavassoli, Peters and Kuipers (2015). This chapter provides a novel particle-fluid heat transfer model inspired by studies on wall-fluid heat transfer in pipes.

9.2 Characterising particle-fluid conduction using the Nusselt number

9.2.1 Energy transport equation and the role of the Nusselt number in a CFD-DEM framework

As discussed in Chapter 7, a CFD-DEM framework is required to accurately simulate heat transfer in a granular medium if the pore fluid is flowing in the medium.

Heat transfer in the pore fluid in granular materials is governed by the advection diffusion equation (or energy transport equation), introduced in Eq. (7.3). Adding a source term, η, which represents the energy input per volume via particle-fluid conduction (in W/m^3), the advection diffusion equation is rewritten as:

$$\rho_{\mathrm{f}} c_{\mathrm{f}} \frac{\partial T}{\partial t} + \rho_{\mathrm{f}} c_{\mathrm{f}} (\mathbf{u} \cdot \nabla T) = k_{\mathrm{f}} \nabla^2 T + \eta \tag{9.1}$$

Here, the fluid velocity is assumed to be small so that the viscous dissipation is negligible. This is a reasonable assumption for ground source energy applications. In a FVM, taking advantage of the divergence theorem, Eq. (9.1) is rewritten as

$$\frac{\partial}{\partial t} \int_V \rho_{\mathrm{f}} c_{\mathrm{f}} T \mathrm{d}V + \int_{\partial V} \rho_{\mathrm{f}} c_{\mathrm{f}} T (\mathbf{u} \cdot \mathbf{n}) \mathrm{d}A = \int_{\partial V} k_{\mathrm{f}} (\nabla T \cdot \mathbf{n}) \mathrm{d}A + \int_V \eta \mathrm{d}V \tag{9.2}$$

where

- $\frac{\partial}{\partial t} \int_V \rho_{\mathrm{f}} c_{\mathrm{f}} T \mathrm{d}V$ is the time derivative of the energy of the fluid cell and is equal to zero at a steady state.
- $\int_{\partial V} \rho_{\mathrm{f}} c_{\mathrm{f}} T (\mathbf{u} \cdot \mathbf{n}) \mathrm{d}A$ represents the fluid advection term.
- $\int_{\partial V} k_{\mathrm{f}} (\nabla T \cdot \mathbf{n}) \mathrm{d}A$ represents the fluid conduction (diffusion) term.
- $\int_V \eta \mathrm{d}V$ represents the particle-fluid conduction term.

Henceforth the particle-fluid conduction term $\int_V \eta \mathrm{d}V$ is denoted as H.

Energy transport equation in thermal PNM

Caulk et al. (2020) proposed a thermal PNM framework by considering the energy transport equation (Eq. (9.2)). The first term in Eq. (9.2) is rewritten using the fluid volume, V_{f}, of pore a as

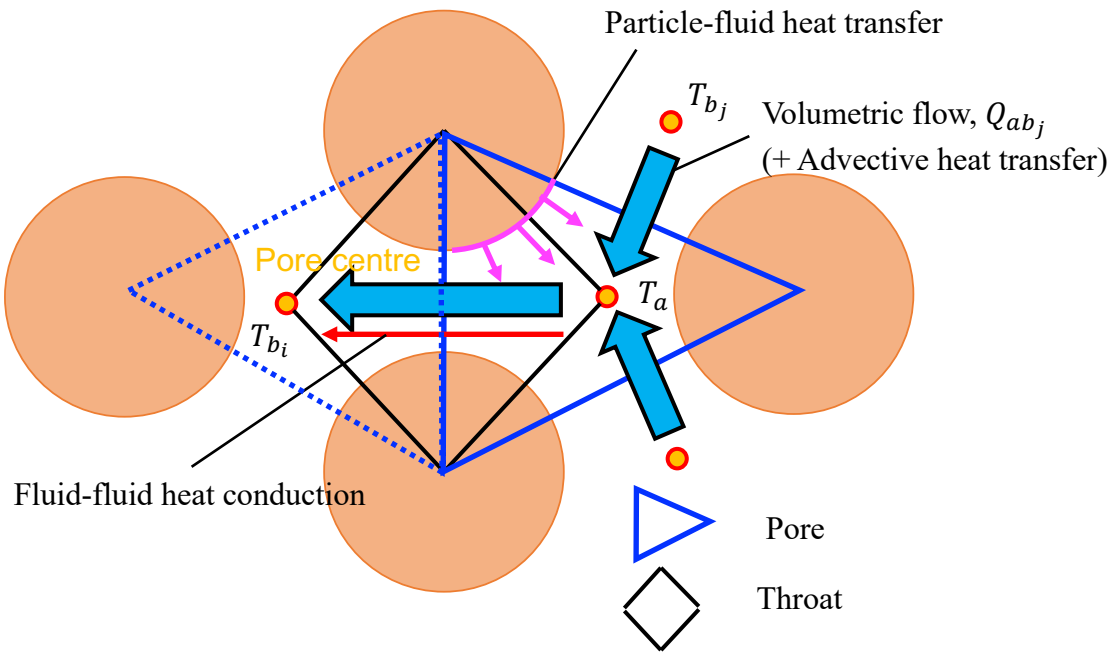


Figure 9.1: Schematic illustration of the thermal PNM proposed by Caulk et al. (2020) (in 2D for simplicity).

$$\frac{\partial}{\partial t}\int_V \rho c_{\mathrm{f}} T_{\mathrm{f}} \mathrm{d}V = \frac{\partial}{\partial t}(\rho_{\mathrm{f}} c_{\mathrm{f}} T_{\mathrm{f},a} V_{\mathrm{f}}) \tag{9.3}$$

where $T_{\mathrm{f},a}$ is the temperature of pore a, which is defined at the node of pore a. Following Chareyre et al. (2012), Caulk et al. (2020) considered the Voronoi vertices to be the nodes. The second term (the fluid advection term) can be rewritten as

$$\int_{\partial V} \rho_{\mathrm{f}} c_{\mathrm{f}} T_{\mathrm{f}} (\mathbf{u}\cdot\mathbf{n}) \mathrm{d}A = \sum_{i=1}^{4} \rho_{\mathrm{f}} c_{\mathrm{f}} T_{\mathrm{f},ab_i} Q_{ab_i} \tag{9.4}$$

where Q_{ab_i} is the volumetric flow rate from pore a to pore b_i and T_{f,ab_i} is the temperature of the throat connecting pore a and b_i (illustrated in Fig. 8.3). Caulk et al. (2020) proposed defining $T_{\mathrm{f},ab}$ as

$$T_{\mathrm{f},ab_i} = \begin{cases} T_{\mathrm{f},a} & (Q_{ab_i} > 0) \\ T_{\mathrm{f},b} & (Q_{ab_i} < 0) \end{cases} \tag{9.5}$$

In other words, in the approach by Caulk et al. (2020), the temperature value of the upstream pore node determines T_{ab_i}. While not explicitly stated by Caulk et al. (2020), this approach of defining the face temperature value is known as the first-order "upwind" scheme (Versteeg & Malalasekera, 2007; Niyogi, 2009) in CFD.

The third term, representing fluid conduction, was rewritten by Caulk et al. (2020) as

$$\iint_A k_{\mathrm{f}}(\nabla T \cdot \mathbf{n})\mathrm{d}A = \sum_{i=1}^{4} k_{\mathrm{f}} \frac{T_{b_i} - T_a}{L_{ab_i}} A_{\mathrm{f},ab_i} \tag{9.6}$$

where A_{f,ab_i} is the area of the fluid phase of the face connecting pores a as b defined in Fig. 8.2.

The final term, H, is the sum of the heat transfer rate between pore a and particle k_i ($i = 1, 2, 3, 4$) which bound the pore. This can be expressed as

$$H = \sum_{i=1}^{4} H_{k_i a} \tag{9.7}$$

Denoting the surface area of particle k that bounds pore a as γ_{ka} as illustrated in Fig. 8.3, the mean heat flux from the surface of particle k to pore a is H_{ka}/γ_{ka}. The heat transport coefficient h (in [W/(m^2·K)]) is defined as the mean heat flux from the solid surface divided by a "temperature driving force" ϑ, which is defined using the temperatures of the solid surface and the fluid:

$$h_{ka} = \frac{H_{ka}/\gamma_{ka}}{\vartheta_{ka}} \tag{9.8}$$

The definition of ϑ proposed by Caulk et al. (2020) is simply the difference between the solid surface temperature $T_{\mathrm{s},k}$ and the pore fluid temperature $T_{\mathrm{f},a}$.

$$\vartheta = T_{\mathrm{s},k} - T_{\mathrm{f},a} \tag{9.9}$$

Caulk et al. (2020) proposed calculating the h value from the Nusselt number, which is defined as

$$Nu_{\mathcal{L}} = \frac{h\mathcal{L}}{k_{\mathrm{f}}} \tag{9.10}$$

where $\mathcal{L}$ is a characteristic length. Caulk et al. (2020) proposed use of the diameter of particle k as a characteristic length. Therefore, in Caulk et al. (2020), the Nusselt number for particle k and pore a was written as

$$Nu_{D_k,ka} = \frac{h_{ka} D_k}{k_{\mathrm{f}}} \tag{9.11}$$

Combining Eqs. (9.7) to (9.9) and (9.11),

$$H = \sum_{i=1}^{4} Nu_{D_k,k_i a} \frac{\gamma_{k_i a} k_{\mathrm{f}} (T_{\mathrm{s},k_i} - T_{\mathrm{f},a})}{D_{k_i}} \tag{9.12}$$

In existing CFD-DEM frameworks, which include Caulk et al. (2020) as well as Shimizu (2006) and Kloss et al. (2012), the Nusselt number is calculated from empirical correlations developed from either experimental data or numerical simulation data. A tabular summary of existing models calculating the Nusselt number and their application to existing CFD-DEM frameworks is shown in Table 9.1. It can be seen that the Nusselt number has been correlated to the Reynolds number (defined in Eq. (7.12)), the Prandtl number (defined in Eq. (7.19)), and the porosity of the granular packing (n). Peng, Doroodchi and Moghtaderi (2020) also provides a useful summary of models to calculate the Nusselt number. Amongst the models reviewed in Table 9.1, Caulk et al. (2020) used Tavassoli, Peters and Kuipers (2015)'s model which gives the Nusselt number as:

$$Nu_{ka} = (7 - 10n_a + 5n_a^2)(1 + 0.1Re_a^{1/5} Pr_a^{1/3}) + (1.33 - 2.19n_a + 1.15n_a^2) Re_a^{0.7} Pr_a^{1/3} \tag{9.13}$$

where n_a is the porosity of pore a, Re_a is the Reynolds number at pore a, and Pr_a is the Prandtl number at pore a.

9.2.2 Another perspective: Nusselt number of fluid flow in a pipe

In the previous section (Section 9.2.1), the calculation and application of the Nusselt number to existing CFD-DEM frameworks were discussed. Caulk et al. (2020) proposed a pragmatic thermal PNM-DEM framework; however, the calculation of the Nusselt number was derived from the global porosity, the global Reynolds number, and the global Prandtl number by Tavassoli, Peters and Kuipers (2015) to predict pore-scale heat transfer phenomenon. As discussed in Chapter 8, the advantage of PNMs is their ability to consider local heterogeneities existing in granular packings. The further refinement of the model predicting the Nu value at a pore-scale is therefore possible in a coupling approach that is based on a PNM.

In Section 8.2.2, it was shown that, for the local conductance model of fluid pipes (throats) the PNM, is based on the Hagen-Poiseuille equation for a circular pipe (although some modifications were needed to obtain accurate results). However, there has been no consistent approach, documented in the literature, that calculates a Nusselt number for the throats (edges in PNM) based on the calculation of the Nusselt number of a pipe. This

Table 9.1: Tabular summary of models predicting the Nusselt number

Source	Expression adopted	Also used in
Ranz and Marshall (1952)	$Nu = 2.0 + 0.6Re^{1/2}Pr^{1/3}$ (Single sphere)	
Whitaker (1972)	• $Nu = 2.0 + (0.4Re^{1/2} + 0.06Re^{2/3})Pr^{0.4}$ (Single sphere) • $Nu = (0.5Re^{1/2} + 0.2Re^{2/3})Pr^{0.4}$ (Packed bed)	Shimizu (2006)
Gunn (1978)	$Nu = (7 - 10n + 5n^2)(1 + 0.7Re^{1/5}Pr^{1/3}) + (1.33 - 2.4n + 1.2n^2)Re^{0.7}Pr^{1/3}$	
Li and Mason (2000)	• $Nu = 2 + 0.6n^{3.5}Re^{1/2}Pr^{1/3}$ $(Re < 200)$ •$Nu = 2 + 0.5n^{3.5}Re^{1/2}Pr^{1/3} + 0.02n^{3.5}Re^{0.8}Pr^{1/3}$ $(200 < Re < 1500)$ •$Nu = 2 + 0.000045n^{3.5}Re^{1.8}$ $(Re > 1500)$	Kloss et al. (2012)
Tavassoli, Peters and Kuipers (2015)	$Nu = (7 - 10n + 5n^2)(1 + 0.1Re^{1/5}Pr^{1/3}) + (1.33 - 2.19n + 1.15n^2)Re^{0.7}Pr^{1/3}$	Caulk et al. (2020)

subsection reviews models to predict the Nu of fluid flow in pipes with a range of cross sectional geometries. Specifically, this subsection considers the following points:

- Types of laminar flow in a pipe
- Definition of the bulk fluid temperature T_{f}
- Definition of the temperature driving force ϑ
- Asymptotic value of the Nusselt number of various flow types

Types of laminar flow in a pipe

It has been well-established e.g. Shah and London (1978) that at the entrance to fluid pipes the fluid velocity profile changes along the flow direction as illustrated in Fig. 9.2 and flow in this region is considered to be "hydrodynamically developing flow". Hydrodynamically developing flow is characterised by a hydrodynamic boundary layer thickness δ_h, so that inside hydrodynamic boundary layer the fluid velocity is constant (Fig. 9.2). At a cross-section sufficiently far from the entrance of the pipe, the fluid velocity profile does not change in the flow direction (Fig. 9.2) and this type of flow is often referred to as "hydrodynamically fully-developed flow" (Shah & London, 1978). This change in the velocity profile of flow in a pipe can be characterised by non-dimensional hydrodynamic length L^+ defined as:

$$L^+ = \frac{L}{Re\mathcal{L}} \tag{9.14}$$

where L is the length or position from the entrance of the pipe (Shah & London, 1978; Muzychka & Yovanovich, 2002a) and in this context, a characteristic length $\mathcal{L}$ is chosen so that it represents the cross-sectional geometry of the pipe e.g. the hydraulic diameter of the pipe and the square root of the cross-sectional area of the pipe.

A similar definition of the types of laminar fluid flow in a pipe in terms of the temperature profile can also be made. Fig. 9.3 shows a case where cold fluid flows into a pipe with a constant wall temperature. At the entrance of the pipe, there is a thermal boundary layer where the the hot pipe wall influences the temperature profile of the flowing fluid. The thermal boundary layer grows as the distance from the entrance region L increases. Unlike the velocity profile, the temperature profile keeps changing in the flow direction since there is energy input from the pipe wall. However, at a region far from the entrance region, the heat transport coefficient (defined in Eq. (9.8)) and thus the Nusselt number (Eq. (9.10)) become constant. This region is often called as the thermally fully-developed region. Just as was the case for the hydrodynamic problem, a non-dimensional thermal length can be defined as

$$L^* = \frac{L}{RePr\mathcal{L}} = \frac{L}{Pc\mathcal{L}} \tag{9.15}$$

(Shah & London, 1978; Muzychka & Yovanovich, 2002b), where Pc is the Peclet number defined in Eq. (7.17).

The non-dimensional lengths L^+ and L^* required to reach fully-developed velocity and thermal profiles respectively are approximately:

$$L^+_{\text{fully-developed}} \approx 0.05 \tag{9.16}$$

$$L^*_{\text{fully-developed}} \approx 0.05 \tag{9.17}$$

according to Muzychka (1999) although the values are slightly different in different sources (e.g. Favre-Marinet and Tardu (2013) used $L^+_{\text{fully-developed}} \approx 0.04$ and $L^*_{\text{fully-developed}} \approx 0.04$). Comparing Eq. (9.14) and Eq. (9.15), if $Pr > 1$, $L^+ < L^*$. Supposing that $L^+_{\text{fully-developed}} \approx L^*_{\text{fully-developed}}$, it is possible to have fluid flow which is hydro-dynamically fully-developed but thermally developing for $Pr > 1$. Consequently, fluid flow in a pipe can be classified into:

1. Hydrodynamically and thermally fully-developed flow (Fully-Developed (FD) flow)
2. Hydrodynamically fully-developed but thermally developing flow (Graetz (GZ) flow)
3. Hydrodynamically and thermally developing flow (Simultaneously-Developing (SD) flow)

as in Shah and London (1978) and Muzychka and Yovanovich (2002b) did. In this study, an abbreviation is given for each of the three types of flow. The abbreviations used here for the first (FD) and the third (SD) flow types were given after Shah and London (1978). The abbreviation used here for the second flow type was given because some sources e.g. Bennett (2019a) call this flow type "Graetz flow" (or condition). One may think that if $Pr < 1$ e.g. air, it is possible to have thermally fully-developed but hydro-dynamically developing flow; however, the energy transport equation (Eq. (9.1)) includes an advection term, so it is impossible to have a thermally fully-developed flow profile while the velocity profile is still developing.

This study only considers

1. A constant wall temperature boundary condition
2. Hydrodynamically fully-developed flow (only 1. FD flow and 2. GZ flow)

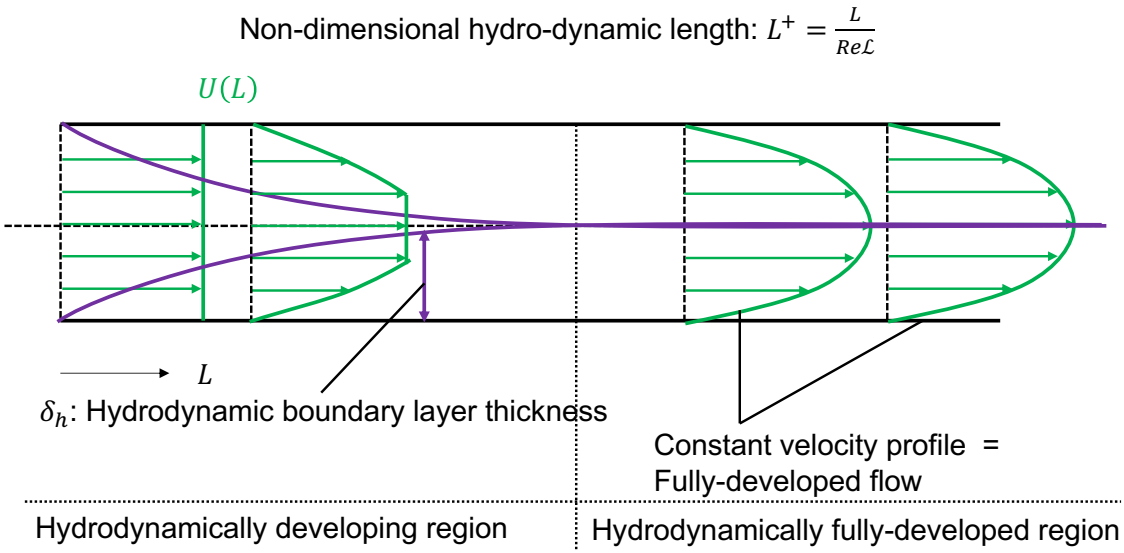


Figure 9.2: Schematic illustration of velocity profile of laminar fluid flow in a pipe.

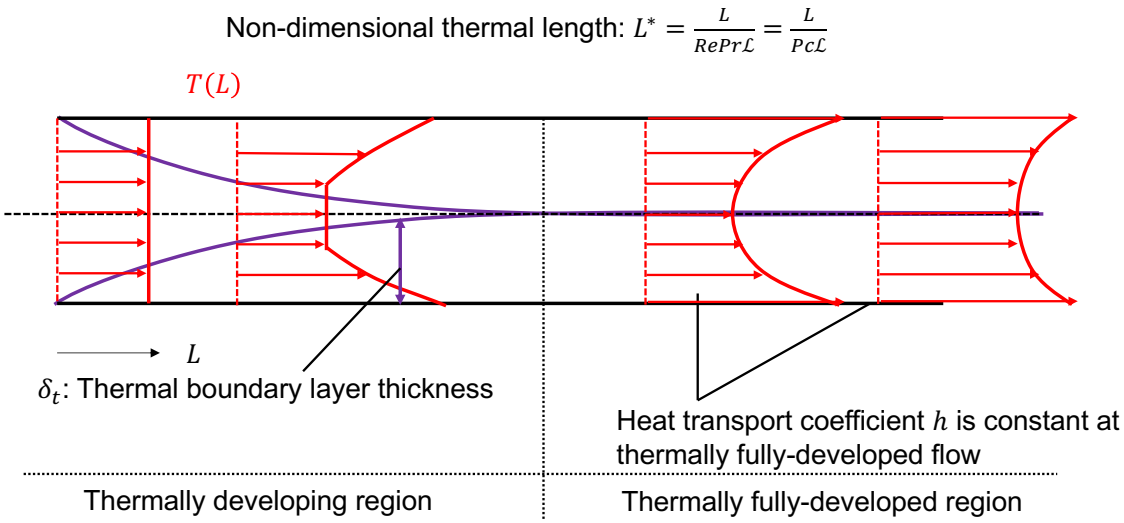


Figure 9.3: Schematic illustration of temperature profile of laminar fluid flow in a pipe.

Many of previous studies (Shah & London, 1978; Muzychka & Yovanovich, 2004; Bennett, 2019a) investigating heat transfer in pipes considered a constant heat flux boundary condition and according to these studies, the expressions for Nu for different boundary conditions are similar; therefore, although the consideration of different boundary conditions including a constant heat flux boundary condition remains to be a future study, it should not need substantial modifications. On the other hand, some extensive model developments would be required to consider the second scenario as the conductance model developed in Chapter 8 has not been developed to include the case of a hydrodynamically developing flow.

Definition of the bulk fluid temperature

The volume averaged temperature, which can be written as

$$T_{\mathrm{f}} = \frac{\int_V T \mathrm{d}V}{\int_V \mathrm{d}V} \tag{9.18}$$

, does not represent the bulk temperature of the fluid; if the fluid is flowing, the concept of a "mixing cup temperature" can better describe the fluid temperature, T_{f} (Whitaker, 1972). This concept considers fluid flow in a pipe, a cross-section is cut through the pipe. Fluid through the cross-section is poured into an adiabatic (i.e. insulated) cup; the mixing cup temperature is the temperature after "mixing" the fluid in the cup until the temperature distribution of the fluid is uniform. The mixing cup temperature at cross-section A is given by:

$$T_{\mathrm{f},A} = \frac{\int_A \rho_{\mathrm{f}} c_{\mathrm{f}} T(\mathbf{u}\cdot\mathbf{n})\mathrm{d}A}{\int_A \rho_{\mathrm{f}} c_{\mathrm{f}} (\mathbf{u}\cdot\mathbf{n})\mathrm{d}A} \tag{9.19}$$

Definition of the temperature driving force

Existing CFD-DEM frameworks (Shimizu, 2006; Kloss et al., 2012; Caulk et al., 2020) define the temperature driving force between particle k and fluid cell a as

$$\vartheta = T_{\mathrm{s},k} - T_{\mathrm{f},a} \tag{9.20}$$

Some studies (Romkes et al., 2003; Yang et al., 2010) investigating particle-fluid heat transfer defined the temperature driving force using the average value of the mixing cup temperature for inlet cross-section A_{in} and outlet cross-section A_{out}:

$$\vartheta = T_{\mathrm{s}} - \frac{T_{\mathrm{f},A_{\mathrm{in}}} + T_{\mathrm{f},A_{\mathrm{out}}}}{2} \tag{9.21}$$

where they considered the inlet and outlet cross-sections of granular samples perpendicular to the flow direction and did not consider pore-scale particle-fluid conduction.

However, a change in the mixing cup temperature of FD fluid flowing through a pipe with a constant temperature is non-linear as explained below, which indicates Eqs. (9.20) and (9.21) do not accurately characterise the temperature driving force. Fig. 9.4 shows a case where fluid with a constant density (ρ_{f}) and specific heat (c_{f}) flows in a pipe with a constant wall temperature of T_{s}. The mixing cup temperature of the fluid (T_{f}) is a function

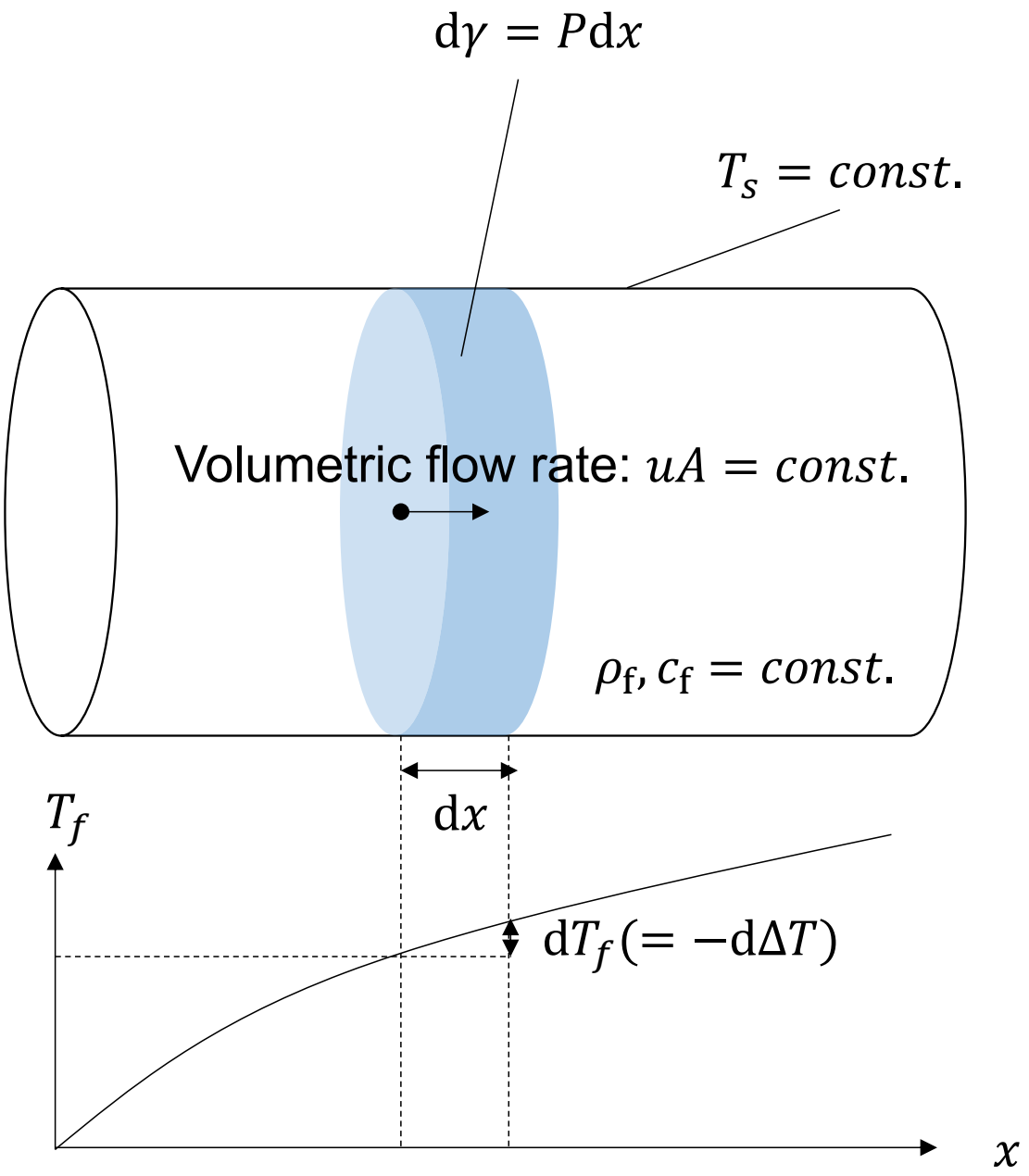


Figure 9.4: Schematic illustration on the calculation of an analytically-derived temperature driving force

of the distance from the inlet (x). The temperature difference between the solid surface temperature and the mixing cup temperature is denoted as ΔT:

$$\Delta T(x) = T_{\mathrm{s}} - T_{\mathrm{f}}(x) \tag{9.22}$$

In this case, the volumetric flow rate (the fluid velocity u multiplied by the cross-sectional area A) is constant. Considering a slice through the pipe with a small length $\mathrm{d}x$, the bulk temperature difference between the inlet and outlet of the slice are denoting as $\mathrm{d}T_{\mathrm{f}}$. Also taking wall surface area of the slice, $\mathrm{d}\gamma$, is equal to $P\mathrm{d}x$, where P is the perimeter of the pipe. If the heat conduction in the flow direction is negligible, the heat transfer rate from the wall surface to the fluid is equal to the energy change per unit time between the inlet and outlet of the slice. This can be written as

$$h\Delta T P\mathrm{d}x = \rho_{\mathrm{f}} c_{\mathrm{f}} u A \mathrm{d}T_{\mathrm{f}} \tag{9.23}$$

where h is constant as FD flow is assumed. As the wall surface temperature (T_{s}) is constant, $\mathrm{d}T_{\mathrm{f}} = -\mathrm{d}(\Delta T)$. Eq. (9.23) becomes a differential equation, which is written as

$$\frac{\mathrm{d}(\Delta T)}{\Delta T} = -\frac{hP}{\rho_{\mathrm{f}} c_{\mathrm{f}} u A}\mathrm{d}x \tag{9.24}$$

Integrating Eq. (9.24) and denoting the temperature driving force at the inlet of the pipe ($x = 0$) as ΔT_{in},

$$\Delta T = \Delta T_{\text{in}} \exp\left(-\frac{hP}{\rho_{\mathrm{f}} c_{\mathrm{f}} u A} x\right) \tag{9.25}$$

Taking the pipe length to be L, the temperature driving force at the outlet is written as

$$\Delta T_{\text{out}} = \Delta T_{\text{in}} \exp\left(-\frac{hP}{\rho_{\mathrm{f}} c_{\mathrm{f}} u A} L\right) \tag{9.26}$$

Rearranging Eq. (9.26),

$$\rho_{\mathrm{f}} c_{\mathrm{f}} u A = \frac{hPL}{\ln(\Delta T_{\text{in}}) - \ln(\Delta T_{\text{out}})} \tag{9.27}$$

The total amount of heat moving from the pipe wall to the fluid per unit time is

$$H = \rho_{\mathrm{f}} c_{\mathrm{f}} u A(\Delta T_{\text{in}} - \Delta T_{\text{out}}) \tag{9.28}$$

Substituting Eq. (9.27) into Eq. (9.28),

$$H = hPL\frac{\Delta T_{\text{in}} - \Delta T_{\text{out}}}{\ln(\Delta T_{\text{in}}) - \ln(\Delta T_{\text{out}})} \tag{9.29}$$

Rearranging Eq. (9.29) and denoting the total solid surface area as $\gamma = PL$,

$$h = \frac{\frac{H}{\gamma}}{\frac{\Delta T_{\text{in}} - \Delta T_{\text{out}}}{\ln(\Delta T_{\text{in}}) - \ln(\Delta T_{\text{out}})}} \tag{9.30}$$

Comparing Eq. (9.8) and Eq. (9.30), the analytically-derived temperature driving force is obtained as

$$\vartheta = \frac{\Delta T_{\text{in}} - \Delta T_{\text{out}}}{\ln(\Delta T_{\text{in}}) - \ln(\Delta T_{\text{out}})} \tag{9.31}$$

This temperature driving force is often termed as the logarithmic mean temperature difference (LMTD). In this study, the temperature driving force defined in Eq. (9.21) is called as the mean temperature difference (MTD).

The two definitions of the temperature driving force are compared in Fig. 9.5. In Fig. 9.5, the inlet mixing cup temperature and the solid surface temperature are constant at $T_{\text{f,in}}$ and T_{s}, respectively and the outlet mixing cup temperature $T_{\text{f,out}}$ was varied. Fig. 9.5 shows that the MTD and LMTD are equal if the inlet and the outlet mixing cup temperatures are equal i.e. $T_{\text{f,in}} - T_{\text{f,out}} = 0$. However, the discrepancy between the MTD and LMTD increases as the difference between these two quantities increase.

Asymptotic value of Nusselt number of various flow types

Referring to Table 9.1, there is poor agreement between existing models predicting the Nusselt number for granular materials especially regarding the exponents of Re and Pr. One of the main reasons for discrepancy may be the complexity of the pore space in granular materials meaning that it is difficult to find the asymptotic values of the Nusselt number. Consequently, any model predicting the Nusselt number in granular materials is typically based on the regression from experimental or numerical data.

In contrast to the models which have been proposed to predict the Nusselt number for granular materials, models predicting the Nusselt number for pipes are established based on asymptotic analysis. Such models have several advantages: for example, the exponents of Re and Pr can be clearly found and the number of fitting parameters can be reduced. In this section, the results of the previous asymptotic analyses of the Nusselt number in a pipe are summarised.

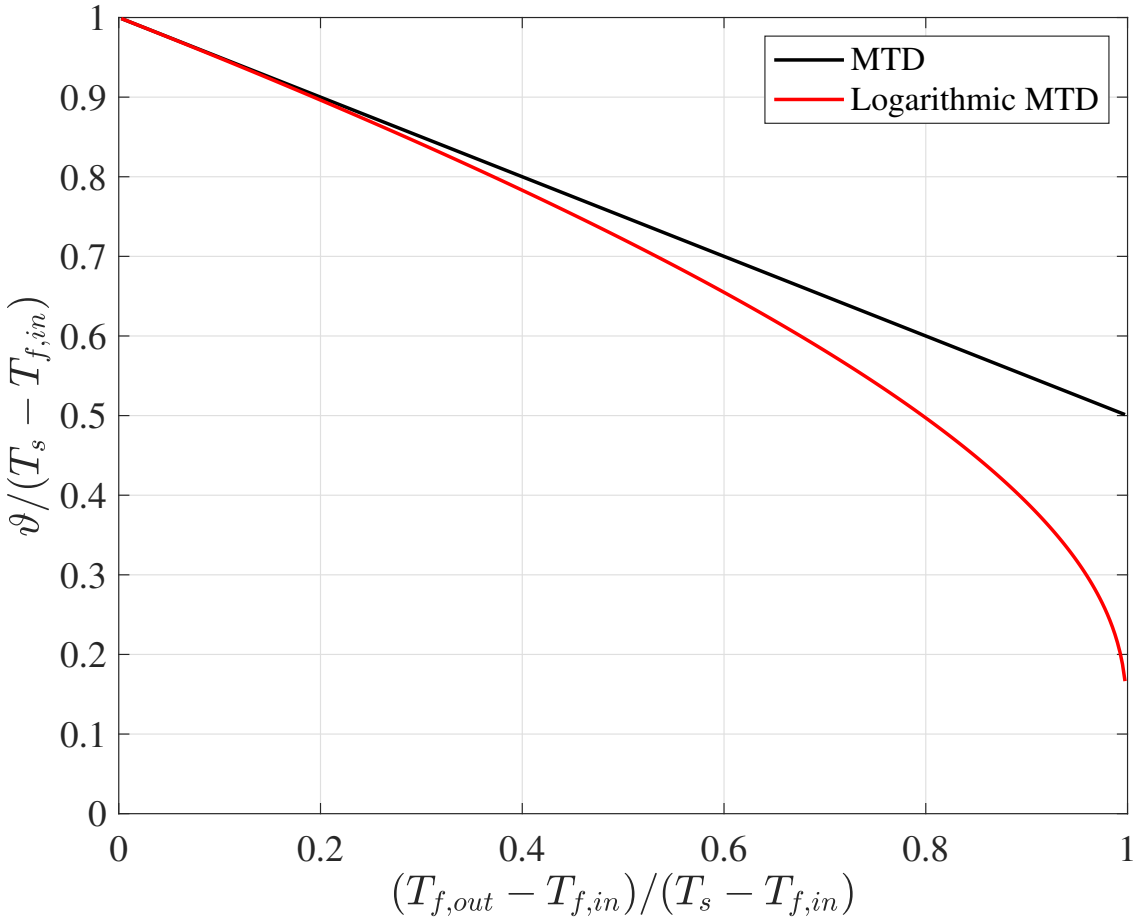


Figure 9.5: Comparison of the MTD and the LMTD

FD flow

As summarised in Shah and London (1978), experimental results for pipes with a variety of cross-section shapes show that the Nusselt number becomes constant in a thermally fully-developed flow i.e. $L^* \gg L^*_{\text{fully-developed}}$.

$$Nu_{FD} = const. \tag{9.32}$$

GZ flow

Considering the asymptotic Nusselt number for GZ flow, Lévêque (1928) studied cases where $L^* \to 0$. These cases have been often referred to as the Leveque (LV) limit or solution (Churchill & Ozoe, 1973; Shah & London, 1978; Muzychka & Yovanovich, 2002b; Bennett, 2019a). Muzychka and Yovanovich (2002b) and Bennett (2019b) expressed the assymptotic Nusselt number as

$$Nu_{LV} \propto \left(\frac{fRe}{L^*}\right)^{1/3} \tag{9.33}$$

where f is the friction factor defined as

$$f = \frac{\overline{\tau}}{\frac{1}{2}\rho_{\text{f}}\overline{u}^2} \tag{9.34}$$

where $\overline{\tau}$ is the mean shear stress on the pipe wall in the flow direction and $\overline{u}$ is the mean flow velocity at a representative cross-section.

In a hydro-dynamically fully-developed flow, the value of fRe can be related to the shape factor α introduced in Section 8.2.2. By taking the characteristic length used to calculate Re as the hydraulic diameter d_{h}, the following relationship can be derived:

$$\frac{2}{fRe_{d_{\text{h}}}} = \alpha_{\text{HR}} \tag{9.35}$$

The detailed derivation of the relationship is shown in Appendix E. In a hydro-dynamically fully-developed flow, $fRe_{d_{\text{h}}}$ is constant e.g. for a circular pipe, $fRe_{d_{\text{h}}} = 16$ while $\alpha_{\text{HR}} = 1/8$.

SD flow

Although SD flow is not examined in this study, it is useful to review the asymptotic Nusselt number for SD flow i.e. $L^+ \ll L^+_{\text{fully-developed}}$ and $L^* \ll L^*_{\text{fully-developed}}$. The asymptotic Nusselt number can be obtained using boundary layer theory (Schlichting

& Kestin, 1961). Following Schlichting and Kestin (1961), Churchill and Ozoe (1973) expressed the asymptotic relationship between the Nusselt number, Re, and Pr as:

For $Pr \to 0$,

$$Nu_{SD} \propto Re^{\frac{1}{2}} Pr^{\frac{1}{2}} \tag{9.36}$$

For $Pr \to \infty$,

$$Nu_{SD} \propto Re^{\frac{1}{2}} Pr^{\frac{1}{3}} \tag{9.37}$$

Muzychka and Yovanovich (2002b) expressed the above asymptotic relationships as

$$Nu_{SD} \propto \frac{f(Pr)}{\sqrt{L^*}} \tag{9.38}$$

where $f(Pr)$ is a certain function with $f(Pr) \to 1$ for $Pr \to 0$ and $f(Pr) \to Pr^{1/6}$ for $Pr \to \infty$.

Generalised formulation of Nu

The assymptotic analysis reviewed above helps to derive a generalised formulation of Nu for a wide range of Re and Pr (Churchill & Ozoe, 1973; Muzychka & Yovanovich, 2002b; Muzychka & Yovanovich, 2004). Amongst these prior studies, Muzychka and Yovanovich (2004) expressed the generalised Nu formulation as

$$Nu = \left[\left(Nu_{FD}^n + Nu_{LV}^n \right)^{\frac{m}{n}} + Nu_{SD}^m \right]^{\frac{1}{m}} \tag{9.39}$$

where m and n are parameters whose values are determined by fitting to the experimental data.

Consideration of pipe shapes

As shown in Fig. 8.2, throat face geometries are much more complex than circular pipes. Therefore, it is useful to review previous studies which modelled the Nusselt number in non-circular pipes. According to Bennett (2019b), there are only three studies (Yilmaz & Cihan, 1993; Muzychka & Yovanovich, 2004; Bennett, 2019b), which derived models to predict the Nusselt number of fluid flow in non-circular pipes.

In this study, we only consider FD and LV flows so only Nu_{FD} and Nu_{LV} need to be modelled. The models predicting Nu_{FD} by Yilmaz and Cihan (1993) and Bennett (2019b)

are complex and difficult to extend to the throats in a PNM . On the other hand, Muzychka and Yovanovich (2004)'s model predicting Nu_{FD} is based on fRe, which can be related to the throat shape factor in a PNM (Appendix E). Their expression is:

$$Nu_{FD,\sqrt{A_\mathrm{f}}} = 3.24\frac{fRe_{\sqrt{A_\mathrm{f}}}}{8\sqrt{\pi}} \tag{9.40}$$

The original formulation by Muzychka and Yovanovich (2004) includes a term considering the aspect ratio of the cross-section of the pipe; however, the term was neglected in this study as it is difficult to define the aspect ratio of the throat face. Muzychka and Yovanovich (2004)'s model predicting the local Nu_{LV} value at cross-section at a distance L from the inlet is

$$Nu_{LV,\sqrt{A_\mathrm{f}}} = 0.409\left(\frac{fRe_{\sqrt{A_\mathrm{f}}}}{L^*}\right)^{\frac{1}{3}} \tag{9.41}$$

They also defined the averaged Nusselt number, $\overline{Nu}$, which is defined using the total heat flux from the pipe wall and the temperature driving force between the inlet and the outlet. The averaged Nusselt number for the Leveque limit then reads:

$$\overline{Nu}_{LV,\sqrt{A_\mathrm{f}}} = \frac{3}{2}0.409\left(\frac{fRe_{\sqrt{A_\mathrm{f}}}}{L^*}\right)^{\frac{1}{3}} \tag{9.42}$$

Combining Eqs. (9.39), (9.40) and (9.42) and ignoring the term related to SD flow, the general Nusselt number for a non-circular pipe was modelled as:

$$\overline{Nu}_{\sqrt{A_\mathrm{f}}} = \left[\left(3.24\frac{fRe_{\sqrt{A_\mathrm{f}}}}{8\sqrt{\pi}}\right)^5 + \left(\frac{3}{2}0.409\left(\frac{fRe_{\sqrt{A_\mathrm{f}}}}{L^*}\right)^{\frac{1}{3}}\right)^5\right]^{\frac{1}{5}} \tag{9.43}$$

This formulation is based on fRe, which can be related to the shape factor α, and L^* defined from the length of the pipe, Re, and Pr (Eq. (9.15)). The current study aims to develop a model predicting the Nusselt number in fluid flow through a throat in PNM based on the model developed by Muzychka and Yovanovich (2004).

9.3 Development and validation of model predicting Nu of fluid flow in a throat in PNM based on fully-resolved CFD simulations

9.3.1 Overview of fully-resolved CFD simulations

A set of fully-resolved CFD simulations considered cold fluid flow through hot particles that have a constant temperature. Both regular packings and monodisperse random packings were considered; the particle position and radius data for the random packings were generated using Discrete Element Method (DEM) simulations just as was the case in the study presented in Chapter 8. Fully-resolved meshes for CFD simulations for regular packings and random packings were created as documented in Section 8.4.3. `BuoyantSimpleFOAM`, a steady-state compressible fluid solver in `OpenFOAM`, was employed to solve the continuity, momentum, and energy transport equations. The first-order upwind scheme was used as the discretisation scheme for the divergence term ($u \cdot \nabla T$) in the energy transport equation as it was difficult to obtain the convergence using a higher order scheme. Second-order discretisation schemes were used except for the rest. The effect of gravity, the changes in material properties of the fluid due to a temperature change, and radiative heat transfer were neglected, which means that the change in temperature of fluid did not affect the flow behaviour of fluid.

9.3.2 Validation of fully-resolved CFD simulations

A SC packing consisting of 8 particles was considered to validate the CFD simulation approach following Romkes et al. (2003) (Fig. 9.6). The radius and the position of the particles were imported into `MeshSpherePacking` to discretise the void space and create a mesh for the CFD simulations. Romkes et al. (2003) provided numerical simulation results and experimental data with a wide range of Re values. Their experimental set-up should be noted here because it is relevant to CFD simulation conditions. In a laboratory, it is difficult to maintain a constant particle temperature, thus they employed an analogy of mass transfer and heat transfer. They used particles made with naphthalene and measured the decrease in the mass of the naphthalene particles over a controlled time period. In this case, the Schmidt number Sc is equivalent to Pr, where Sc is defined as:

$$Sc = \frac{\nu_{\text{vis}}}{\mathcal{D}} \tag{9.44}$$

where ν_{vis} is the kinematic viscosity in [m^2/s] and $\mathcal{D}$ is the mass diffusivity in [m^2/s]. Thus, for CFD simulations, Pr should be equal to Sc for naphthalene to air at 298 K (their experimental condition) i.e. $Pr = 2.28$ (Goldstein & Cho, 1995). Following Yang et al. (2010), the particle diameter (D) is 12 mm and the distance between adjacent particles is 12.12 mm. The temperature of hot particles is 313 K while the temperature of fluid at the inlet is 273 K. The temperature gradient at the outlet was set to be zero i.e. there is no heat conduction across the boundary. For hydro-dynamic boundary conditions, similar

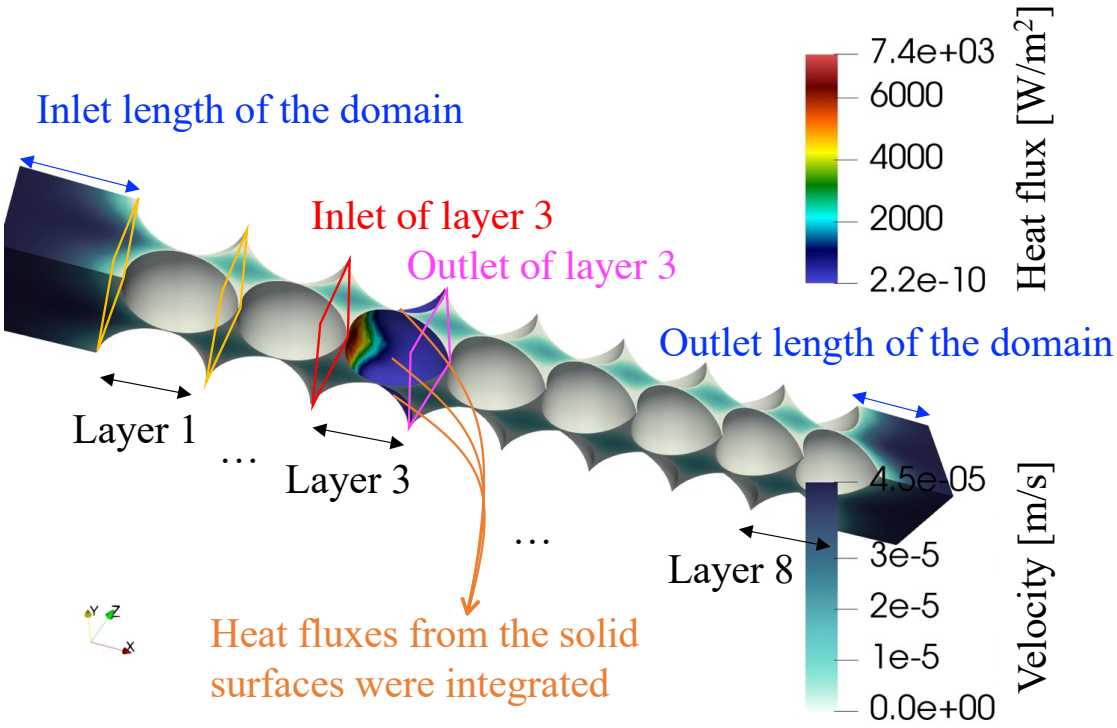


Figure 9.6: The geometry of the validation case.

conditions to Section 8.4.3 were applied, where the inlet velocity was specified to control the Re value, and the outlet pressure was set to be zero.

Mesh data with cell attribute values (e.g. temperature, velocity field) were output in `vtk` format from `OpenFOAM`, and `Paraview` was used to post-process these data. As there are 8 particles, 8 "layers", each containing one particle, were considered. As shown in Fig. 9.6, inlet and outlet planes were considered for each layer. The bulk temperature at the inlet and the outlet of each layer was calculated using Eq. (9.19). In `Paraview`, the `slice` filter was applied and the `integrateVariables` function was used to calculate the total volumetric flow rate in the x-direction. The total heat rate from the particle surface was integrated using the `integrateVariables` filter as well. The definition of the thermal driving force adopted was the MTD (Eq. (9.21)) following Romkes et al. (2003).

The validation study was conducted in terms of the inlet/outlet region lengths and the mesh size. Both cases, two Re values of 0.7 and 7 were considered. For $Re = 0.7$, the temperature of particle 3 was set to be 313 K, while the thermal boundary condition at the surface of the other particles was adiabatic, following Romkes et al. (2003). This particular case with $Re = 0.7$ considers the scenario of a very low Reynolds number and a situation where the temperature of fluid is nearly the same value as the particle temperature. In this case, the temperature difference between the solid surfaces and the fluid after layer 3 in Fig. 9.6 becomes so close to zero that the calculation of Nu tends to give a large error.

For $Re = 7$, the temperature of all particles was 313 K. The Nu values for a layer were calculated following Romkes et al. (2003):

$$Nu_{d_\mathrm{h}} = \frac{\frac{H}{\pi D^2} d_\mathrm{h}}{k_\mathrm{f} \vartheta} \tag{9.45}$$

where H is the magnitude of the total heat flow from the particle surfaces indicated in Fig. 9.6 and the thermal driving force ϑ is defined as:

$$\vartheta = T_\mathrm{s} - \frac{1}{2}(T_\mathrm{f,in} + T_\mathrm{f,out}) \tag{9.46}$$

following Romkes et al. (2003). $T_\mathrm{f,in}$ and $T_\mathrm{f,out}$ were calculated following Eq. (9.19) at the inlet and outlet cross-sections shown in Fig. 9.6, respectively.

For a given layer the friction factor f was calculated following Calis et al. (2001):

$$f = \frac{\Delta p}{\frac{1}{2}\rho_\mathrm{f} \left(\frac{u_\mathrm{inlet}}{(1-\phi)}\right)^2 \frac{L}{d_\mathrm{h}}} \tag{9.47}$$

where u_inlet is the inlet velocity, ϕ is the solid fraction, L is the length of the layer, d_h is the hydraulic diameter and Δp is pressure change through the layer defined using area averaged pressures at the inlet and outlet cross-sections (p_in and p_out) as:

$$\Delta p = p_\mathrm{in} - p_\mathrm{out} = \frac{\iint_{A_\mathrm{in}} p \mathrm{d}A_\mathrm{in}}{\iint_{A_\mathrm{in}} \mathrm{d}A_\mathrm{in}} - \frac{\iint_{A_\mathrm{out}} p \mathrm{d}A_\mathrm{out}}{\iint_{A_\mathrm{out}} \mathrm{d}A_\mathrm{out}} \tag{9.48}$$

For the analysis, the Nu and f values for layer 3 were used as the Nu and f values were nearly constant for layers 3- 7, in agreement with Romkes et al. (2003).

Domain inlet/outlet region lengths

The effects of the inlet/outlet region lengths in the granular samples were examined using the configuration shown in Fig. 9.6. Both the L_in and L_out were taken to be either D or $2D$, where D is the diameter of the particles; thus $2 \times 2 = 4$ cases were considered for the particle configuration.

As shown in Tables 9.2 and 9.3, very small differences ($< 2\%$) were observed both for the Nusselt number and the friction factor when L_in and L_out were varied. Thus, in this study, $L_\mathrm{in} = L_\mathrm{out} = D$ is used for the rest of the analayses.

Table 9.2: Effect of inlet and outlet region lengths on Nu

L_{in}	D	D	$2D$	$2D$
L_{out}	D	$2D$	D	$2D$
$Re = 0.7$	3.32	3.36	3.37	3.34
$Re = 7.0$	3.32	3.36	3.37	3.34

Table 9.3: Effect of inlet and outlet region lengths on f

L_{in}	D	D	$2D$	$2D$
L_{out}	D	$2D$	D	$2D$
$Re = 0.7$	235.2	235.1	233.6	233.5
$Re = 7.0$	24.4	24.4	24.3	24.2

Mesh size dependency at low Pc numbers

From a hydro-dynamic perspective (i.e. where heat transfer is not considered), Knight (2018) and Morimoto et al. (2022) concluded that $D/ds_c = 30$ is sufficient to simulate accurately laminar flow through lattice packings of uniform spheres; however, the mesh dependency of the predicted thermal response must also be considered. Previous studies on advective heat transfer employed finer mesh than that used by Knight (2018) and Morimoto et al. (2022). Calis et al. (2001) and Romkes et al. (2003) considered very thin prismatic layers (500 times smaller than the particle diameter) near the particle surface. Yang et al. (2010) used tetrahedral meshes with $D/ds_c = 60$ and conducted simulations up to $Pc \approx 5000$. Following Yang et al. (2010), this study varied D/ds_c values from 30 to 60.

Table 9.4 and Table 9.5 show the effect of mesh size on Nu and f, respectively. According to Table 9.4 and Table 9.5 , the Nu and f values were constant for D/ds_c values larger than 50, where the relative difference between the results obtained using $D/ds_c = 50$ and $D/ds_c = 60$ was <1% for both the Nu and f values.

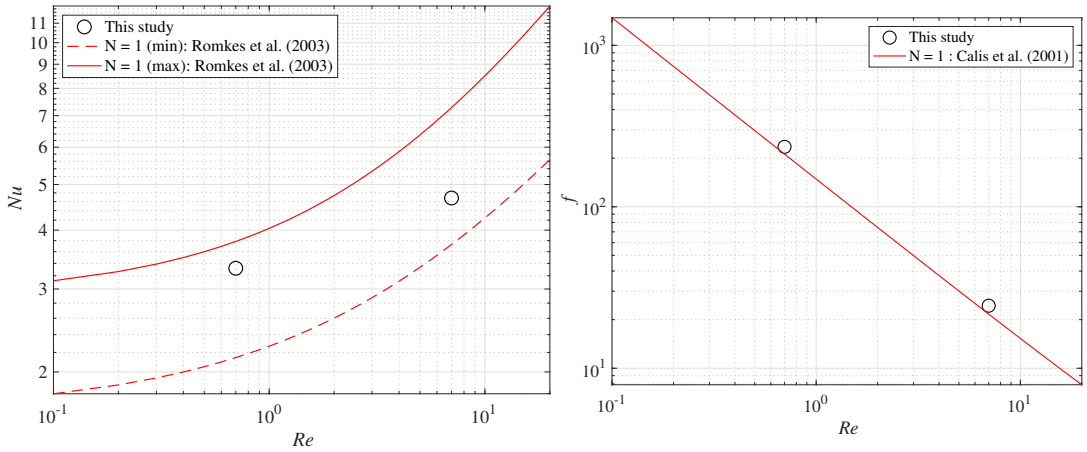
Fig. 9.7 compares the Nu and f values obtained in this study at $D/ds_c = 50$ with previous studies. Romkes et al. (2003), The Nu values were compared with Romkes et al. (2003), who considered the same particle configuration of the particles (they denoted the particle configuration shown in Fig. 9.6 as "$N = 1$"). While the Romkes et al. (2003) data exhibited some scatter for the Nu values, they provided the 95% confidence intervals, which are shown as max and min lines in Fig. 9.7(a). The f values were compared with data from Calis et al. (2001). Fig. 9.7 shows that the CFD studies in this study agree with the previous studies.

Table 9.4: Effect of mesh size on Nu ($Pr = 2.28$)

D/ds_c	30	40	50	60
$Re = 0.7$	3.36	3.35	3.32	3.34
$Re = 7.0$	4.85	4.73	4.68	4.65

Table 9.5: Effect of mesh size on f

D/ds_c	30	40	50	60
$Re = 0.7$	227.7	229.9	235.2	235.9
$Re = 7.0$	23.7	23.8	24.4	24.5



(a) Nu. **(b)** f.

Figure 9.7: Comparison results at $D/ds_c = 50$ against previous CFD studies (Romkes et al., 2003; Calis et al., 2001).

Table 9.6: Effect of mesh size on Nu ($Pr = 7000$)

D/ds_c	30	40	50	60
$Re = 0.7$	38.5	40.4	41.75	41.88

Table 9.7: Regular packings considered in this chapter

	D [mm]	$D/D_{\max}$	e	L_{ab} [mm]	$d_{\mathrm{h},ab}$ [mm]	L_{ab}/D
SC	12.00	1.00	0.910	12.00	7.28	1.00
	10.80	0.90	1.620	12.00	11.66	1.11
BCC	12.00	1.00	0.470	4.90	3.76	0.41
	11.04	0.92	0.888	4.90	6.54	0.44
	9.84	0.82	1.666	4.90	10.93	0.50
FCC	12.00	1.00	0.350	7.35	2.80	0.61
	10.68	0.89	0.916	7.35	6.52	0.69
	9.60	0.80	1.638	7.35	10.48	0.77

Mesh size dependency at a high Pc number

The mesh size dependency of the CFD simulation results was examined for a high Pc value. The Pr was set to be 7000 in instead of 2.28 while $Re = 0.7$ i.e. $Pc = 4900$. The Nu values obtained using different D/ds_c values were summarised in Table 9.6. In contrast to the mesh size dependency study considering low Pc values, the Nu values increased as the mesh becomes finer. The Nu became constant for $D/ds_c \geq 50$. Therefore, these mesh dependency studies support to use $D/ds_c = 50$ for a wide range of Pc values.

9.3.3 Fluid flow through regular packings

Simulation conditions

Studies using regular lattice packings of uniform spheres can provide useful insight into fluid-particle interactions (Zick & Homsy, 1982; Morimoto et al., 2022). In this study three types of regular packings were considered, namely Simple Cubic (SC), Body Centred Cubic (BCC), and Face Centred Cubic (FCC) packings. The void ratio, e, was varied by changing the particle radius as summarised in Table 9.7. The geometries of the densest SC, BCC, and FCC packings are shown in Fig. 9.8 (a), (c), and (e), respectively. The positions and radii of particles were used to generate unstructured meshes that discretized the void space using `MeshSpherePacking` (Knight, 2021), as described above, taking $D/ds_c = 50$.

The fluid velocity for each packing was chosen so that the local Reynolds number was approximately 1 to ensure that the flow was hydro-dynamically fully-developed. Here the local Reynolds number of throat ab connecting pores a and b is defined as:

$$Re_{ab,d_\mathrm{h}} = \frac{\rho_\mathrm{f} \frac{Q_{ab}}{A_{\mathrm{f},ab}} d_{\mathrm{h},ab}}{\mu_\mathrm{f}} \tag{9.49}$$

where Q_{ab}, $A_{\mathrm{f},ab}$, and $d_{\mathrm{h},ab}$ are the volumetric flow rate through the throat face, the area of the throat face, and the hydraulic diameter of the throat, respectively. The hydraulic diameter ($d_{\mathrm{h},ab}$) is four times the hydraulic radius, which is the ratio of the fluid volume Θ_{ab} to the solid surface area γ_{ab} (referring to Fig. 8.3 in Chapter 8). The dynamic viscosity of the fluid, μ_f, and the density of the fluid, ρ_f, were fixed at 1×10^{-3} [Pa·s] and 1000 [kg/m^3], respectively, for all cases. As $Re = 1$ for all the cases, the Peclet number ($Pc = RePr$), which is relevant to heat transport phenomena, was varied by varying Pr. Keeping the thermal conductivity of fluid k_f fixed at 1 [W/(K·m)], $Pr = (c_\mathrm{f}\mu_\mathrm{f})/k_\mathrm{f}$, was varied by varying the heat capacity, c_f, of the fluid. In this study, a variety of Pr values are considered, namely 1.5, 4.5, 15, 45, 150, 450, 1500, and 4500, which cover the range of Pr encountered in practice as summarised in Table 7.1.

Calculation of the Nusselt number of fluid flow in a throat

The throats (i.e. the pore connections) shown in Fig. 9.8 (b), (d), and (f) were considered in the detailed analysis. To calculate Nu for a given throat, the thermal driving force ϑ, the total heat flux H_{ab}, the solid surface area γ_{ab} and the characteristic length $\mathcal{L}$ were required following Eq. (9.8) and Eq. (9.10). As can be seen in Fig. 9.8 (b), (d), and (f), three inlet faces were defined. The mixing cup temperature at the inlet (T_in) of a particular throat was defined as

$$T_\mathrm{in} = \frac{\sum_{k=1}^{3} \iint_{A_\mathrm{in}^{(k)}} T\mathbf{u}_\mathrm{in} \cdot \mathbf{n}_\mathrm{in}^{(\mathbf{k})} \mathrm{d}A_\mathrm{in}^{(k)}}{\sum_{k=1}^{3} \iint_{A_\mathrm{in}^{(k)}} \mathbf{u}_\mathrm{in} \cdot \mathbf{n}_\mathrm{in}^{(\mathbf{k})} \mathrm{d}A_\mathrm{in}^{(k)}} \tag{9.50}$$

Similar to the inlet mixing cup temperature, the mixing cup temperature at the outlet T_out of a particular throat was defined as

$$T_\mathrm{out} = \frac{\sum_{k=1}^{3} \iint_{A_\mathrm{out}^{(k)}} T\mathbf{u}_\mathrm{out} \cdot \mathbf{n}_\mathrm{out}^{(\mathbf{k})} \mathrm{d}A_\mathrm{out}^{(k)}}{\sum_{k=1}^{3} \iint_{A_\mathrm{out}^{(k)}} \mathbf{u}_\mathrm{out} \cdot \mathbf{n}_\mathrm{out}^{(\mathbf{k})} \mathrm{d}A_\mathrm{out}^{(k)}} \tag{9.51}$$

where $\mathbf{u}_\mathrm{in}$, $\mathbf{n}_\mathrm{in}^{(\mathbf{k})}$, $\mathbf{u}_\mathrm{out}$, and $\mathbf{n}_\mathrm{out}^{(\mathbf{k})}$ are defined in Fig. 9.9 (2D for simplicity). Using the `Paraview` software, the numerator terms in Eq. (9.50) and Eq. (9.51) were calculated by

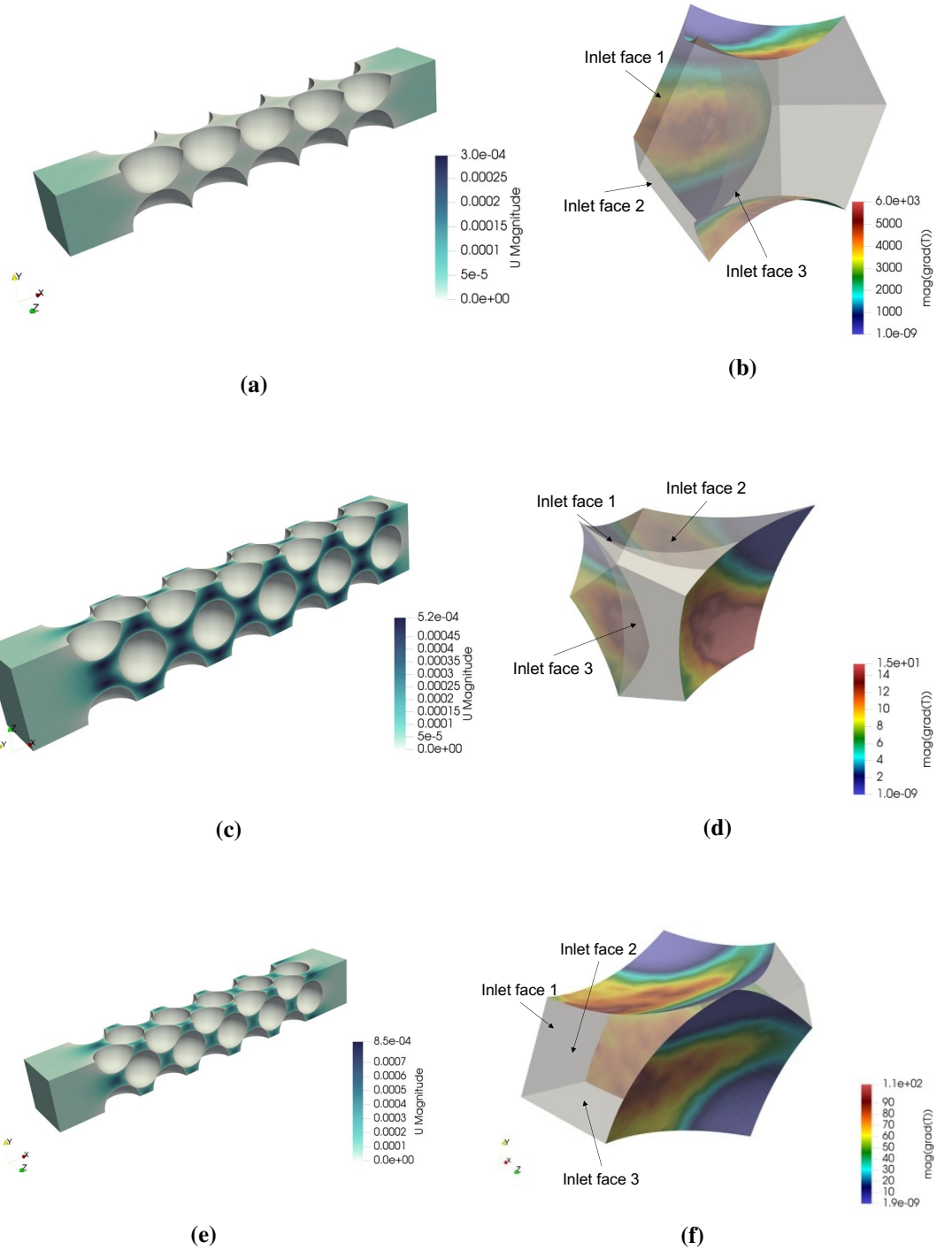


Figure 9.8: Geometry of regular packings. (a) SC (b) SC throat (c) BCC (d) BCC throat (e) FCC (f) FCC throat. (a), (c), and (e) are coloured based on the velocity and (b), (d), and (f) are coloured based on the heat flux.

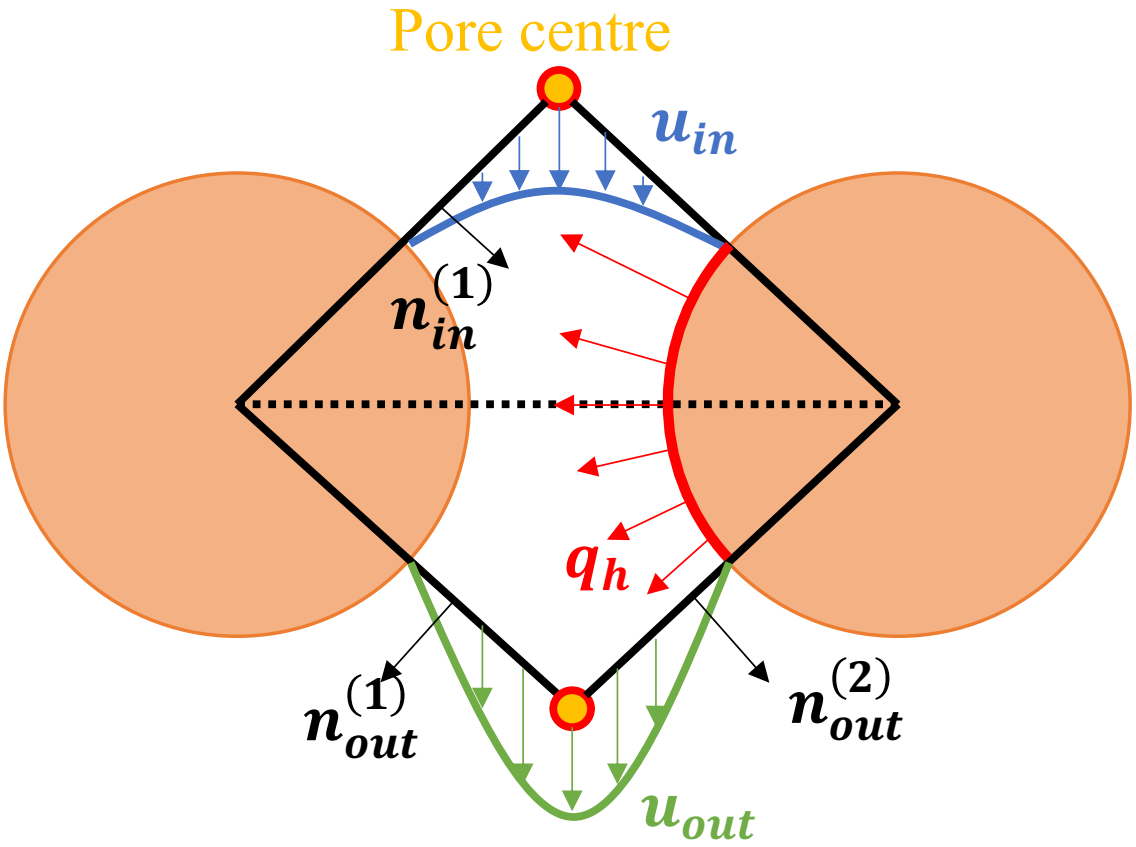


Figure 9.9: 2D Schematic illustration of the definition of inlet and outlet velocities ($\mathbf{u}_{\text{in}}$ and $\mathbf{u}_{\text{out}}$), inlet and outlet face normal ($\mathbf{u}_{\text{in}}$ and $\mathbf{u}_{\text{out}}$) and particle surface heat flux q_{h} for analysis of a whole throat.

isolating the subset of the mesh defining the face of interest using the `slice` and `clip` filters, applying the `calculator` filter which calculates the inner product of the velocity field and the normal multiplied by temperature, and applying the `integrateVariables` filter on the `calculator` filter to conduct the area integration of T. The denominator can be calculated in a similar manner, but the calculator filter only calculates $\mathbf{u} \cdot \mathbf{n}^{(\mathbf{k})}$. Both MTD (Eq. (9.21)) and LMTD (Eq. (9.31)) were used to define the temperature driving force. The results of the simulations are presented in Section 9.4.1 below.

9.3.4 Fluid flow through random packings

The regular packings can represent only a limited number of throat shapes; a wider range of throat morphologies is found in random packings. Data for packings with for $Cu = 1.01$ and $e = 0.536, 0.610, 0.763$ developed by Knight (2018) were used to enable consideration of a more random pore topology with various packing densities. As before `MeshSpherePacking` was used to create the unstructured meshes for the CFD simulations. The number of particles in these systems was much larger than that considered

for the regular packings so the computational cost prohibited use of $D/ds_c = 50$ for these simulations. Therefore, $D/ds_c = 30$ was used for the random packings; according to the result reported in Table 9.4, this may give an over-prediction of approximately 3% for a low Pc value and 8% for a high Pc in the Nu data compared to $D/ds_c = 60$. The cases considered were $Pc = 15$ with $Re = 0.1$ and $Pr = 150$ and $Pc = 150$ with $Re = 0.1$ and $Pr = 1500$.

In post-processing, the fluid domain was discretised into pores using the modified Delaunay triangulation following Chareyre et al. (2012). The post-processing approach used to calculate the Nusselt number at throats was similar to that described above for the regular packings. Similar to the post-process analysis outlined in Section 8.4.3, throats with $\theta^{\mathfrak{q}} > \pi/4$ and throats crossing one of periodic boundaries were not considered for the post-process. In addition, throats with $\vartheta < 1 \times 10^{-3}$ were excluded from plots because the Nusselt number of the throats was susceptible for precision errors.

9.4 Results

9.4.1 Regular packings

LMTD and MTD

Before proceeding with the discussion on the development of an expression for the Nusselt number of the throats in a PNM, it is useful to discuss how the definition of the temperature driving force affects the Nusselt number. Fig. 9.10 compares the averaged Nusselt numbers calculated using the two types of temperature driving force, namely LMTD and MTD, for the BCC packings with three e values. It can be seen that for $L^* > 5 \times 10^{-2}$ the two definitions of the temperature driving forces induce noticeable difference in the calculation of the $\overline{Nu}_{d_\mathrm{h}}$. When the LMTD is used, the $\overline{Nu}_{d_\mathrm{h}}$ value is constant for a larger L^*, which is in agreement with the previous studies on the Nusselt number of FD flow in a pipe. Therefore, the LMTD is used in a later discussion to define the temperature driving force.

Comparison between throats with a similar α_{HR}

The value of $\overline{Nu}_{\sqrt{A_\mathrm{f}}}$ (Eq. (9.43)) depends on $fRe_{\sqrt{A_\mathrm{f}}}$, which can be related to the shape factor for the HR model as described here. Muzychka and Yovanovich (2004) proposed use of the square root of the cross-sectional area of the pipe, $\sqrt{A_\mathrm{f}}$, as a characteristic length for both of the Nusselt number and Reynolds number; however, the cross-section of a throat in PNM is not constant so it is difficult to define the cross-sectional area. Therefore, first of all, the Nusselt number and the Reynolds number with $\sqrt{A_\mathrm{f}}$ as a characteristic length in

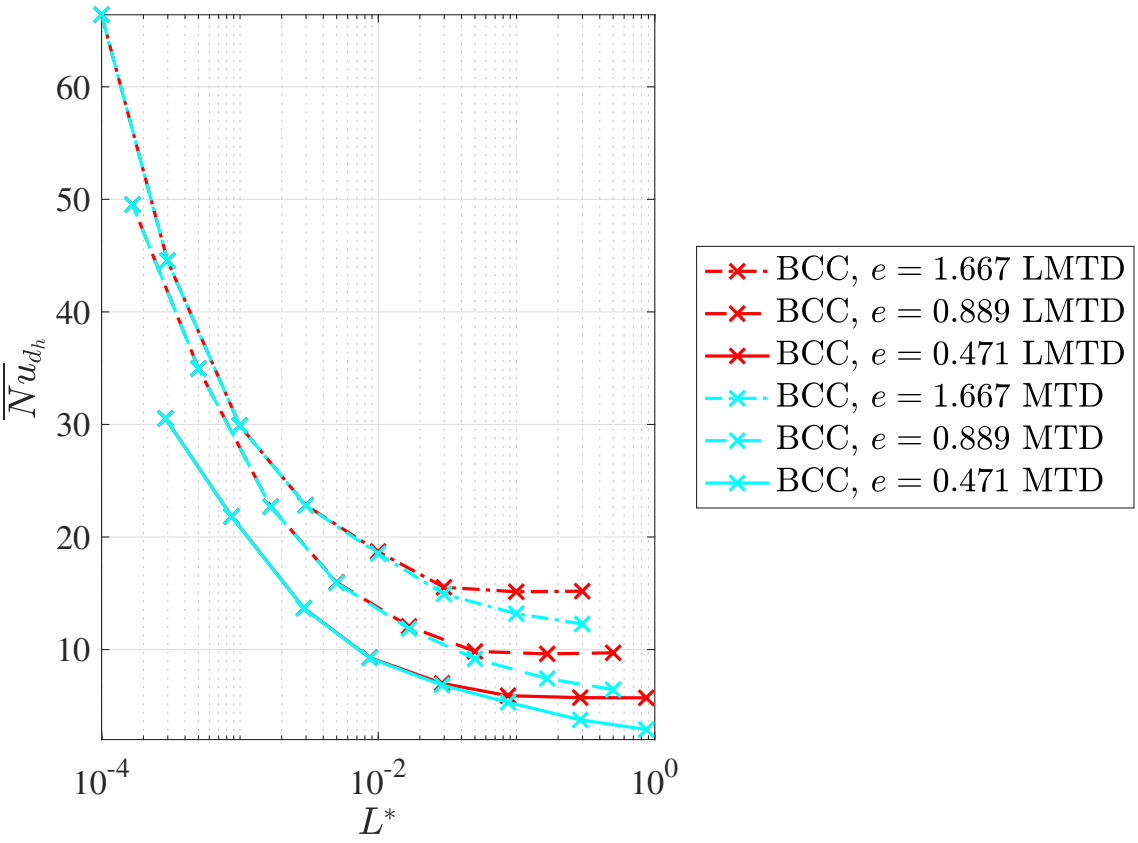


Figure 9.10: Variation of $\overline{Nu}_{d_h}$ with L^*: comparison between two definitions of ϑ (LMTD and MTD).

Eq. (9.43) are converted into those with d_h as a characteristic length. In a circular pipe, $d_\mathrm{h} = d$, thus, the relationship between $\sqrt{A_\mathrm{f}}$ and d_h is:

$$\sqrt{A_\mathrm{f}} = \frac{\sqrt{\pi}}{2} d_\mathrm{h} \tag{9.52}$$

Eq. (9.43) can be rewritten using Eq. (9.52) as

$$\overline{Nu}_{d_\mathrm{h}} = \frac{2}{\sqrt{\pi}} \left[\left(3.24 \frac{f Re_{d_\mathrm{h}}}{16} \right)^5 + \left(\frac{3}{2} 0.393 \left(\frac{f Re_{d_\mathrm{h}}}{L^*} \right)^{\frac{1}{3}} \right)^5 \right]^{\frac{1}{5}} \tag{9.53}$$

Substituting Eq. (9.35) to Eq. (9.53),

$$\overline{Nu}_{d_\mathrm{h}} = \frac{2}{\sqrt{\pi}} \left[\left(\frac{3.24}{8\alpha_\mathrm{HR}} \right)^5 + \left(\frac{3}{2} 0.393 \left(\frac{2}{\alpha_\mathrm{HR} L^*} \right)^{\frac{1}{3}} \right)^5 \right]^{\frac{1}{5}} \tag{9.54}$$

From Eq. (9.54), it is clear that the $\overline{Nu}_{d_\mathrm{h}}$ is related to only α_HR and L^* following the expression by Muzychka and Yovanovich (2004). It implies that throats or pipes with a similar α_HR have a similar $\overline{Nu}_{d_\mathrm{h}}$-$L^*$ relationship.

Section 8.3 proposed that the shape factor of throats in regular packings can be analytically determined from Zick and Homsy (1982)'s data. In Fig. 8.5, it is evident that the densest FCC packing with $e = 0.351$, the densest BCC packing with $e = 0.471$, and the densest SC packing $e = 0.908$ all have α_HR similar to that of a circular pipe (denoted as HP, Hagen-Poiseuille, in Fig. 8.5); $\alpha_\mathrm{HR} = 0.125$ for a circular pipe, $\alpha_\mathrm{HR} = 0.1308$ for the densest FCC, $\alpha_\mathrm{HR} = 0.1246$ for the densest BCC, and $\alpha_\mathrm{HR} = 0.1277$ for the densest SC. Fig. 9.11 gives the $\overline{Nu}_{d_\mathrm{h}}$ values of a circular pipe and the densest SC, BCC, and FCC packings. The data for a circular pipe were extracted from Shah and London (1978). Fig. 9.11 shows that the $\overline{Nu}_{d_\mathrm{h}}$-$L^*$ relationships for the four types of fluid pipes are similar, where the $\overline{Nu}_{d_\mathrm{h}}$ is high for a low L^* and reaches at a constant value for a high L^*. In the entrance region (a small L^* value), the $\overline{Nu}_{d_\mathrm{h}}$ values of the three types of the throats are proportional to $L^{*-1/3}$. Fig. 9.11 supports the hypothesis that Muzychka and Yovanovich (2004)'s model is applicable for a throat in a PNM.

Comparison between throats with a similar void ratio

As summarised in Table 9.1, existing expressions for the Nusselt number of granular materials depend on the packing density. On the other hand, as shown in Fig. 8.6, α_HR varies if the local void ratio, e^*, of the throat varies. Fig. 9.12 shows $\overline{Nu}_{d_\mathrm{h}}$-$L^*$ plots for the

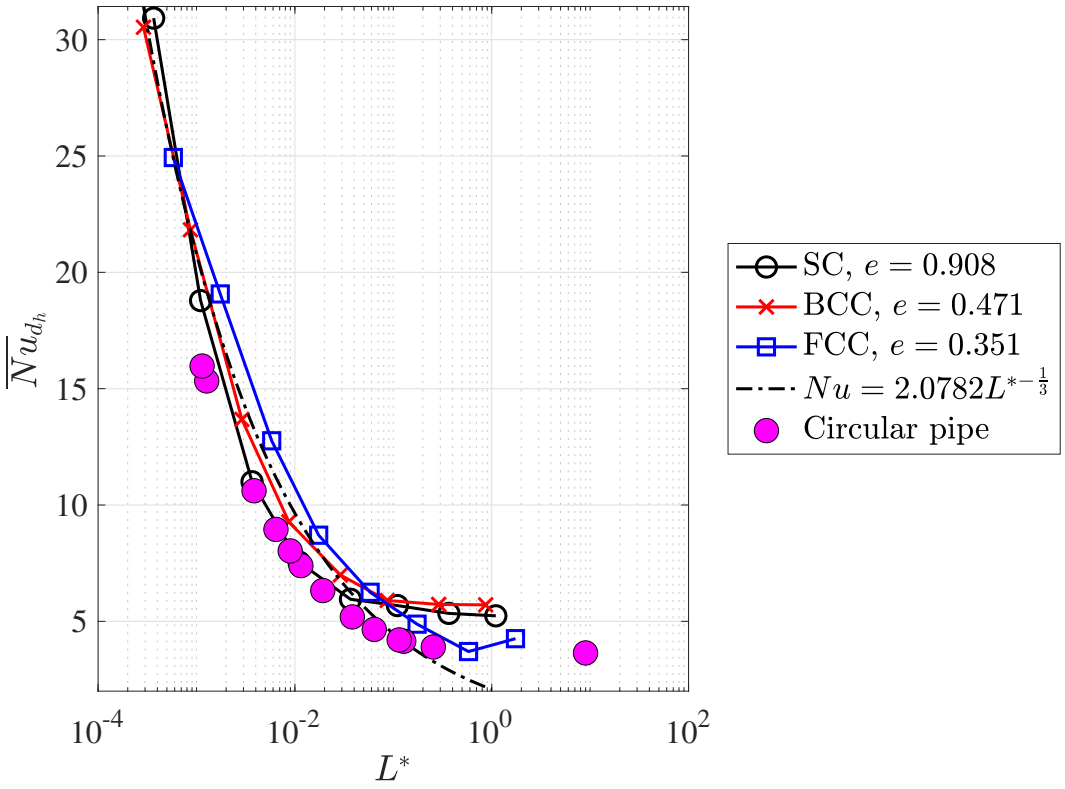


Figure 9.11: Variation of $\overline{Nu}_{d_h}$ with L^*: comparison between the densest SC, BCC, FCC packings, and a circular pipe.

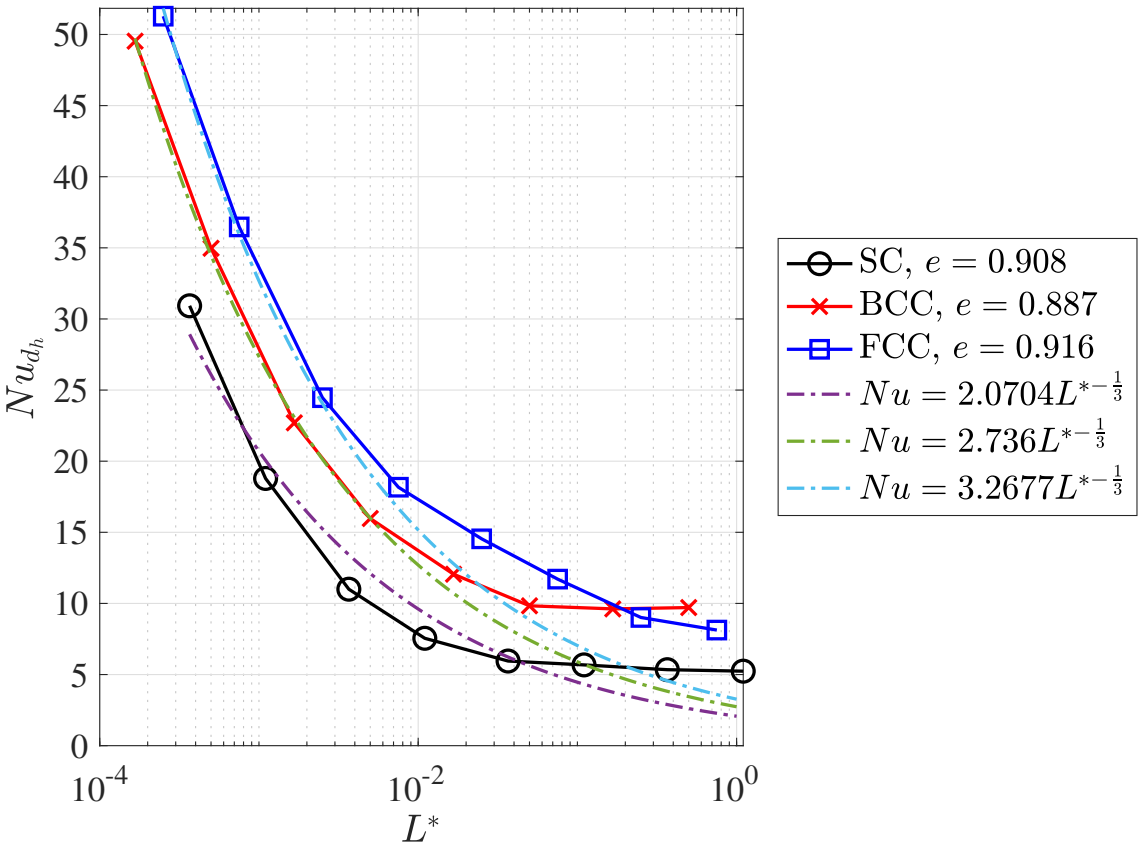


Figure 9.12: Variation of $\overline{Nu}_{d_h}$ with L^*: comparison between SC, BCC and FCC packings with a similar density.

three types of the regular packings with similar void ratio values. In Fig. 9.12, $\overline{Nu}_{d_h}$ values of the three packings are distinct although they have a similar void ratio and differences cannot by captured by the existing models summarised in Table 9.1. At a similar density, FCC has the highest $\overline{Nu}_{d_h}$ value, followed by BCC and SC, except in the very high L^* region. Section 8.3 shows that for $e \approx 0.9$, the α_{HR} value for the SC packing is larger than the α_{HR} values for the BCC and FCC packings, which suggests that consideration of α_{HR} can correct the difference between the $\overline{Nu}_{d_h}$ values in the SC and BCC (or FCC) packings.

Consideration of α_{HR}

Fig. 9.10 shows that BCC packings with different e values have different Nu values. In this section, we discuss how this difference can be corrected by considering the value of α_{HR}. Eq. (9.54) predicts that $\alpha_{\text{HR}}\overline{Nu_{d_h}}$ is constant for $L^* \to \infty$ and $\alpha_{\text{HR}}^{1/3}\overline{Nu_{d_h}} \propto L^{*-1/3}$ for $L^* \to 0$.

Fig. 9.13 plots the product of α_{HR} and $\overline{Nu_{d_h}}$ against L^*, where α_{HR} is obtained following the analytical study detailed in Section 8.3. It is obvious that the differences in $\overline{Nu_{d_h}}$ at high L^* values observed in Fig. 9.10 can be corrected by considering α_{HR}. Fig. 9.14 shows a correlation between $\alpha_{\text{HR}}^{1/3}\overline{Nu_{d_h}}$ and L^* for the packings considered in Fig. 9.10.

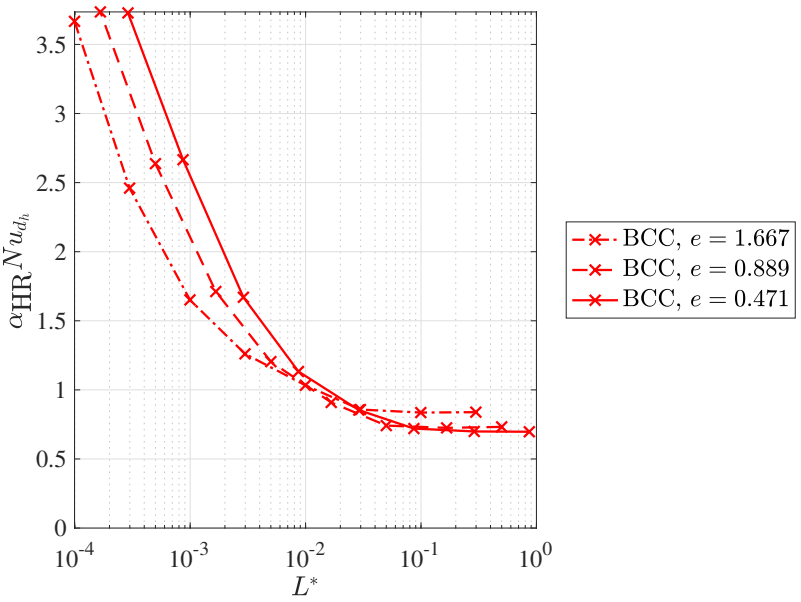


Figure 9.13: $\alpha_{\mathrm{HR}}\overline{Nu}_{d_\mathrm{h}}$ versus L^* for the BCC packings with different void ratios.

$\alpha_{\mathrm{HR}}^{1/3}\overline{Nu}_{d_\mathrm{h}}$ is approximately unique for a low L^*, and proportional to $L^{*-1/3}$ as predicted by Muzychka and Yovanovich (2004)'s model.

Novel expression for Nu of throat in a PNM based on Muzychka and Yovanovich (2004)'s model

The above analyses and discussion indicate that that the model predicting the Nu number of fluid flow in a pipe proposed by Muzychka and Yovanovich (2004) is qualitatively applicable to fluid flow through throats in PNMs i.e. the local flow in granular materials. Fig. 9.15 compares the actual Nu_{d_h} number of throats obtained from the OF simulations of the lattice packings and the Nu number predicted by Muzychka and Yovanovich (2004)'s model ($Nu_{\mathrm{MY},d_\mathrm{h}}$). Fig. 9.15 shows that the relationship between Nu_{d_h} and $Nu_{\mathrm{MY},d_\mathrm{h}}$ is roughly linear, which indicates that Muzychka and Yovanovich (2004)'s model for pipes is qualitatively applicable to throats in PNMs. A linear regression between Nu_{d_h} and $Nu_{\mathrm{MY},d_\mathrm{h}}$ was conducted and a relationship $Nu_{d_\mathrm{h}} = 1.453Nu_{\mathrm{MY},d_\mathrm{h}}$ was obtained with $R^2 = 0.965$. Based on this result, a novel expression for the Nusselt number of throat in a PNM is proposed as

$$\overline{Nu}_{PNM,d_\mathrm{h}} = 1.453\frac{2}{\sqrt{\pi}}\left[\left(\frac{3.24}{8\alpha_{\mathrm{HR}}}\right)^5 + \left(\frac{3}{2}0.393\left(\frac{2}{\alpha_{\mathrm{HR}}L^*}\right)^{\frac{1}{3}}\right)^5\right]^{\frac{1}{5}} \tag{9.55}$$

The α_{HR} can be calculated by combining Eqs. (8.10), (8.12) and (8.41) as

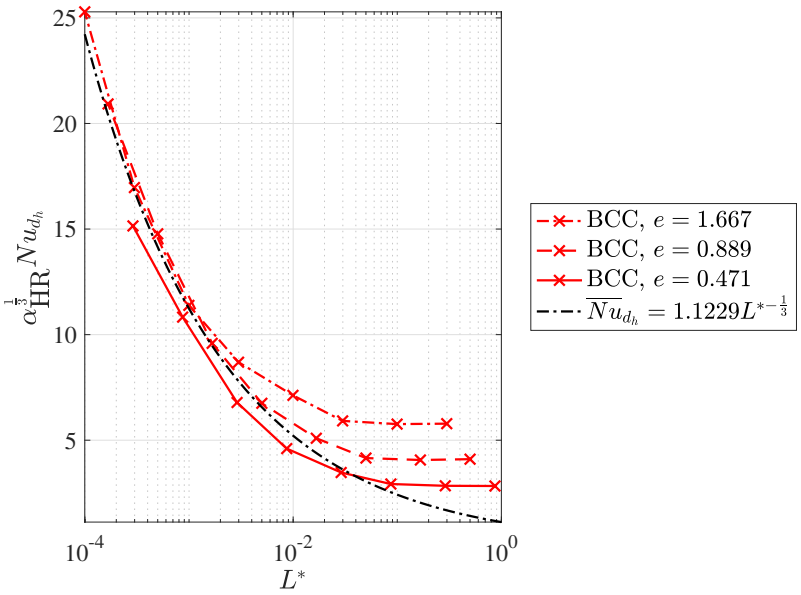


Figure 9.14: $\alpha_{\mathrm{HR}}^{1/3}\overline{Nu_{d_\mathrm{h}}}$ versus L^* for the BCC packings with different void ratios.

$$\alpha_{\mathrm{HR}} = \frac{{r_{\mathrm{eff}}}^2}{{r_{\mathrm{eq}}}^2}\alpha_{\mathrm{ERHR}} = \frac{{r_{\mathrm{eff}}}^2}{{r_{\mathrm{eq}}}^2}\left(0.510\left(\frac{1}{1+e^*}\right)^3 - 0.441\left(\frac{1}{1+e^*}\right)^2 + 0.286\left(\frac{1}{1+e^*}\right)\right) \tag{9.56}$$

where r_{eff}, r_{eq}, and e^* can be determined from the throat geometry. Therefore, the only one additional empirical parameter, 1.453, which was determined from the CFD simulation results, is introduced in this study and the rest of terms are based on well-established experimental data using circular and non-circular pipes (Shah & London, 1978; Muzychka & Yovanovich, 2002b; Muzychka & Yovanovich, 2004) and the analytical study outlined in Section 8.3 based on well-established Zick and Homsy (1982)'s analytical study results.

9.4.2 Random packings

Fig. 9.16 shows the comparison between the Nu values obtained from the OF simulation data and the Nu values predicted from Eq. (9.55) for throats in monodisperse packings with a variety of void ratios for a global Pc of 150. A line with a $1:1$ slope, which indicates the perfect agreement of the Nu from the OF simulation results and the Nu from Eq. (9.55), is shown in Fig. 9.16. In Fig. 9.16, the Re value of the throats required to calculate L^* was calculated from the PNM simulation results. In Fig. 9.16, each data point was coloured based on the ratio of the throat length to the particle diameter. Fig. 9.16 shows that the majority of data points are located around the line of equality, which indicates the applicability of Eq. (9.55) to random packings.

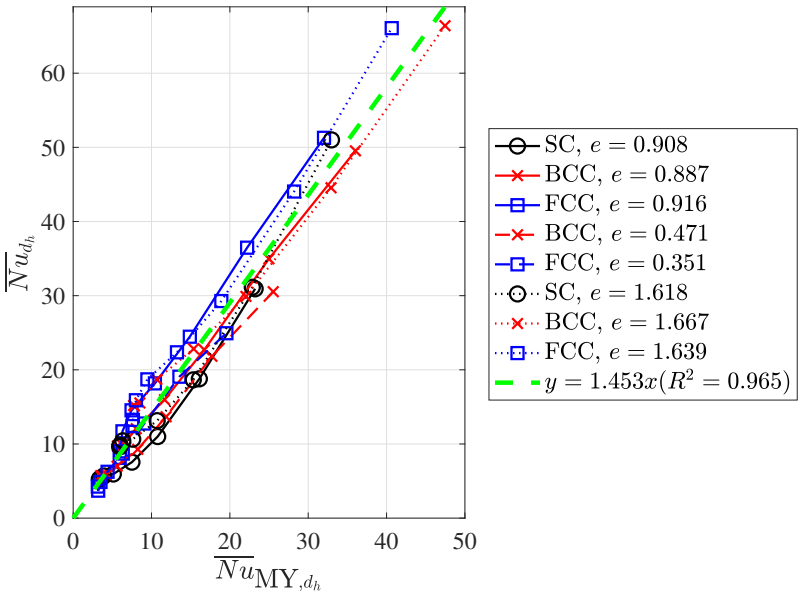
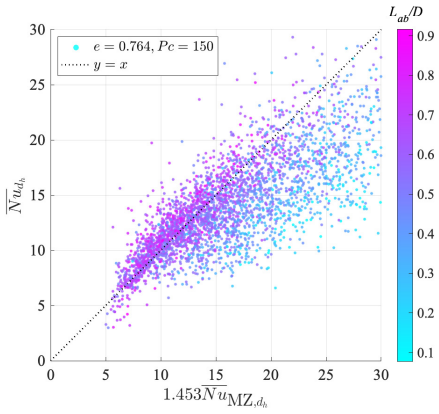


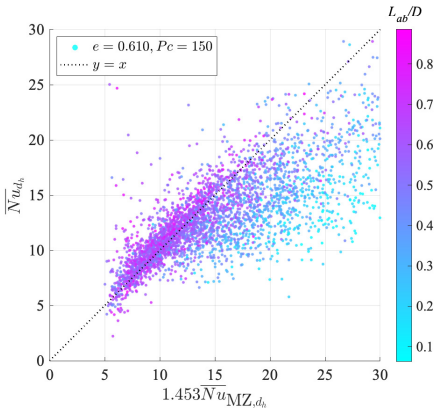
Figure 9.15: Nu of throats in three types of regular packings with various void ratios and Nu predicted by Eq. (9.54).

Fig. 9.16 shows two noticeable issues in regard to Eq. (9.55). The first issue is related to the throat length. As the marker color in Fig. 9.16 indicates, the Nusselt number of "short" throats, which have a low throat length, tends to be lower than the predicted Nusselt number. These short throats have $L_{ab}/D = 0.1 - 0.2$, which is much shorter than those of the throats in the regular packings used for the model development as summarised in Table 9.7 ($L_{ab}/D = 0.41 - 1.11$). The observation reflects the fact that the throat geometries of the regular packings in Table 9.7 are not fully representative for throat geometries in random packings. Additional future work may be useful to correct the error by adding the correction term depending on L_{ab} or elaborating the definition of L^*.

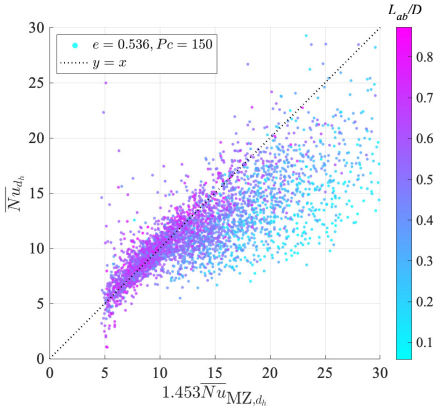
The other issue which can be seen in Fig. 9.16 is the scatter in the results for a low predicted Nu value ($5 < Nu < 10$). These low Nu values are related to a large L^* according to Eq. (9.55). Referring to Eq. (9.15), a large L^* can be associated with a low Re number and thus a low flow velocity. In these throats, the heat transfer via thermal conduction through fluid is not negligible compared to the heat transfer via advection and consequently, the LMTD based model is less reliable because the LMTD is derived ignoring the thermal conduction through fluid. This issue is more prominent if a lower Pc value was considered as shown in Fig. 9.17, which considers data equivalent to those presented in Fig. 9.16 but with a different Pc of 15.



(a) $e = 0.764$.

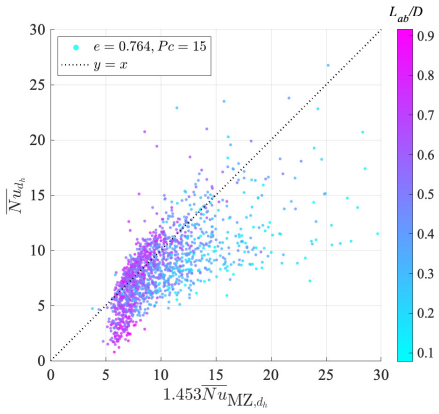


(b) $e = 0.610$.

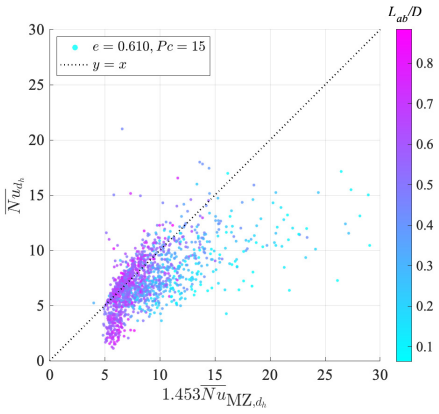


(c) $e = 0.536$.

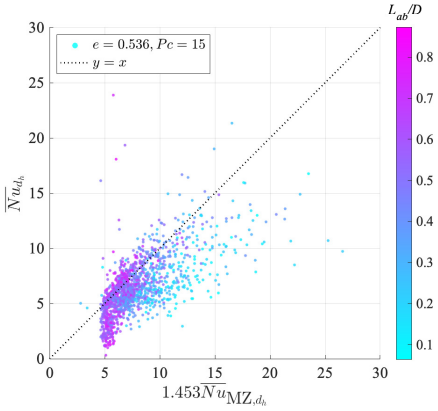
Figure 9.16: Actual Nu and predicted Nu for $Pc = 150$.



(a) $e = 0.764$.



(b) $e = 0.610$.



(c) $e = 0.536$.

Figure 9.17: Actual Nu and predicted Nu for $Pc = 15$.

9.5 Summary

This chapter discussed modelling of heat transfer mechanisms which are of great importance when there is fluid flow in granular materials, namely fluid conduction, fluid advection, and particle-fluid conduction. This chapter specifically focused on extending a PNM-DEM framework for heat transfer simulations. Previous particle-fluid conduction models were reviewed and a novel particle-fluid conduction model was proposed based on a model developed for pipes (Muzychka & Yovanovich, 2004) and CFD results developed in this chapter.

In Section 9.2, an existing PNM-DEM framework proposed by Caulk et al. (2020) was reviewed. Section 9.2.1 reviewed the formulations of heat transfer due to fluid advection, fluid conduction, and particle-fluid conduction in the existing PNM-DEM framework. In addition, Section 9.2.1 discussed the definition of the Nusselt number (Nu) and how Nu can be related to the particle-fluid conduction phenomenon. Existing expressions for Nu in granular materials were reviewed in Table 9.1. Section 9.2.2 first pointed out that the models reviewed in Table 9.1 were derived from the global packing density and the global Reynolds number and that none of the existing models was developed to predict the pore-scale Nu. Section 9.2.2 reviewed the previous studies modelling the Nu of fluid flow in a pipe to summarise useful insight into modelling the Nu of fluid flow in a throat. The definition of the fluid temperature, temperature driving force, and asymptotic values of the Nu were clarified. It was proposed that the model, proposed by Muzychka and Yovanovich (2004), might be applicable for throats in a PNM as the model only considers on the thermal length L^* and the product of f and Re, which can be related to the the throat shape data.

Fully-resolved CFD simulation data were generated to develop and validate the model predicting the Nu of throats in granular materials in Section 9.3. Meshes similar to those used in Chapter 8 were used while the energy transport equation was considered in addition to the continuity equation and the momentum equation as outlined in Section 9.3.1. The verification and validation of the meshes and the solver were detailed in Section 9.3.2. Both regular and random packings (Sections 9.3.3 and 9.3.4) were considered for the CFD simulations and the calculation procedure adopted to determine the Nu value of fluid flow in a throat was provided in Section 9.3.3.

The results were summarised in Section 9.4. Section 9.4.1 shows the results for the regular packings, where a similar asymptotic behaviour of the Nu value of throats to that of pipes was observed. In Section 9.4.1, a novel expression for the Nusselt number of throats in granular materials was proposed just by adding a parameter to Muzychka and Yovanovich (2004)'s model and a good agreement between the novel model and the CFD-generated data

was demonstrated. In Section 9.4.2, the model prediction was compared with the Nusselt number of the throats in random packings. A good agreement between the developed model prediction and the CFD data was observed for some throats; however, the accuracy of the model decreased for throats with a low Pc value or a low L.

The developed expression for the Nu has less empirical parameters than previously available expressions and considers pore-scale geometries. A thermal PNM with the developed expression is an efficient and accurate option to simulate heat transfer phenomena in granular materials with the pore fluid flowing. In addition, the finding obtained by this section, where the Nu expression for pipes can be used for local-scale particle-fluid conduction in granular materials, enhances the scientific understand of heat transfer phenomena in granular materials.

CHAPTER 10

CONCLUSIONS

10.1 Summary

This study has combined a variety of numerical methods to examine the thermal behaviour of granular materials across multiple scales to improve understanding of the mechanisms underlying the complex thermo-hydro-mechanical behaviour of granular materials. This thesis has been written in two parts: the first part considers a specific case where the pore flow is stagnant while the second part considers both heat transfer as well as the fluid flow.

Chapter 2 summarised key thermal phenomena in granular materials where pore fluid is stagnant. The Chapter highlighted that in this specific case only the conductive heat transfer needs ot be considered but the conductive heat transfer in granular materials is much more complex than is the case for single phase materials. The review of prior experimental studies showed that the thermal expansion of particles in granular materials leads to a complex thermo-mechanical behaviour. Existing numerical simulation tools were reviewed and the Discrete Element Method (DEM) and heat pipe network models were identified as efficient numrical tools to simulate the complex thermo-mechanical behaviour of granular materials.

Chapter 3 focused on ideal assemblies of granular materials subject to a confining pressure with a stagnant pore fluid, where heat transfer can be studied by restricting consideration to three phenomena (conduction through particles, conduction via particle-particle contact, and particle-fluid-particle conduction). A heat pipe network model was employed to simulate heat transfer between particles efficiently. The adopted modified BOB model, which was originally proposed by Batchelor and O'Brien (1977) and later modified by Dai, Hanaor and Gan (2019), was used to model the three key heat transfer mechanisms. The modified BOB model was validated by solving the heat equation for two contacting or separated particles surrounded by stagnant air using a Finite Element Method (FEM)

simulation with a fine mesh. In addition, a heat pipe network model was validated for a simple cubic packing by comparison with FEM data. Thermal expansion of particles was considered by varying the radius of the particles based on their temperature. A thermal DEM was developed by coupling the DEM with the above mentioned heat pipe network model and adopting a thermal expansion model. The developed thermal DEM is novel since the developed code is MPI parallelised and there is control in the stress state of the sample while considering heat conduction and the thermal expansion of particles. Using the developed thermal DEM, three thermo-mechanical behaviours of granular materials were examined; namely, effective thermal conductivity (Chapter 4), thermal stresses (Chapter 5), and thermal volume changes (Chapter 6).

Chapter 4 described an analytical study using the heat pipe network model and effective medium theory (EMT) and developed a relationship between the effective (bulk) thermal conductivity and the elastic stiffness of granular materials. To validate the result of the analytical study, a variety of granular samples with different stresses, void ratios and anisotropy degrees were created using the Discrete Element Method and heat transfer simulations were conducted to measure the effective thermal conductivity of the granular materials. The numerical simulation results also showed a correlation between the effective thermal conductivity and the Young's modulus of the virtual granular samples especially in a high thermal conductivity ratio (κ) of the solid phase to the fluid phase, and so they confirmed the findings from the analytical study. Finally, the Chapter developed a model predicting the effective thermal conductivity of granular samples only using the void ratio and the Young's modulus; the data presented showed a good agreement between the effective thermal conductivity values obtained from the model and the numerical simulations.

Chapter 5 conducted an analytical study predicting the stress generated in a granular medium due to an increase in the temperature. The EMT and the Hertzian contact model were used to develop a model predicting the thermal stress only from the packing characteristic of the granular sample and the material properties of the particles (without any empirical fitting parameters). To validate the model, DEM simulations were conducted using monodisperse virtual granular samples where the particle radius was varied to mimic the thermal expansion of the granular particles. A good agreement between the thermal stress values obtained from the model and the simulations for dense granular materials; however, a large discrepancy was observed for loose granular materials. More detailed analysis of the DEM data showed that the error was caused because the analytical model neglects the movement of the particles. Based on the observation, empirical fitting parameters were introduced in the model and eventually a good agreement was obtained for a wide range of void ratios.

Chapter 6 showed the thermal DEM simulation results where thermal cycles were introduced in virtual granular samples with a different packing characteristics. A continuous contraction resulting from the thermal cycles was observed for the most of the samples. It was clearly shown that the volumetric strain introduced by a thermal cycle depends on the initial packing characteristics of the granular samples. Samples with a higher initial anisotropic degree resulted in a larger contraction during thermal cycles.

Granular materials with pore fluid flowing were considered in the latter part of this thesis. The literature review in Chapter 7 showed the governing equations of an incompressible Newtonian fluid flow. It was stated that the computational fluid dynamics (CFD) is needed to simulate the fluid flow in granular materials due to the complexity of the equations and pore space geometry. Three types of CFDs, namely fully-resolved CFD, coarse-grid CFD, and pore network model (PNM), were introduced.

Chapter 8 was dedicated to developing an accurate conductance model to simulate fluid flow through granular materials using the PNM. This type of model that operates at the pore-scale is essential to model the heat transfer mechanisms associated with pore fluid advection and particle-fluid conduction. Chapter 8 argued that, while PNMs are an efficient method to simulate fluid flow, their accuracy has been compromised due to a poor understanding of fluid flow phenomenon at the pore-scala. To improve the accuracy of existing PNM algorithms, an analytical study using regular packings was conducted and novel expressions for local hydraulic conductance were proposed. To validate the proposed conductance models, fully-resolved CFD simulations, which consider fluid flow in random packings, were conducted and local conductance values were back-calculated from the simulation results. The comparison between data generated using a PNM with the new conductance models and the results from fully-resolved CFD simulations demonstrated that the novel conductance models are applicable to random packings. Chapter 8 also explored the ability of a PNM that includes the new conductance models to predict the fluid-particle interaction force when compared with a PNM that adopts existing conductance models. The new model was also shown to perform well in comparison with empirical methods for predicting the fluid-particle interaction force, that have been used in coarse-grid CFD-DEM frameworks. In each of the PNM approaches the fluid-particle interaction forces were calculated following Chareyre et al. (2012). In assessing the empirical expressions used in coupled coarse grid DEM-CFD frameworks the fluid-particle interaction forces were calculated using expressions proposed by Ergun (1952) and van der Hoef, Beetstra and Kuipers (2005). The data from the fully-resolved CFD simulations revealed that there can be a distribution of fluid-particle interaction forces acting on particles with the same diameter, this observation highlights a key shortcoming of the coarse-grid DEM-CFD coupling approach which predict the fluid-particle interaction force considering only the particle diameter, the global porosity, and the global Reynolds number. On the other hand,

a detailed comparison between PNMs adopting a variety of conductance models, and the fully-resolved CFD simulations showed that the PNM using the $\alpha_{\text{ERHR}}(\xi)$ conductance model (Eq. (8.42)) can predict the magnitude and direction of the particle-fluid interaction force on particles accurately for a variety of PSDs and packing densities.

Chapter 9 firstly reviewed a thermal PNM framework proposed by Caulk et al. (2020) and confirmed that the modelling of fluid advection and fluid conduction are relatively straightforward. It was reviewed that the Nusselt number (Nu) has been used to characterise the fluid-particle conduction phenomenon for general thermal CFD-DEM frameworks. However, it was also argued that the model for fluid-particle conduction had potential for refinement or improvement as previously proposed models contain multiple empirical expressions. To give more detailed insights into the pore-scale fluid-particle conduction phenomenon, Chapter 9 included a review of previous studies expressing the Nu for fluid flow through circular and non-circular pipes. Among the existing models, that developed by Muzychka and Yovanovich (2004) was chosen for comparison with the pore-scale Nu. The pore-scale Nu values for regular and random packings were obtained using fully-resolved CFD simulations. Comparisons between the Muzychka and Yovanovich (2004) model and the pore-scale Nu for the regular packings showed that the pore-scale Nu can be predicted just by introducing one additional empirical parameter to its original formulation. The Nu expression developed here was compared with the random packings and a good agreement was obtained for a high Pc.

10.2 Key findings

The key findings from the first part (Chapters 4 to 6) are:

- An analytical study that considers the effective thermal conductivity (ETC) of granular materials showed that theoretically, this property can be predicted using the elastic modulus E and the packing density.

- Heat pipe network analyses using DEM samples with different mean coordination numbers, void ratios, degrees of anisotropy and κ values revealed that the dependency of the ETC on e is high for a low κ value but decreases as the κ value increases. On the other hand, the correlation between ETC and E increases as the κ value increases.

- A novel expression for the effective thermal conductivity of granular materials using E and e was proposed based on the analytical study and the observations obtained from the heat pipe network analyses. A good agreement between the expression for the ETC and the heat pipe network analyses was obtained.

- An analytical model predicting the thermal stress of a monodisperse granular medium was derived using an Effective Medium Theory (Walton, 1987; Rothenburg & Bathurst, 1989) and it was proposed that the thermal stress can be related to the packing density and the coordination number as well as the material properties of the particles.
- A comparison between the analytical model and DEM analyses demonstrated that the analytical model can predict the stress induced by changes in temperature in regular packings and medium-dense or dense random packings; however, the model accuracy decreases when loose random packings were considered.
- The detailed analyses of the DEM data showed that the accuracy of the analytical model decreases as the particle movement increases. The analytical model was modified by introducing an empirical factor, which reflects how likely it is for particle movement to occur. With the correction factor, the analytical model increased its accuracy, with a maximum error of 11.6%.
- Thermal DEM simulations where a granular sample was subjected to thermal cycles were conducted with a variety of packings densities, isotropic stresses and the degrees of anisotropy. The degree of anisotropy, as well as the void ratio, were shown to be an important factor to determine the volume change behaviour of the granular sample. A looser and more anisotropic sample showed a more contractive behaviour.

The key findings regarding the hydro-mechanical study in the second part of this the (Chapter 8) are:

- Existing local conductance models to describe flow between adjacent pores under laminar flow conditions were reviewed and compared with the local conductance of throats in regular packings analytically obtained from Zick and Homsy (1982). The accuracy of the models was shown to be poor because the models do not fully capture the geometry of the throats.
- Novel local conductance models, which can predict the local conductance of the various regular packings with a wide range of e values, were proposed. The local void ratio (e^*) or the non-dimensional ratio of the fluid volume to the solid surface area was found to be the key to obtain an accurate local conductance.
- The comparison between the fully-resolved CFD simulations and a PNM showed that the local conductance models are applicable to random packings. Amongst the considered models, the local conductance model based on ξ, which is the non-dimensional ratio of the fluid volume Θ to the solid surface area γ ($\xi = \Theta^{\frac{1}{3}}/\gamma^{\frac{1}{2}}$), was shown to be the most robust model and demonstrated a good agreement with

the fully-resolved CFD data for samples with a variety of PSDs and e values (the $\alpha_{\text{ERHR}}(\xi)$ model).

- An empirical method to predict the fluid-particle interaction force used in coarse-grid CFD-DEM frameworks showed a limited accuracy when it was compared to the fully-resolved CFD result because it only considers the global pressure drop and the diameter of particles and cannot consider the heterogeneity in the flow field in the pore space. On the other hand, the fluid-particle interaction forces predicted by a PNM with the $\alpha_{\text{ERHR}}(\xi)$ model was in agreement with the force values obtained from the fully-resolved CFD simulations.

The key findings from the thermo-hydraulic study in the second part of the thesis (Chapter 9) are:

- A literature review showed that previous CFD-DEM frameworks use the Nu number, which is non-dimensional ratio of particle-fluid condution to the thermal conductivity of the fluid, to model the particle-fluid conduction. It was argued that the model predicting the Nu number has been empirical.
- The Nu of fluid flow though throats in regular packings converged to a constant value for a low Peclet (Pc) number, where the Peclet number is the product of the Reynolds number and Prandtl number. For a high Pc number, the Nu of fluid flow through throats in regular packings was proportional to $L^{*-1/3}$, where L^* is the non-dimensionalised thermal length. These observations are in agreement with the previous studies considering the Nu of fluid flow through circular and non-circular pipes.
- A novel model predicting the Nu of fluid flow through throats in granular materials was developed by adding a single empirical parameter to the model proposed by Muzychka and Yovanovich (2004). The new model agreed well with the fully-resolved CFD simulation results with a variety of regular packings.
- A dataset of the Nu values of throats in random packings was developed for two Pc values. The accuracy of the proposed model decreased for throats with a shorter length and slower flow. However, the developed model was in agreement with the fully-resolved CFD data for most of throats.

10.3 Recommendations for future work

Based on the research completed in this project and the understanding of the literature developed during this research a number of future developments were identified. A summary overview of ideas for future research is presented here.

10.3.1 Additional research into the effective thermal conductivity of granular materials

Laboratory experiments

In Chapter 4, analytical and numerical studies linking the elastic stiffness and the effective thermal conductivity of granular materials were conducted and a novel model that predicts the effective thermal conductivity from the Young's modulus and void ratio was proposed. An experimental campaign measuring both effective thermal conductivity and Young's modulus of granular materials would be useful to examine the efficacy of the proposed model for real granular materials under real physical experimental conditions.

Consideration of surface roughness

The modified BOB model used in this study assumes that contacting spheres are smooth. It is also useful to consider the effect of surface roughness on the local thermal conductance as in the study by Bahrami, Culham and Yovanovich (2004). Models predicting the contact force for rough particles have been well-studied (Yimsiri & Soga, 2000; Otsubo et al., 2017). Interestingly, the thermal conductance model by Bahrami, Culham and Yovanovich (2004) and the contact force model by Otsubo et al. (2017) use the same quantification of surface roughness (the root mean squared roughness), which indicates that the analytical study relating effective thermal conductivity and Young's modulus of granular particles can be extended to rough particles.

Consideration of polydispersity

It is now well established that, in a polydisperse granular sample with a broad range of particles sizes, the PSD and stress state influence whether or not fine particles participate in stress transmission (Liu, O'Sullivan & Carraro, 2021; Sufian et al., 2021). Therefore, in polydisperse granular samples, conventional empirical relationships between the effective or small strain Young's modulus and the void ratio tends to break down (Liu et al., 2022). Thus, future work studying effect of polydispersity on the relationship between effective thermal conductivity, Young's modulus and void ratio of granular materials would be of value. A criteria to establish whether or not a heat pipe is considered between two given particles should be carefully defined. One appoach that is tractable is to conduct the weighted Voronoi tessellation and consider a heat pipe between two particles if their cells are adjacent to each other as Chen et al. (2019).

Consideration of particle shape

It has been shown that particle shape affects the mechanical properties of a granular packing (Cho, Dodds & Santamarina, 2006; Salot, Gotteland & Villard, 2009; Katagiri, Matsushima & Yamada, 2010; Altuhafi, Coop & Georgiannou, 2016). Studying the effect

of particle shape on the effective thermal conductivity of a granular materials would be an interesting topic. The "clump" approach, where multiple spheres are clumped to represent an irregularly shaped particle, may be possibly used for a heat pipe network model. Alternatively, ellipsoids may be used instead of spheres as the Hertzian contact model can be applied to ellipsoids and the model proposed by Batchelor and O'Brien (1977) model was derived based on Hertzian contact theory.

10.3.2 Future study on stress induced by temperature change

Consideration of polydispersity

As discussed above, the stress state in a polydisperse granular medium influences the balance of stress transmission between the fine and coarse particles. In the analytical model (Eq. (5.15)) developed in Chapter 5, the mean coordination number of the granular medium was assumed to be constant and the comparison with the DEM results summarised in Section 5.3 showed that this assumption does not induce a large error for monodisperse granular media. However, this assumption may induce a larger error in a polydisperse sample due to the complex stress transmission mechanisms in a polydisperse samples. Therefore, a future study on the thermal stresses in polydisperse granular materials could be explored.

Consideration of particle shape

This study considered only spherical particles using a simple thermal expansion model; however, the thermal expansion of non-spherical particles could be easily considered using "clump"s or ellipsoidal particles. Future work studying thermal stresses in non-spherical particles is thus recommended. For example, the effects of anisotropy in particle orientation on thermal stresses would be an interesting topic.

10.3.3 Future study on volume change behaviour when thermal cycles are applied

Comparison with laboratory experiments

There are still a limited number of experimental studies that have considered the response of granular materials to thermal cycles in the triaxial apparatus. If high-quality thermal triaxial test data can be developed, comparisons between the DEM results developed in Chapter 6 and laboratory experiments would be useful to validate the DEM simulation approach employed in Section 6.2.

Consideration of particle shape

The DEM data presented in Chapter 6 exhibited a much smaller volumetric strain than the experimental data obtained by Ng, Wang and Zhou (2016). The difference in the datasets can possibly be attributed to the difference in particle shape between DEM particles and Toyoura sand particles. Elongated particles have a wider gap between the maximum and minimum void ratios (Cho, Dodds & Santamarina, 2006; Salot, Gotteland & Villard, 2009; Adesina et al., 2022; Morimoto, Otsubo & Koseki, 2021), which means that the same magnitude of change in the relative density ($= (e_{\max} - e)/(e_{\max} - e_{\min})$) results in a higher change in the volumetric strain of a sample with irregularly-shaped particles than a sample with spherical particles. As discussed above, it is not technically difficult to consider the thermal expansion of non-spherical particles; thus, it is recommended to simulate thermal volume change simulations using irregularly-shaped DEM particles.

Consideration of surface roughness

Suo et al. (2021) simulated elasto-plastic granular particles under thermal cycles and observed a larger thermal volume contraction than elastic granular particles. Their results indicate that a hysteresis in thee force-displacement relationship of particle-particle contacts may enhance the thermal volume contraction. Although soil particles are believed to break before they exhibit elasto-plastic behaviour according to laboratory experiments studying the tribology of sand particles e.g. Cavarretta (2009), the asperity of particle surface may induce a non-recoverable displacement at particle-particle contact. Therefore, it would be worthwhile to study the effect of surface roughness on thermal volume change in both experimental and numerical studies.

Meso-scale analyses on fundamental mechanism underlying a volume change of granular materials under thermal cycles

In Sections 6.4 and 6.5, some packing characteristics of the DEM samples, the mean coordination number and the degree of anisotropy were analysed to be related to the volume change behaviour of the samples. The microscopic parameters considered in this study are all defined at contact-scale; thus, meso-scale analysis, which considers a few particles and a pore space surrounding the particles, is highly recommended in future.

10.3.4 Hydro-mechanical behaviour of granular materials

Consideration of particle shape

Another feature of the local conductance models developed in this study are that they are based on geometric parameters which can be defined for non-spherical particles. Future studies examining the applicability of the developed models for granular materials with non-spherical particles are recommended; however, substantial experimental and numerical work will be required. Unlike fluid flow through sphere packings, no theoretical expression,

such as Zick and Homsy (1982)'s study, is available for fluid flow through packings of non-spherical particles; so the verification data for a fully-resolved CFD simulation need to be obtained from a laboratory permeameter test using soil samples. To reproduce the soil sample in the fully-resolved CFD simulations, a micro CT image of the sample following Taylor et al. (2017) or a non-spherical DEM simulation following Zhao and O'Sullivan (2022) is required. In addition, an alternative meshing tool will be required to generate a mesh representing the complex pore space in the sample with non-spherical particles.

Hydro-mechanical coupled simulations

This study focused on the development of accurate local conductance models for PNMs and demonstrated that a PNM with proposed local conductance models can predict local flow field in granular materials and fluid-particle interaction force accurately. The result is encouraging for future studies using hydro-mechanical coupled simulations based on a PNM-DEM framework with the novel local conductance models. PNM-DEM frameworks can be found in e.g. Catalano, Chareyre and Barthélemy (2014) and `YADE` is an open-source software which can consider a PNM-DEM coupling. There are various interesting practical problems which can be considered using a PNM-CFD framework; suffusion (Wautier, Bonelli & Nicot, 2017; Kawano, Shire & O'Sullivan, 2018), liquefaction (El Shamy & Aydin, 2008). More accurate simulation results than were possible in previous studies are expected based on the results obtained from this study.

High Reynolds number

Practical applications outside geotechnical engineering, e.g. packed-bed energy storage, consider a Reynolds number higher than 1, where fluid flow in the pore space is hydrodynamically developing. For fluid flow through granular materials at a relatively high Reynolds number, Ergun and Orning (1949) considered an inertial term in the Hagen-Poiseuille flow expressions and Wu, Hou and Yu (2019) applied Ergun and Orning (1949)'s model for fluid flow through throats and captured decrease in the overall friction factor although they did not examine local flow field. The local conductance models developed in this study are much more accurate than the model employed in Wu, Hou and Yu (2019) for hydrodynamically fully-developed flow; thus, future work extending the developed model for developing flow is recommended.

10.3.5 Heat transfer mechanisms in granular materials with fluid flow

High Reynolds number

As discussed above, extending the particle-fluid conduction model proposed in Section 9.4 to a high Reynolds number would be very useful for practical applications in fields outside geotechnical engineering. Previous studies e.g. Shah and London (1978) and Muzychka

and Yovanovich (2004) considering fluid flow in pipes classified this type of flow as simultaneously developing flow and a different formulation of the Nusselt number will be required (Eq. (9.38)).

Relating local Nusselt number to global Nusselt number in granular materials

One of interesting findings obtained from the literature review summarised in Section 9.2 on the formulation of the Nusselt number in pipes and granular materials is that the exponent of the Reynolds number in the formulation of the Nusselt number for granular materials is much higher than that for pipes. It may be attributed to heterogeneity existing in local fluid flow. A thermal PNM framework proposed by Caulk et al. (2020) with the novel particle-fluid conduction model would enable fundamental analysis relating local Nusselt number to global Nusselt number in granular materials.

10.3.6 Thermo-hydro-mechanical coupled simulations

There are a variety of practical problems associated with thermo-hydro-mechanical behaviour of granular materials, including frictional heat-induced landslide (Alonso, Zervos & Pinyol, 2016) and packed-bed energy storage (Anderson et al., 2015). This study addressed a number of key challenges involved in thermo-hydro-mechanical coupled simulations. The outcomes of this study will enable fast and accurate thermo-hydro-mechanical coupled simulations, which will be useful to obtain engineering or scientific insights into complex thermo-hydro-mechanical coupled problems.

– REFERENCES –

Adesina, P., O'Sullivan, C., Morimoto, T. & Otsubo, M. (2022) Determining a representative element volume for DEM simulations of samples with non-circular particles. *Particuology*. 68, 29–43.

Agar, J. G. (1984) *Geotechnical behaviour of oil sands at elevated temperatures and pressures.* PhD thesis. University of Alberta.

Ahrens, J., Geveci, B. & Law, C. (2005) Paraview: an end-user tool for large data visualization. *The visualization handbook*. 717 (8).

Alonso, E., Zervos, A. & Pinyol, N. (2016) Thermo-poro-mechanical analysis of landslides: from creeping behaviour to catastrophic failure. *Géotechnique*. 66 (3), 202–219.

Altuhafi, F. N., Coop, M. R. & Georgiannou, V. N. (2016) Effect of particle shape on the mechanical behavior of natural sands. *Journal of Geotechnical and Geoenvironmental Engineering*. 142 (12), 04016071.

Anderson, R., Bates, L., Johnson, E. & Morris, J. F. (2015) Packed bed thermal energy storage: a simplified experimentally validated model. *Journal of Energy Storage*. 4, 14–23.

Appel, T. (2021) Thbtppl/latex-thesis-imperial: template for writing an imperial college london phd thesis in latex. DOI: 10.5281/zenodo.4452435.

Askari, R, Ikram, M. & Hejazi, S. (2017) Pore scale evaluation of thermal conduction anisotropy in granular porous media using lattice boltzmann method. *International Journal of Numerical Methods for Heat & Fluid Flow*. 27 (4), 867–888.

Azeiteiro, R. J. N., Coelho, P. A. L. F., Taborda, D. M. G. & Grazina, J. C. D. (2017) Critical state based interpretation of the monotonic behavior of hostun sand. *Journal of Geotechnical and Geoenvironmental Engineering*. 143 (5), 04017004. DOI: 10.1061/(ASCE)GT.1943-5606.0001659.

Bagi, K. (1996) Stress and strain in granular assemblies. *Mechanics of materials*. 22 (3), 165–177.

Bagi, K. (2006) Analysis of microstructural strain tensors for granular assemblies. *International Journal of Solids and Structures*. 43 (10), 3166–3184.

Bahrami, M, Culham, J. & Yovanovich, M. (2004) Modeling thermal contact resistance: a scale analysis approach. *J. Heat Transfer*. 126 (6), 896–905.

Balay, S., Abhyankar, S., Adams, M., Brown, J., Brune, P., Buschelman, K., Dalcin, L., Dener, A., Eijkhout, V., Gropp, W et al. (2019) PETSc users manual.

Balay, S., Gropp, W. D., McInnes, L. C. & Smith, B. F. (1997) Efficient management of parallelism in object-oriented numerical software libraries. In: *Modern software tools for scientific computing*. Springer, pp. 163–202.

Barreto, D (2009) *Numerical and experimental investigation into the behaviour of granular materials under generalised stress states*. PhD thesis. Imperial College London.

Batchelor, G. K. (1967) *An introduction to fluid dynamics*. Cambridge, Cambridge University Press.

Batchelor, G. K. & O'Brien, R. (1977) Thermal or electrical conduction through a granular material. *Proceedings of the Royal Society of London. A. Mathematical and Physical Sciences*. 355 (1682), 313–333.

Beetstra, R, van der Hoef, M. A. & Kuipers, J. (2007) Drag force of intermediate reynolds number flow past mono-and bidisperse arrays of spheres. *AIChE journal*. 53 (2), 489–501.

Bennett, T. D. (2019a) Correlations for the Graetz problem in convection–Part 1: for round pipes and parallel plates. *International Journal of Heat and Mass Transfer*. 136, 832–841.

Bennett, T. D. (2019b) Correlations for the Graetz problem in convection–Part 2: for ducts of arbitrary cross-section. *International Journal of Heat and Mass Transfer*. 135, 1327–1334.

Beyer, T., Schaller, G., Deutsch, A. & Meyer-Hermann, M. (2005) Parallel dynamic and kinetic regular triangulation in three dimensions. *Computer Physics Communications*. 172 (2), 86–108.

Birkholz, O., Gan, Y. & Kamlah, M. (2019) Modeling the effective conductivity of the solid and the pore phase in granular materials using resistor networks. *Powder Technology*. 351, 54–65.

Bortolotto, M. S., Taborda, D. M. G. & O'Sullivan, C. (2021) Thermal effects on the hydraulic conductivity of a granular geomatereial. In: *Proceedings of the 20th Internatioal Conference on Soil Mechanics and Geotechnical Engineering*. Sydney.

Bourne-Webb, P., Amatya, B, Soga, K, Amis, T, Davidson, C & Payne, P (2009) Energy pile test at Lambeth College, London: geotechnical and thermodynamic aspects of pile response to heat cycles. *Géotechnique*. 59 (3), 237–248.

Brigaud, F. & Vasseur, G. (1989) Mineralogy, porosity and fluid control on thermal conductivity of sedimentary rocks. *Geophysical Journal International*. 98 (3), 525–542.

Bryant, S. & Blunt, M. (1992) Prediction of relative permeability in simple porous media. *Physical review A*. 46 (4), 2004.

Calis, H., Nijenhuis, J., Paikert, B., Dautzenberg, F. & Van Den Bleek, C. (2001) CFD modelling and experimental validation of pressure drop and flow profile in a novel structured catalytic reactor packing. *Chemical Engineering Science*. 56 (4), 1713–1720.

Calvet, T., Vanson, J.-M. & Masson, R. (2022) A DEM/FFT approach to simulate the effective thermal conductivity of granular media. *International Journal of Thermal Sciences*. 172, 107339.

Catalano, E., Chareyre, B. & Barthélemy, E. (2014) Pore-scale modeling of fluid-particles interaction and emerging poromechanical effects. *International Journal for Numerical and Analytical Methods in Geomechanics*. 38 (1), 51–71.

Caulk, R., Scholtès, L., Krzaczek, M. & Chareyre, B. (2020) A pore-scale thermo–hydro-mechanical model for particulate systems. *Computer Methods in Applied Mechanics and Engineering*. 372, 113292.

Caulk, R. A. & Bruno, C. (2019) An open framework for the simulation of coupled thermo-hydro-mechanical processes in discrete element systems. In: *Proceedings of the 8th Internatioal Conference on Discrete Element Methods (DEM8)*. Enchede, Netherlands.

Cavarretta, I. (2009) *The influence of particle characteristics on the engineering behaviour of granular materials*. PhD thesis. Imperial College London (University of London).

Cecinato, F., Zervos, A. & Veveakis, E. (2011) A thermo-mechanical model for the catastrophic collapse of large landslides. *International journal for numerical and analytical methods in geomechanics*. 35 (14), 1507–1535.

Chang, C. S. & Liao, C. L. (1994) Estimates of elastic modulus for media of randomly packed granules. *Applied Mechanics Reviews*. 47 (1 part 2), S197–S206.

Chang, C. S., Sundaram, S. S. & Misra, A. (1989) Initial moduli of particulated mass with frictional contacts. *International Journal for Numerical and Analytical Methods in Geomechanics*. 13 (6), 629–644.

Chareyre, B., Cortis, A., Catalano, E. & Barthélemy, E. (2012) Pore-scale modeling of viscous flow and induced forces in dense sphere packings. *Transport in porous media*. 94 (2), 595–615.

Chen, K, Cole, J, Conger, C, Draskovic, J, Lohr, M, Klein, K, Scheidemantel, T & Schiffer, P (2006) Packing grains by thermal cycling. *Nature*. 442 (7100), 257–257.

Chen, L., Wang, C., Moscardini, M., Kamlah, M. & Liu, S. (2019) A DEM-based heat transfer model for the evaluation of effective thermal conductivity of packed beds filled with stagnant fluid: thermal contact theory and numerical simulation. *International Journal of Heat and Mass Transfer*. 132, 331–346.

Cheng, G., Yu, A. & Zulli, P (1999) Evaluation of effective thermal conductivity from the structure of a packed bed. *Chemical Engineering Science*. 54 (19), 4199–4209.

Cho, G.-C., Dodds, J. & Santamarina, J. C. (2006) Particle shape effects on packing density, stiffness, and strength: natural and crushed sands. *Journal of Geotechnical and Geoenvironmental Engineering*. 132 (5), 591–602.

Churchill, S. W. & Ozoe, H. (1973) Correlations for laminar forced convection in flow over an isothermal flat plate and in developing and fully developed flow in an isothermal tube. *Journal of Heat Transfer*. 95 (3), 416–419.

Coulibaly, J. B., Shah, M. & Rotta Loria, A. F. (2020) Thermal cycling effects on the structure and physical properties of granular materials. *Granular Matter*. 22 (4), 1–19.

Coulson, J. M., Richardson, J. F., Backhurst, J. R. & Harker, J. H. (1999) *Fluid flow, heat transfer and mass transfer*. San Diego, Butterworth-Heinemann.

Cundall, P. A. & Strack, O. D. L. (1979) A discrete numerical model for granular assemblies. *Géotechnique*. 29 (1), 47–65.

Dai, W., Hanaor, D. & Gan, Y. (2019) The effects of packing structure on the effective thermal conductivity of granular media: A grain scale investigation. *International Journal of Thermal Sciences*. 142, 266–279.

Dassault Systèmes (2019) *Abaqus user's manual 2019 version 6.14*. USA.

Deen, N. G., Peters, E., Padding, J. T. & Kuipers, J. (2014) Review of direct numerical simulation of fluid–particle mass, momentum and heat transfer in dense gas–solid flows. *Chemical Engineering Science*. 116, 710–724.

Di Felice, R. (1994) The voidage function for fluid-particle interaction systems. *International journal of multiphase flow*. 20 (1), 153–159.

El Shamy, U. & Aydin, F. (2008) Multiscale modeling of flood-induced piping in river levees. *Journal of Geotechnical and Geoenvironmental Engineering*. 134 (9), 1385–1398.

El Shamy, U., De Leon, O. & Wells, R. (2013) Discrete element method study on effect of shear-induced anisotropy on thermal conductivity of granular soils. *International Journal of Geomechanics*. 13 (1), 57–64.

Ergun, S. (1952) Fluid flow through packed columns. *Chem. Eng. Prog.* 48, 89–94.

Ergun, S. & Orning, A. A. (1949) Fluid flow through randomly packed columns and fluidized beds. *Industrial & Engineering Chemistry*. 41 (6), 1179–1184.

Evans, T. M., Mojarrad, H., Cunningham, C. & Tayebali, A. A. (2009) 'Grain size distribution effects in 2D discrete numerical experiments'. In: *Contemporary Topics in In Situ Testing, Analysis, and Reliability of Foundations*, pp. 58–65.

Favre-Marinet, M. & Tardu, S. (2013) *Convective heat transfer: solved problems*. John Wiley & Sons.

Fei, W. & Narsilio, G. A. (2020) Network analysis of heat transfer in sands. *Computers and Geotechnics*. 127, 103773.

Feng, Y., Han, K & Owen, D. (2010) Combined three-dimensional lattice Boltzmann method and discrete element method for modelling fluid–particle interactions with experimental assessment. *International journal for numerical methods in engineering*. 81 (2), 229–245.

Fonseca, J, O'sullivan, C, Coop, M. & Lee, P. (2013) Quantifying the evolution of soil fabric during shearing using scalar parameters. *Géotechnique*. 63 (10), 818–829.

Fourier, J. B. J. (1878) *The analytical theory of heat*. The University Press.

Garrett, D. & Ban, H. (2011) Compressive pressure dependent anisotropic effective thermal conductivity of granular beds. *Granular Matter*. 13 (5), 685.

Goddard, J. D. (1990) Nonlinear elasticity and pressure-dependent wave speeds in granular media. *Proceedings of the Royal Society of London. Series A: Mathematical and Physical Sciences*. 430 (1878), 105–131.

Goldstein, R. & Cho, H. H. (1995) A review of mass transfer measurements using naphthalene sublimation. *Experimental Thermal and Fluid Science*. 10 (4), 416–434.

Gunn, D. (1978) Transfer of heat or mass to particles in fixed and fluidised beds. *International Journal of Heat and Mass Transfer*. 21 (4), 467–476.

Hanley, K. J., O'Sullivan, C. & Huang, X. (2015) Particle-scale mechanics of sand crushing in compression and shearing using dem. *Soils and Foundations*. 55 (5), 1100–1112.

Hardin, B. O. & Richart, F. (1963) Elastic wave velocities in granular soils. *Journal of Soil Mechanics & Foundations Div*. 89, 33–65.

Hertz, H. R. (1882) Uber die beruhrung fester elastischer korper und uber die harte. *Verhandlung des Vereins zur Beforderung des GewerbefleiBes, Berlin*. 449.

Hoque, E. & Tatsuoka, F. (1998) Anisotropy in elastic deformation of granular materials. *Soils and Foundations*. 38 (1), 163–179.

Horai, K. (1971) Thermal conductivity of rock-forming minerals. *Journal of Geophysical Research*. 76 (5), 1278–1308.

Huang, X., Hanley, K. J., O'Sullivan, C. & Kwok, C. Y. (2014a) Exploring the influence of interparticle friction on critical state behaviour using dem. *International Journal for Numerical and Analytical Methods in Geomechanics*. 38 (12), 1276–1297.

Huang, X., Hanley, K. J., O'Sullivan, C. & Kwok, F. C. (2014b) Effect of sample size on the response of DEM samples with a realistic grading. *Particuology*. 15. Energy storage: Materials and processes, 107–115.

Iliev, P. S., Giacomazzi, E., Wittel, F. K., Mendoza, M., Haselbacher, A. & Herrmann, H. J. (2019) Behavior of confined granular beds under cyclic thermal loading. *Granular Matter*. 21 (3), 1–7.

Itasca (2007) *PFC3D version 4.0 user manual*. Minneapolis, MN, USA.

Jardine, R. (1992) Some observations on the kinematic nature of soil stiffness. *Soils and Foundations*. 32 (2), 111–124.

Johansen, O. (1977) *Thermal conductivity of soils*. Cold Regions Research and Engineering Lab Hanover NH. Tech. rep.

Kanuparthi, S., Subbarayan, G., Siegmund, T. & Sammakia, B. (2008) An efficient network model for determining the effective thermal conductivity of particulate thermal interface materials. *IEEE Transactions on Components and Packaging Technologies*. 31 (3), 611–621.

Katagiri, J., Matsushima, T. & Yamada, Y. (2010) Simple shear simulation of 3D irregularly-shaped particles by image-based dem. *Granular Matter*. 12 (5), 491–497.

Kawano, K., Shire, T. & O'Sullivan, C. (2018) Coupled particle-fluid simulations of the initiation of suffusion. *Soils and foundations*. 58 (4), 972–985.

Khalili, M. H., Roux, J.-N., Pereira, J.-M., Brisard, S. & Bornert, M. (2017) Numerical study of one-dimensional compression of granular materials. II. Elastic moduli, stresses, and microstructure. *Physical Review E*. 95 (3), 032908.

Kloss, C., Goniva, C., Hager, A., Amberger, S. & Pirker, S. (2012) Models, algorithms and validation for opensource DEM and CFD–DEM. *Progress in Computational Fluid Dynamics, an International Journal*. 12 (2-3), 140–152.

Knight, C. (2021) *Mesh-sphere-packing*. https://github.com/chrisk314/mesh-sphere-packing.

Knight, C., O'Sullivan, C., van Wachem, B. & Dini, D. (2020) Computing drag and interactions between fluid and polydisperse particles in saturated granular materials. *Computers and Geotechnics*. 117, 103210.

Knight, C. (2018) *Fluid flow and drag in polydisperse granular materials subject to laminar seepage flow*. PhD thesis. Imperial College London.

Krüger, T., Kusumaatmaja, H., Kuzmin, A., Shardt, O., Silva, G. & Viggen, E. M. (2017) The lattice Boltzmann method. *Springer International Publishing*. 10 (978-3), 4–15.

Kuwano, R & Jardine, R. (2002) On the applicability of cross-anisotropic elasticity to granular materials at very small strains. *Géotechnique*. 52 (10), 727–749.

La Ragione, L. & Magnanimo, V. (2012) Evolution of the effective moduli of an anisotropic, dense, granular material. *Granular Matter*. 14 (6), 749–757.

Ladd, A. J. (1994) Numerical simulations of particulate suspensions via a discretized Boltzmann equation. part 1. theoretical foundation. *Journal of fluid mechanics*. 271, 285–309.

Laloui, L. & Di Donna, A. (2013) *Energy geostructures: innovation in underground engineering*. John Wiley & Sons.

Lee, S.-J., Kim, K.-Y., Choi, J.-C. & Kwon, T.-H. (2016) Experimental investigation on the variation of thermal conductivity of soils with effective stress, porosity, and water saturation. *Geomech. Eng*. 11 (6), 771–785.

Li, J. & Mason, D. (2000) A computational investigation of transient heat transfer in pneumatic transport of granular particles. *Powder Technology*. 112 (3), 273–282.

Lide, D. R. (ed.) (2004) *CRC handbook of chemistry and physics, 85th edition*. CRC Press.

Liu, D., Morimoto, T., Carraro, J. A. H. & O'Sullivan, C. (2022) A semi-empirical re-evaluation of the influence of state on elastic stiffness in granular materials. *Granular Matter*. 24 (2), 1–22.

Liu, D., O'Sullivan, C. & Carraro, J. A. H. (2021) Influence of particle size distribution on the proportion of stress-transmitting particles and implications for measures of soil state. *Journal of Geotechnical and Geoenvironmental Engineering*. 147 (3), 04020182.

Lu, Z., Abdou, M. & Ying, A. (2001) 3D micromechanical modeling of packed beds. *Journal of nuclear materials*. 299 (2), 101–110.

Lubarda, V. & Chen, M. (2008) On the elastic moduli and compliances of transversely isotropic and orthotropic materials. *Journal of Mechanics of Materials and Structures*. 3 (1), 153–171.

Lévêque, A. M. (1928) *Les lois de la transmission de chaleur par convection*. Vol. 13. Annales des Mines, pp. 201–415.

Magnanimo, V., La Ragione, L., Jenkins, J. T., Wang, P & Makse, H. A. (2008) Characterizing the shear and bulk moduli of an idealized granular material. *EPL (Europhysics Letters)*. 81 (3), 34006.

Makse, H. A., Gland, N., Johnson, D. L. & Schwartz, L. M. (1999) Why effective medium theory fails in granular materials. *Physical Review Letters*. 83 (24), 5070.

Mason, G. & Morrow, N. R. (1991) Capillary behavior of a perfectly wetting liquid in irregular triangular tubes. *Journal of Colloid and Interface Science*. 141 (1), 262–274.

MathWorks (2020) *MATLAB (R2020a)*. USA, The MathWorks Inc.

Matsumoto, M. & Nishimura, T. (1998) Mersenne twister: a 623-dimensionally equidistributed uniform pseudo-random number generator. *ACM Transactions on Modeling and Computer Simulation (TOMACS)*. 8 (1), 3–30.

Mindlin, R. D. (1949) Compliance of Elastic Bodies in Contact. *Journal of Applied Mechanics*. 16 (3), 259–268.

Mindlin, R. D. & Deresiewicz, H. (1953) Elastic Spheres in Contact Under Varying Oblique Forces. *Journal of Applied Mechanics*. 20 (3), 327–344.

Morimoto, T., Otsubo, M. & Koseki, J. (2021) Microscopic investigation into liquefaction resistance of pre-sheared sand: Effects of particle shape and initial anisotropy. *Soils and Foundations*. 61 (2), 335–351.

Morimoto, T., O'Sullivan, C. & Taborda, D. M. G. (2021) Analytical and DEM studies of thermal stress in granular materials. *EPJ Web Conf.* 249, 14018.

Morimoto, T., O'Sullivan, C. & Taborda, D. M. G. (2022) Exploiting DEM to link thermal conduction and elastic stiffness in granular materials. *Journal of Engineering Mechanics*. 148 (2), 04021139.

Morimoto, T., Zhao, B., Taborda, D. M. & O'Sullivan, C. (2022) Critical appraisal of pore network models to simulate fluid flow through assemblies of spherical particles. *Computers and Geotechnics*. 150, 104900.

Muzychka, Y. & Yovanovich, M. (2004) Laminar forced convection heat transfer in the combined entry region of non-circular ducts. *J. Heat Transfer*. 126 (1), 54–61.

Muzychka, Y. S. & Yovanovich, M. M. (2002a) Laminar flow friction and heat transfer in non-circular ducts and channels part I: hydrodynamic problem. In: *Compact Heat Exchangers: a festschrift on the 60th birthday of Ramesh K. Shah : proceedings of the International Symposium on Compact Heat Exchangers*. Grenoble.

Muzychka, Y. S. & Yovanovich, M. M. (2002b) Laminar flow friction and heat transfer in non-circular ducts and channels part II: thermal problem. In: *Compact Heat Exchangers: a festschrift on the 60th birthday of Ramesh K. Shah : proceedings of the International Symposium on Compact Heat Exchangers*. Grenoble.

Muzychka, Y. S. (1999) *Analytical and experimental study of fluid friction and heat transfer in low Reynolds number flow heat exchangers*. PhD thesis. University of Waterloo.

Nadimi, S & Fonseca, J (2016) Enhancing soil sample preparation by thermal cycling. *Géotechnique*. 66 (11), 953–958.

Ng, C. W. W., Wang, S. & Zhou, C. (2016) Volume change behaviour of saturated sand under thermal cycles. *Géotechnique Letters*. 6 (2), 124–131.

Nijemeisland, M. & Dixon, A. G. (2001) Comparison of CFD simulations to experiment for convective heat transfer in a gas–solid fixed bed. *Chemical Engineering Journal*. 82 (1-3), 231–246.

Niyogi, P. (2009) *Introduction to computational fluid dynamics*. eng. 1st edition. Place of publication not identified, Pearson Education Canada. ISBN: 93-325-0132-7.

Nozad, I, Carbonell, R. & Whitaker, S (1985) Heat conduction in multiphase systems—II: experimental method and results for three-phase systems. *Chemical Engineering Science*. 40 (5), 857–863.

Otsubo, M. (2016) *Particle scale analysis of soil stiffness and elastic wave propagation*. PhD thesis. London, UK: Imperial College London.

Otsubo, M. & O'Sullivan, C. (2018) Experimental and DEM assessment of the stress-dependency of surface roughness effects on shear modulus. *Soils and Foundations*. 58 (3), 602–614.

Otsubo, M., O'Sullivan, C., Hanley, K. J. & Sim, W. W. (2017) The influence of particle surface roughness on elastic stiffness and dynamic response. *Géotechnique*. 67 (5), 452–459.

Otsubo, M., O'Sullivan, C. & Shire, T. (2017) Empirical assessment of the critical time increment in explicit particulate discrete element method simulations. *Computers and Geotechnics*. 86, 67–79.

Pan, Y., Coulibaly, J. B. & Rotta Loria, A. F. (2022) An experimental investigation challenging the thermal collapse of sand. *Géotechnique*. 1–27.

Patzek, T. & Silin, D. B. (2001) Shape factor and hydraulic conductance in noncircular capillaries: I. one-phase creeping flow. *Journal of colloid and interface science*. 236 (2), 295–304.

Peng, Z., Doroodchi, E. & Moghtaderi, B. (2020) Heat transfer modelling in discrete element method (dem)-based simulations of thermal processes: Theory and model development. *Progress in Energy and Combustion Science*. 79, 100847.

Plimpton, S. (1995) Fast parallel algorithms for short-range molecular dynamics. *Journal of Computational Physics*. 117 (1), 1–19.

Ranz, W & Marshall, W (1952) Evaporation from drops. *Chemical Engineering Progress*. 48, 141–146.

Recchia, G., Magnanimo, V., Cheng, H. & La Ragione, L. (2020) DEM simulation of anisotropic granular materials: elastic and inelastic behavior. *Granular Matter*. 22 (4), 1–13.

Romkes, S., Dautzenberg, F., Van den Bleek, C. & Calis, H. (2003) CFD modelling and experimental validation of particle-to-fluid mass and heat transfer in a packed bed at very low channel to particle diameter ratio. *Chemical Engineering Journal*. 96 (1-3), 3–13.

Rong, L., Dong, K. & Yu, A. (2020) Lattice-Boltzmann computation of hydraulic pore-to-pore conductance in packed beds of uniform spheres. *Chemical Engineering Science*. 224, 115798.

Rothenburg, L. & Bathurst, R. J. (1989) Analytical study of induced anisotropy in idealized granular materials. *Géotechnique*. 39 (4), 601–614.

Salot, C., Gotteland, P. & Villard, P. (2009) Influence of relative density on granular materials behavior: DEM simulations of triaxial tests. *Granular matter*. 11 (4), 221–236.

Sarkar, S, van der Hoef, M. A. & Kuipers, J. (2009) Fluid–particle interaction from lattice boltzmann simulations for flow through polydisperse random arrays of spheres. *Chemical engineering science*. 64 (11), 2683–2691.

Schlichting, H. & Kestin, J. (1961) *Boundary layer theory*. Vol. 121. Springer.

Senetakis, K., Coop, M. R. & Todisco, M. (2013) Tangential load–deflection behaviour at the contacts of soil particles. *Géotechnique Letters*. 3 (2), 59–66.

Shah, R. K. & London, A. L. (1978) *Laminar flow forced convection in ducts : a source book for compact heat exchanger analytical data*. eng. Advances in heat transfer, supplement ; 1. New York ; Academic Press. ISBN: 0120200511.

Shimizu, Y. (2006) Three-dimensional simulation using fixed coarse-grid thermal-fluid scheme and conduction heat transfer scheme in distinct element method. *Powder Technology*. 165 (3), 140–152.

Shire, T & O'Sullivan, C (2016) Constriction size distributions of granular filters: a numerical study. *Géotechnique*. 66 (10), 826–839.

Sholokhova, Y., Kim, D. & Lindquist, W. B. (2009) Network flow modeling via lattice-Boltzmann based channel conductance. *Advances in water resources*. 32 (2), 205–212.

Si, H. (2015) TetGen, a Delaunay-based quality tetrahedral mesh generator. *ACM Trans. Math. Softw*. 41 (2), 11.

Siu, W. & Lee, S.-K. (2004) Transient temperature computation of spheres in three-dimensional random packings. *International journal of heat and mass transfer*. 47 (5), 887–898.

Smilauer, V., Angelidakis, V., Catalano, E., Caulk, R., Chareyre, B., Chèvremont, W., Dorofeenko, S., Duriez, J., Dyck, N., Elias, J., Er, B., Eulitz, A., Gladky, A., Guo, N., Jakob, C., Kneib, F., Kozicki, J., Marzougui, D., Maurin, R., Modenese, C., Pekmezi, G., Scholtès, L., Sibille, L., Stransky, J., Sweijen, T., Thoeni, K. & Yuan, C. (November 2021) *YADE documentation*. The Yade Project. DOI: 10.5281/zenodo.5705394. Available from: URL: https://doi.org/10.5281/zenodo.5705394.

Song, C., Wang, P. & Makse, H. A. (2008) A phase diagram for jammed matter. *Nature*. 453 (7195), 629–632.

Sufian, A., Artigaut, M., Shire, T. & O'Sullivan, C. (2021) Influence of fabric on stress distribution in gap-graded soil. *Journal of Geotechnical and Geoenvironmental Engineering*. 147 (5), 04021016.

Sufian, A., Knight, C., O'Sullivan, C., van Wachem, B. & Dini, D. (2019) Ability of a pore network model to predict fluid flow and drag in saturated granular materials. *Computers and Geotechnics*. 110, 344–366.

Suo, S., Moscardini, M., Becker, V., Gan, Y. & Kamlah, M. (2021) Cyclic thermo-mechanical performance of granular beds: effect of elastoplasticity. *Powder Technology*. 394, 705–713.

Sweijen, T., Hassanizadeh, S. M., Chareyre, B. & Zhuang, L. (2018) Dynamic pore-scale model of drainage in granular porous media: The pore-unit assembly method. *Water resources research*. 54 (6), 4193–4213.

Tang, Y, Peters, E., Kuipers, J., Kriebitzsch, S. & van der Hoef, M. (2015) A new drag correlation from fully resolved simulations of flow past monodisperse static arrays of spheres. *AIChE journal*. 61 (2), 688–698.

Tavassoli, H, Peters, E. & Kuipers, J. (2015) Direct numerical simulation of fluid–particle heat transfer in fixed random arrays of non-spherical particles. *Chemical Engineering Science*. 129, 42–48.

Taylor, H. F., O'Sullivan, C., Sim, W. W. & Carr, S. J. (2017) Sub-particle-scale investigation of seepage in sands. *Soils and Foundations*. 57 (3), 439–452.

Tenneti, S, Garg, R & Subramaniam, S (2011) Drag law for monodisperse gas–solid systems using particle-resolved direct numerical simulation of flow past fixed assemblies of spheres. *International journal of multiphase flow*. 37 (9), 1072–1092.

Thompson, K. E. & Fogler, H. S. (1997) Modeling flow in disordered packed beds from pore-scale fluid mechanics. *AIChE Journal*. 43 (6), 1377–1389.

Tsuji, Y., Kawaguchi, T. & Tanaka, T. (1993) Discrete particle simulation of two-dimensional fluidized bed. *Powder technology*. 77 (1), 79–87.

Tsuji, Y., Tanaka, T. & Ishida, T (1992) Lagrangian numerical simulation of plug flow of cohesionless particles in a horizontal pipe. *Powder technology*. 71 (3), 239–250.

Uhlmann, M. (2005) An immersed boundary method with direct forcing for the simulation of particulate flows. *Journal of computational physics*. 209 (2), 448–476.

Van Antwerpen, W, Du Toit, C. & Rousseau, P. (2010) A review of correlations to model the packing structure and effective thermal conductivity in packed beds of mono-sized spherical particles. *Nuclear Engineering and design*. 240 (7), 1803–1818.

Van der Hoef, M. A., Beetstra, R & Kuipers, J. (2005) Lattice-Boltzmann simulations of low-Reynolds-number flow past mono-and bidisperse arrays of spheres: results for the permeability and drag force. *Journal of fluid mechanics*. 528, 233–254.

Van der Hoef, M. A., van Sint Annaland, M & Kuipers, J. (2004) Computational fluid dynamics for dense gas–solid fluidized beds: a multi-scale modeling strategy. *Chemical Engineering Science*. 59 (22-23), 5157–5165.

Van der Linden, J. H., Sufian, A., Narsilio, G. A., Russell, A. R. & Tordesillas, A. (2018) A computational geometry approach to pore network construction for granular packings. *Computers & Geosciences*. 112, 133–143.

Van Oosterom, A. & Strackee, J. (1983) The solid angle of a plane triangle. *IEEE transactions on Biomedical Engineering*. (2), 125–126.

Vargas, W. L. & McCarthy, J. J. (2001) Heat conduction in granular materials. *AIChE Journal*. 47 (5), 1052–1059.

Vargas, W. L. & McCarthy, J. J. (2007) Thermal expansion effects and heat conduction in granular materials. *Physical Review E*. 76 (4), 041301.

Versteeg, H. K. & Malalasekera, W. (2007) *An introduction to computational fluid dynamics: the finite volume method*. Pearson education.

Voight, B & Faust, C (1982) Frictional heat and strength loss in some rapid landslides. *Geotechnique*. 32 (1), 43–54.

Wakao, N. & Kato, K. (1969) Effective thermal conductivity of packed beds. *Journal of Chemical Engineering of Japan*. 2 (1), 24–33.

Walton, K (1987) The effective elastic moduli of a random packing of spheres. *Journal of the Mechanics and Physics of Solids*. 35 (2), 213–226.

Wautier, A., Bonelli, S. & Nicot, F. (2017) Scale separation between grain detachment and grain transport in granular media subjected to an internal flow. *Granular Matter*. 19 (2), 1–15.

Wei, J. & Wang, G. (2017) Discrete-element method analysis of initial fabric effects on pre-and post-liquefaction behavior of sands. *Géotechnique Letters*. 7 (2), 161–166.

Weller, H. G., Tabor, G., Jasak, H. & Fureby, C. (1998) A tensorial approach to computational continuum mechanics using object-oriented techniques. *Computers in physics*. 12 (6), 620–631.

Whitaker, S. (1972) Forced convection heat transfer correlations for flow in pipes, past flat plates, single cylinders, single spheres, and for flow in packed beds and tube bundles. *AIChE Journal*. 18 (2), 361–371.

White, F. M. (2009) *Fluid mechanics*. eng. 7th ed. McGraw-Hill series in mechanical engineering. New York, NY, McGraw-Hill. ISBN: 9780073529349.

Wu, Y., Hou, Q., Qi, Z. & Yu, A. (2021) Particle–pore scale modelling of particle–fluid flows. *Chemical Engineering Science*. 235, 116500.

Wu, Y., Hou, Q. & Yu, A. (2019) Pore-scale study of fluid flow and drag force in randomly packed beds of different porosities. *Industrial & Engineering Chemistry Research*. 58 (12), 5041–5053.

Xu, B. & Yu, A. (1997) Numerical simulation of the gas-solid flow in a fluidized bed by combining discrete particle method with computational fluid dynamics. *Chemical Engineering Science*. 52 (16), 2785–2809.

Yang, J., Wang, Q., Zeng, M. & Nakayama, A. (2010) Computational study of forced convective heat transfer in structured packed beds with spherical or ellipsoidal particles. *Chemical engineering science*. 65 (2), 726–738.

Yilmaz, T & Cihan, E (1993) General equation for heat transfer for laminar flow in ducts of arbitrary cross-sections. *International journal of heat and mass transfer*. 36 (13), 3265–3270.

Yimsiri, S & Soga, K (2000) Micromechanics-based stress–strain behaviour of soils at small strains. *Géotechnique*. 50 (5), 559–571.

Yimsiri, S & Soga, K (2010) DEM analysis of soil fabric effects on behaviour of sand. *Géotechnique*. 60 (6), 483–495.

Yun, T. S. & Evans, T. M. (2010) Three-dimensional random network model for thermal conductivity in particulate materials. *Computers and Geotechnics*. 37 (7-8), 991–998.

Yun, T. S. & Santamarina, J. C. (2008) Fundamental study of thermal conduction in dry soils. *Granular Matter*. 10 (3), 197.

Zhao, B & O'Sullivan, C (2022) Fluid particle interaction in packings of monodisperse angular particles. *Powder Technology*. 395, 133–148.

Zhao, S., Evans, T. M., Zhou, X. & Zhou, S. (2017) Discrete element method investigation on thermally-induced shakedown of granular materials. *Granular Matter*. 19 (1), 1–11.

Zick, A. & Homsy, G. (1982) Stokes flow through periodic arrays of spheres. *Journal of fluid mechanics*. 115, 13–26.

APPENDIX A

COPYRIGHT PERMISSIONS

Name of work	Source of work	Copyright holder	Permission obtained	Permission note
Template of this thesis	Appel (2021)	T. Appel		Cited as the copy right holder requested in DOI 10.5281 /zenodo.4452435
Fig. 2.3	Birkholz, Gan and Kamlah (2019)	Elsevier	7 Dec 2022	Written permission received
Figs. 2.5, 2.6, 3.1 and 3.2 and Section 3.3.1, and all figures and text in Chapter 4	Morimoto, O'Sullivan and Taborda (2022)	American Society of Civil Engineers	25 July 2022	Written permission received
Fig. 2.9	Otsubo (2016)	M. Otsubo		Creative Commons Attribution Non-Commercial No-Derivatives 4.0 International (CC BY-NC-ND 4.0)

Fig. 3.3(a)	Yun and Evans (2010)	Elsevier	29 Nov 2022	Written permission received
Figures and text in Chapter 5	Morimoto, O'Sullivan and Taborda (2021)	T. Morimoto		Creative Commons Attribution 4.0 International (CC BY 4.0
Figures and text in Chapter 8	Morimoto et al. (2022)	Elsevier		Creative Commons Attribution 4.0 International (CC BY 4.0)

APPENDIX B

REPEATABILITY OF EFFECTIVE THERMAL CONDUCTIVITY OF DEM SAMPLES

This appendix shows the repeatability of the effective thermal conductivity value reported in Chapter 4. Four sets of samples among the samples studied in Chapter 4 were picked:

1. The densest IC (isotropically consolidated) sample (The sample created using $\mu_{\text{fric}} = 0.01$ during the isotropic compression).
2. The loosest IC sample (The sample created using $\mu_{\text{fric}} = 0.34$ during the isotropic compression).
3. The TCUL (triaxial compression and unloaded) sample, which was created by applying the triaxial compression to the densest IC sample up to $\varepsilon_{zz} = 10\%$ and conducting the unloading until the isotropic stress state was attained.
4. The TCUL sample, which was created by applying the triaxial compression to the loosest IC sample up to $\varepsilon_{zz} = 10\%$ and conducting the unloading until the isotropic stress state was attained.

The isotropic stress was 100 kPa for all the four cases. Two additional samples for each case were created following the same procedure reported in Chapter 4 and the effective thermal conductivity values of them in x and z-directions were measured by the same procedure as Section 4.3.3. The smallest and largest κ values, 10 and 500, were used.

All the results are summarised with the mean, the standard deviation (SD), and the coefficient of variation (CV) in Tables B.1 to B.4. The coefficient of variation is the standard deviation divided by the mean value. Each of "Sample 1" in Tables B.1 to B.4 is equivalent to the sample used in Chapter 4. The CV values for the effective thermal conductivity of the samples were $< 0.23\%$, which demonstrates that the effective thermal conductivity values reported in Chapter 4 are repeatable.

Table B.1: The densest IC samples.

	Sample 1	Sample 2	Sample 3	Mean	SD	CV
N_p	21217	21222	21221	21220	2.65	0.01%
e	0.605	0.607	0.606	0.606	0.001	0.17%
$\overline{Z}$	5.653	5.671	5.670	5.665	0.010	0.18%
$k^*{}_{xx}/k_\mathrm{f}$ ($\kappa = 10$)	5.703	5.691	5.691	5.695	0.007	0.12%
$k^*{}_{zz}/k_\mathrm{f}$ ($\kappa = 10$)	5.702	5.679	5.684	5.688	0.012	0.21%
$k^*{}_{xx}/k_\mathrm{f}$ ($\kappa = 500$)	23.299	23.337	23.357	23.331	0.029	0.13%
$k^*{}_{zz}/k_\mathrm{f}$ ($\kappa = 500$)	23.311	23.288	23.254	23.284	0.029	0.12%

Table B.2: The loosest IC samples.

	Sample 1	Sample 2	Sample 3	Mean	SD	CV
N_p	21217	21222	21221	21220	2.65	0.01%
e	0.719	0.717	0.717	0.717	0.001	0.18%
$\overline{Z}$	4.323	4.352	4.318	4.331	0.018	0.42%
$k^*{}_{xx}/k_\mathrm{f}$ ($\kappa = 10$)	4.808	4.809	4.815	4.811	0.004	0.08%
$k^*{}_{zz}/k_\mathrm{f}$ ($\kappa = 10$)	4.803	4.816	4.819	4.813	0.009	0.18%
$k^*{}_{xx}/k_\mathrm{f}$ ($\kappa = 500$)	18.328	18.371	18.414	18.371	0.043	0.23%
$k^*{}_{zz}/k_\mathrm{f}$ ($\kappa = 500$)	18.354	18.405	18.375	18.378	0.026	0.14%

Table B.3: The TCUL samples using the densest IC samples as the input.

	Sample 1	Sample 2	Sample 3	Mean	SD	CV
N_p	21217	21222	21221	21220	2.65	0.01%
e	0.663	0.664	0.662	0.663	0.001	0.12%
$\overline{Z}$	4.759	4.762	4.766	4.762	0.003	0.07%
$k^*{}_{xx}/k_\mathrm{f}$ ($\kappa = 10$)	5.233	5.219	5.233	5.229	0.008	0.15%
$k^*{}_{zz}/k_\mathrm{f}$ ($\kappa = 10$)	5.269	5.260	5.270	5.266	0.005	0.10%
$k^*{}_{xx}/k_\mathrm{f}$ ($\kappa = 500$)	19.164	19.128	19.148	19.146	0.018	0.09%
$k^*{}_{zz}/k_\mathrm{f}$ ($\kappa = 500$)	20.979	20.986	20.977	20.981	0.005	0.02%

Table B.4: The TCUL samples using the loosest IC samples as the input.

	Sample 1	Sample 2	Sample 3	Mean	SD	CV
N_{p}	21217	21222	21221	21220	2.65	0.01%
e	0.703	0.702	0.702	0.702	0.001	0.08%
$\overline{Z}$	4.725	4.737	4.735	4.732	0.006	0.13%
${k^*}_{xx}/k_{\mathrm{f}}$ ($\kappa = 10$)	4.911	4.909	4.913	4.911	0.002	0.05%
${k^*}_{zz}/k_{\mathrm{f}}$ ($\kappa = 10$)	4.946	4.952	4.954	4.951	0.004	0.09%
${k^*}_{xx}/k_{\mathrm{f}}$ ($\kappa = 500$)	18.418	18.484	18.477	18.460	0.036	0.20%
${k^*}_{zz}/k_{\mathrm{f}}$ ($\kappa = 500$)	19.858	19.856	19.871	19.862	0.008	0.04%

APPENDIX C

VERIFICATION OF ANALYTICALLY DETERMINED Γ VALUE

The analytical approach to determine the Γ values employed in Section 8.3.1 requires some assumptions: (a) the pressure gradient is constant through the packing; and (b) the flow direction at the throat face is normal to the throat face. Therefore, the derived Γ values need independent verification. The analytically-derived Γ values determined by analysing the Zick and Homsy (1982) data were verified using the OpenFOAM (OF) simulation results for the FCC packings introduced above. The Γ value of the throat indicated in Fig. C.1(a) was calculated following the post-processing procedure outlined in Section 8.4.3.

A comparison between values calculated from the OF generated data for regular packings, Γ^{RP}, and those obtained from Eq. (8.35) is shown in Table C.1. For a wide range of e values ($0.35 < e < 1.64$), a good agreement was obtained, which confirms the viability of using the Zick and Homsey data to estimate Γ^{RP}.

Table C.1: Tabular summary of comparison between Γ^{RP} values of OpenFOAM and analytical studies for FCC packings.

D	e	OF Γ^{RP} $[m^4]$	Analytical Γ^{RP} $[m^4]$
0.8Δ	1.64	3.152×10^{-14}	3.095×10^{-14}
0.9Δ	0.85	8.617×10^{-15}	8.828×10^{-15}
Δ (densest)	0.35	1.367×10^{-15}	1.202×10^{-15}

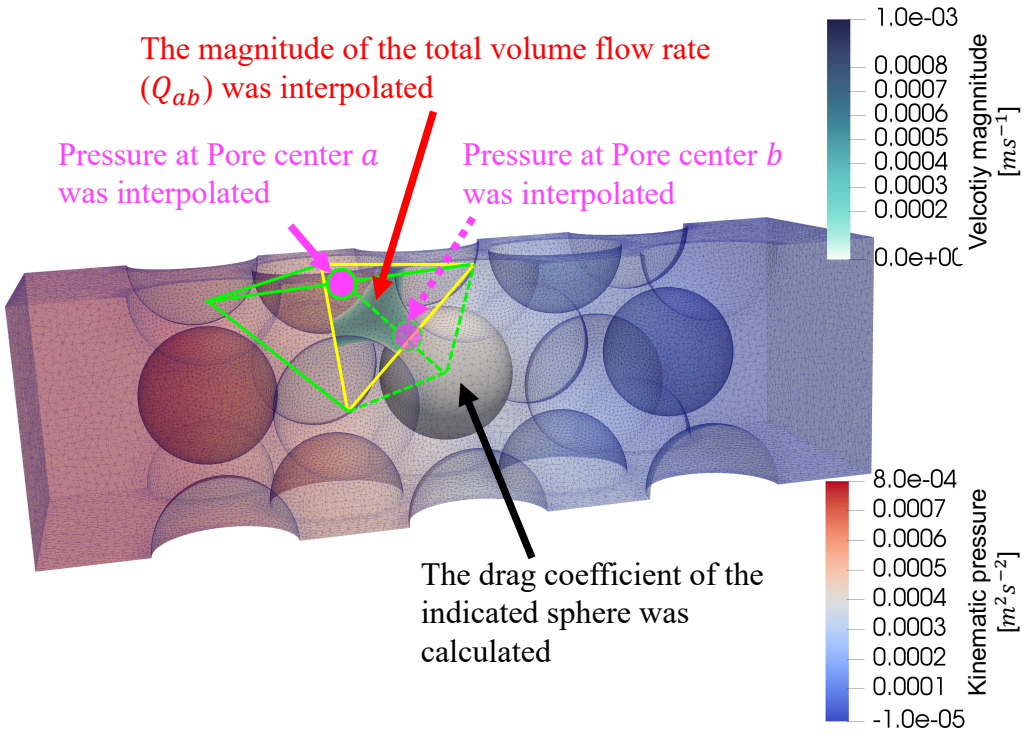


Figure C.1: Schematic illustration of OF simulations using FCC packings for validation. The geometry of an FCC model and the throat considered for validation.

APPENDIX D

CONSIDERATION OF PERIODIC BOUNDARIES IN A PORE NETWORK MODEL

This study considers periodic boundaries for the x- and y-directions to minimise boundary effects. Here, referring to Fig. D.1, the way in which the periodic boundaries were implemented for completeness.

(1) A "cut-off distance" is specified adjacent to the periodic boundaries and the particles whose distance from one side of a periodic boundary is smaller than the cut-off distance are copied to the corresponding position just outside the opposite periodic boundary. This procedure is conducted $3^n - 1$ times, where n is the number of directions where periodic boundaries considered in the simulation. The original domain is called the "local" domain and the other domains created by this procedure are termed "ghost" domains. There are $3^n - 1$ ghost domains in the PNM simulation. Particles, whose centres are in the local domain, are "local" particles and the that are copied and mapped are "ghost" particles. There are two ID systems for the particles: (1) the local ID system, where a ghost particle has a different ID from the original particle, and (2) the global ID system, where ghost particles have the same IDs as the original particles. Local particles have the same local ID and global ID. When a new particle is created, a new local ID is assigned to the particle and the ID of the original particle is also stored as the global ID.

(2) The local IDs, positions, and radii of the local and ghost particles are passed to `TetGen` and a weighted Delaunay triangulation is carried out. The weighting on the triangulation is the square of the particle radius. TetGen returns the local IDs of particles which define each pore and connectivity information between pores.

(3) The “local” and “ghost” pores are defined following Beyer et al. (2005). For each pore, there is a check to assess the particles defining the pore are local or ghost particles. If all the particles are local, the pore is a local pore. When a mixture of local and ghost particles define a pore, the pore is assigned to whichever the domain is associated with the largest particle.

(4) There is a system of local and global IDs for the pores. Once the local and ghost pores are determined, we assign identical local and global IDs to the local pores starting from zero. Once the IDs are assigned to the local pores, a hashmap is created which stores the global pore ID of each local pore with the global particle IDs consisting of the local pore being the key.

(5) After creating the hashmap, each ghost pore is assigned for a new local pore ID, and the global ID of the original pore is assigned to the ghost pore, with the original pore being detected using the global particle IDs of the particles consisting of the ghost pore. There are two scenarios where the original local pore of a ghost pore not being found. One occurs when the cut-off distance is too small and can be resolved by increasing the cut-off distance. The other case is where there is a lattice-like particle configuration (which can occur in regular packings), for this scenario the weighted Delaunay triangulation is not unique. In this case, a very small perturbation in the particle positions can resolve the problem.

(6) Each local pore is checked and for each pore connection the local pore has, the Γ value is calculated, and the elements of the conductivity matrix is filled using the global pore IDs of the local pore and adjacent pore.

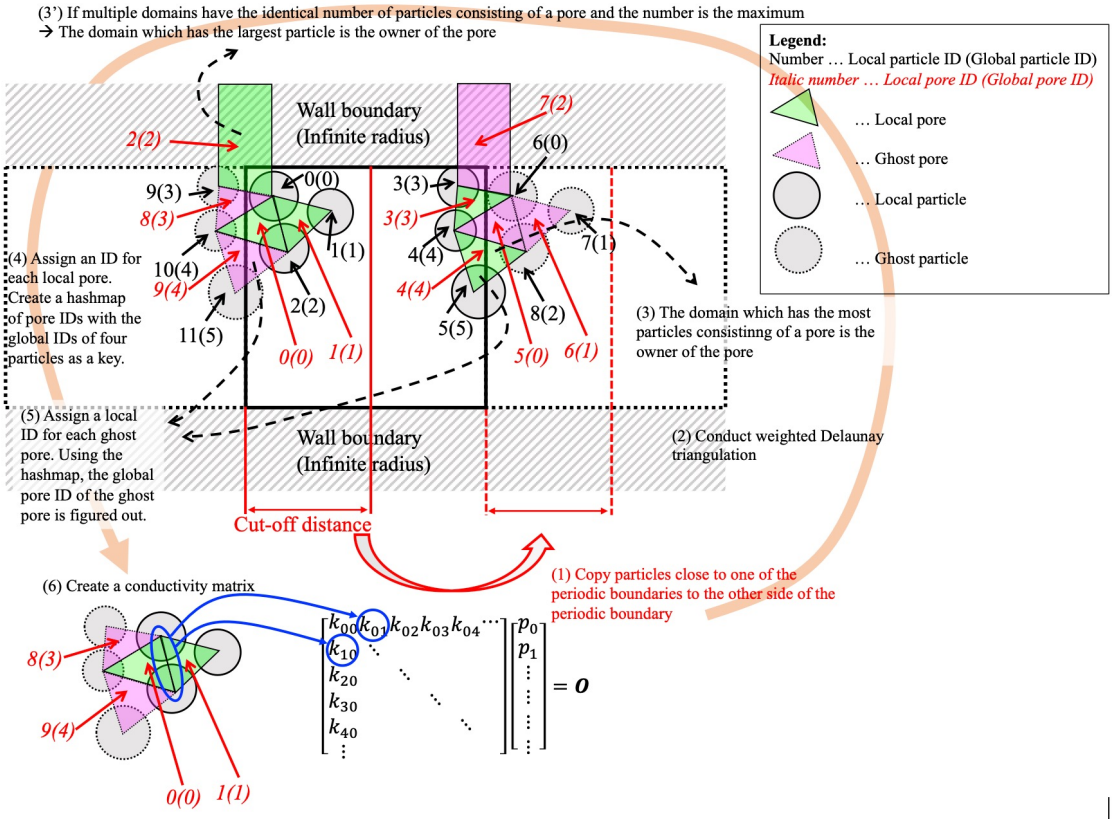


Figure D.1: Schematic illustration of OF simulations using FCC packings for validation. The geometry of an FCC model and the throat considered for validation.

APPENDIX E

RELATIONSHIP BETWEEN fRe AND SHAPE FACTOR FOR A HYDRODYNAMICALLY FULLY-DEVELOPED FLOW IN A PIPE

In Chapter 8, a shape factor, α, was used to characterise the shape of a pipe (or a throat connecting two pores) following a study on local conductance models in PNMs (Patzek & Silin, 2001; Chareyre et al., 2012). On the other hand, the literature review in Chapter 9 showed that the product of the friction factor f and the Reynolds number Re has been used in some previous studies (Muzychka & Yovanovich, 2002b; Bennett, 2019b) to predict the Nusselt number in pipes with a variety of cross-sectional shapes. This α can be related to the product fRe.

If the flow is steady i.e. when there is no acceleration in the fluid movement, the pressure drop in the pipe is related to the sum of the shear stress (equal to mean shear stress $\overline{\tau}$ multiplied by the surface area of the pipe γ) as

$$\overline{\tau}\gamma = \Delta p A \tag{E.1}$$

Therefore, $\overline{\tau}$ can be written in terms of the pressure drop Δp, the length of the pipe L, and the hydraulic diameter ($d_{\text{h}} = 4\Theta/\gamma = 4AL/\gamma$) as

$$\overline{\tau} = \Delta p \frac{A}{\gamma} = \Delta p \frac{d_{\text{h}}}{4L} \tag{E.2}$$

Using Eq. (E.2), the friction factor f, defined in Eq. (9.34), can be rewritten as

$$f = \frac{\Delta p \frac{d_\mathrm{h}}{L}}{2\rho_\mathrm{f}\overline{u}^2} \tag{E.3}$$

The Reynolds number for a characteristic length of $\mathcal{L}$ is

$$Re_\mathcal{L} = \frac{\rho_\mathrm{f}\overline{u}\mathcal{L}}{\mu_\mathrm{f}} \tag{E.4}$$

Therefore, the product of f and $Re_\mathcal{L}$ is

$$fRe_\mathcal{L} = \frac{\Delta p d_\mathrm{h}\mathcal{L}}{2\mu_\mathrm{f}\overline{u}L} \tag{E.5}$$

With $\overline{u} = Q/A$, Eq. (E.5) can be rearranged to a form that is similar to Darcy's law as

$$Q = \frac{1}{2fRe_\mathcal{L}}\frac{Ad_\mathrm{h}\mathcal{L}}{\mu_\mathrm{f}L}\Delta p \tag{E.6}$$

Taking the hydraulic diameter d_h to be the characteristic length,

$$Q = \frac{1}{2fRe_{d_\mathrm{h}}}\frac{A{d_\mathrm{h}}^2}{\mu_\mathrm{f}L}\Delta p = \frac{8}{fRe_{d_\mathrm{h}}}\frac{A{r_\mathrm{h}}^2}{\mu_\mathrm{f}L}\Delta p \tag{E.7}$$

The intrinsic conductance of the pipe is calculated as defined in Eqs. (8.3) and (8.4):

$$\mathcal{G} = \frac{8}{fRe_{d_\mathrm{h}}}\frac{A{r_\mathrm{h}}^2}{L} \tag{E.8}$$

Comparing this conductance expression to the HR model in Eq. (8.10), a relationship between fRe_{d_h} and α_HR is obtained as

$$\frac{2}{fRe_{d_\mathrm{h}}} = \alpha_\mathrm{HR} \tag{E.9}$$